Effects of Helium Ion Implantation on the Surface Morphology of Tungsten at High Temperature for the First Wall Armor and Divertor Plates of Fusion Reactors

Samuel J. Zenobia

June 2010

UWFDM-1377

Ph.D. thesis.

FUSION TECHNOLOGY INSTITUTE

UNIVERSITY OF WISCONSIN

MADISON WISCONSIN

Effects of Helium Ion Implantation on the Surface Morphology of Tungsten at High Temperature for the First Wall Armor and Divertor Plates of Fusion Reactors

Samuel J. Zenobia

Fusion Technology Institute
University of Wisconsin
1500 Engineering Drive
Madison, WI 53706

http://fti.neep.wisc.edu

June 2010

UWFDM-1377

Ph.D. thesis.

EFFECTS OF HELIUM ION IMPLANTATION ON THE SURFACE MORPHOLOGY OF TUNGSTEN AT HIGH TEMPERATURE FOR THE FIRST WALL ARMOR AND DIVERTOR PLATES OF FUSION REACTORS

By

Samuel J. Zenobia

A dissertation submitted in partial fulfillment of

The requirements for the degree of

Doctor of Philosophy

(Nuclear Engineering and Engineering Physics)

at the

UNIVERSITY OF WISCONSIN-MADISON

2010

Abstract

Tungsten is a primary candidate material for the first wall armor in inertial fusion reactors and the divertor plates in magnetic fusion reactors. The work presented in this thesis addresses a key challenge to tungsten's (and tungsten's alloys) survivability as a fusion material – resistance to surface damage from the energetic bombardment of helium ions emanating from the fusion events. Initial investigations of surface damage effects on W and W alloys after helium implantation at high temperatures utilized the HOMER device at the University of Wisconsin-Madison Inertial Electrostatic Confinement (UW IEC) laboratory. To examine a larger set of reactor relevant conditions, the implantation parameter space was expanded by transitioning to the HELIOS IEC device and then to the Materials Irradiation Experiment (MITE-E). Each of these devices was used to study the effects of high energy He^+ implantation on the surface morphology of high temperature tungsten, although the MITE-E was specifically designed and built to simulate some unique features of the in-vessel radiation environment.

Early UW work on silicon carbide, carbon velvet, W-coated carbon velvet, fine-grain W, nano-grain W, W needles, and single- and polycrystalline W showed that none of these materials are resistant to He^+ implantation above ~800 °C. Unalloyed W developed a "coral-like" surface morphology after He^+ implantation, but appeared to be the most robust material investigated.

The MITE-E used a modified ion gun technology developed within the UW IEC group to implant tungsten with an 8 mm diameter beam of nearly mono-energetic helium ions at energies between 20 and 130 keV, ion currents between 20 and 180 µA, and implantation temperatures between 400 and 1100 °C. The MITE-E also decoupled specimen implantation temperature and voltage difference from the input ion

power. Polycrystalline W specimens were implanted at 900 °C to total average fluences of $6x10^{16}$ – $6x10^{18}$ He^+/cm^2. Other specimens were implanted to a total average fluence of $5x10^{18}$ He^+/cm^2 at temperatures between 500 and 900 °C. Micrographs of the implanted specimens revealed the development of three distinct surface morphologies. These were "blistering", "pitting", and "orientated ridges".

Preferential sputtering of the W by the energetic He appears to be largely responsible for the pitting and orientated ridges which developed at high fluences (10^{19} He^+/cm^2) in the MITE-E. The orientated ridge morphology was dominant on the surface above 700 °C, while pitting was prevalent below the 700 °C transition temperature. The blistering morphology was observed at all of the examined temperatures at fluences $\geq 5x10^{17}$ He^+/cm^2 but disappeared above fluences of $\sim 10^{19}$ He^+/cm^2. This surface deformation is attributed to pressure buildup from coalescence helium bubbles near the W surface.

The coral-like surface morphology on W inherent to He^+ implantation experiments in HOMER and HELIOS developed from a combination of sources: multi-angular ion incidence, ion energy spread (softening), and electron field emission from nano-scale surface features induced by He^+ implantation. The HOMER and HELIOS devices were found to be better suited for simulation of magnetic fusion environments with off-normal particle incidences, and the MITE-E was found to be more suited for simulating the normal particle incidence of inertial fusion environments.

Acknowledgments

My time spent at the University of Wisconsin has been a full and life-shaping experience that would not have been possible, or as enjoyable, without the help of my colleagues, family, and friends. First and above all else, I want to thank my Lord and Savior Jesus Christ who has provided me the opportunity and ability to pursue my dreams. As it is written, without Him I can do nothing, but through Him I can do all things.

My deepest and sincerest thanks go to Professor Gerald Kulcinski, a phenomenal advisor, but also a true mentor whose professional and wise conduct has inspired me to excel in every aspect of my education. I would like to thank Robert Ashley and Richard Bonomo for their technical support and patience to help me work through what seemed to be insurmountable obstacles and setbacks. I am grateful to John Santarius who was always willing to answer my questions and offer insight.

Moreover, I am especially thankful to the members UW IEC research group: Eric Alderson, David Donovan, Gabriel Becerra, Lauren Garrison, Craig Schuff, Matt Michalak, and Logan Campbell. Their commitment to teamwork, as well as scientific rigor, has made the UW IEC laboratory a great place to work. I also want to acknowledge and thank Greg Piefer, Ross Radel, Dave Boris, and Brian Egle, who have since moved on, but were never too busy to lend a helping hand or provide a much needed word of encouragement.

My thanks go to the faculty and staff of the Engineering Physics Department and the Fusion Technology Institute, specifically Professor Todd Allen, Joan Welc-LePain, Dennis Bruggink, and Nancy Griego.

I also want to acknowledge the DOE for funding the majority this work, and the Greatbatch Foundation and the Grainger Foundation for their generous financial gifts. Specifically, I am grateful to Dr. John Sethian whose support made continuation of this work possible.

My sincerest thanks go to my church “family” in Sun Prairie and especially Rev. Basil Wilber who have motivated me to do the best I can for my fellow man and for God. I owe many thanks to my family. I want to thank my brothers Frank, Laddie, Bill, and Anthony and my sisters Christy, Karen, and Martina who have always been supportive and loving. Lastly, I want to thank my parents Frank and Judy, who have stood behind every good endeavor of my life with all that they had. I am grateful for their love, for their discipline, and for their Christian example.

TABLE OF CONTENTS

TABLE OF FIGURES

TABLE OF TABLES

CHAPTER 1. INTRODUCTION

Magnetically or inertially confined plasmas in commercial fusion reactors will only be economically viable if major maintenance procedures and down time is minimized. Most often, these maintenance requirements are compromised by failure of the in-vessel materials, such as the first wall armor or divertor plates. In Inertial Fusion Energy (IFE) and Magnetic Fusion Energy (MFE) devices, the ability of these components to withstand temperatures near their operational limit and endure significant radiation damage due to ion, neutron, and x-ray fluxes is crucial to their success. Recently, the materials challenges which lie on the path to fusion energy have gained considerable attention among the international fusion community. As large research programs, such as the IFE National Ignition Facility (NIF) [1], prepare to come online and projects like the MFE device ITER [2] ratchet up, more emphasis is being placed on materials testing and the possibility of new materials testing facilities [3]. In fact, as of October 2009, the European tokamak JET commenced removal of the existing in-vessel carbon tiles and began their replacement with beryllium tiles for the first wall and tungsten tiles for the divertor plates. This materials testing project is in direct preparation for the operation of ITER. In speaking about the JET upgrade and ensuing materials tests, the Internal Components Head of the ITER project, summed up the tone of the international fusion community in his statement:

> "*…they* [the materials tests] *will provide us with information on the lifetime of components, and from a physics standpoint, how the plasma behaves with a combination of beryllium and tungsten. We are very keen on getting these results.*" -Mario Merola, [4]

Clearly, the development, testing, and survival of the chosen plasma facing material under fusion relevant conditions are pivotal to the future success of fusion energy. One of the primary candidate materials for many IFE systems such as the High Average Power Laser (HAPL) program [5] and the MFE ITER divertor is tungsten. Any such device utilizing a D-T fuel cycle for fusion will experience substantial charged particle fluxes of D, T, and He which bombard these components over a wide range of energies. The research presented in this dissertation focuses on the energetic alpha particles present in these devices and tungsten's response to this radiation. Several materials besides tungsten were tested and analyzed, but are not stressed in this thesis.

Materials implantation studies for fusion reactor designs began at the Inertial Electrostatic Confinement (IEC) laboratory at the University of Wisconsin – Madison in 2004. [6] The focus of this research is to study the effects of helium ion bombardment on candidate materials for plasma facing components in fusion reactors. The initial studies performed on tungsten metallics [7,8] showed a poor response of these materials to high temperature helium implantation.

The work presented in this thesis is comprised of materials implantation experiments carried out in three devices within the UW IEC group: HOMER, HELIOS, and the Materials Irradiation Experiment (MITE-E). The HOMER device was used to implant helium into silicon carbide, carbon velvet, and tungsten-coated carbon velvet at high temperatures. These implantation studies were then transitioned to the IEC device HELIOS in which carbon velvet, tungsten-coated carbon velvet, single- and polycrystalline tungsten, nano- and fine-grain tungsten and tungsten needles were examined. Although none of the examined materials exhibited acceptable resistance to high temperature helium implantation, tungsten appeared to respond the best under experimental conditions. At this point, the idea for the MITE-E was proposed and accepted in an effort to determine at what conditions tungsten – or any candidate material for fusion reactor in-vessel components – could acceptably withstand bombardment with helium ions. With this information in-hand, the next step was to understand the mechanism by which this microstructure is developed in a given material. The objective was to make recommendations for engineered materials capable of withstanding the harsh environments intrinsic to fusion reactors.

The MITE-E was designed and constructed around the primary goal of this dissertation – to examine the response of plasma facing components in fusion reactors to light ion bombardment (H, D, ^{3}He and ^{4}He). To accomplish this task, the MITE-E was designed and built with the ability to operate over a wide range of implantation parameters which were previously unavailable in the HOMER and HELIOS devices. A versatile, compact ion gun technology developed within the UW IEC group for the SIGFE [9], was modified into a collimated particle beam capable of irradiating materials. Integrating the ion gun technology with an independent laser heating system, enhanced diagnostics and control, and improved data monitoring has allowed the MITE-E to further explore the fusion materials studies initiated at the UW IEC laboratory in 2004.

The primary objective of this dissertation was to construct the Materials Irradiation Experiment and investigate the response of pure tungsten to implantation with energetic helium ions under fusion reactor relevant conditions. A secondary goal of this work was to compare the results of previous materials implantation experiments carried out in the UW IEC devices HOMER and HELIOS. Both of these objectives were accomplished and agreed with previous high temperature implantation studies. [7,8,10]

One major discovery of this thesis was that the MITE-E implants ions in a fundamentally different way than HOMER and HELIOS. The MITE-E irradiated tungsten specimens with a collimated beam of helium ions normally incident to the sample surface over a range of temperatures and doses. This resulted in pore formation, blistering, “pitting,” and “grass-like” surface morphology changes which were highly dependent upon crystallographic orientation of individual grains. In HOMER and HELIOS, tungsten was implanted at high temperature with helium ions at multiple angles of incidence. The high temperature helium implantation of tungsten in this environment produced a random porous, “coral-like” surface morphology, uniformly on the specimen. This thesis shows that the observed morphology response of tungsten is a result of the angle at which helium ions are implanted.

In IFE systems, alpha particles bombard the first wall armor normal to its surface. Conversely, in MFE systems, the alpha particle flux (helium ash) will impact the first wall and divertor with a wide range of incidence angles off normal to these surfaces. The behavior of the ions in these two classes of fusion reactors are illustrated in Figure 1-1. In light of these behaviors, it has been suggested that the MITE-E would be best used in IFE studies, as it better simulates the flux of ions bombarding the first wall armor of IFE reactors. On the other hand, the HOMER and HELIOS apparatus are best employed in MFE studies to more accurately simulate the flux of helium ash experienced on the first wall and divertors.

Several of the topics that are presented and discussed in this thesis have also been published in peer-reviewed articles by this author. They are directly referenced here for the reader's benefit:

- **Zenobia, S. J**., Radel, R. F., Cipiti, B. B., and Kulcinski, G. L., (2009) High temperature surface effects of He^+ implantation in ICF fusion first wall materials. *Journal of Nuclear Materials*, 389, 213-220.

- **Zenobia, S. J.** and Kulcinski, G. L., (2009) Retention and surface pore formation in helium implanted tungsten as a fusion first wall material. *Fusion Science and Technology*, 52, 544.

- **Zenobia, S. J.** and Kulcinski, G., (2009) Formation and retention of surface pores in helium-implanted nano-grain tungsten for fusion reactor first-wall materials and divertor plates. *Physica Scripta*, T138, 014049.

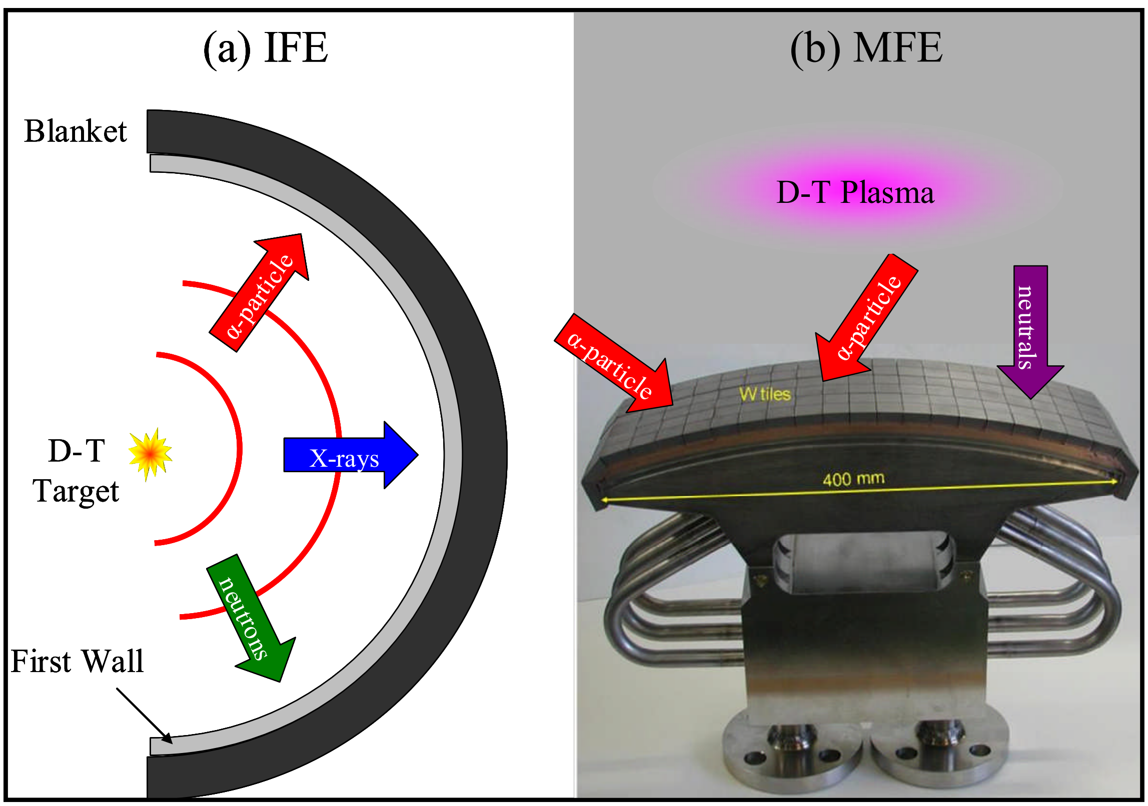

Figure 1-1: Schematic representation of the alpha-particle flux in (a) IFE systems, where ion incidences are normal to the first wall armor surface in a spherical vacuum vessel, and (b) in MFE systems, where the ITER divertor prototype [11] illustrates the multi-angular incidence of alpha-particles to the first wall and divertor.

1.1. References for Chapter 1

1. Hogan, W. J., (2001) The national ignition facility. *Nuclear Fusion*, 47, 567.

2. Shimomura, Y. et al., (1999) ITER overview. *Nuclear Fusion*, 39, 1295.

3. Moeslang, A. et al., (2006) The IFMIF test facilities design. *Fusion Engineering and Design*, 81, 263-271.

4. Feder, T., (2010) JET gets new wall to prep for ITER. *Physics Today*, December, 24-25.

5. Sethian, J.D., et al., (2003) Fusion energy with lasers, direct-drive targets, and dry wall chambers. *Nuclear Fusion*, 42, 1963.

6. Santarius, J. F. et al., (2005) Overview of university of wisconsin inertial-electrostatic confinement fusion research. *Fusion Science and Technology*, 47 (4), 1238-1244.

7. Cipiti, B.B. (2004). The fusion of advanced fuels to produce medical isotopes using inertial electrostatic confinement. (Doctoral dissertation, University of Wisconsin - Madison)

8. Radel, R. F. (2007). Detection of highly enriched uranium and tungsten surface damage studies using a pulsed inertial electrostatic confinement fusion device (Doctoral dissertation, University of Wisconsin – Madison)

9. Egle, B. J. (2010). Nuclear fusion of advanced fuels using converging focused ion beams (Doctoral dissertation, University of Wisconsin – Madison)

10. Zenobia, S. J. and Kulcinski, G. L., (2009) Retention and surface pore formation in helium implanted tungsten as a fusion first wall material. *Fus. Sci. and Technology*, 52, 544.

11. Merola, M., (2008) Qualification process – Russian divertor prototype exceeds requirements. Available at http://www.iter.org/newsline/Pages/48/Article.aspx?645.

Chapter 2. PREVIOUS WORK

2.1. Introduction

By the 1960s, the negative effects of helium production in fission reactor components (cladding, fuel, and fuel assemblies) by neutron capture became a recognized phenomenon and challenge to the nuclear science community. This was evidenced by a comprehensive report by Barnes and Nelson [1] and echoed in the 1980s by Behrisch and Scherzer. [2] Also in the 1960s, researchers began investigating the response of refractory materials in conceptual fusion reactors to radiation damage, specifically, helium ion bombardment. [3] As the idea of fusion power gained momentum, a new challenge on the path to fusion power emerged - helium damage to the in-vessel reactor components became an economic issue as well as a scientific issue. In the present day, helium production by neutron capture and surface damage by energetic bombardment of light ions, like helium, remain a major hurdle for the successful operation of plasma facing components for nuclear reactors. [4,5,6,7,8]

2.2. ITER divertor plates and the High Average Power Laser (HAPL) program

A primary economic concern of magnetically fusion energy (MFE) and inertial fusion energy (IFE) fusion reactor studies is the down time due to equipment failure. Premature failure of the in-vessel reactor components can severely compromise the scheduled maintenance procedures, which are necessary to keep fusion power commercially competitive. The divertor plate area in magnetic fusion energy reactors and the first-wall armor for chambers in inertial confinement fusion reactors must withstand high temperatures and significant radiation damage from D–T plasmas. Though a plethora of refractory materials are being considered for these components, tungsten's high melting point and low sputtering coefficient have kept it at the forefront of international fusion materials research. [9] Therefore, this thesis focuses on tungsten, though analyses of other materials are presented.

The International Thermonuclear Experimental Reactor (ITER) has been the primary focus of many national fusion science programs since United States President Ronald Reagan and former Soviet Union Premier Mikhail Gorbachev signed the initiative that led to the ITER Conceptual Design Activities (CDA) at the 1985 Geneva Summit. [10] The most recent plans for the ITER divertor are to use a carbon fiber-reinforced carbon for the initial startup, but switch to a fully tungsten divertor in subsequent years. [11] The divertor is comprised of many separate tiles, each water-cooled, and each with 1 cm of cladding material facing the plasma. A computer-aided design (CAD) representation of a recent design of the ITER divertor is given in Figure 2-1. During operation the first wall and divertor of ITER will sustain particle fluxes (H, D, T, and He) in excess of 10^{23} $m^{-2}s^{-1}$ and temperatures $\geq$700 °C [12]. The materials used must operate under these conditions for a year without failure or unacceptable erosion. While the majority of particles are deuterium and tritium isotopes, there will be a substantial flux of He ash to these components. [12] Figure 2-2 gives the estimated lifetime of the ITER divertor for W, C, and Be materials and for a plasma discharge lasting 1000 s.

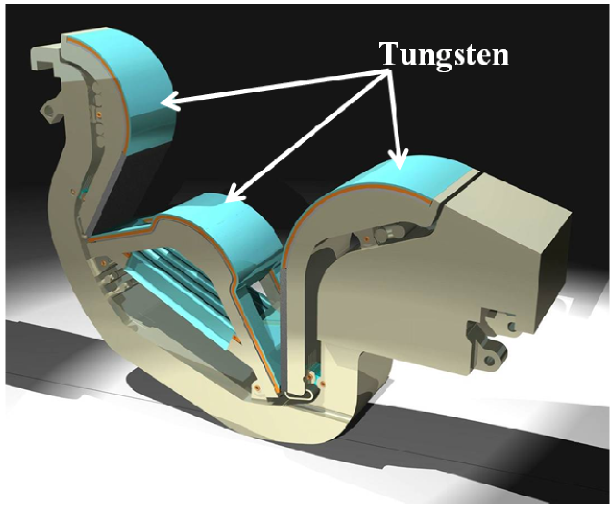

Figure 2-1: Computer-aided design (CAD) rendering of the ITER divertor [11]

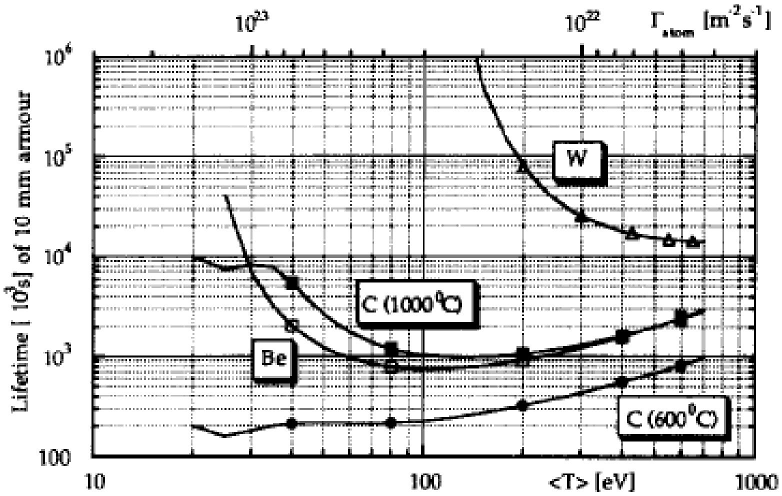

Figure 2-2: Erosion lifetime of divertor armor at side walls and baffle (in number of 1000 s discharges) versus neutral particle energy <T> (in eV) for Be, C, and W, 10 mm thick. Incident power is assumed constant at 0.5 MW/m^2 without redeposition. The range of neutral energies is ~5 to 100 eV, but for each data point, a monoenergetic distribution with energy <T> is assumed for calculation. [12]

The High Average Power Laser (HAPL) program focuses on the design of a commercial, direct-drive IFE reactor. [13] A principle concern in the development of this project is the fusion chamber's first wall armor. The reference HAPL chamber design is spherical with a radius of 10.5 m. High intensity laser pulses implode deuterium-tritium ice pellets encased in plastic and gold layers at a repetition rate of ~10 Hz. Once the target is injected and reaches the chamber's center the external laser system is focused onto the target through a series of mirrors (Figure 2-3). This laser heating ablates the outer shell of the target and compresses a cryogenic D-T fuel inner shell in the center of the target pellet. Compression and heating of the D-T fuel initiates the fusion burn, and results in the energetic expulsion of fusion products (neutrons, x-rays, and unburned fuel ions) toward the first wall.

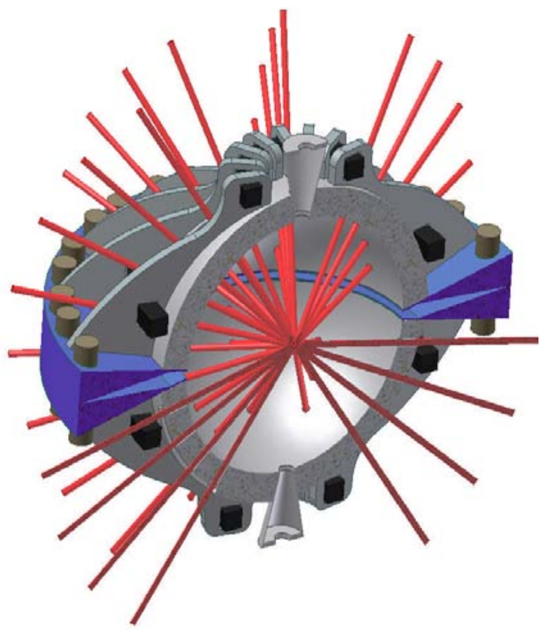

Figure 2-3: Computer-aided design (CAD) representation of the reference HAPL chamber [14]

Proposed first wall armor coatings are 250 – 500 µm thick and are bonded to a ferritic steel vacuum vessel. As mentioned, the HAPL chamber's first wall armor endures light ion fluxes ranging in energy from ~10 keV to several MeV. These ion fluxes have the potential to degrade the armor through sputtering, blistering, and exfoliation. Over time, such events can create radioactive dust, contaminate laser optics, and, if released, could harm the public. Though the surface temperature of the first wall armor will reach transient temperatures above 2000 ºC, the baseline temperature of the wall will be ~1000 ºC. [15] Because this thesis is primarily concerned with the surface damage to W caused by He^+ implantation, the helium ion threat spectrum (per shot) for the baseline 350 MJ target design of the HAPL program is shown in Figure 2-3.

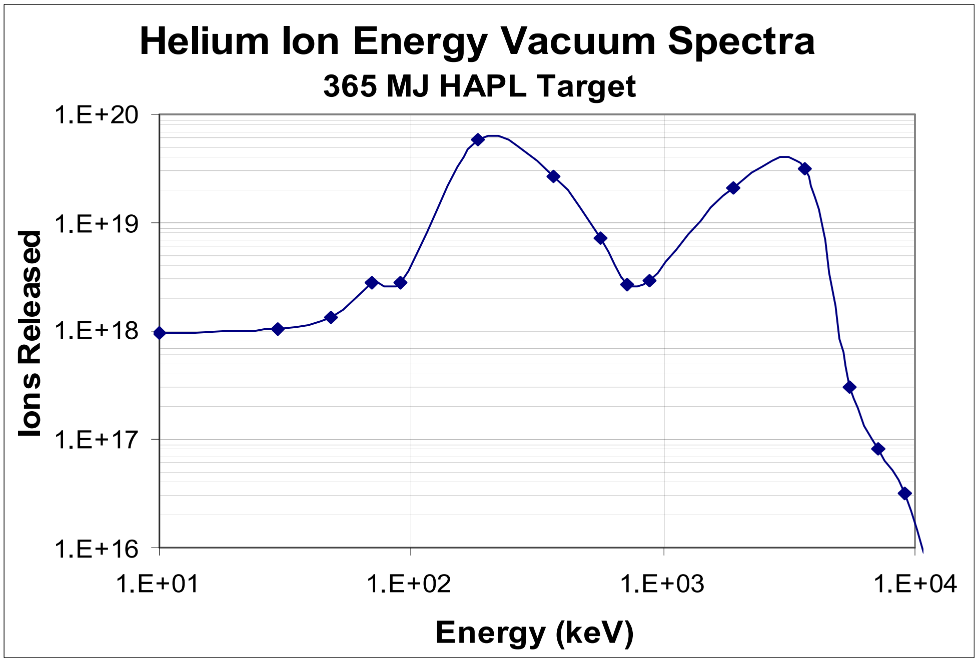

Figure 2-4: HAPL target threat spectrum, per shot, into the first wall for helium ions [16]

Several universities and laboratories are studying the effects of these energetic ions, x-rays, and neutrons on candidate first wall materials. [5,17,18,19,20,21] Most of the published work has focused on diagnosing helium effects in tungsten. The pulsed ion implantation experiment, Repetitive High Energy Pulsed Power (RHEPP), at Sandia National Laboratory, [17] is analyzing ion effects from short duration pulses to simultaneously investigate material response to high thermal stresses and ion fluxes. The University of North Carolina is addressing the high energy (> 1 MeV) portion of the HAPL helium ion threat spectrum [18], while previous research in the University of Wisconsin-Madison Inertial Electrostatic Confinement Fusion laboratory (UW IEC) has focused on the 10-100 keV portion of the spectrum. [5,19] The modeling of helium implantation effects in tungsten is also progressing, as Sharafat and Ghoneim (UCLA) have developed the HEROS code [20] and a kinetic Monte-Carlo code [21] to simulate helium implantation and its migration and bubble growth, respectively.

2.3. Helium implantation studies

Recently, large scale fusion reactor projects, like the National Ignition Facility (NIF) & ITER, have revived a global effort to study the erosion and embrittlement of plasma facing components by ion bombardment. [22] These investigations cover a wide range of temperatures, ion dose, ion species mix, and energy. For the purposes of this report, the surveys of previous ion implantation studies will be confined to those performed on tungsten or tungsten alloys, and involve helium ions. Ion implantation energy will be classified into the following energy ranges: 1) low, 0 – 1 keV, 2) intermediate, 1 – 300 keV, and 3) high, >300 keV. Because of the large differences in the modes of operation between IFE and MFE fusion reactors, there are also substantial differences in the ion threat spectra of each of these devices. [23] Despite these differences, this section attempts to emphasize points of commonality between the two systems in order to provide continuity while discussing the various observations from experiments using He^+ to implant W.

2.3.1. Helium implantation at low energy (0 – 1000 eV)

Early work by Nishijima, et al. in 2003 [24] showed that helium ion bombardment resulted in micron-sized pores on and beneath the tungsten surface at ion energies as low as ~15 eV. Specimen conditions in these studies were implanted to very high fluences (~10^{22} He^+/cm^2) and high temperatures (~1600-2600 °C). Figure 2-5 shows some of the results of the work performed by this group. [25] Additional investigation on W revealed that the threshold for these pores to form under exposure to helium plasmas was ~5 eV,the energy required for He ions to penetrate tungsten's surface barrier potential. [26] These effects were observed at plasma exposure temperatures >1300 °C. Another fascinating aspect of this research is the penetrating nature of these pores. Cross sections of the implanted specimens confirm the existence of these pores far below the range of these ions in tungsten (Figure 2-5). [25,27]

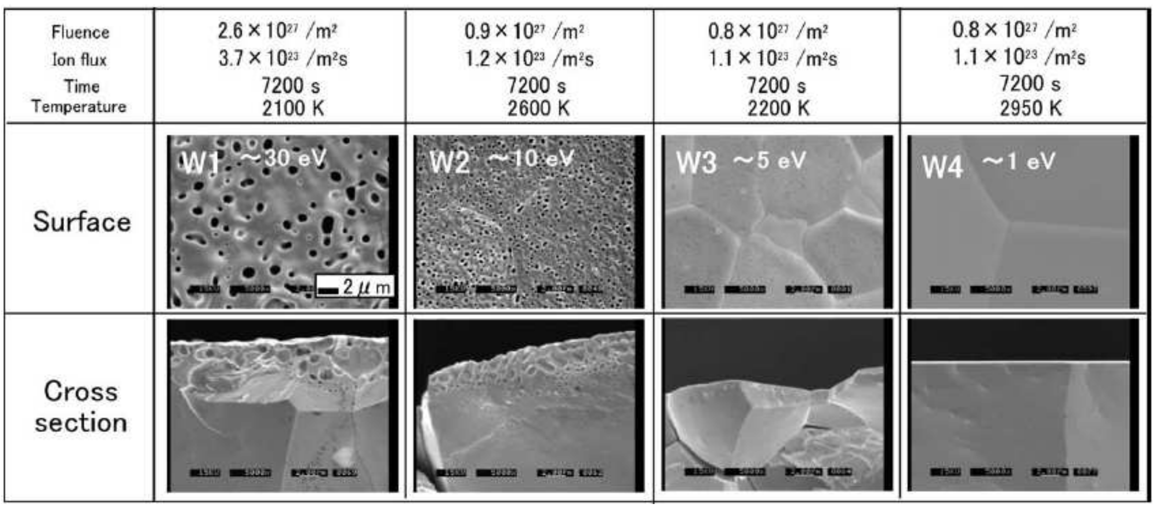

Figure 2-5: Results of helium plasma exposure on PCW, from Nishijima, et al. [25]

Yoshida et al. [7] also observed bubble formation at a smaller, nanometer sized scale. These experiments implanted at higher energies (~250 eV) but much lower doses and temperatures. TEM analysis showed bubble formation at fluences as low as 10^{17} He^{+}/cm^{2} and temperatures ranging from room temperature to 1000 °C. Similar to other work, bubble size was shown to be strongly dependent on implantation temperature.

Perhaps the most striking phenomenon observed after He implantation at low energies is the formation of nano-scale "fuzz" or "fiberform." Findings reported by Baldwin and Doerner [28] showed that the surface growth of this amorphous tungsten structure increased with increased fluence to the specimen. Much like Nishijima, et al. [24,25,27], this microstructure was observed at implantation energies as low as ~5 eV, well below the sputter threshold of tungsten (~100 eV). [29] Figure 2-6 shows the progression of this fiberform structure with increasing irradiation time (ion dose). Doses ranged from ~10^{21} – 10^{23} He^+/cm^2 at temperatures between ~850 – 1050 °C. Final analysis revealed that the length of these structures was on the micron scale, although the thickness of these spindles did not exceed ~ 50 nm. [28]

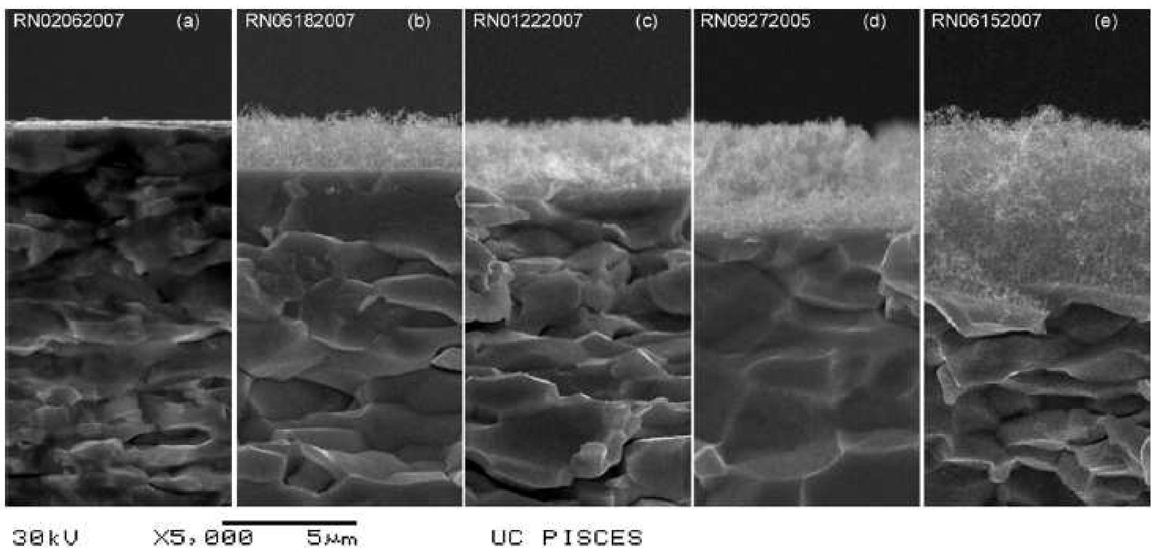

Figure 2-6: Fiberform structure observed in the Pisces B experiment. Cross-sectional SEM images of W targets exposed to pure He plasma for exposures times of (a) 300 s, (b) 2.0×10^3 s, (c) 4.3×10^3 s, (d) 9.0×10^3 s and (e) 2.2×10^4 s. Targets were exposed at a fixed temperature of ~850 ºC. Ion energies varied slightly in the parameter ranges between 6–8 eV, and the flux ranged between $(4–6) \times 10^{18}$ cm^{-2} s^{-1}. [28]

Further investigations by Kajita, et al. [30] independently confirmed results by other authors [28,31] regarding the formation of the fiberform structure on tungsten, as well as observing the same behavior on molybdenum. In an earlier report (2007) by Kajita, et al. it was observed that the fiberform structure itself was a complex network of much smaller voids induced by helium implantation (Figure 2-7). [32] It is hypothesized that the growth of these spindles is facilitated by the swelling of these smaller helium voids within the fibers.

Implantation results of helium ions on tungsten were reported by Kajita et al. for a wide range of temperatures (~300 – 2300 °C) and fluences (10^{21} - 10^{23} cm^{-2}), but with incident ion energies below 100 eV. This study identified and summarized the known surface effects of helium ion bombardment on tungsten, along with the necessary energy, fluence, and temperature conditions required to generate the fiberform structure. It was reported that the fiberform structure is formed on tungsten at temperatures between ~725 – 1725 °C, when the incident ion energy is above ~20 eV and the ion dose is $\geq 10^{21}$ He^+/cm^2. [30] Figure 2-8 visually summarizes the various morphology changes on tungsten after low energy helium bombardment.

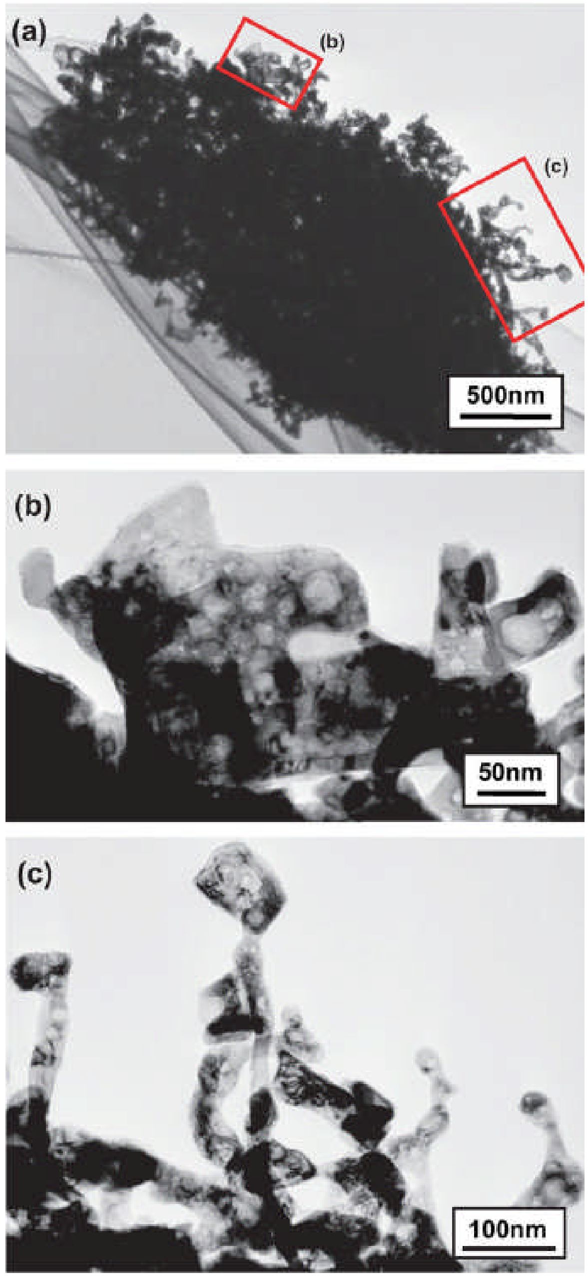

Figure 2-7: (a) TEM image of a the fine structure of W irradiated to $4x10^{23}$ He^{+}/cm^{2} at 1327 °C, (b) and (c) show the enlarged views. [32]

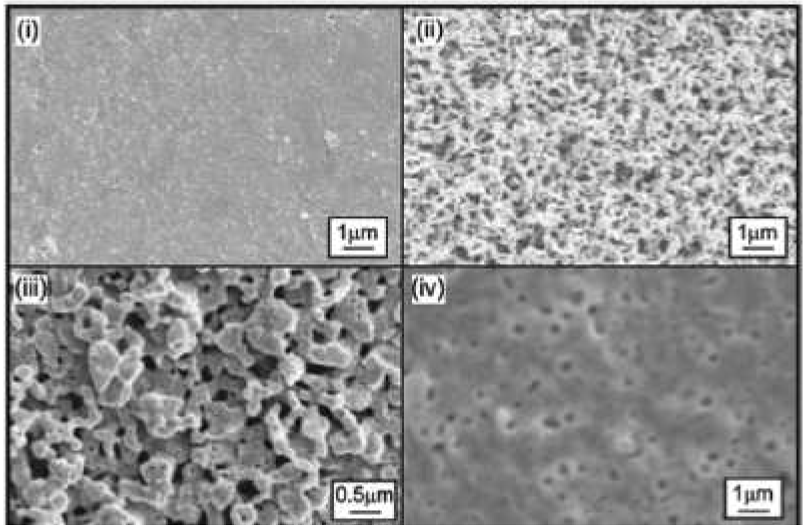

Figure 2-8: SEM micrographs for PCW under conditions of: (i) implantation temperature is below ~725 °C, resulting in surface roughness, but no pinholes or fiberform, (ii) surface temperature in the range ~725 – 1725 °C, resulting in the fiberform, (iii) surface temperature above ~1725 °C, producing micrometer-sized structure with many pinholes, and (iv) the ion energy is below approximately 20 eV, which produces a pinhole surface morphology. [30]

Very recently (2010), a re-crystallized W-1.1%TiC alloy has been developed by Kurishita et al. [33] which appears to show enhanced ductility over that of pure tungsten as well as improved radiation performance. Miyamoto et al. [34] showed reduced surface damage and D and He retention after this W alloy was exposed to helium-seeded deuterium plasmas with energies of ~55 eV. The combined D and He fluence was $\leq 4.5 \times 10^{22}$ He^{+}/cm^{2} at temperatures of ~300 ºC. Helium concentration ranged from ~1 – 20%. Investigation of this W alloy, as well as others, is part of a continuing campaign to find fusion materials resistant to low energy helium plasma exposure.

2.3.2. Helium implantation at intermediate energy (1 keV – 300 keV)

As the energy of the helium implanted in W is increased, the characteristic morphology changes brought on by helium implantation will take on new forms and structures. From the previous discussion, one observes that roughening, pores, and nano-structured fibers result from helium implantation into W at the low energies. Research has shown that when the implantation energy of the He in metals exceeds ~1 keV that surface morphology changes can be characterized by blisters, flakes, and pores. [2] The chart shown below in Figure 2-9 illustrates the regions where these three morphology changes dominate morphology changes on seven different metals. These materials include Nb, Mo, and V, which one expects to respond similarly to W due to their similar crystalline structure (BCC) and physical properties. Typically, the helium fluence threshold for surface morphology change in W decreases at intermediate energies from the helium fluence threshold observed at low energies.

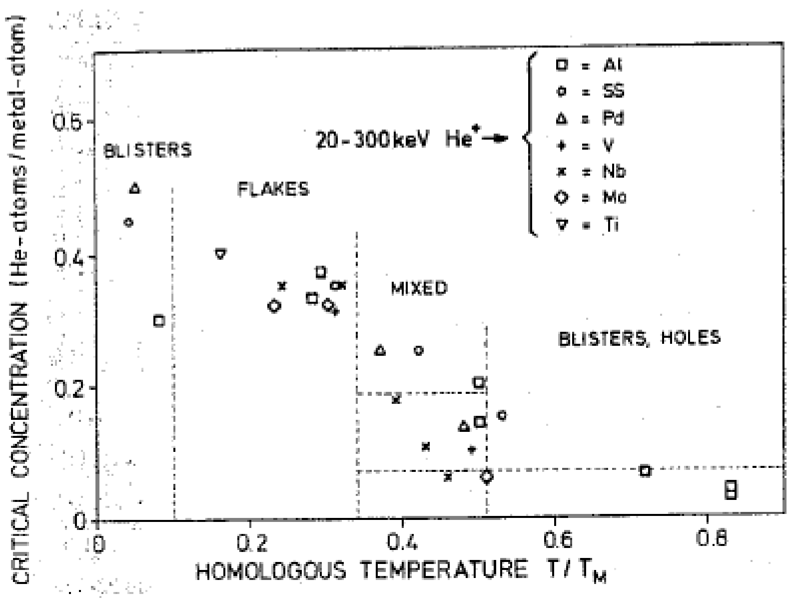

Figure 2-9: Summary of He^+ implantation data for seven different materials implanted at energies from 20 – 300 keV. [2]

In fact, Fu et al. [35] observed blisters and pore formation on polycrystalline tungsten after it was implanted with 8 keV He^+. This study showed that surface morphology had a strong dependence on the temperature at which the helium was implanted and post-implantation annealing for thermal desorption measurements. After helium implantation at room temperature to moderate fluencies (~10^{17} He^+/cm^2) little morphology change was observed until the specimens were examined using thermal desorption spectroscopy (TDS). During this process small blisters and pores appeared on the surface. When Fu et al. implanted the helium at higher temperatures (~600 ºC) to fluences ≤4×10^{17} He^+/cm^2, blisters were observed before the TDS was performed (Figure 2-10(a)-(b)). After this anneal, most of the blister caps flaked off, leaving a porous surface (Figure 2-10(c)-(d)). The work also reported an increase in the blister size as implantation temperature was increased from room temperature to 600 ºC.

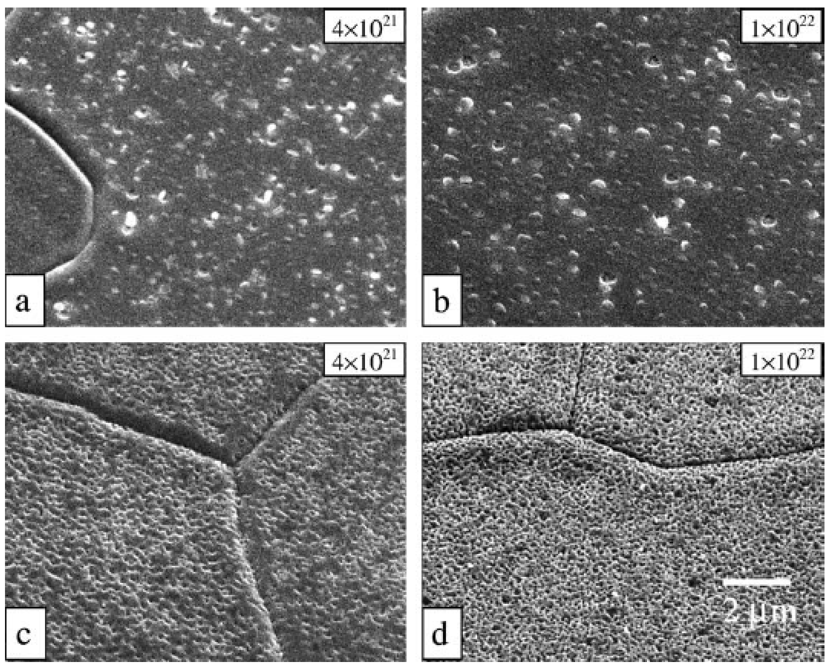

Figure 2-10: Surface modifications of specimens irradiated by 8 keV He^+ at 600 ºC to (a) 4×10^{17} He^+/cm^2 and (b) 10^{18} He^+/cm^2 before thermal desorption and (c) – (d) after thermal desorption. [35]

Other authors have seen similar surface structure develop on polycrystalline W after exposure to helium. These results have been observed at a wide range of intermediate implantation energies. In 2004, Tokunaga, et al. [6] observed the formation of micron sized blisters after implantation with 19 keV helium ions to fluences of 1.7 – 3.3×10^{18} He^+/cm^2 at 800 ºC (Figure 2-11(a)-(b)). The same work reported a coral-like structure developed on W after He^+ implantation at high temperatures (≤2600 ºC) and fluences of 1.7 – 3.3x10^{19} He^{+}/cm^{2} (Figure 2-11(c)-(d)). One very noticeable feature of Figure 2-11(d) is the depth to which the coral-like morphology and accompanying pores penetrate the W surface. The dimension of the sub-surface features (pores and coral) are well over the predicted range of 19 keV He^{+} (~50 nm), showing the strong diffusional effects of helium implantation at high temperatures.

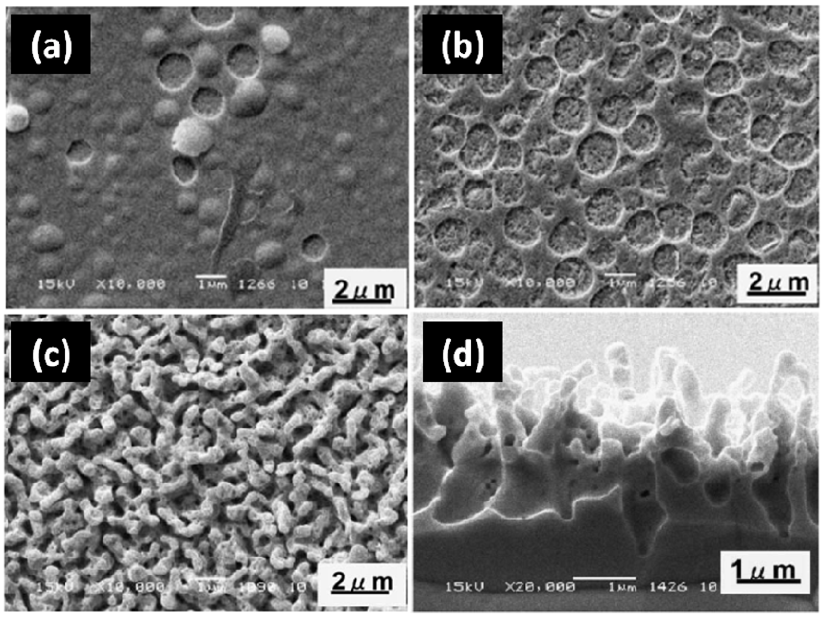

Figure 2-11: PCW implanted with helium to (a) 1.7x10^{18} He^{+}/cm^{2} and (b) 3.3x10^{18} He^{+}/cm^{2} at 800 ºC and at (c) – (d) 3.3x10^{19} He^{+}/cm^{2} at a peak temperature of 2600 °C - the sample surface and a cross-section of the sample are shown. [6]

The self-retention characteristics of helium in W after helium implantation and the ability of helium implantation to affect hydrogenic species retention in W are also of great importance to the fusion community. [36] Hino et al. [37] reported a maximum retained helium fluence in W of 10^{17} He^{+}/cm^{2} after implantation with 5 keV He^{+} at a total implanted helium fluence of 3x10^{18} He^{+}/cm^{2}. The study also reported that the helium retention in W appear to saturate, reaching its maximum as fluences exceeded ~10^{18} He^{+}/cm^{2}.

The effect of pre-helium implantation on deuterium retention was investigated by Iwakiri et al. [38] Results from Iwakiri et al.'s work showed that after pre-implantation of W with 8 keV He^+ at room temperature, the retained D in the W was a much as three times higher than that observed for specimens not pre-implanted with He. The enhanced retention of hydrogenic species in W after helium implantation could have a strong effect on the design of both MFE and IFE fusion devices as a minimum tritium inventory is of critical importance to the safety of fusion reactors. [39]

2.3.3. *Helium implantation at high energy (>300 keV)*

At high energies (>300 keV) helium implantation has also been observed to cause significant damage to W surfaces. Renk et al. [40] reported extreme surface morphology changes on powder metallurgy W after implantation with 500-600 keV He^+ to fluences of ~10^{13} He^+/cm^2 (Figure 2-12). The average surface roughness of implanted W specimens was shown to be on the order of tens of micrometers. Moreover, W responded less favorably to He^+ implantation than to N^+ implantation at similar implantation conditions (temperature, ion energy, and fluence), showing an increased average surface roughness.

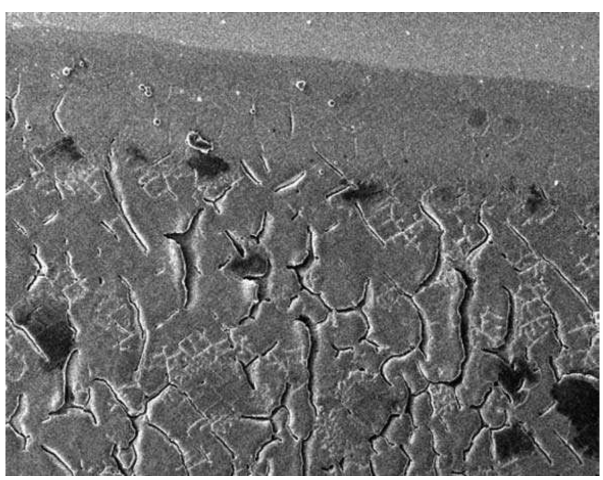

Figure 2-12: Single crystalline W after 450 pulses with a 500-600 keV helium ion beam at 600 ºC. The total fluence was 1-1.3 J/cm^2 (~10^{13} He^+/cm^2). SEM micrograph is taken at the interface of the beam irradiated region and unimplanted region. [40]

Experiments using even higher energy ion beams have shown substantial blistering on W surfaces. Gilliam et al. [18] observed blisters ranging in size from ~20 – 150 µm after tungsten was implanted with 1.3 MeV He^+ at average temperatures of 850 ºC and flash anneals of 2000 ºC. The fluence threshold for these blisters was near 10^{17} He^+/cm^2 (Figure 2-13). One of the unique aspects of the research was the manner in which the ions where implanted. Total fluence was implanted incrementally over 1, 100, or 1000 steps with a 2000 ºC flash heating between each step. Retention data showed that the total retained helium fluence decreased as the number of implant steps increased. This data suggest that limiting the helium ion fluence to a plasma facing component below a certain threshold per fusion event may be beneficial. This would be especially applicable to IFE systems operating at a high rep-rate. Because the implanted helium may be released from the first wall armor after each pulse due to the high temperature excursions [15], the damaging effects of helium implantation could be substantially alleviated.

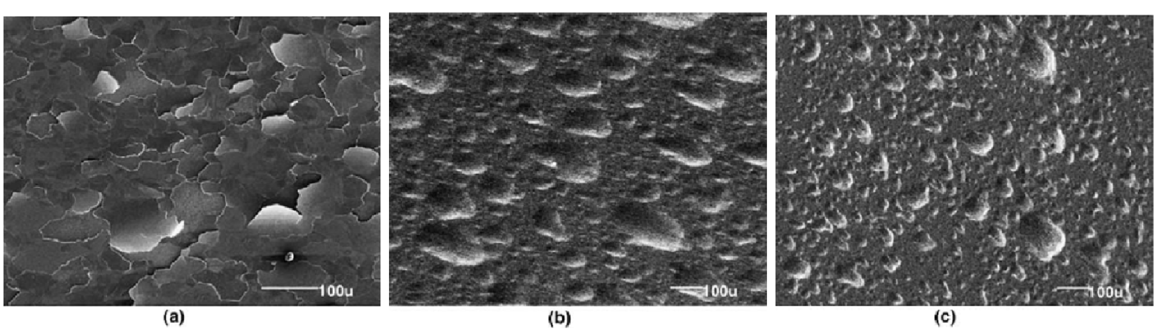

Figure 2-13: SEM images of polycrystalline W implanted at (a) 10^{18} He^+/cm^2, (b) $2x10^{17}$ He^+/cm^2, and (c) 10^{17} He^+/cm^2 at 850 ºC and then flash heated at 2000 ºC. [18]

2.4. Previous He^+ implantation experiments at the UW IEC laboratory in HOMER

2.4.1. Single- and polycrystalline W

Although the following research could have been presented in the preceding section (2.3.2) of this report, the close relationship of these experiments to results discussed in this thesis and by this author merits a thorough and separate presentation of this work. Previous high temperature ion implantation studies in the device HOMER – located at the University of Wisconsin-Madison Inertial Electrostatic Confinement (UW IEC) fusion laboratory – have used electrostatic potentials to radially accelerate ions to intermediate energies (10 – 100 keV) into materials specimens. Chapter 4 of this thesis addresses the experimental setup of the aforementioned devices.

Initial experiments of the UW IEC group by Cipiti [19] and Radel [41] involved steady state implantation of W alloys, and W metallic foams. Both helium and deuterium implantation studies were performed at a variety of temperatures and fluences. [5,19,41,42,43] Additional studies aimed at improving simulations of an IFE environment, introduced the capability to operate the UW IEC device HOMER in a pulsed regime. [44] These results will be presented along with a brief discussion. This is done to give the reader a sense of context regarding the work done for this thesis, as it is discussed and compared with the previous results from the UW IEC device HOMER.

Studies performed by Cipiti and Kulcinski [19] focused on the steady-state irradiation of polycrystalline tungsten (PCW) and included scans of ion fluence, implantation temperature, and ion energy. These experiments scanned irradiation temperatures between 800 – 1200 ºC and revealed preferential collection of the implanted helium on grain boundaries. This behavior motivated the experimentation with single-crystalline tungsten (SCW).

Using the UW-IEC device HOMER in steady-state mode, Radel and Kulcinski [41] implanted SCW samples to determine the threshold for surface erosion and pore formation as a comparison to PCW. Ion doses ranged from $6x10^{17}$ – 10^{19} He^+/cm^2 at irradiation temperatures of ~1100 ºC (This reflects a temperature correction made to the aforementioned work that was originally reported at 800 °C). It was found that the calibration of the Raytek® Marathon MR pyrometer used to measure specimen temperature drifted, causing an ~300 °C error. This resulted in a correction to the irradiation temperature from 800 ºC to ~1100 ºC for each of the specimens reported in Ref. 41. Results revealed significant pore formation at fluences of ~$3x10^{18}$ He^+/cm^2, though random pore distribution was observed as low as 10^{18} He^+/cm^2. At higher implant fluences, ~10^{19} He^+/cm^2, pore formation and surface roughening became extensive. Scanning electron microscopy (SEM) images of these irradiations are shown in Figure 2-14.

At 1100 °C the onset of pore formation in PCW occurred at ~10^{17} He^+/cm^2, but became extensive as fluences increased from 10^{18} to 10^{19} He^+/cm^2 (Figure 2-15). The fluences stated in [19] have been corrected in this thesis, based on more accurate calibration. Initial estimates of the PCW secondary electron emission coefficient in the IEC environment were high and yielded fluences of ~10^{16} - $6x10^{17}$ He^+/cm^2. New information for the secondary emission coefficient of these samples resulted in a correction to the previously reported fluences, which now range from ~10^{17} – 10^{19} He^+/cm^2. Additionally, very few quantitative conclusions were able to be drawn from Cipiti's [19] temperature and ion energy scans, due to extensive pore formation at those high doses.

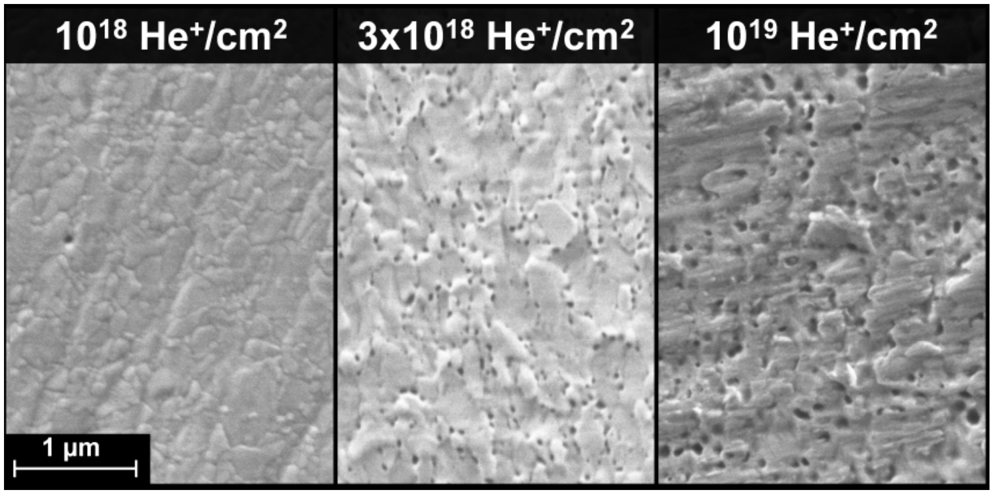

Figure 2-14: Single crystalline tungsten irradiated at ~1100 °C to fluences of 10^{18}, $3x10^{18}$, 10^{19} He^{+}/cm^{2}. [19,41] Temperatures from [41] corrected from 800 °C in the original report.

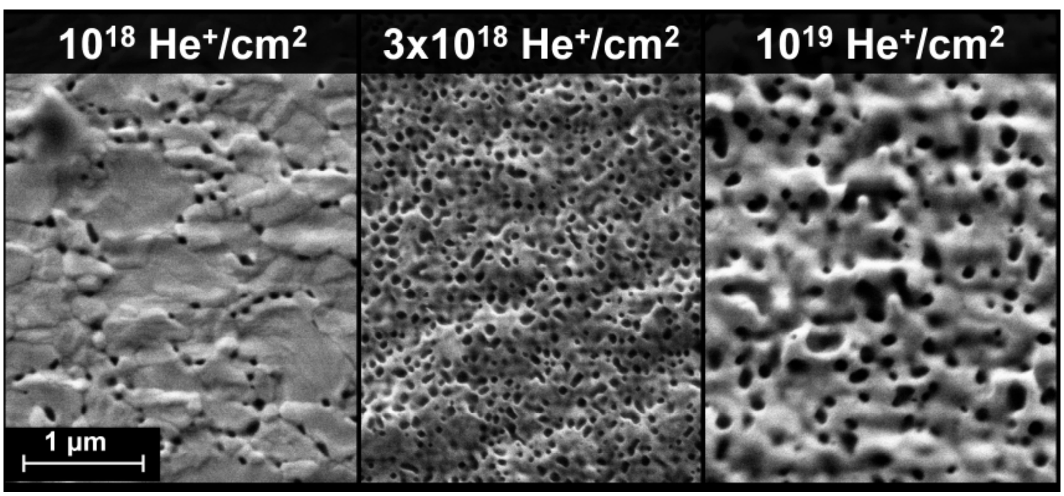

Figure 2-15: PCW irradiated at ~1100 °C to fluences of 10^{18}, $3x10^{18}$, 10^{19} He^{+}/cm^{2}. [5]

Pulsed implantation experiments on PCW specimens at fluences of 10^{18} – 10^{19} He^{+}/cm^{2} and irradiation temperatures as high as 1170 ºC revealed extensive damage to the surface. [44] Radel showed that the pore density for each of the pulsed specimens appeared to saturate. Furthermore, the pore density in the pulsed specimens exceeded the maximum pore density observed in the steady-state samples of $4x10^{9}$ pores/cm^{2}. In addition, an extended sub-surface semi-porous layer was observed in the pulsed specimens. At a given fluence, the depth of this semi-porous layer extended ~2-3 times deeper in pulsed samples (300 – 700 nm) than in those irradiated in steady state mode (90 – 300 nm). In every case, the penetration of this semi-porous layer extended beyond the predicted range of 30 keV helium ions. At room temperature, SRIM calculations predict an ion range of ~70 nm for 30 keV $^{4}He^{+}$ in W. This extended porous layer depth was attributed to processes of He diffusion in W at high temperatures during the irradiation process.

Another expansion of Radel's work was the preliminary characterization of total retained helium fluence and depth profiling using elastic recoil detection. This analysis reported the percentage of ^{4}He in the near surface region of the PCW specimen at ~40 at%. [5,43,45] Furthermore, it was observed that the maximum retained helium fluence in PCW saturated at 1.2×10^{13} He atoms/cm^3, independent of the implanted fluence. A comparison of surface damage effects is given in Figure 2-16 for SCW, steady-state PCW, and pulsed PCW specimens each implanted to a fluence of 10^{19} He^{+}/cm^2 at implantation temperatures >1100 ºC.

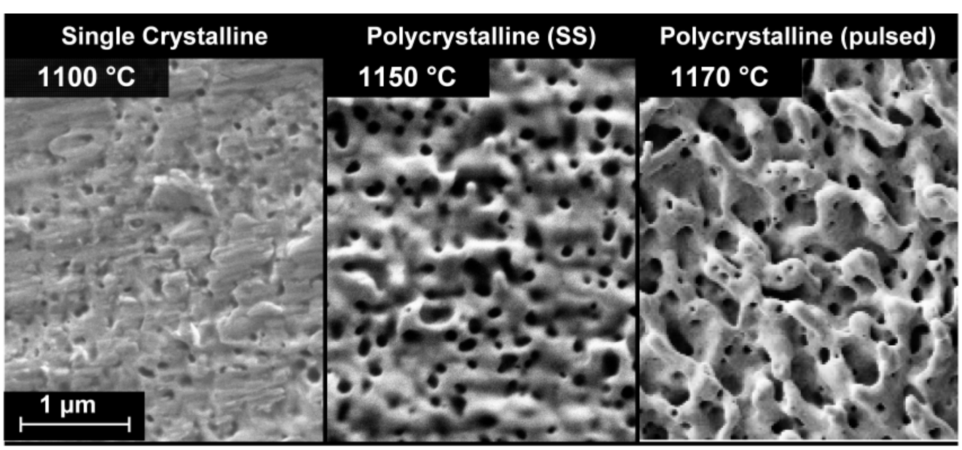

Figure 2-16: Comparison of steady-state irradiated SCW, PCW and pulsed implanted PCW at a fluence of 10^{19} He^{+}/cm^2. [5,41]

2.4.2. Tungsten-rhenium alloy

Irradiations on a W-Re alloy (25% Re) were performed concurrently with the investigations on pure tungsten. [5] The impetus to examine this material was due to the improved mechanical properties of W-Re alloy despite its lower melting point. [46] Steady-state irradiations were performed to fluences between $6x10^{17} – 10^{19}$ He^+/cm^2 at 1100 °C. The results of this work are illustrated in Figure 2-17. A PCW specimen implanted to a fluence of 10^{18} He^+/cm^2 is compared to the W-Re alloy implanted to the same fluence at approximately the same temperature. Both specimens exhibit surface pore formation; however, the W-Re showed an obvious increase in the surface pore density and average pore size compared to pure W. W-Re alloys consistently sustained greater surface modification than pure W.

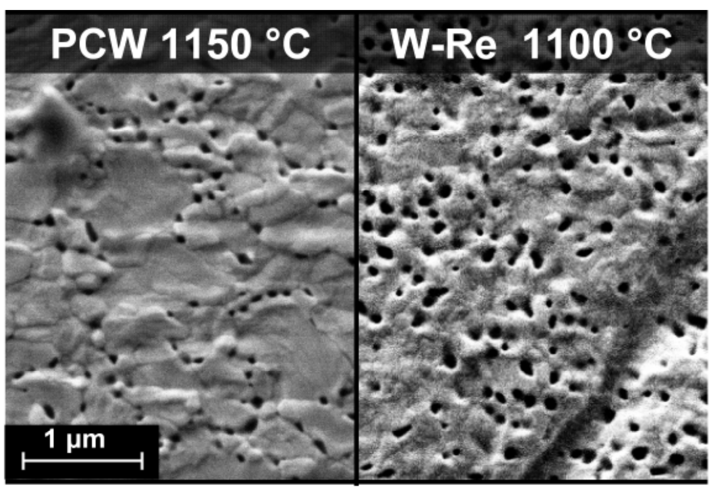

Figure 2-17: Comparison of PCW and W-Re alloy irradiated to 10^{18} He^+/cm^2. [5]

2.4.3. W-coated tantalum carbide foams

As a response to the poor performance of the PCW and W-Re alloy after helium ion bombardment, Radel investigated various W-coated tantalum carbide (TaC) foams. [41] Specimens with a large, medium, and fine grain W-coating were also examined.

Both the medium- and fine-grain coatings were considered high emissivity or “high ε” samples due to the addition of fine grain tungsten dendrites. Tungsten coatings were ~40 μm in thickness on the foam.

Each of the three types of W-coated TaC foam samples was vacuum annealed at 1200 °C for 30 minutes prior to implantation with He^+ to differentiate between thermal effects and ion damage. The thermal anneals caused minor roughening of the foam surfaces, but no pore formation. Each of the foam grain sizes (large, medium, and fine-grain W) was implanted to a fluence of 10^{19} He^+/cm^2 at ~1100 °C. SEM analysis revealed that all three samples incurred substantial changes in surface morphology after irradiation (Figure 2-18).

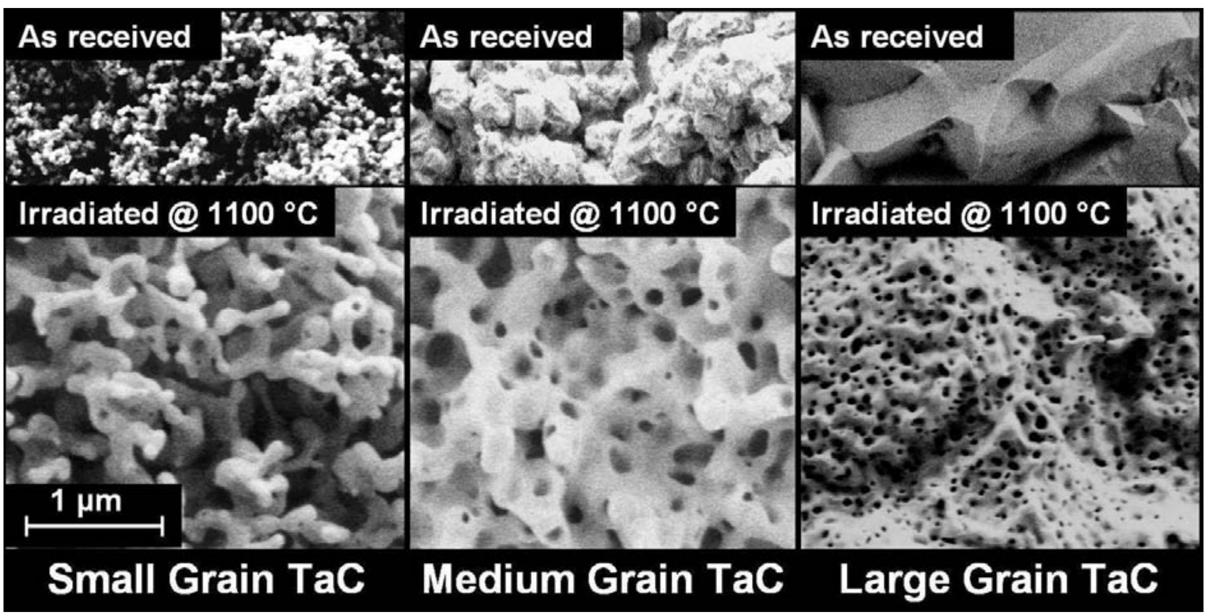

Figure 2-18: Comparison of small-, medium-, and large-grain W-coated TaC foams irradiated at 1100 °C to 10^{19} He^+/cm^2. [41]

Helium implantation resulted in extensive surface pore formation on both large and medium grained specimens. Pores are smaller and more numerous on the large grain sample, while the medium grain exhibited a lower pore density but greater average pore diameter. Comparing Figure 2-18(a) and Figure 2-18(b) with the pure PCW specimen in

Figure 2-16, it appears the dendrites on the small and medium grain samples have "swollen" and resemble the "coral-like" surface observed on the pure PCW. As grain and dendrite size decreased it was observed that swelling increased, while pore density decreased. Most likely, swelling of the dendrites was caused by the formation and expansion of helium-filled voids in the tungsten. As these voids coalesced, grew, and intersected the material surface they became visible and released the trapped helium. The smaller dendrites are not able to support the larger, visible surface pores, but certainly are full of smaller helium voids. The existence or creation (from ion damage) of such dendrites on W surfaces is undesirable for first wall armors and divertor plate materials, as they may break off easily, producing radioactive dust or even serve as crack propagation sites.

2.4.4. Tungsten materials summary & comparison

Figure 2-19 gives a final comparison of the tungsten materials investigated by Cipiti and Radel. Each of the specimens in Figure 2-19 was irradiated in steady-state mode to 10^{19} He^{+}/cm^{2} at a temperature between ~1100 – 1150 ºC. These SEM micrographs reveal that the SCW responded the most favorably to irradiation conditions and had a lower pore density relative to the other samples. The W-Re alloy incurred the worst damage from irradiation, sustaining a saturated pore density and larger average pore diameters than any other specimen. While pore formation in the PCW sample is extensive, pore density has not saturated and the "coral-like" microstructure is not dominant as in pulsed irradiations (Figure 2-16). W-coated TaC foams sustained increasing pore formation and decreased swelling with increased grain size.

Overall, the SCW showed superior resilience to the high temperature ion implantation (>10^{18} He^+/cm^2) followed by the PCW, large grain W-coated TaC, and W-Re alloy in order of reduced resistance to radiation damage. Unfortunately, SCW is probably unusable in a first wall or divertor plate application, as the technology to grow and implement single crystalline W on such a large scale is currently unavailable.

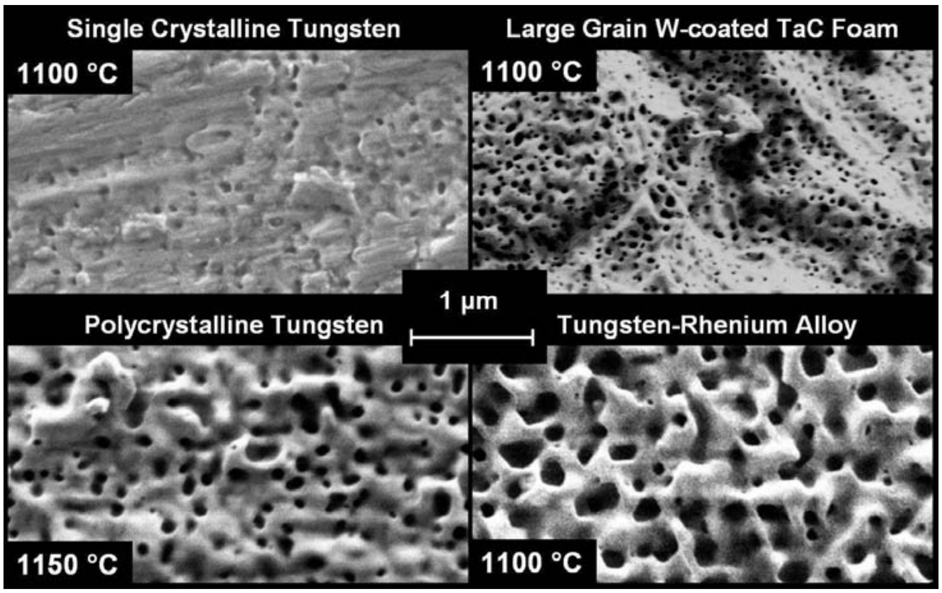

Figure 2-19: Comparison of SCW, PCW, W-Re alloy, and large grain W-coated TaC foam irradiated to 10^{19} He^+/cm^2. [5,44]

2.4.5. Summary of observations from previous high temperature He^+ implantations studies in HOMER

From the research presented in the above section, the tentative conclusions found by the original authors are presented for each of the materials. Discussion of the work done on these, or similar, materials by this author will be presented in Chapters 5 and 6 and the resulting conclusions given in Chapter 7 of this thesis.

- SCW exhibits a slightly higher threshold fluence for pore formation than PCW. Additionally, at higher fluences the average pore density of SCW is lower than that of PCW specimens.

- Steady-state irradiation of PCW revealed the onset of pore formation at ~10^{17} He^+/cm^2, becoming extensive at fluences >10^{18} He^+/cm^2. The concentration of helium atoms in the surface layer of PCW saturates at ~40 at%.
- Pulsed implantation experiments on PCW resulted in an apparent saturation of pore density at all examined fluences. At 10^{19} He^+/cm^2, the semi-porous layer extended up to 700 nm into the surface after pulsed bombardment with 30 keV $^4He^+$, while for equivalent steady-state fluences this layer extended only 300 nm.
- Vacuum annealing of W-coated carbide foams caused minor surface roughening. Large and medium grain carbide foams experienced extensive pore formation after He^+ bombardment similar to that of PCW. The small grain carbide foam showed a reduction in pore density, but substantial swelling of the tungsten dendrites comprising the surface.
- Tungsten-rhenium alloys showed a larger average pore diameter than PCW, as well as lower threshold fluence for pore formation.

2.5. References for Chapter 2

1. Barnes, R. and Nelson, R, (1967) *Theories of Swelling and gas Retention in Reactor Materials in Radiation Effects,* (New York: Gordon and Breach).

2. Behrisch, M and Scherzer, B. M. U., (1982) *Surface topography due to light ion implantation.* Springer-Verlag, New York.

3. M. Kaminsky, M., (1965) *Atomic and Ionic Impact Phenomena on Metal Surfaces*. Springer-Verlag, New York.

4. Zenobia, S. J. et al., (2009) High temperature surface effects of He^+ implantation in ICF fusion first wall materials. *Journal of Nuclear Materials*, 389, 213-220.

5. Radel, R. F. and Kulcinski, G. L., (2007) Implantation He^+ in candidate fusion first wall materials. *Journal of Nuclear Materials*, 367, 434-439.

6. Tokunaga, K. et al., (2004) Synergistic effects of high heat loading and helium irradiation on tungsten. *Journal of Nuclear Materials*, 329-333, 757-760.

7. Yoshida, N. et al., (2005) Impact of low energy helium irradiation on plasma facing materials. *Journal of Nuclear Materials*, 337–339, 946.

8. Yoshida, N., (1999) Review of recent works in development and evaluation of high-Z plasma facing materials. *Journal of NuclearMaterials*, 266-269, 197-206.

9. Feder, T., (2010) JET gets new wall to prep for ITER. *Physics Today*, December, 24-25.

10. Dolan, T. J. et al., (1995) Global co-operation in nuclear fusion: record of steady progress. *IAEA Bulletin*, 37 (4), 16-21.

11. Source: http://www.iter.org/MACH/Pages/Divertor.aspx

12. Janeschitz, G. et al., (1995) The ITER Diverter Concept. *Journal of Nuclear Materials*. 220-222, 73-88.

13. Sethian, J. D. et al., (2005) An overview of the development of the first wall and other principal components of a laser fusion power plant. *Journal of Nuclear Materials,* 347, 61.

14. Raffray, A., et al, (2006) Progress Towards Realization of a Laser IFE Solid Wall Chamber. *Fusion Engineering and Design*, Vol. 81, Issues 8-14, p. 1627, 2006

15. Heltemes, T. A. et al., (2007) Simulation of thermal response and ion deposition in the HAPL target chamber 1 mm tungsten armor layer using the improved BUCKY code. *Fusion Engineering and Design*, 82, 175-187.

16. Private communication, J. Perkins.

17. Renk, T.J. (2005) Chamber wall materials response to pulsed ions at power-plant level fluences. *Journal of Nuclear Materials*, Vol. 347, Issue 3, p 266-288.

18. Gilliam, S.B., et al (2005) Retention and Surface Blistering of Helium Irradiated Tungsten as a First Wall Material. *Journal of Nuclear Materials*, Vol. 347, Issue 3, p 289-297.

19. Cipiti, B.B. and Kulcinski, G.L. (2005) Helium and deuterium implantation in tungsten at elevated temperatures. *Journal of Nuclear Materials*, **347**(3), 298.

20. Hu, Q, et al (2007) Modeling space-time dependent helium bubble evolution in tungsten armor under IFE conditions. *Fusion Science and Technology*, 52 (3), p. 574-578.

21. Takahashi, A., et al (2006) MC Simulation of Tungsten Surface Pores Formed by Low-Energy Helium Implantation. presented at the 15th High Average Power Laser Program Workshop, August 8, 2006, San Diego, CA

22. Baluc, N. et al., (2007) Status of R&D activities on materials for fusion power reactors. *Nuclear Fusion*, 47, S696-S717.

23. Raffray, A. R. et al., (2003) IFE chamber walls: requirements, design options, and synergy with MFE plasma facing components. *Journal of Nuclear Materials*, 313-316, 23-31.

24. Nishijima, D. et al., (2003) Incident ion energy dependence of bubble formation on tungsten surface with low energy and high flux helium plasma irradiation. *Journal of Nuclear Materials*, 313-316, 97-101.

25. Nishijima, D. et al., (2004) Formation mechanism of bubbles and holes on tungsten surface with low-energy and high-flux helium plasma irradiation in NAGDIS-II. *Journal of Nuclear Materials,* 329-333, 1029-1033.

26. Ullmaier, H., (1984) The influence of helium on the bulk properties of fusion reactor structural materials. *Nuclear Fusion,* 24, 1039.

27. Nishijima, D. et al., (2005) Characteristic changes of deuterium retention on tungsten surfaces due to low-energy helium plasma pre-exposure, *Journal of Nuclear Materials,* 337-339, 927-931.

28. Baldwin, M.J. and Doerner, R.P., (2008) Helium induced nanoscopic morphology on tungsten under fusion relevant plasma conditions, *Nuclear Fusion*, 48, 035001.

29. Eckstein, W. and Laszlo, J., (1991) Sputtering of tungsten and molybdenum. *Journal of Nuclear Materials*, 182 (1-2), 19-24.

30. Kajita, S. et al, (2009) Formation process of tungsten nanostructure by the exposure to helium plasma under fusion relevant plasma conditions, *Nucl. Fusion*, 49, 095005.

31. Takamura, S. et al., (2006) Formation of nanostructured tungsten with arborescent shape due to helium plasma irradiation. *Plasma Fusion Research*, 1, 051.

32. Kajita, S. et al., (2007) Sub-ms laser pulse irradiation on tungsten target damage by exposure to helium plasma. *Nuclear Fusion*, 47, 1358-1366.

33. Kurishita, H. et al., (2010) Development of re-crystallized W-1.1%TiC with enhanced room-temperature ductility and radiation performance. *Journal of Nuclear Materials*, 398, 87-92.

34. Miyamoto, M., (2009) Observations of suppressed retention and blistering for tungsten exposed to deuterium-helium mixture plasmas. *Nuclear Fusion*, 49, 065035.

35. Fu, Z. et al., (2004) Thermal desorption and surface modification of He^+ implanted into tungsten. *Journal of Nuclear Materials*, 329-333, 692-696.

36. Abramov, E. and Eliezer, D., (1992) Hydrogen trapping in helium damaged metals: a theoretical approach. *Journal of Materials Science*, 27, 2595-2598.

37. Hino, T. et al., (1999) Helium retention of plasma facing materials. *Journal of Nuclear Materials*, 266-269, 538-541.

38. Iwakiri, H. et al., (2002) Effects of helium bombardment on the deuterium behavior in tungsten. *Journal of Nuclear Materials*, 307-311, 135-138.

39. Frederici, G. et al., (1998) Tritium inventory in the ITER PFC's: predictions, uncertainties, R&D status and priority needs. *Fusion Engineering and Design*, 39-40, 445-464.

40. Renk, T. J. et al., (2005) Chamber wall materials response to pulsed ions at power-plant fluences. *Journal of Nuclear Materials*, 347, 266-288.

41. Radel, R. F. and Kulcinski, G. L., (2005) Implantation of D and He in W-coated refractory carbides. *Fusion Science and Technology*, 47 (4), 1250.

42. Cipiti, B.B. (2004). The fusion of advanced fuels to produce medical isotopes using inertial electrostatic confinement. (Doctoral dissertation, University of Wisconsin - Madison).

43. Radel, R. F. (2007). Detection of highly enriched uranium and tungsten surface damage studies using a pulsed inertial electrostatic confinement fusion device (Doctoral dissertation, University of Wisconsin – Madison).

44. Radel, R. F. and Kulcinski, G. L., (2006) Effects of high temperature pulsed helium implantation on tungsten surface morphology. *Fusion Science and Technology*, 52 (3), 544-548.

45. Radel, R. F. et al., (2006) *Transactions of the American Nuclear Society*, 95, 12.

46. Goodfellow Corporation online database. W and W-Re properties. http://www.goodfellow.com/csp/active/gfHome.csp

Chapter 3. IMPLANTATION THEORY

3.1. Ion range

In any ion implantation experiment, accurate determination of the depth and spatial distribution of the implanted ions is critical. Because collisions result in a distribution of ions throughout the implanted region, the depth (range) of the ions is only the average position of the ion deposition in the material. For a given medium, the range, *R(E),* of the particle of interest is dependent on the stopping power, *S(E)*, of the medium, where *E* is the particle energy:

$$Range = R(E) = \int_0^E \frac{dE'}{S(E')}. \qquad \text{Equation 3-1}$$

One of the most important physical quantities of interest for this thesis is the implantation range of He^+ in W. The depth distribution of the implanted ions will range from the material surface to the peak distance these ions have penetrated. For solid W implanted with 30 keV He^+ SRIM [1] predicts the peak concentration of $^4He^+$ to be at 61 nm from the surface and at 73 nm for $^3He^+$. Additionally, both inertial fusion and magnetic fusion reactors will experience very high baseline temperatures. Therefore, a complete analysis of the He atom distribution in the material of in-vessel reactor components requires knowledge of the implanted range and the inclusion of diffusion processes. It should also be noted that the SRIM program homogenizes all compounds and assumes that the materials are amorphous.

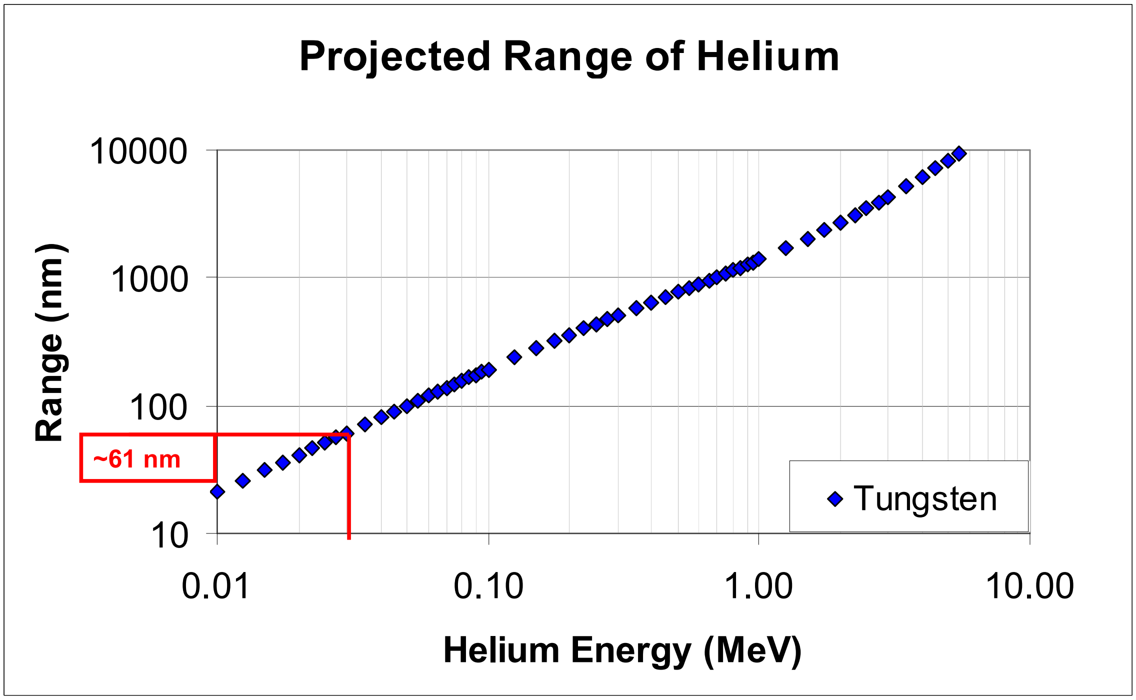

Figure 3-1: SRIM calculation of projected helium range into W plotted against the initial ion energy. [1]

3.2. Sputtering

As energetic ions (or neutrals) bombard the surface of a given material some of the ions will cause the energetic ejection of an atom on or near the material surface. This process is called physical sputtering and can be described using a general equation developed by Sigmund [2]:

$$Yield = S(E,\eta) = \frac{3}{4\pi^2}\alpha\frac{4M_1M_2}{(M_1+M_2)^2}\frac{E}{U_0}, \qquad \text{Equation 3-2}$$

where S is the sputtering yield measured in atoms ejected per ion implanted, η is the cosine of the angle of incidence, M_1 and M_2 are the masses of the incident and bombarding particles, respectively. E is the bombarding particle's energy, α is a dimensionless quantity depending upon the relative masses and angle of incidence, and U_0 is the surface binding energy. From Equation 3-2 one sees that the sputtering yield from a given material depends on several variables, several of which can be highly sensitive to the experimental setup.

One of these variables is the ion's angle of incidence, which is contained in the quantity of Equation 3-2, α. Sigmund reported that sputtering yield would increase in proportion to the inverse cosine of the incident angle. [2] Equation 3-3 shows the ratio in sputtering yields for off normal incidence (*S(η)*) to normal incidence, *S(1)*:

$$\frac{S(\eta)}{S(1)} = \eta^{-f} = (\cos\upsilon)^{-f}, \qquad \text{Equation 3-3}$$

where υ is the angle of incidence and f is a constant based on the interacting particle masses. The strong angular dependence on sputtering yield was verified experimentally by Bay and Bohdansky [3] and their results are shown in Figure 3-1. The sputter yield at nearly glancing angles (~80°) can increase by almost one order of magnitude from yields at normal ion incidence, which is a substantial variation in sputtering yield.

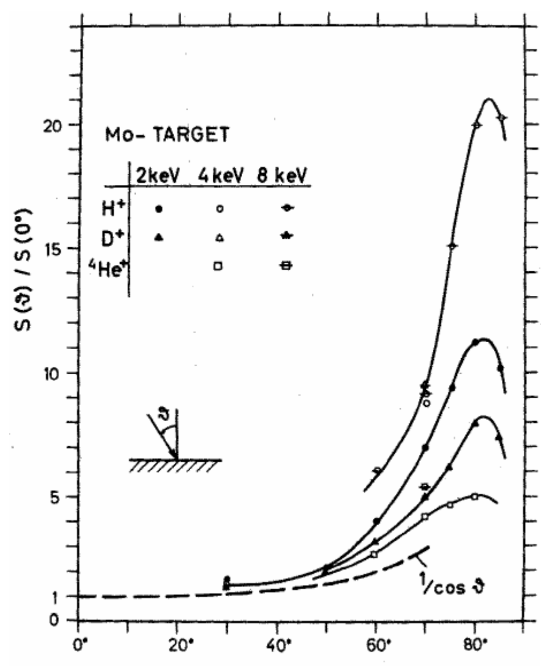

Figure 3-2: Sputtering yields for Mo at varying angles of ion incidence. [3]

As Equation 3-2 shows, the surface binding energy of the bombarded material can also affect sputtering yields from incident ions. In order for an atom to be ejected from a surface the bombarding particle, or a cascading particle whose energy has been transferred from the bombarding ion, must impart enough momentum (directed out of the material) to the atom to overcome its surface binding energy. For a polycrystalline material, one expects that different grains will have different crystalline planes exposed to the beam. Depending on the orientation of the crystal lattice to the incoming ion, it is possible that some fraction of the momentum imparted by the ion is focused into an unproductive sequence of collisions which limits the multiplication of displacement atoms. [4] This scarcity of displaced atoms in the near surface region of the material can reduce the sputter yield for a specific orientation of a crystal lattice to the incoming beam. Therefore, one can predict that sputtering yield will vary depending on the orientation of the grain (crystal) under bombardment. Southern et al. [5] successfully predicted and observed this variation in sputtering yield (Figure 3-3).

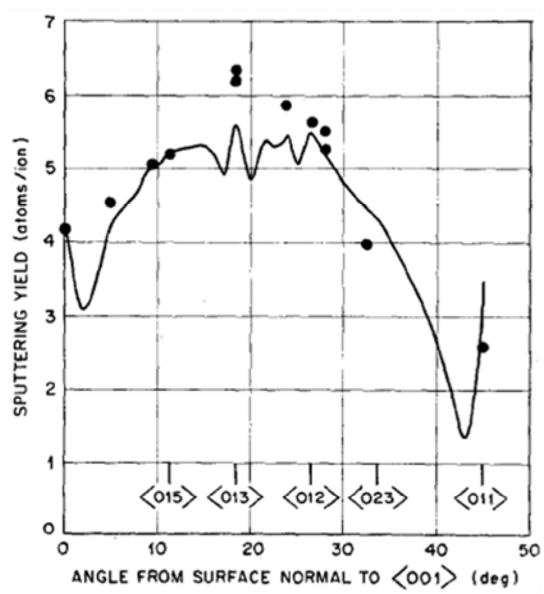

Figure 3-3: Sputtering yields of <0*kl*> Cu monocrystals under normally incident 5 keV Ar^+, plotted against the angle between the surface normal and <001>. The line represents the theoretical yield, the points are the experimental data. [5]

Any material chosen as a first wall armor or divertor plate will receive high ion fluxes and must successfully withstand the aforementioned sputtering effects. Furthermore, ion implantation studies must be cognizant of the wide variations in sputtering yield that results from angular incidence of the ions and crystallographic orientation of the target material.

3.3. Secondary electron emission

Secondary electrons are produced when a particle of sufficient energy bombards a material surface or passes through a material and induces the emission of an electron from the material. Although secondary electron emission will certainly occur in a reactor, it is not of direct importance to the material response of the in-vessel components. Yet, it is briefly treated in this chapter because of the role it plays in almost all materials testing experiments, especially those discussed in Chapters 4, 5, and 6 of this thesis. To calculate the true ion current (I_{ion}) to an implanted specimen, a correction (based on secondary electron emission) must be applied according to the equation:

$$I_{ion} = \frac{I_{meas}}{(1+\gamma)}, \qquad \text{Equation 3-4}$$

where I_{meas} is the experimentally measured current, γ is the secondary electron emission coefficient, and all secondary electrons are assumed to be collected as measured current. Unless secondary electrons are suppressed by some technique, such as target biasing, this equation applies. The yield of secondary electrons can be characterized the by Sternglass theory [6], which is shown in Equation 3-5 below as taken from reference [7].

$$\gamma = Y_{ion} = \frac{Pd_s}{E_* \cos\theta}\left(\frac{dE}{dx}\right)_{ion}, \qquad \text{Equation 3-5}$$

where P is ½ the probability that an ionization electron is liberated in the surface at depth d_s, d_s is the mean escape depth of the secondary electrons, θ is the angle of incidence of the ion normal to the material surface, E_* is the mean energy deposited into the material by the fast ions, and $(dE/dx)_{ion}$ is the electronic stopping power of the target material.

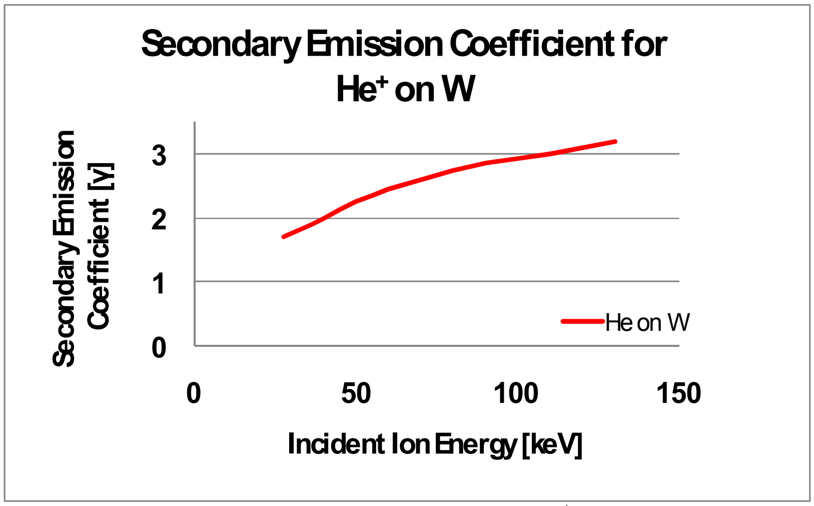

Figure 3-4: Secondary emission coefficient for He^+ incident on W. [11]

The main variable of importance to this thesis is the angular dependence of emission yield, which can significantly affect the calculations of ion flux to an implanted specimen [8] and thereby, produce uncertainty in the time integrated flux (fluence). A study by Baroody [9] showed that the work function of a material will affect the yield of secondary electrons, and Kustner [10] reported that surface roughness can change the effective sputtering yield from redeposition of initially sputtered atoms. These dependencies provide a strong incentive to simplify experiments by using very smooth initial surfaces placed at perpendicular orientations to the incoming ion beam. Figure 3-4 shows the energy dependence of the secondary emission coefficient for He^+ incident on

W. This plot was generated for a normally incident ion beam on a polished tungsten surface from data reported by Large [11].

3.4. Bubble formation and growth

Up to this point, this chapter has focused on some of the fundamental phenomena regarding the implantation of ions into a material: ion range, ionic sputtering, and ion-induced electron emission. While each of these phenomena may contribute to, or even drive, surface morphology change of ion implanted specimens; they do not consider the behavior of the implanted ions after they have implanted and stopped in a material. Some general theory describing the behavior of the bombarding ion after implantation is discussed in the following section. This discussion will emphasize the formation and evolution of blisters and bubbles formed by implantation of inert gas atoms, specifically helium.

A wide range of research has focused on studying the detrimental effects of helium once it is present in metals or alloys, including volumetric swelling, high temperature embrittlement and tensile strength. [12,13,14] These effects can have large impacts on fusion reactor systems which have tight mechanical and space tolerances, operate at high temperature, and must maintain their structural integrity over the lifetime of the in-vessel components.

For the purposes of this discussion, helium is considered to be insoluble in metals. Once a He atom is implanted into a material it can occupy an interstitial site or a substitutional site, with the interstitials being fairly mobile at room temperature. [15] However, because these He atoms are insoluble, they become trapped by defects or impurities resident in the implanted material, barring their release through other processes, such as thermal desorption. In fact, according to Barnes and Nelson [16], it is only necessary to consider the behavior of implanted helium atoms as individual atoms at very low concentrations. As soon as helium (or any inert gas) bubbles are formed, the migration of individual atoms is inconsequential since they will be readily absorbed into the numerous bubbles now existent in the material. In this thesis, the work presented deals with atomic concentrations of He in W that are quite high; therefore, this discussion will stress the behavior of helium after it has coalesced into clusters or bubbles. For a discussion of atomistic helium transport the reader is referred to a report by Ghoneim et al. [17]

Once helium bubbles are formed they can modify a material's surface morphology through several processes, including pore formation and blister formation. This is not a new phenomenon as pores or "pinholes" were seen in vanadium by Thomas and Bauer [18] as early as 1974. A kinetic rate theory code developed at UCLA called HEROS [19] is able to model the formation and growth of helium bubbles in a material and predict the effect of these bubbles on a material's surface. A report by Sharafat et al. [20] used the HEROS code to model the bubble formation and growth observed on polycrystalline W specimens after they were implanted with He^+ at the University of Wisconsin-Madison Inertial Electrostatic Confinement (UW IEC) laboratory. [21,22] Inputting the experimental parameters of these implantations into the HEROS code showed good agreement with the observed average surface pore diameter of implanted W specimens. The results of this work are shown in Figure 3-5.

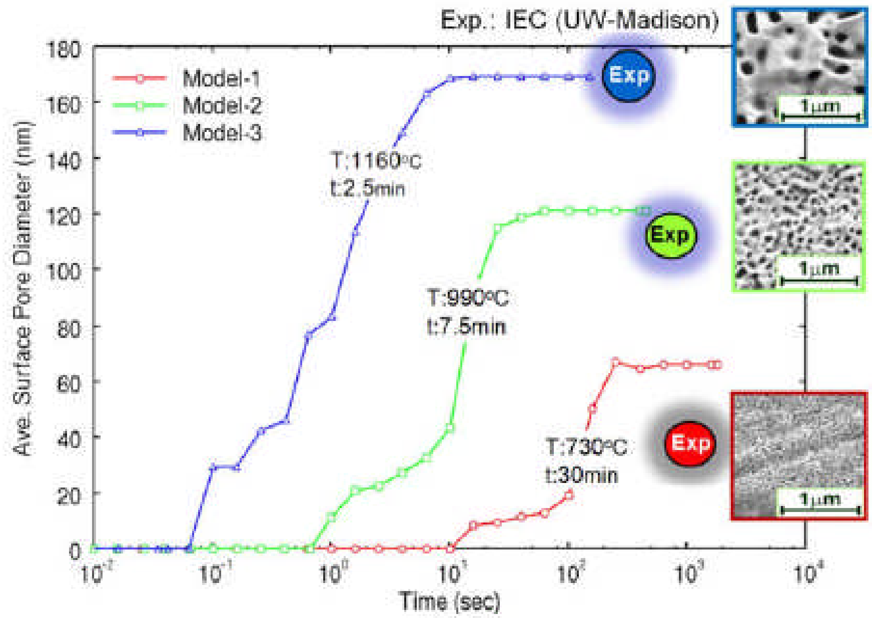

Figure 3-5: Simulation of the surface bubble average diameter as a function of the irradiation time for W implanted with 30 keV He^+ to a fluence of ~$3x10^{17}$ He^+/cm^2. [20]

For the specimens implanted at 990 °C and 1160 °C, the code shows very good agreement with the observed average surface bubble size of the irradiated W specimens. Yet, at the lowest implantation temperature of 730 °C, the model was not as accurate. The report attributed this to the lower homologous implantation temperature (below ~0.3 T/T_m) where the nucleation and growth of He bubbles cannot be treated as sequential stages in the He bubble evolution. [20] Despite this discrepancy at lower implantation temperatures, the model shows good agreement with experimental results at higher implantation temperatures.

Although the core diffusion equations used in the HEROS code [17,19] are not treated in this thesis, a brief discussion of bubble migration by surface diffusion is presented. The work presented in reference [20] also assumed that surface diffusion drove any diffusion of helium bubbles as they formed in the implanted W. The following discussion of bubble diffusion is motivated by results at the UW IEC laboratory that were initially reported by Radel and Kulcinski [22,23] which showed the formation of a sub-surface semi-porous layer in the implanted W as well as the porous surface structure (Figure 3-6).

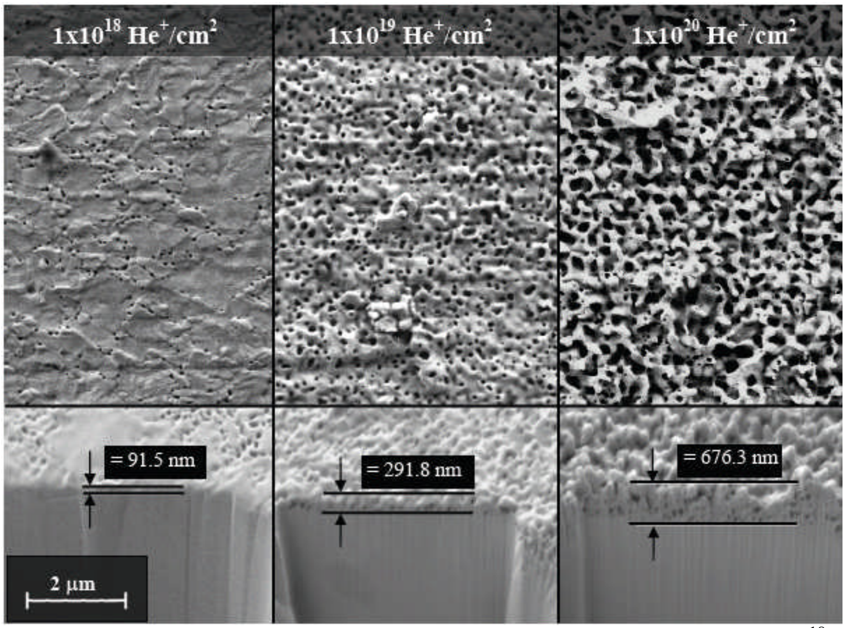

Figure 3-6: Polycrystalline W irradiated with 30 keV He^+ at a 1150 °C to fluences of $10^{18} – 10^{20}$ He^+/cm^2 showing the sub-surface semi-porous layer as well as the porous and coral-like surface morphology. [22]

For helium bubbles existing in a metal, the internal pressure *(P)* of individual helium bubbles and coalesced bubbles and the number of inert gas atoms *(m')* can be described by the following equations:

$$Pressure = P = \frac{2\gamma}{r_B}, \qquad \text{Equation 3-6}$$

where γ is the surface tension of tungsten and r_B is the bubble radius, and

$$m' = \frac{8\pi\gamma r_B^3}{3(kTr_B + 2\gamma b)}, \qquad \text{Equation 3-7}$$

where b is the Van der Waal's gas constant, k is the Boltzmann constant, and T is the temperature. By applying known constants and experimental observations of average bubble radius to Equation 3-6 and Equation 3-7, one could estimate the retained atomic concentration of He after implantation. As a note, enhanced bubble diffusion resulting from temperature or stress gradients on the implanted material is not discussed in the thesis; instead the reader is referred to reports by Barnes and Nelson [16] and Sharafat et al. [20] that address some of the various driving forces involved in bubble diffusion. For this model, bubble migration is assumed to be dominated by surface diffusion at the relevant implantation temperatures. [24] The surface diffusion coefficient D_s is defined as,

$$D_S = D_O \exp(\frac{-E_A}{kT}), \qquad \text{Equation 3-8}$$

where D_o is the pre-exponential and E_A is the surface activation energy in W. Using values listed by Ehrhart [25] and Cottrell, [26] values of ~1x10^{-3} cm^2/s and ~7x10^{-11} cm^2/s are chosen for D_o and D_s, respectively at 1000 ºC. The bubble diffusion coefficient D_B, for surface diffusion, is defined as,

$$D_B = \frac{3\Omega^{4/3}}{2\pi r_B^4} D_S, \qquad \text{Equation 3-8}$$

where Ω is the atomic volume. The analyzed diffusion mechanisms for bubble transport are Brownian motion and grain boundary tension (applicable to polycrystalline materials). At any temperature where Brownian motion can occur, after some time t, the migrating bubble's center of gravity will have moved a distance $\overrightarrow{l_B}$ from its starting point. If one also considers the driving force F_{gb} of grain boundary tension on the helium bubbles the resultant displacement is $\overrightarrow{l_{gb}}$. The average displacement $\overrightarrow{l_{gb}}$ from the bubble's center of gravity is the quadrature sum of the two random and uncorrelated vectors $\overrightarrow{l_B}$ and $\overrightarrow{l_{gb}}$ as described by Barnes and Nelson [16]:

$$\overrightarrow{l_{tot}}^{2} = \overrightarrow{l_B}^{2} + \overrightarrow{l_{gb}}^{2} = (6D_B t) \ + (\frac{D_B}{kT} F_{gb} t)^2, \qquad \text{Equation 3-9}$$

where t is the irradiation time and D_B is the bubble diffusion coefficient derived from Equation 3-9. To achieve an upper estimate of He bubble diffusion distances in W for the experiments analyzed in this thesis, it is assumed that grain boundary diffusion is directed downward from the surface. Furthermore, if the assumption that Brownian diffusion acts to move the bubble around this mean position drifting under the force F_{gb} is applied here, then the diffusion enhanced maximum of the range *(R_{diff})* of the implanted He can be estimated using Equation 3-1 and Equation 3-10 as given below,

$$R_{diff} \approx R_{SRIM} + l_B + l_{gb} \qquad \text{Equation 3-11}$$

where R_{diff} is directed downward from the surface normal. This is meant to be a simple approximation which bounds the average range of He bubbles in W when these diffusion processes are incorporated. Inputting values from Radel and Kulcinski [22] yields values for l_{tot} <10 nm, a small fraction of the implanted range. Combining this analysis with the results of Sharafat et al [20], suggests that it is the growth and coalescence of helium bubbles which causes them to break the W surface and extend into the W bulk to form the sub-surface semi-porous layers.

Another surface morphology change resulting from trapped helium in metals is blistering. According to Behrisch and Scherzer [27], blistering can be brought on by 1) the formation of an interface of reduced strength between the surface layer and the bulk, or 2) the deformation of the surface layer. Although the various models governing the size and shape of blisters formed under helium implantation are not of primary concern to this thesis, an illustration of the two aforementioned processes is given in Figure 3-7. It has also been observed that blisters required a certain amount of implanted helium fluence, called the critical fluence, before blistering could occur. Several studies reported a critical fluence of ~5×10^{17} He^+/cm^2 for molybdenum [28] and ~3×10^{17} $ions/cm^2$ for rhenium [29]. Conversely, at high enough fluences blisters will disappear. Martel el al. [30] implanted niobium to fluences up to 6×10^{19} He^+/cm^2 and measured a sputtered layer of ~800 nm. During these experiments it was observed that as the fluence increased the blister size gradually decreased until enough of the niobium was sputtered away (130-260 nm) to cause the blisters to disappear completely [30].

To summarize the bubble formation and growth section of this chapter, recent theoretical work has been done to assess the formation, migration, and coalescence of these bubbles in W as a result of He^+ implantation. [19,20, 31] At implantation temperatures above ~0.3 T/T_m, these models predict the surface average bubble diameter quite well. The surface diffusion model for helium bubbles does not appear to explain the extended depth (or range) of the sub-surface semi-porous layer observed in He^+ implanted W. Coalescence of smaller bubbles and bubble growth are suspected to be at least partially responsible for this semi-porous layer. Finally, blister formation is observed on metals for critical fluences ≥$3\text{-}5 \times 10^{17}$ ion/cm^2 in molybdenum and rhenium, but blisters can also disappear at very high fluences (>10^{19} He^+/cm^2).

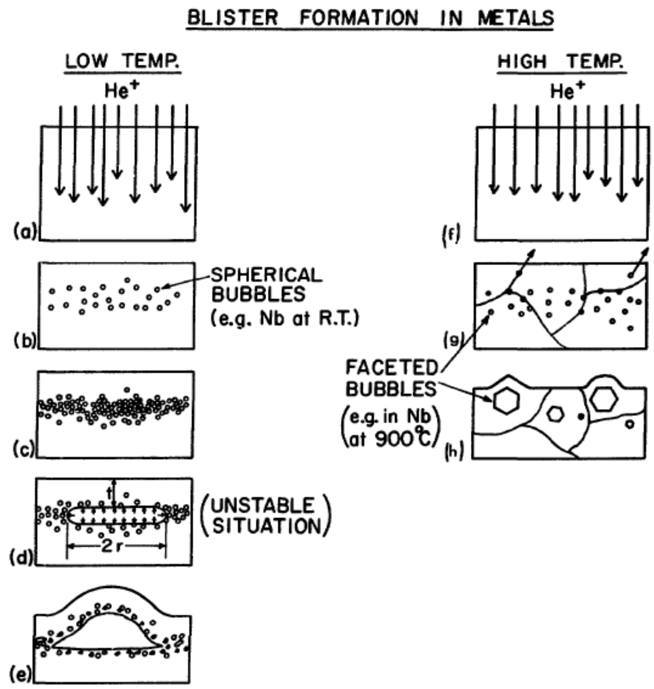

Figure 3-7: Schematic diagrams of blister formation at low temperatures (a) – (e) and at high temperatures (f) – (h). The progression of pictures in (a) – (e) shows the formation of a blister resulting from a reduction in strength between the surface layer and the bulk of the metal. [32]

3.5. References for Chapter 3

1. Ziegler, J. F. et al., (1985) *The Stopping and Range of Ions in Solids*. Pergamon Press, New York.

2. Sigmund, P., (1969) Theory of sputtering I: sputtering yield of amorphous and polycrystalline targets. *Physical Review*, 184 (2), 383-416.

3. Bay, H. L. and Bohdansky, J., (1979) Sputtering yields for light ions as a function of angle of incidence. *Applied Physics*, 19, 421-426.

4. Nelson, R. S. and Thompson, M. W., (1961) Atomic collision sequences in crystals of copper, silver and gold revealed by sputtering in energetic ion beams. *Proceedings of the Royal Society of London. Series A, Mathematical and Physical Sciences*, 259 (1299), 458-479.

5. Southern, A. L. et al., (1963) Sputtering experiments with 1- to 5-keV Ar^+ ions. *Journal of Applied Physics*, 34 (1), 153-163.

6. Sternglass, E. J., (1957) Theory of secondary electron emission by high-speed ions. *Physical Review*, 108 (1),
1-12.

7. Suszcynsky, D. M. and Borovsky, J. E. (1992) Modified Sternglass theory for the emission of secondary electrons by fast-electron impact. *Physical Review A*, 45 (9), 6424.

8. Piefer, G. R. (2006). Performance of a low-pressure, helicon driven IEC 3He fusion device (Doctoral dissertation, University of Wisconsin – Madison).

9. Baroody, E. M. (1950) A theory of secondary electron emission from metals. *Physical Review*, 78 (6), 780-787.

10. Kustner, M. et al., (1998) The influence of surface roughness on the angular dependence of the sputter yield. *Nuclear Instruments and Methods in Physics Research B*, 145, 320-331.

11. Large, L.N. (1963) Secondary electron emission from a clean tungsten surface bombarded by various positive ions. *Proc. Phys. Soc.*, **81**, 1101-1103.

12. Farrell, K., (1980) Experimental effects of helium on cavity formation during irradiation – a review. *Radiation Effects*, 53, 175.

13. Braski, D. N., et al., (1979) The effect of tensile stress on the growth of helium bubbles in an austentitic stainless steel. *Journal of Nuclear Materials*, 83 (2), 265-277.

14. Bloom, E. E., (1979) Mechanical properties of materials in fusion reactor first-wall and blanket systems. *Journal of Nuclear Materials*, 85-86, 795-804.

15. Abd El Keriem, M. S. et al., (1993) Helium-vacancy interactions in tungsten. *Physical Review B*, 47 (22), 14771-14777.

16. Barnes, R.S. and Nelson, R.S., (1965) Theories of swelling and gas retention in reactor material. *Atomic Energy Research Establishment Report* AERE-R 4952.

17. Ghoniem, N. M. et al., (1983) Theory of helium transport and clustering in materials under irradiation. *Journal of Nuclear Materials*, 117, 96-105.

18. Thomas, G.J. and Bauer, W., (1974) Surface deformation in He and H implanted metals. *Journal of Nuclear Materials*, 53, 134-141.

19. Hu, Q. et al., (2006) Modeling space-time dependent helium bubble evolution in tungsten armor under IFE conditions. *Fusion Science and Technology*, 52 (3), 574-578.

20. Sharafat, S. et al., (2009) A description of stress driven bubble growth of helium implanted tungsten. *Journal of Nuclear Materials*, 389, 203-212.

21. Cipiti, B.B. and Kulcinski, G.L. (2005) Helium and deuterium implantation in tungsten at elevated temperatures. *Journal of Nuclear Materials*, **347**(3), 298.

22. Radel, R.F. and Kulcinski, G.L. (2007) Implantation of He+ in candidate fusion first wall materials. *Journal of Nuclear Materials*, 367-370 p. 434-439.

23. Radel, R. F. and Kulcinski, G. L., (2006) Effects of high temperature pulsed helium implantation on tungsten surface morphology. *Fusion Science and Technology*, 52 (3), 544-548.

24. Nichols, F.A., (1969) Kinetics of diffusional motion of pores in solids a review. *Journal of Nuclear Materials*, 30, 143-165.

25. Ehrhart, P. (1991) *Atomic Defects in Metals*. Berlin ; New York : Springer-Verlag, Vol. 25.

26. Cottrell, G.A. (2002) Void migration in fusion materials. *Journal of Nuclear Materials*, 302, 220-223.

27. Behrisch, M and Scherzer, B. M. U., (1982) *Surface topography due to light ion implantation*. Springer-Verlag, New York.

28. Nagata, S. et al., (2002) Ion beam analysis of helium and its irradiation effect on hydrogen trapping in W single crystals. *Nuclear Instruments and Methods in Physics Research B*, 190, 652-656.

29. Fahlstrom, C. R. and Sinha, M. K., (1978) Surface blistering of molybdenum irradiated with 75 – 350 keV helium ions. *Journal of Vacuum Science Technology*, 15 (2), 675,

30. Martel, J. G. et al., (1974) Preliminary observation of blistering of niobium by 1-15 keV helium ions. *Journal of Nuclear Materials*, 53, 142-146.

31. Takahashi, A. et al, (2006) MC simulation of tungsten surface pores formed by low-energy helium implantation. presented at the 15th High Average Power Laser Program Workshop, August 8, 2006, San Diego, CA.

32. Das, S.K. and Kaminsky, M., (1975) Radiation blistering in metals and alloys. *Proceedings of the "Symposium on Radiation Effects on Solid Surfaces" Advances in Chemistry Series*.

CHAPTER 4. EXPERIMENTAL SETUP

Prior to the construction of the Materials Irradiation Experiment (MITE-E), two devices at the University of Wisconsin-Madison Inertial Electrostatic Confinement (UW IEC) laboratory were capable of high temperature ion implantation experiments: HOMER and HELIOS. The initial experimental work done by Cipiti [1] and Radel [2] (discussed in Chapter 2 of this report) was carried out exclusively in HOMER. The research presented in this dissertation was carried out in each of the three implantation devices at the UW IEC group: HOMER, HELIOS, and the newly constructed MITE-E. The experimental setup of the HOMER and HELIOS devices are only briefly described here, as well as the features of each of the devices which motivated the transition of high temperature materials implantation studies from HOMER to HELIOS in 2006 and then from HELIOS to the MITE-E design and construction in 2008 – 2009. Since the work in this thesis is only concerned with the HOMER and HELIOS devices as ion implantation facilities, a description of their nominal operation for fusion experiments is not discussed here and the reader is referred to the open literature. [3,4]

The core technology behind the operation of the MITE-E is an ion gun module. This ion gun module was initially designed and built within the UW IEC group by Brian Egle for the Six Ion Gun Fusion Experiment (SIGFE). [5] For details on the design and construction of these ion gun modules, such as the plasma source and extraction, electrostatic optics, and assembly and alignment techniques the reader is referred to the original thesis on this technology [5], where a thorough discussion of the ion gun modules is given. This thesis does not treat the development and construction of the ion gun module itself, but rather the integration of the ion gun technology with the MITE-E infrastructure to develop a stand alone facility for materials implantation studies.

4.1. HOMER and HELIOS as implantation facilities

HOMER is illustrated in Figure 4-1 and consists of a cylindrical aluminum vacuum chamber measuring 65 cm high with a diameter of 91 cm. The vacuum system uses a Leybold Trivac® rotary vane roughing pump and Varian® turbo pump (500 L/s). Nominal base pressures can reach the low 10^{-6} Torr range and are measured with an MKS® ion gauge.

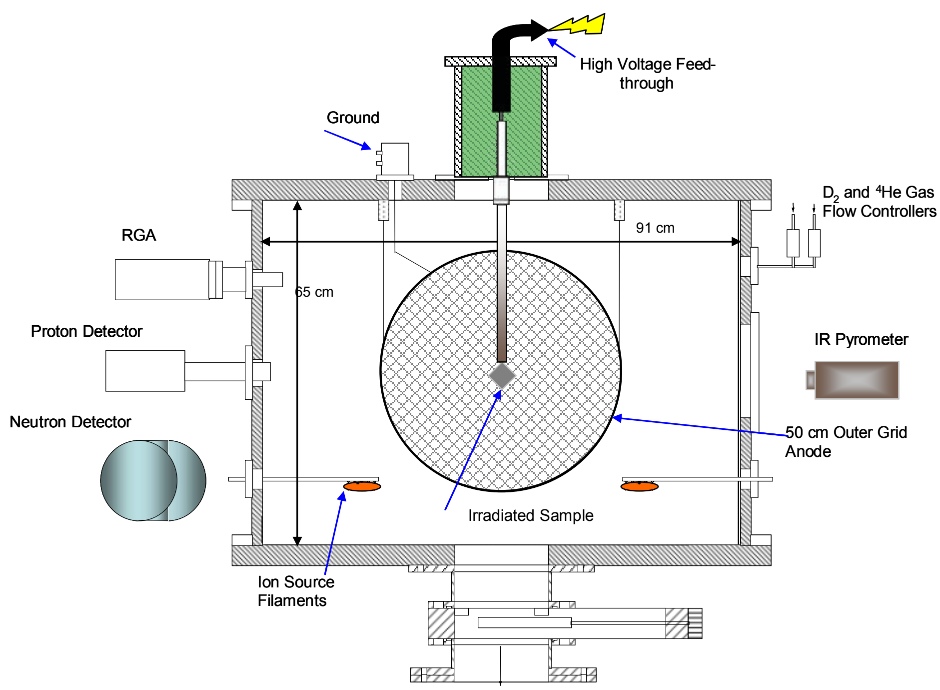

Figure 4-1: Schematic of the IEC device HOMER as a materials implantation facility.

The second implantation apparatus, HELIOS, is shown in Figure 4-2. The spherical stainless-steel main vacuum chamber has a 61 cm inner diameter and a sealed water jacket around the main vessel, which enables the chamber to be water-cooled. Routine base pressures near ~10^{-6} Torr are achieved by a 550 L/s Varian Macro Torr®

turbo molecular pump. A Leybold® direct drive roughing pump (1.1 kW) is used to exhaust the turbo pump.

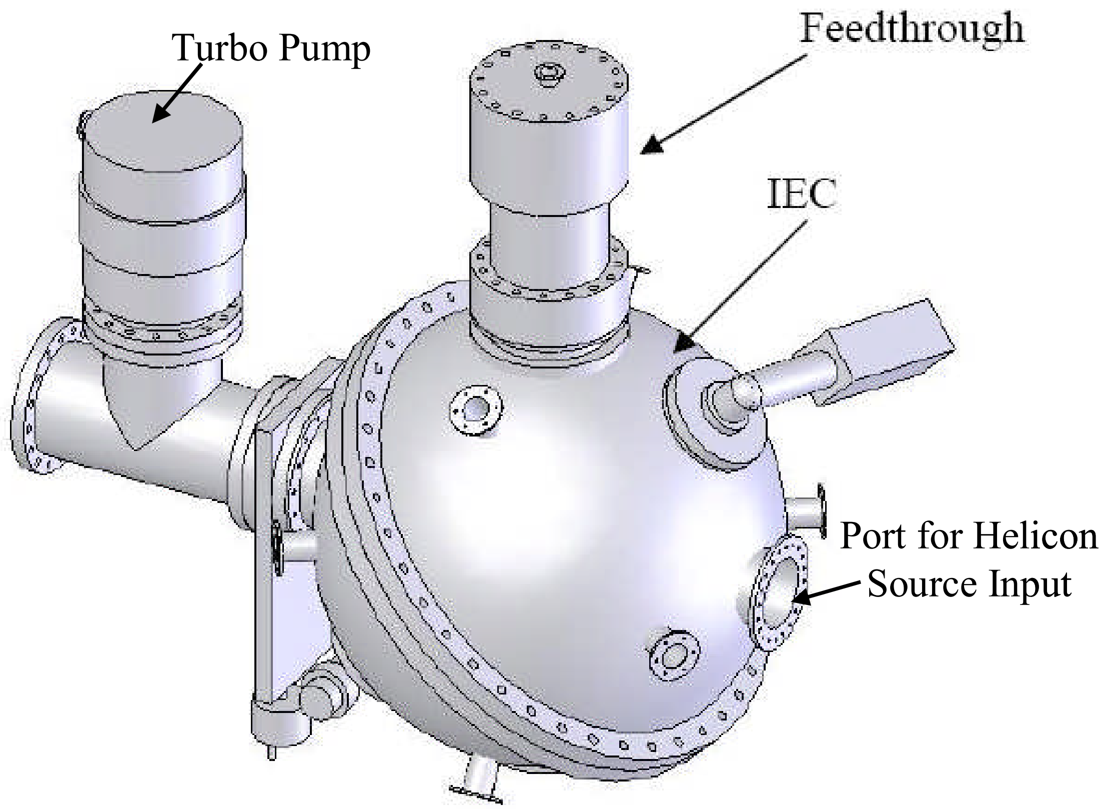

Figure 4-2: Computer-aided design (CAD) drawing of the HELIOS device showing the water-cooled vacuum vessel, turbo pump, high voltage feedthru, and the extraction port for the helicon ion source (the source is omitted). [6]

4.1.1. Materials implantation experiments in HOMER and HELIOS

For materials implantation experiments the operation in HELIOS is nearly identical to that of HOMER, except that in HELIOS, ions are produced with a helicon plasma source instead of electron filaments. HOMER uses six (3 pairs) of 200 W light bulb filaments spaced radially around the vacuum vessel by ~120º to produce fast electrons which ionize the fuel gas. A unique characteristic of HELIOS is the helicon ion source which uses RF power coupled with a magnetic field to ionize and confine plasmas. The helicon ion source uses the cathode voltage and inherent plasma pressure of the source to extract the ions. For illustration, Figure 4-3 shows the HELIOS apparatus with the helicon ion source while the source is a generating a plasma.

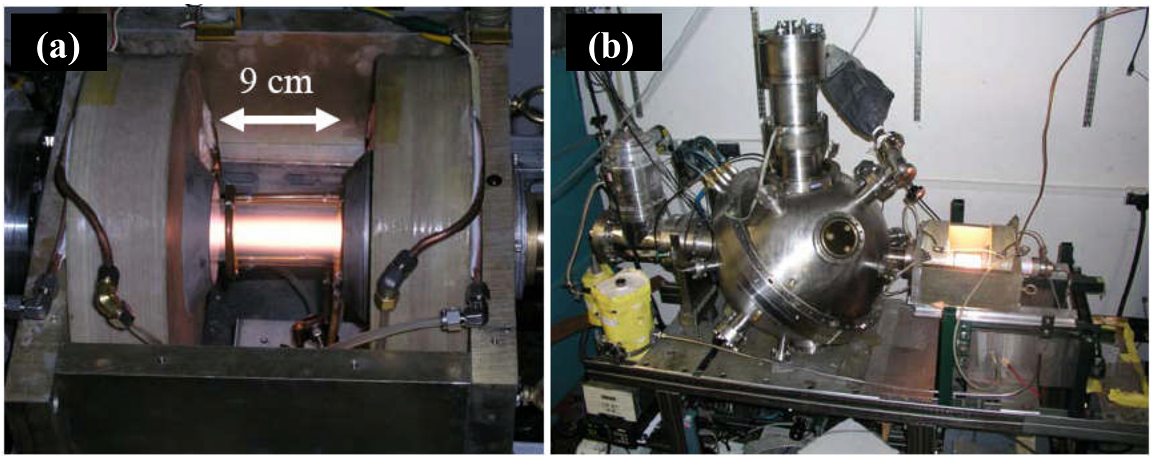

Figure 4-3: (a) The helicon ion source with a plasma, and (b) the HELIOS IEC vacuum vessel coupled with the helicon ion source (shown in operation). [6]

Because of the operational similarities between HOMER and HELIOS, the general setup for materials implantation experiments is only described using the HOMER device. During operation, the fuel gas is injected into the HOMER vacuum chamber at anywhere from 5-20 sccm (standard cubic centimeters per minute) using MKS Mass-Flo® controllers. The gate valve between the main vacuum vessel and the turbo-molecular pump is partially closed until the pressure read by the MKS Baratron® transducer is ~500 μTorr. A Stanford Research Systems CIS 200® residual gas analyzer (RGA) was used to measure impurities. The high voltage supply used for all of the materials implantation experiments performed in the HOMER and HELIOS devices employed a -200 kV and 75 mA Hipotronics® model 8200-75 high voltage transformer and controller. It is important to note that all of the implantations performed in the MITE-E used a -300 kV and 200 mA high voltage power supply, delivered to the UW IEC laboratory in the summer of 2009.

For materials implantation experiments in HOMER, the specimen undergoing ion bombardment acts as the cathode of the device. The specimens which are to be implanted are brought into electrical contact with the central conductor of the IEC device using W-Re mounting wire (Figure 4-4(a)). This central conductor is a molybdenum rod which transfers the large negative potentials (-30 kV) from the high voltage feedthru (an oil-filled environment at atmospheric pressure) into the vacuum vessel. Electrical isolation between the center conductor and the vacuum vessel is maintained by a BN stalk. The goal of these mounting schemes is to provide a direct connection between the specimen which is to be irradiated and the high voltage power supply.

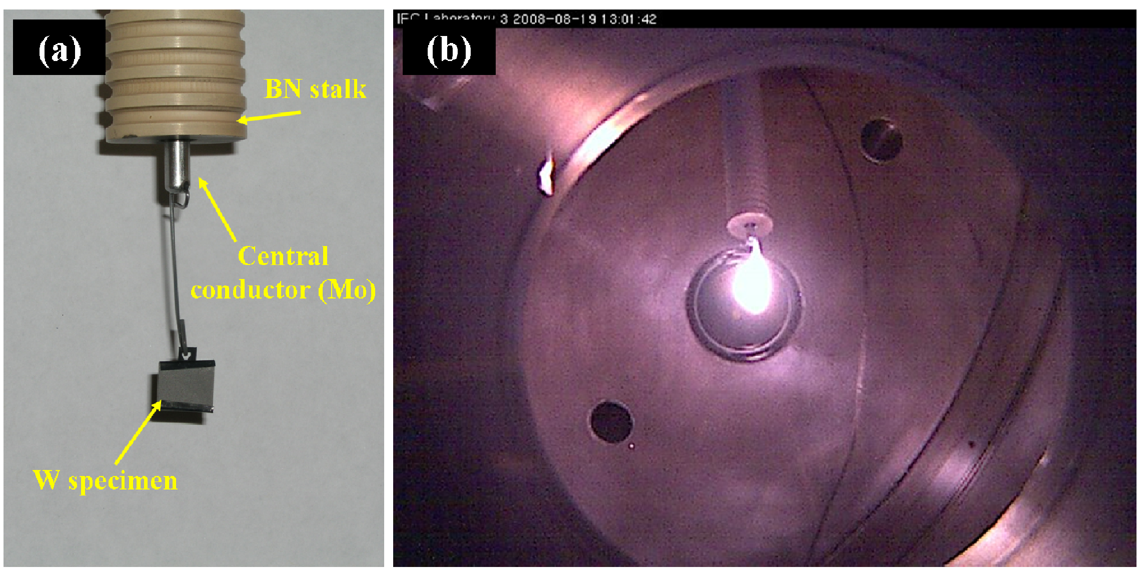

Figure 4-4: (a) Mounting setup for a W specimen prior to implantation in the HELIOS device and shown hanging from the Mo conductor via a W-Re wire. The insulating BN stalk is also pictured. (b) The W specimen during implantation with He^+ at ~1000 °C in HELIOS. Specimen mounting procedures are the same for the HOMER and HELIOS devices.

The -30 kV potential on the sample attracts and accelerates most of the positively ionized fuel gas (in this case He) to energies equivalent to the applied cathode voltage (30 keV). As the He^+ energetically bombards the cathode (specimen), these ions deposit their kinetic energy into the cathode as they slow down in the material and eventually stop after penetrating to some depth. This kinetic energy deposition simultaneously implants and heats the specimen. The ion fluxes provided by the IEC devices HOMER and HELIOS can easily heat samples to temperatures between 800 – 1200 ºC (Figure 4-4(b)).

The equilibrium irradiation temperature is set by the ion energy (cathode voltage) and the ion flux (cathode current). The fluence incident on the samples is determined by integrating the ion current over the runtime. Because the conduction heat loss to the W-Re mounting wire is small compared to nominal power inputs, it is assumed that the heat loss is dominated by radiative cooling. Convective and conduction heat losses to the gas are assumed to be negligible and are not considered. Given these assumptions, the power balance between the input ion heating power and power loss by radiative cooling can be used to calculate the sample's steady state irradiation temperature. The general equation for this calculation is shown below:

$$P_{heating} = \frac{I_{meter} V_{cathode}}{1+\gamma} = \varepsilon A_{sample} \sigma_{SB} T^4, \qquad \text{Equation 4-1}$$

where I_{meter} is the current read from the power supply, γ is the secondary electron emission coefficient (SEC) of the cathode (irradiated specimen), ε is the total normal emissivity of the irradiated sample, A_{sample} is the irradiated area, σ_{SB} is the Stefan Boltzmann constant, and T is the temperature. The true ion current (I_{ion}) and the cathode voltage ($V_{cathode}$) are determined by the following two equations.

$$I_{ion} = \frac{I_{meter}}{1+\gamma} \qquad \text{Equation 4-2}$$

$$V_{cathode} = V_{meter} - I_{meter} R_{barrel}, \qquad \text{Equation 4-3}$$

where V_{meter} is the read supply voltage and R_{barrel} is a 250 kΩ ballast resistor barrel in series with the HOMER device. Rewriting Equation 4-1 with the relationship provided in Equation 4-2 gives a power balance between the input ion power, $P_{in,ION}$, and the output radiative power, $P_{out,RAD}$, for a given specimen:

$$P_{in,ION} = P_{out,RAD} = I_{ion} V_{cathode} = \varepsilon A_{sample} \sigma_{SB} T^4 \qquad \text{Equation 4-4}$$

Comparison of the measured ion currents and cathode voltages with the measured temperatures have shown this power balance can only be used as an approximation of sample temperature. This serves as a guide for planning experimental run conditions, but uncertainties in the SEC, which are necessary for calculation of the true ion current, and sample emissivity make precise calculation difficult. In part, the uncertainties in the SEC and emissivity arise from the specimen mounts used for implantation experiments in HOMER and HELIOS. The presences of multiple materials (Mo, W-Re, W, etc.) which are exposed to the ion flux make it difficult to estimate the effective SEC and the effective emissivity of these specimen mounts. The non-uniform shape of the sample mount also provide a challenge in accurately calculating the surface area of the implanted specimen and mount. It is believed that the lack of repeatability in specimen mounting is the largest source of uncertainty in power balance calculations for materials implantation experiments in the HOMER and HELIOS devices.

4.1.2. Measurement of ion current

When performing materials irradiation experiments, accurate determination of the time integrated flux (fluence) to the specimen is paramount. Direct measurement of the ion current incident on the sample via an ammeter or resistor is difficult in IEC devices due to the large potentials present on the cathode. Any such measurement techniques require additional high voltage feedthroughs and complicate operation. One such system was designed and implemented in the MITE-E and is discussed in the infrastructure section of this chapter. However, in the HOMER device, ion current had to be calculated from the meter current (Equation 4-2), which is measured directly from the power supply. The accurate measurement of ion current mandates well-known SEC values of the implanted sample. SEC's can vary significantly with ion energy, material, and the angle of ion incidence. [7] Therefore, "effective" SEC values had to be estimated for the specimens implanted in the HOMER device because of their unrepeatable and non-uniform geometries. If the measured meter current and the effective SEC are known, one can calculate the fluence to the implanted specimen using the following equation:

$$\varphi = \frac{I_{ion}t}{eA_{\Phi}} = \frac{I_{meter}t}{(1+\gamma)eA_{\Phi}}, \qquad \text{Equation 4-5}$$

where φ is the sample fluence (in *ions/cm*^{2}), t is the irradiation time, e is fundamental unit of charge, and A_{Φ} is the flux area (implanted area) of the sample.

4.1.3. Transition to the HELIOS device and the helicon ion source

In early 2007 the primary materials implantation experiments were switched from HOMER to HELIOS to take advantage of the helicon ion source. The motivation in transitioning between the two devices was to more accurately determine the implanted ion current. At a given set of operation parameters (RF power, magnetic field strength, gas pressure, and ion species) the ion current extracted from the helicon source should be constant and reproducible. If the true ion current extracted from the helicon ion source could be determined for a given set of helicon source parameters and a given cathode voltage, then the need to "guess" a specimen's effective SEC could be eliminated. Instead, the effective sample SEC could be determined by solving Equation 4-2 for a given meter current.

Before materials implantations were carried out, a study to characterize the helicon source was performed. The experimental setup included a large tungsten sheet approximately 10x10x0.1 cm^3 was polished to a mirror finish and mounted in the HELIOS device in place of the smaller specimens used in implantation experiments. Polishing the tungsten ensured a well-known SEC [8,9] allowing calculation of the ion current. Experiments diagnosed the helicon source for three different fuel gases (implant ions): ^4He, ^3He, and D. Several operation parameters of the IEC device (cathode voltage, run pressure) and the helicon source (RF power, magnetic field strength) were varied over pertinent ranges for implantation studies. As a result, typical uncertainties in the measurement of the ion current were reduced from 50 – 100% (in HOMER) down to <10% for the HELIOS device with well-characterized ion source. Figure 4-5 illustrates the output helicon ion current as a function of the magnetic field strength applied to confine the plasma.

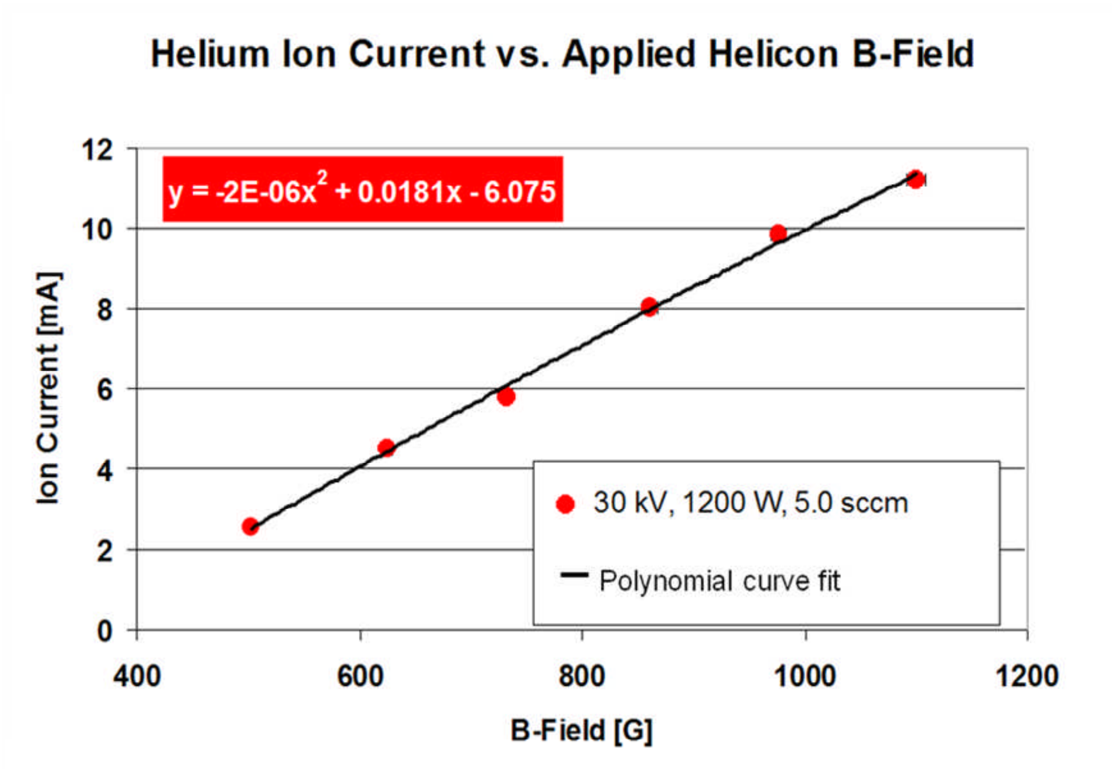

Figure 4-5: ^{4}He ion current extracted from the helicon ion source onto the large (10x10x0.1 cm^3) W sheet as a function of applied magnetic field strength for a given RF antenna power of 1200 W, a cathode voltage of 30 keV, and a gas flowrate of 5.0 sccm.

To apply this data to materials implantation experiments a polynomial curve fit was made to the data – which at a given cathode voltage, RF power, and neutral pressure – correlated the ion current to the applied magnetic field strength. Although this procedure improved the fluence measurements on implanted specimens from those measured in the HOMER device, the model broke down at ion currents below ~2 mA (Figure 4-5). In order for this method to be valid, specimens had to be implanted with ion currents ≥2 mA. Because the average area of implanted specimens are modest (<10 cm^2), minimal ion currents are required to heat samples to high temperatures (>800 ºC). Therefore, constraining the implanted ion current to values of several milliamperes or more, limited the lower temperatures that could be investigated and also prevented implantation to lower fluences. For example, a polycrystalline W specimen with a flux area of ~5 cm^2 was implanted in HELIOS using 30 keV He^+, giving an input ion power of approximately 45 W. For these parameters the equilibrium temperature of the specimen and mount was measured to be 1000 ºC. In order to achieve an implanted fluence of $4x10^{17}$ He^+/cm^2 the specimen only had to be irradiated for 6 minutes. [10]

4.1.4. Summary of implantation experiments in HOMER and HELIOS

To summarize, because the sample heating was initiated by ion bombardment of the specimens in both the HOMER and HELIOS devices, the short implantation time scales of these devices (for low He implant fluences) made temperature equilibration difficult. Furthermore, the time it took to implant most W specimens to fluences below 10^{17} He^+/cm^2 (where the onset of surface morphology change has been observed to occur in W) was usually less than one minute. As previously stated, the input ion power, and consequently, the specimen heating, is the product of the cathode voltage (ion energy) and ion current. Therefore, the energies at which ions could be implanted in HOMER and HELIOS had to remain below ~50 keV in order to keep temperatures from greatly exceeding 1000 ºC. In light of these constraints on materials implantation experiments inherent to the HOMER and HELIOS devices, in early 2008 it was proposed that a dedicated materials implantation facility be designed and constructed. It should be noted that although the HOMER and HELIOS are not well-suited for low temperature, low fluence investigations of ion damage, they are quite effective at implanting materials at high temperatures to large ion fluences. The proposed device, which is now known as the Materials Irradiation Experiment (MITE-E), decouples the main specimen heating from the energetic bombardment of the ions and is able to implant samples over a dynamic range of ion currents.

4.2. Materials Irradiation Experiment (MITE-E) design and construction

One of the objectives of this thesis is to understand the fluence and temperature thresholds of surface damage in helium implanted tungsten and characterize the behavior of W near these thresholds. In order to accomplish this task, it is necessary to investigate fluences at or below 10^{17} He^{+}/cm^{2}. It is also imperative to examine temperatures <800 ºC where some inertial and fusion reactor systems may operate. The MITE-E was designed to accommodate these demands. Some of the major features of the MITE-E which improved the materials implantation studies from those in HOMER and HELIOS were 1) a collimated ion beam with a perpendicular incidence to the specimen surface instead of multi-angular ion bombardment, 2) ion beam currents which could be varied from tens of microamperes to several milliamperes, 3) ion beam energies which ranged from 20 – 130 keV, 4) precise measurement of the implanted current to the specimen from via a fiber optic link, and 5) an infrared heating laser able to anneal specimens prior to irradiation or provide additional heating during irradiation.

The design phase of the MITE-E began in the spring of 2008 and focused on conversion of the ion gun technology developed for the SIGFE [5] to materials implantation studies. Because the prototype ion gun facility used in the SIGFE had already been shown to generate a beam of ions capable of implanting materials, the primary challenge was incorporating the MITE-E's supporting infrastructure with the ion gun. The computer-aided design (CAD) modeling program SolidWorks® was employed to help meet these design criteria and finish construction of the device. A pictorial timeline showing the CAD design, infrastructure development, and operation of the MITE-E is shown in Figure 4-6.

May 2008 October 2009 January 2010

Figure 4-6: A pictorial timeline showing the design, construction, and operation of the MITE-E. In May of 2008 the primary design of the MITE-E was completed using the 3-D computer-aided design (CAD) software Solidworks®. In October 2009 the primary construction phase was completed and "first plasma" was introduced into the MITE-E in January 2010.

4.2.1. Modification of the ion gun for implantation experiments

The baseline design of the ion gun module for the SIGFE is shown below in Figure 4-7. The general assembly of the device consists of the primary mounting brackets and BN mounting rods, a filament plasma source, three lenses for electrostatic focusing and the cathode lens. The filament plasma source is housed in a stainless steel tube 5.1 cm in diameter which houses a 300 W light bulb filament and a Langmuir probe. Two BN feedthrus provide filament heating and bias. Nominal plasma densities were in the mid-10^8 cm^{-3}. Active water cooling was supplied to the plasma source through a 3.2 mm thick copper tube wrapped around the plasma tube and fed outside of the vacuum vessel. The plasma source is capped by the plasma aperture which is 1.3 cm in diameter. The first acceleration of the ions is accomplished with the extraction lens which has an aperture width of 1.8 mm and was nominally held at -6 kV for the implantation experiments reported in this thesis. After initial acceleration, the ion beam passed through the focusing lens (nominal voltages were -3.5 kV) and finally through a grounded deceleration lens which does the final shaping of the beam before it enters the cathode. The cathode lens provides the final acceleration of the ions to the energy at which they will impact the sample (-20 – 130 kV). The BN mounting rods and spacers help to prevent the lenses from contacting each other or becoming misaligned with the rest of the ion gun module.

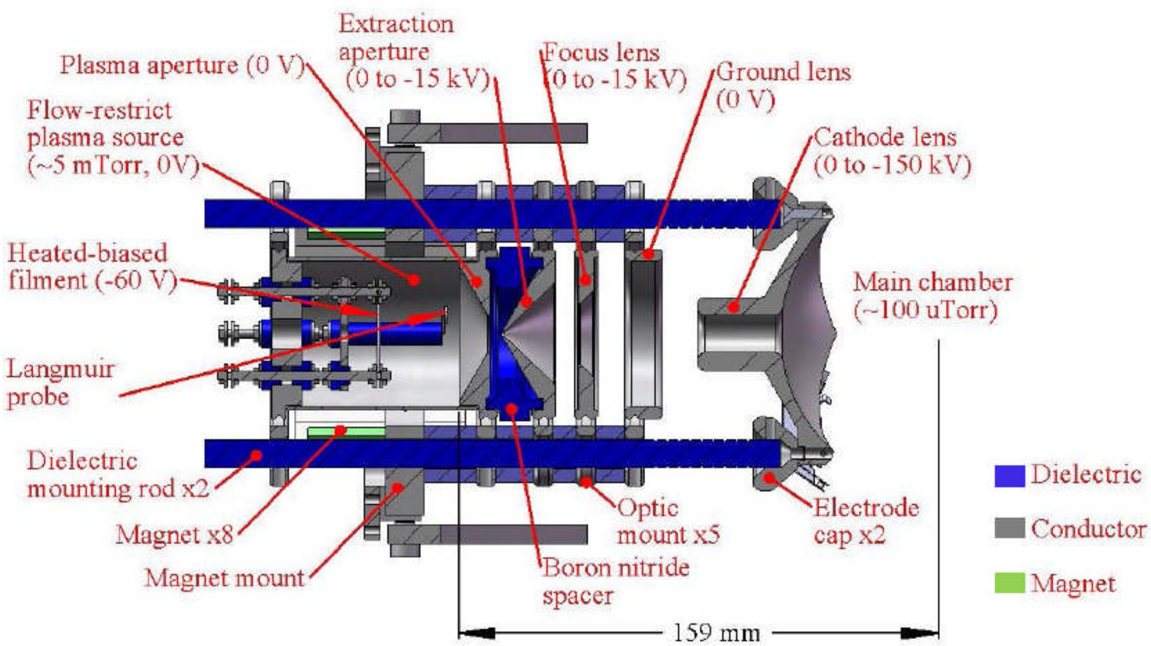

Figure 4-7: A cross section of the baseline ion gun module with major components highlighted. Standard operating pressures and voltages are listed where appropriate. Photograph courtesy of Brian Egle.

The primary difference between the ion gun modules used in the SIGFE and those used in the MITE-E is the cathode lens (Figure 4-8). The new cathode assembly developed for the MITE-E is called the irradiation stage and made up of five main components: 1) the steel cathode cap, 2) the cathode tube, 3) the molybdenum collimation aperture (diaphragm), 4) the sample exchange, and 5) the cathode stage or base plate. Each of these components was manufactured from 304 stainless steel, except for the diaphragm which is made of molybdenum. A CAD rendering of the irradiation stage is shown in Figure 4-9 alongside a picture of the ion gun module after installation in the MITE-E's vacuum vessel.

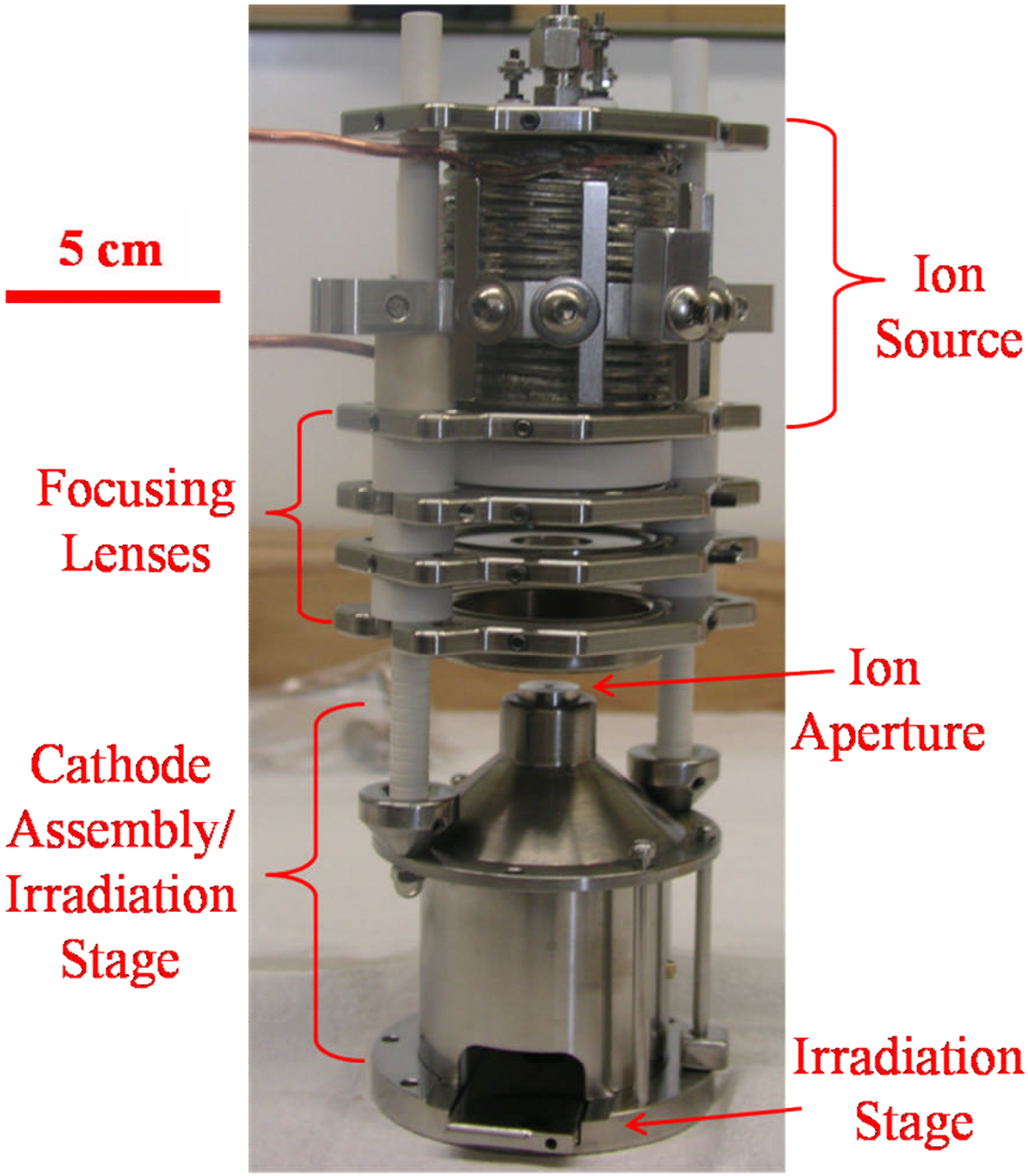

Figure 4-8: Photograph of the MITE-E's ion gun module with modified irradiation stage. A 5 cm scale bar is provided for reference.

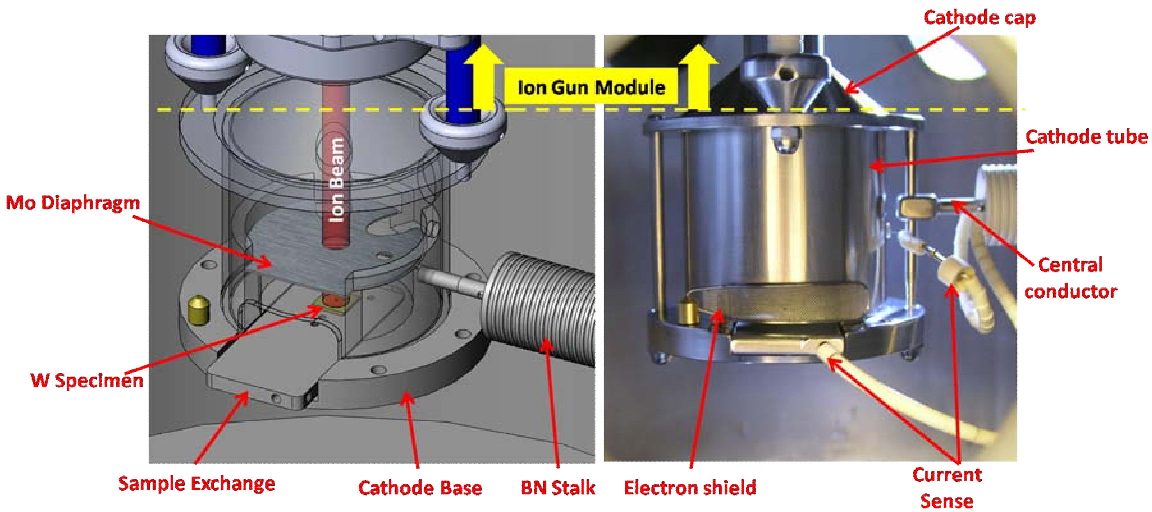

Figure 4-9: Computer-aided design (CAD) rendering of the irradiation stage in the design phase. The red transparent column represents the ion beam approximate size and shape as it enters the cathode assembly and bombards the W specimen (yellow square). For comparison, a picture of the actual irradiation stage is shown.

The components of the cathode assembly are described in the order by which the ion beam passes by them on its way to bombarding the W specimen. The first component is the cathode cap which has a diameter of 8.8 cm and an ion entrance aperture 1.3 cm in diameter. Besides the cathode cap flange which contains holes for the mounting bolts and the primary aperture the electrode is conical in shape. Below the cathode cap is the cathode tube which is 5.7 cm in length, 6.2 cm in diameter, and 1.9 mm thick. Another feature of the cathode tube is the two elliptical diagnostic holes which are 1.3 cm wide on the semi-major axis and spaced 60° apart. These holes provide a direct line of sight down the two CF window view ports on the backside of the MITE-E's vacuum vessel. The viewports are declined 45° from vertical direction of the ion beam, which allows for two additional in situ diagnostics of the specimen surface. A view down one of these view ports to the specimen surface is shown in Figure 4-10.

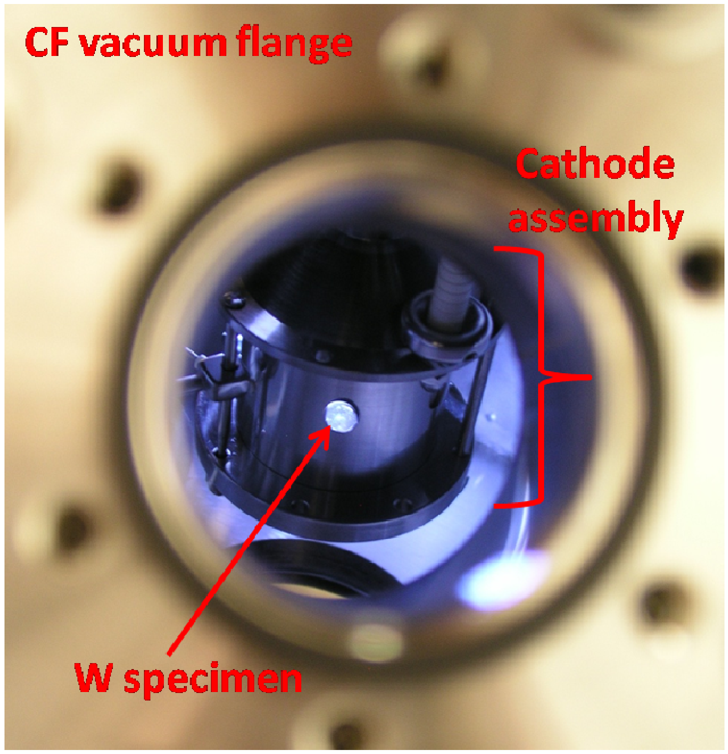

Figure 4-10: View down one of the 45° diagnostic ports of the MITE-E's vacuum vessel showing the line of sight through the cathode tube to the specimen surface.

After its initial entrance into the cathode, the ion beam sees the final 8 mm collimation aperture or "diaphragm." The diaphragm is 1 mm thick and made of pure molybdenum because of its superior sputtering properties over those of stainless steel. It also has two elliptical holes milled into it for the beam diagnostic ports. Additionally, the diaphragm has the ability to monitor any incident ion current from the incoming beam because it is electrically isolated from the rest of the cathode assembly until the current measurement is made in the high voltage feedthru (outside the vacuum vessel). The method for current measurement is deferred until later in this chapter. Two "C" shaped alumina rings suspend the diaphragm 2.5 cm above the specimen surface and keep it off the side of the cathode (Figure 4-11(c)). This current measurement capability serves as an ion beam diagnostic. During implantation experiments the ion gun's beam focusing parameters can be adjusted until the measured current on the diaphragm drops drastically. When this decrease in the diaphragm current occurs, the ion beam has been focused to a diameter smaller than the 8 mm collimation aperture of the diaphragm. This ensures that a lot of beam current is not being “wasted” in the final collimation.

Once the ion beam has undergone this final collimation it bombards the W specimen (or other examined material) that is mounted to the sample exchange (Figure 4-11(a)). The sample exchange was designed to function like a computer “thumb drive” that could be easily inserted and removed from the cathode assembly. The sample exchange dimensions are 3.1 cm wide by 6.4 cm long by 4.4 mm thick. Like the diaphragm, the sample exchange is electrically isolated from the cathode base and the rest of the cathode assembly (including the diaphragm) until the current is measured in the high voltage feedthru. Electrical isolation is accomplished by four insulating alumina “feet” which also keep the sample exchange from moving once it is placed on the cathode base (Figure 4-11(b)-(c)). The sample exchange also has a 10 mm through hole whose center is aligned with the center of the ion beam. During implantation, a W specimen is placed over this through hole with the polished side of the specimen facing upward (toward the incoming ion beam) (Figure 4-11(d)). This allows the ions to implant themselves on the polished side of the specimen, while the infrared laser simultaneously heats the specimen from the back. Further information on the laser heating system is given in the infrastructure section of this chapter.

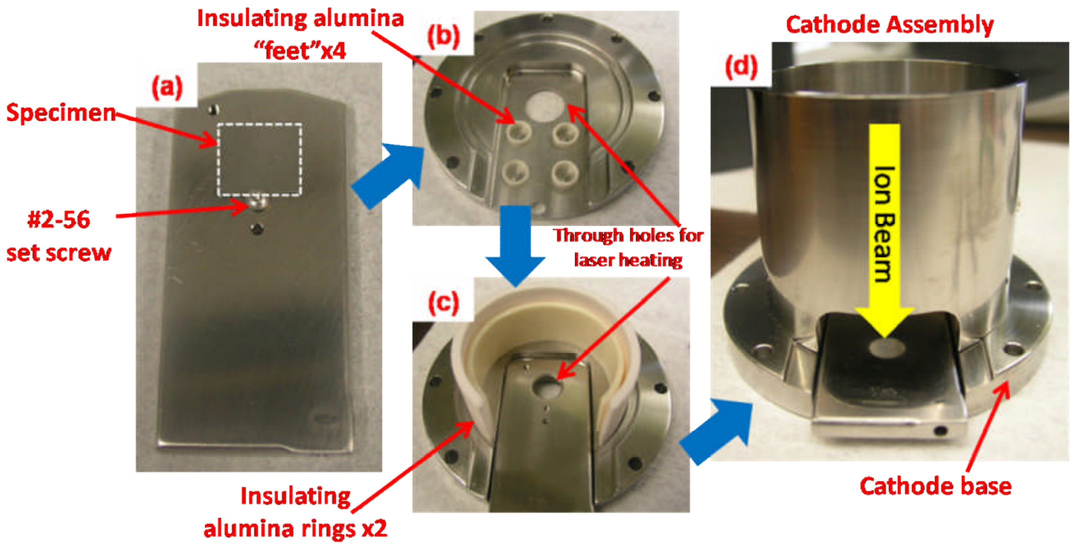

Figure 4-11 Diagram showing the process of assembly for the irradiation stage: (a) the sample exchange with a specimen bolted down, (b) the cathode base with insulating alumina feet in place, (c) the cathode base with the alumina feet, sample exchange, and insulating alumina tubes in place, and (d) the complete cathode assembly showing the direction of the incoming ion beam (electrostatic lenses and plasma source of the ion gun module are not shown).

4.2.2. MITE-E infrastructure

4.2.2.1. Vacuum and high voltage

The ion gun module and irradiation stage of the MITE-E are housed in a cylindrical stainless steel vacuum vessel which is approximately 36 cm in diameter and 53 cm tall. The majority of the flanges on the MITE-E's main vacuum vessel were custom machined and 45° diagnostic ports were added to the vacuum vessel during the construction phase. Base pressures in the mid 10^{-7} Torr range are achieved with a Varian® Macro Torr V250 turbomolecular pump which is exhausted by a Leybold® roughing pump. Using an MKS Mass-Flo® controller, nominal run pressures of 200 μTorr are achieved at a gas flow rates of 2.3 sccm (uncalibrated).

Voltages on the extraction and focus lenses are applied by two -10 kV power supplies that were custom modified at the UW IEC laboratory by Richard Bonomo and

Brian Egle. The focus lens supply is capable sinking up to 5 mA of positive current. Cathode voltages are attained from a first-of-a-kind custom built high voltage supply. This supply, built by Phoenix Nuclear Labs, is capable of supplying 200 mA at -300 kV. The main supply power is passed through a series of ballast resistors (~250 kΩ) immersed in a 50 gallon drum of silicon oil. From this barrel, power is transferred by a low gauge cable into a high voltage feed-through system. The custom high voltage feedthru is fabricated from a schedule 80 PCV tee and several custom PVC adapters. The feedthru is filled with silicon oil to suppress high voltage arcing and breakdown and the feedthru is sealed on either end by a threaded PVC end cap and an o-ring seal against one of the MITE-E's vacuum flanges. Pressure is applied to the o-ring by four threaded rods tightened down on an aluminum plate. This plate transfers the force from the threaded rods to four PVC dowels (Ø = 2.5 cm) cemented into the PVC tee (Figure 4-12). The entire PVC feedthru was coated with a conducting spray paint to prevent charge buildup during high voltage operation.

The internal components of the feedthru consisted of a hollow stainless steel rod surrounded by a boron-nitride insulator and a current sensing fiber optics assembly. Each of these components is immersed in the silicon oil which fills the feedthru. The central conductor accomplished a two-fold purpose: 1) it provided the negative cathode potential to the irradiation stage by direct physical contact and 2) transferred two Kapton® coated wires from the current sensing positions on the sample exchange and diaphragm (in the vacuum region, Figure 4-9) to the fiber optic assembly. These wires carry the current signals which are measured by the fiber optic link. Within the UW IEC laboratory, the hollow stainless steel central conductor and direct measurement of the cathode current is unique to the MITE-E. In fact, it is these capabilities – direct measurement (in real time) of the current to the implanted specimen and the decoupling of the sample temperature from ion current via an infrared heating laser – which make the MITE-E superior to HOMER and HELIOS as a materials implantation facility.

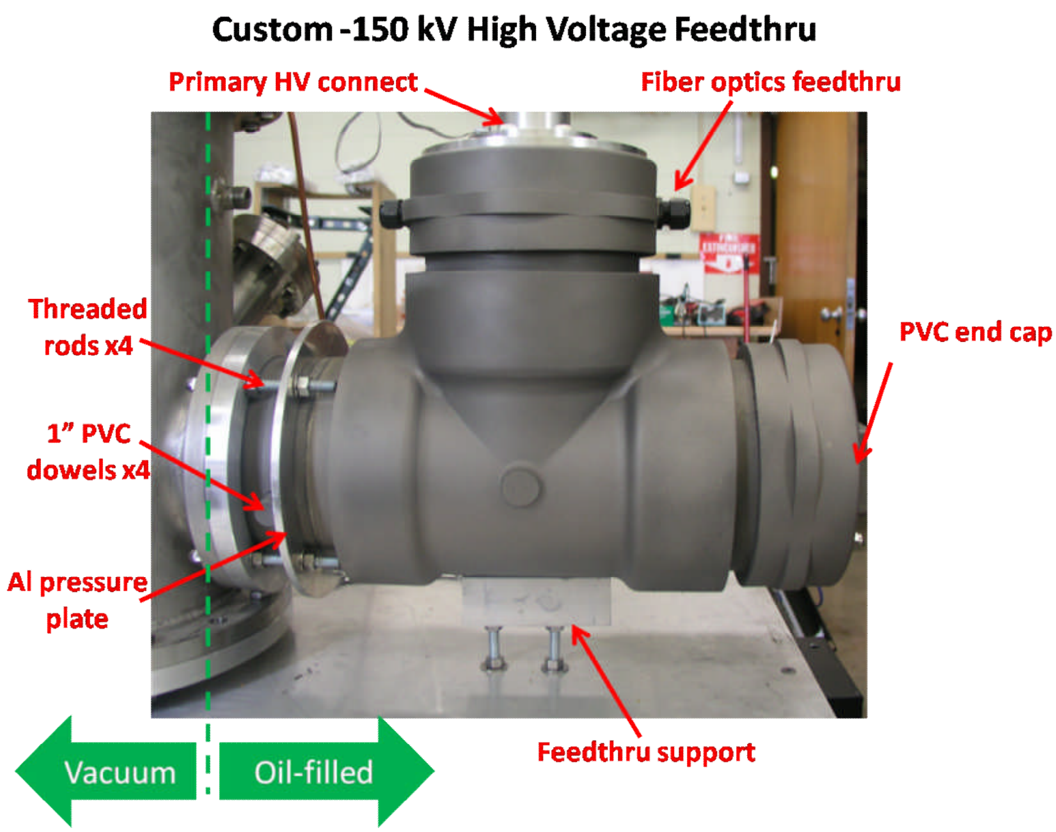

Figure 4-12: Custom PVC high voltage feedthru with important features called out.

4.2.2.2. Fiber optic link and feedthru assembly

The current sensing fiber optic assembly proved to be one of the most formidable challenges on the path to the MITE-E's success. A description of the key features and challenges is presented. Before the individual components and operation are discussed, a rough circuit schematic (Figure 4-13) and internal picture of the feedthru (Figure 4-14) are provided to illustrate the process by which the sample current is measured.

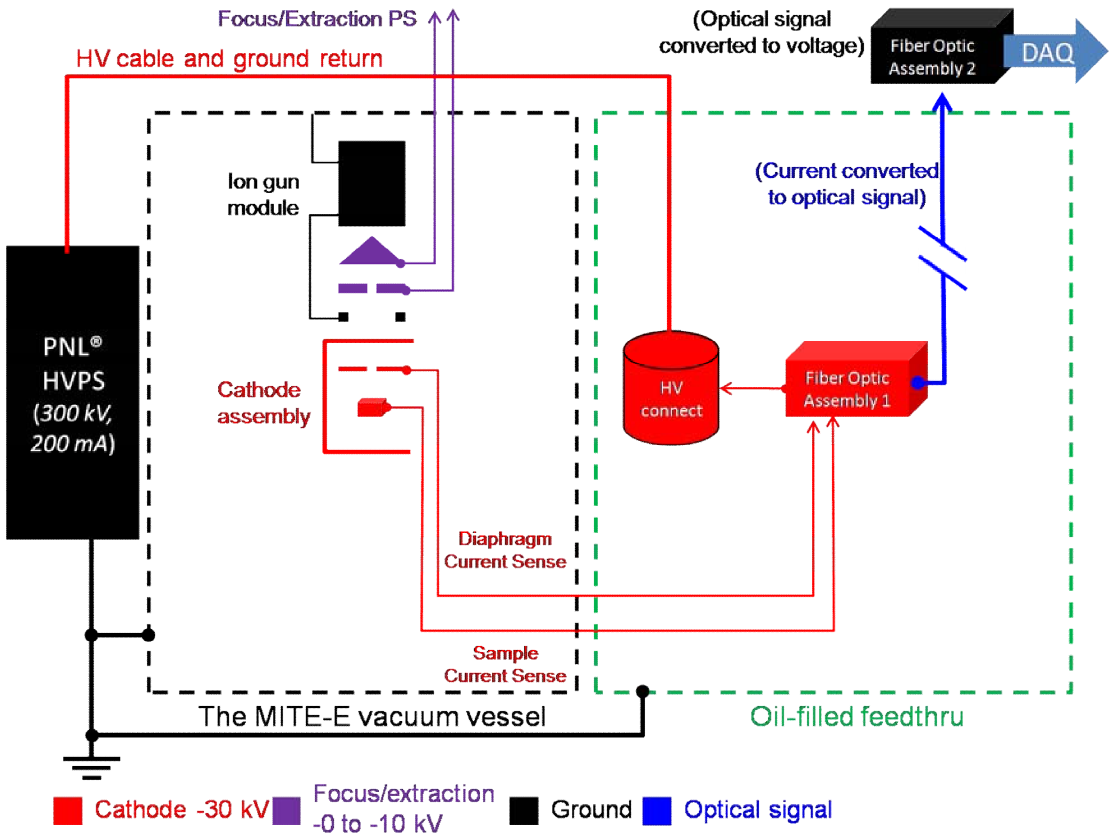

Figure 4-13: Schematic representation of the current measurement circuit.

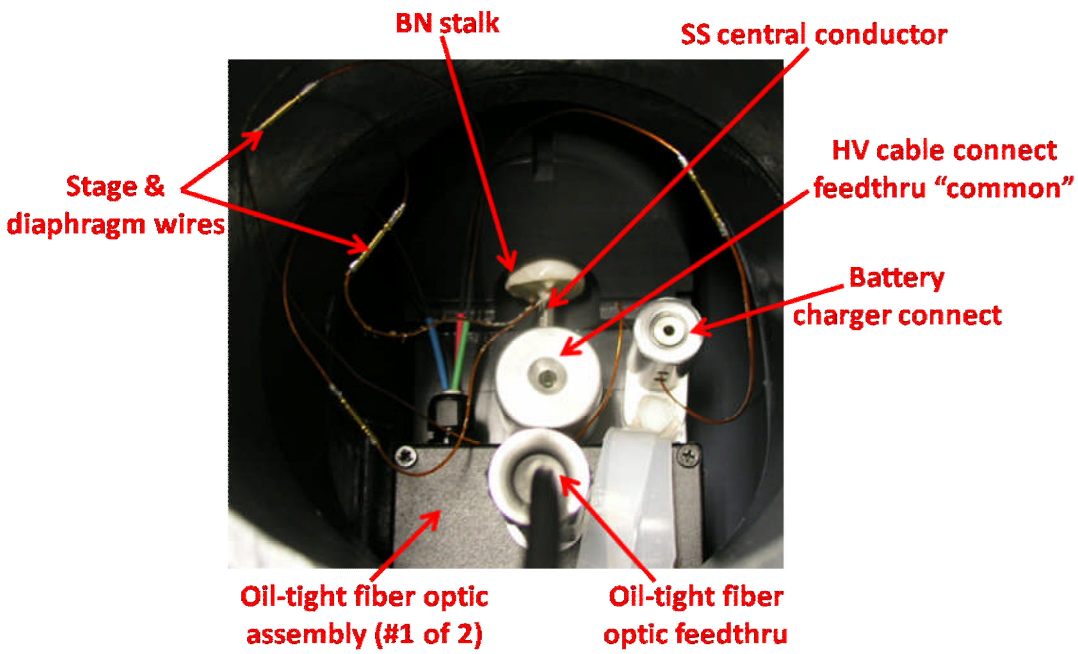

Figure 4-14: Internal view of the high voltage feedthru with the primary components called out.

As shown in Figure 4-9 the two current sensing wires for the sample exchange and diaphragm are fed down the center of the primary stainless steel conductor into the first oil-tight fiber optic assembly. The current signals from the sample exchange and the diaphragm are passed through a small sensing resistor and then are returned to the aluminum high voltage cable connector. This Al connecter serves as the electrical "common" of the feedthru assembly. The measured voltage drop across the sensing resistor is routed into an AFL-200 communications quality fiber optic link manufactured by A.A. Labsystems®. This fiber optic link converts the input voltage signal into a multi-mode optical signal and then transmits the signal out of the oil-tight enclosure through an oil-tight feedthru from Amphenol®. A 12 V lead-acid battery from Werker® powers the internals of the fiber optic assembly and is also placed in the feedthru. The optical signals are carried by a one meter long fiber optic cable to a second AFL-200 receiver unit which converts these signals into a ±10 VDC signal. Each of the components internal to the feedthru and illustrated in Figure 4-14 floats at the cathode potential. Because these voltage signals (at high voltage) cannot be safely transmitted into the control room and to a Labview® data acquisition program through a direct electrical connection, an electrically isolated fiber optic cable must be used to carry the voltage signal into the second fiber optic assembly described above. A small precision current source was used to calibrate the fiber optic receiver and give the correlation between the receiver's output voltage and the current collected by the sample exchange and diaphragm. After calibration, the fiber optic assembly successfully measured total sample currents between 20 and 500 μA with an error of ±10 μA at a total current of 200 μA. Because of the beam collimation system discussed earlier, it is assumed that all of the ions that make it through the diaphragm are incident on the W specimen, making the implanted sample and sample exchange currents equal. Nominal total implantation currents for irradiated W specimens were ~200 μA. For 30 keV He^+ the secondary emission coefficient of pure W (at a normal incidence to the sample surface) is 1.77 [9], which yielded an ion current of ~75 μA (Equation 4-2) and corresponding uncertainty of ±3 μA. This was a large improvement from the previous implantation devices HOMER and HELIOS.

4.2.2.3. Infrared laser heating system

The second major feature of the MITE-E which separates it from the previous UW IEC materials irradiation facilities was the decoupling of the implantation temperature from the input ion heating power. This was accomplished by implanting W specimens at low ion currents (relative to HOMER and HELIOS) and using an infrared laser to heat specimens to temperatures of ~1000°C. A custom Manlight® ML20-CW-R-OEM steady-state fiber laser was acquired from RPMC lasers® which had the capability to produce 20 W of laser light (for Nd:YAG lasers, λ = 1064 nm) in a collimated beam with a spot size of 2.2 mm. At 1064 nm and room temperature, tungsten reflects about 60% of the incident laser light. Furthermore, before impacting the W, laser light must pass through a 1.3 cm thick quartz vacuum glass and 3.2 mm thick quartz safety glass which will attenuate the laser light by ~8%. An illustration of the infrared laser heating system is shown in Figure 4-15.

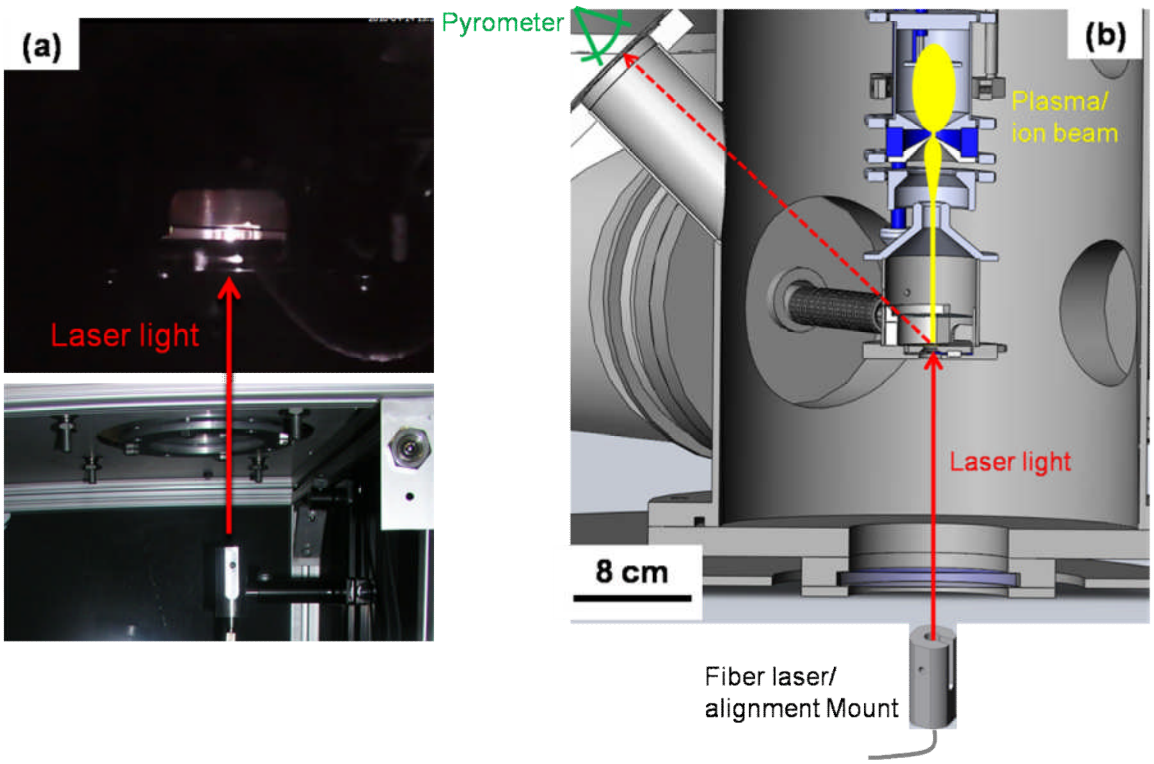

Figure 4-15: (a) Shows a W specimen annealing at 900 °C with a total output laser power of 16.8 W and the laser alignment mount underneath the MITE-E's vacuum vessel. The red arrow illustrates the path of the laser beam. (b) A CAD representation showing the path of the beam through the quartz vacuum glass and incident on the back of the implanted specimen. The plasma and ion beam are represented in yellow. The infrared signal read by the pyrometer (green view cone) is shown with a red dashed line.

Initially, it was observed that the maximum temperature that could be attained for the W specimens at the maximum laser output power (20 W) was approximately 600 °C (without the presence of ions). At low implantation currents, this did not allow the target implantation temperature of 900 °C to be met. To overcome this challenge two solutions were implemented: 1) the addition of a highly absorptive emissive coating (from ZYP Coatings®) on the backside of the W specimens helped couple the infrared laser light to the specimens and 2) the samples were thermally isolated from the stage by six alumina beads 2 mm in diameter. Figure 4-16 illustrates the implementation of both of these solutions. The complement of these two solutions allowed the target implantations to be achieved and successfully implant W specimens at temperatures between 500 and 900 °C.

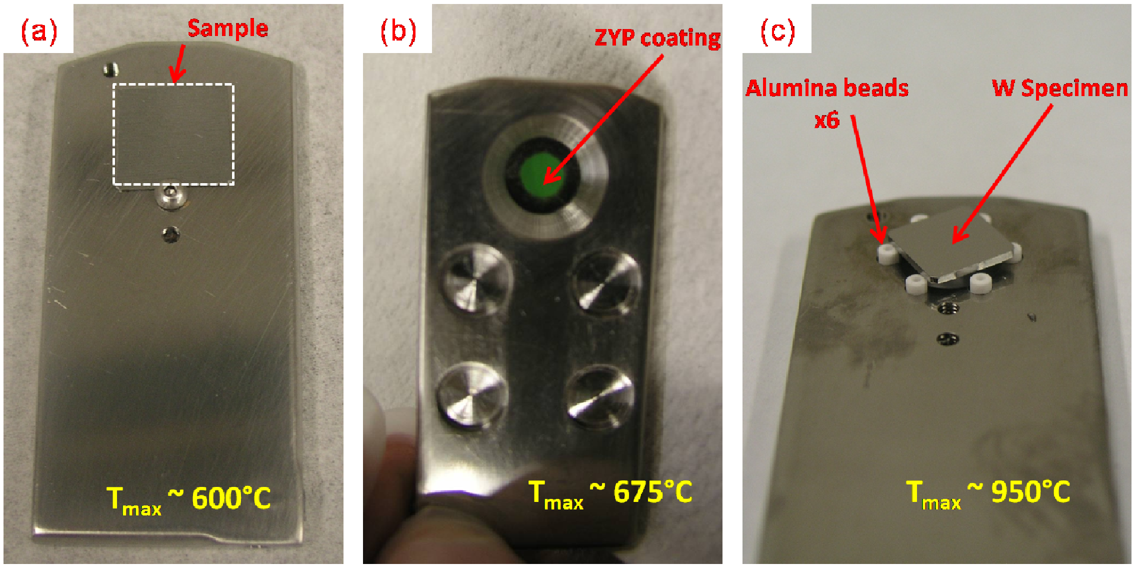

Figure 4-16: (a) Initial setup showing an implanted specimen held in position by a #2-56 set screw and without any ZYP coating on the backside. This configuration achieved a maximum temperature of ~600 °C. (b) A W specimen with the addition of the ZYP coating and mounted using a set screw with a maximum achieved temperature of ~675 °C (backside of sample exchange shown). (c) W specimen coated with ZYP paint and thermally isolated from the sample exchange by six alumina beads. The maximum achieved temperature was ~950 °C. None of the maximum temperatures listed included contributions from ion heating.

4.3. Sample preparation

Prior to implantation in the MITE-E, W specimens were electropolished to remove the damage layer which results from mechanical polishing. The W specimens acquired from Oak Ridge National Laboratory (ORNL) were mechanically polished to a mirror finish and surface roughness of ~3 μm [11]. As Figure 4-17(a) shows this polishing procedure resulted in a damage layer on the surface of the W which eliminates the ability to observe individual grains using a scanning electron microscope. For helium implantation experiments it is desirous to see the grains and grain boundaries of the investigated material, to determine how individual grains, or grain boundaries, respond to the implanted helium ions. To perform the electropolishing procedure, an aqueous solution of 2 wt% KOH in 1800 mL of distilled water was used. A magnetic stir plate and magnetic stir stick were used to flow the solution over the W specimen to ensure pitting of the surface did not occur. A graphite rod acted as the cathode and pair of metallic tweezers was used for the cathode. Samples were electropolished for three 20 second intervals. The power supply voltage was fixed at 20 VDC and resulted in current densities of ~1 A/cm^2. The electropolishing setup and results are given below in Figure 4-17.

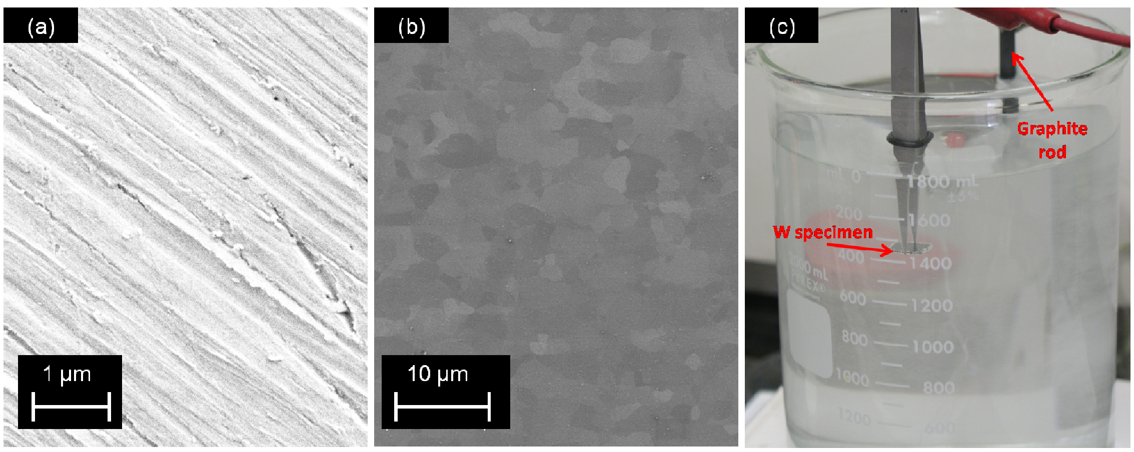

Figure 4-17: (a) W specimen after mechanical polishing and with damage layer present on the surface, (b) electropolished W specimen revealing a flat, smooth surface and an average grain size of ~5 μm, and (c) the electropolishing setup showing the KOH aqueous solution, liquid vortex from the magnetic stir stick and the graphite rod (cathode).

4.4. Temperature measurement and data acquisition

Apart from ion flux, the most important measurement is temperature. Temperature measurements are made using a two color infrared pyrometer model Chino® IRCAQ 2CS. The pyrometer uses three solid state detectors which measure infrared signals at wavelengths of 0.9, 1.35, and 1.55 microns. The term “color” refers the wavelength of the measured light. The dynamic range of this instrument is between

400 and 3100 °C. Each detector is capable of measuring temperature independently by a single color technique, or by a two color "slope" technique. The two color technique (used in these studies) measures temperature by using the slope (ratio) of a sample's emittance at two of the wavelengths measured by the pyrometer. In this case, emittance refers to the total normal spectral emissivity (emittance at single wavelength band) of a specimen. It is important to note that this factor is different from the total normal emissivity (emittance over all wavelengths), which is expressed as ε in Equation 4-1 Ideally, at a set temperature, the slope is constant and fluctuations in the sample's emittance do not affect temperature measurement. This eliminates the need to track signal attenuation from transmission through windows or coatings. Emittance can have a significant effect on the temperature measured by the infrared pyrometer; therefore, it is important to choose values which most closely represent experimental conditions. Unfortunately, there does not appear to be a wealth of emissivity data on W below 1000 °C; therefore, the slope of the pyrometer was set at 1.00 to be consistent for different W specimens implanted over the examined temperature range (500 – 900 ºC). It is shown in [12] that below ~800°C the spectral emittance curve is relatively flat, which would make the slope constant at 1.00, confirming that this is a good estimated value of the slope.

The location of the pyrometer is shown schematically in Figure 4-15(b). Because the infrared laser emits a very strong light signal at 1064 nm, the scattered laser light can interfere with the pyrometer which measures the temperature at wavelengths of 900, 1350, and 1550 nm. In order to eliminate this interference, the pyrometer was placed in one of the 45º off-axis viewports. To confirm this, W specimens were heated to high temperatures (~900 ºC) using the laser and then the laser was abruptly turned off while the pyrometer was recording the temperature. Instantaneous temperatures after shutdown of the laser did not show any change in the specimen temperature (larger than would be expected from exponential temperature decay of a radiatively cooled object).Visual data was gathered using two Ethernet based cameras – an Axis communications model 207 and a D-Link® DCS910 camera.

Figure 4-18 illustrates a typical implantation experiment as recorded by the real time data acquisition software Labview®. A tungsten specimen was implanted to 3×10^{18} He^{+}/cm^{2} at 900 ºC. For the duration of the run time (~65 minutes) the temperature was held very steady at the target temperature. As shown below, the transition from the 15 minute laser anneal to the combination of laser heating and ion heating from the He beam was able to be done smoothly and with little variation in specimen temperature.

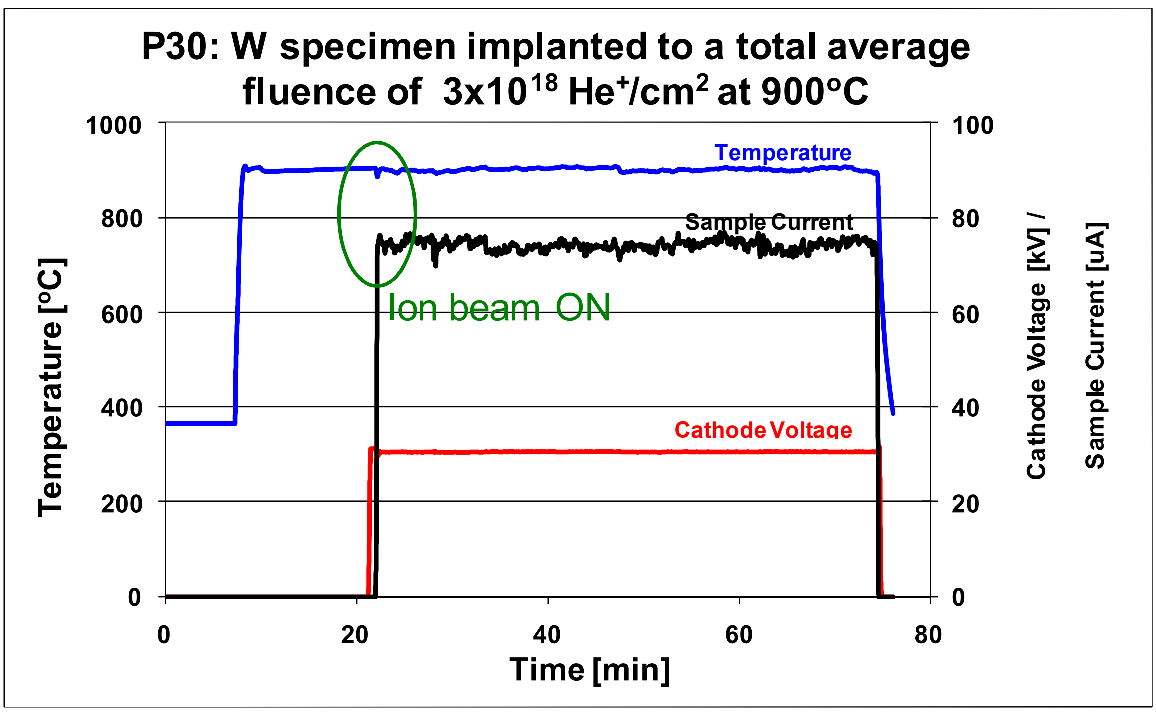

Figure 4-18: Graphical representation of real time data acquired by Labview® software. The red line traces the cathode voltage, the black line the ion current to the W specimen, and the blue line the sample temperature. The green oval points out the transition between the 15 minute specimen laser annealing period and the initiation of the ion beam (combines laser and ion heating). The minimum of the blue line is the default minimum temperature of the pyrometer (370ºC).

For the W specimens implanted in the MITE-E, Table 4-1 gives the nominal values for the primary experimental parameters which are monitored and collected by the Labview® data acquisition program.

Cathode voltage [kV] / ion energy [keV]	Ion current [μA]	Pressure [μTorr]	Extraction lens voltage [kV]	Focus lens voltage [kV]	Implantation temperature [°C]
30	75±3	200	6	3.5	500 - 900

Table 4-1: Table of nominal experimental for primary run parameters. Specimens were W and implanted with $^4He^+$.

4.5. Materials Analysis Techniques

4.5.1. Morphological and chemical analyses

Two apparatus were used to perform pre- and post irradiation analysis on the samples, both of which are in operation at the University of Wisconsin-Madison Materials Science Center. The first of which is the LEO 1530 SEM, which employs a Schottky-type field emission electron source. Tungsten specimens were examined before and after implantation in this device. Using the same SEM LEO 1530 apparatus in a different mode of operation, energy dispersive spectroscopy (EDS) was performed on the W specimens to confirm the absence of large concentrations of impurities.

The second microscopy instrument used was the Zeiss CrossBeam. Though this apparatus is capable of capturing basic SEM micrographs, it was used to mill the surfaces of the irradiated samples. This task is accomplished by using a focused ion beam (FIB) of 30 keV gallium ions. Nominal millings for these investigations consisted of 7 μm x 7 μm mill areas and mill depths of 3 μm. Figure 4-19 shows a micrograph of He^+ implanted W after the FIB device has been used to mill the surface.

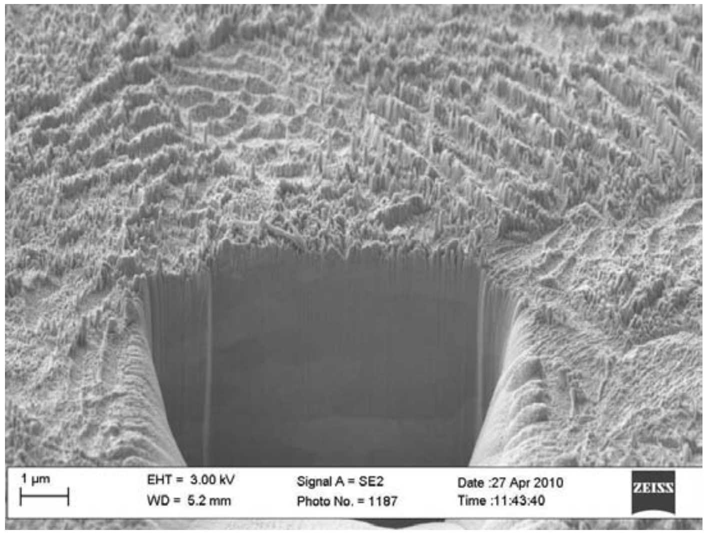

Figure 4-19: FIB micrograph of a W specimen after implantation of 30 keV He^+ to a fluence of $5x10^{18}$ He^+/cm^2 at 700ºC in MITE-E.

X-ray diffraction (XRD) was used in implantation experiments on single crystalline tungsten to determine the crystal orientation and the crystal lattices' offset from the optical normal (polished surface). For these experiments, the PANalytical X'Pert PRO® x-ray diffractometer was used. It is capable of an absolute angular resolution of 0.0001 degrees and samples are mounted on a six-axis high resolution goniometer. This apparatus is located at UW-Madison and is also part of the Materials Science Center. The surface profile of the implanted W specimens was mapped out using data from the ZYGO NewView white light interferometer. This device is capable of measuring surface roughness with a vertical (height) resolution <5 nm and a lateral resolution of ~2 µm. A sample of the data is illustrated in Figure 4-20.

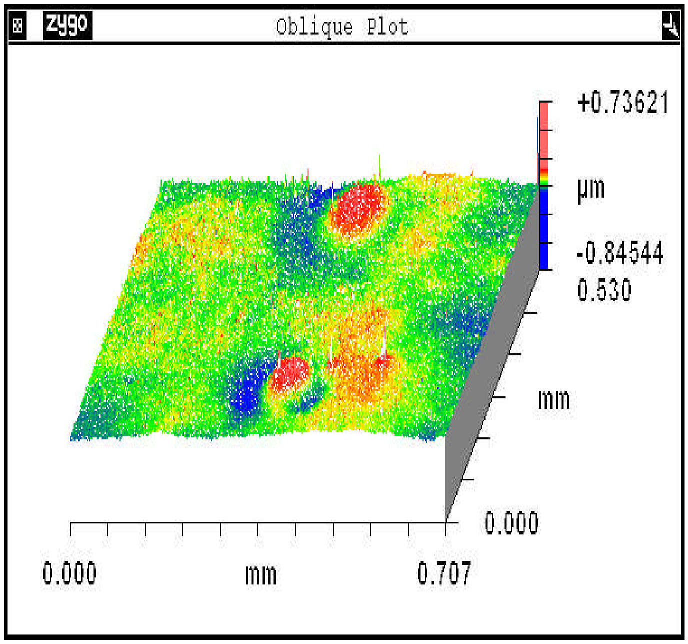

Figure 4-20: Measurement of W surface profile after implantation to 10^{17} He^{+}/cm^{2} at 900°C using a white light optical profilometer.

4.5.2. Retention and depth profiling analysis

The work reported in this thesis two different methods and apparatus to determine the amount of retained helium fluence in W specimens after implantation experiments. These are nuclear reaction analysis (NRA) and neutron depth profiling (NDP). The NRA is performed on-site at UW-Madison using the 1.7 MV Pelletron tandem ion accelerator. [13] The second technique is performed at the National Institute of Standards and Technology (NIST) at the Center for Neutron Research. [14] Using a third retention analysis technique called elastic recoil detection (ERD), Radel [15] reported both helium retention and helium concentration as a function of implantation depth in polycrystalline tungsten. One disadvantage to the ERD techniques is that the beam can only penetrate ~130 nm into the sample surface. FIB analysis (Figure 4-19) has shown the depth of surface damage exceeds this number, and it is assumed that helium atoms implanted in the specimen diffuse even further. In order to ensure accurate values of helium retention, the entire implanted region must be included. For this reason, ERD was not used by this author to measure helium retention in W. Instead, helium retention values employed the NRA and NDP techniques. To use the NRA and NDP methods, implanted ions must be able to undergo a nuclear reaction with an incident ion beam (NRA) or with an incident beam of cold neutrons (NDP).

In order to use NRA the ^{3}He isotope was used to specimens and the ^{3}He(D,p)^{4}He nuclear reaction was utilized. A 2 MeV D^{+} ion beam is incident normal to the sample surface and then reacts with a ^{3}He nucleus to produce a 14.7 MeV proton and a 3.7 MeV alpha particle. The protons are first attenuated through ~500 μm of Al foil, which decreases their energy before they are counted using a solid state detector. While NRA is ideal for determining the magnitude of the retained fluence, it is not optimal for determining the concentrations of helium as a function of implant depth (depth profile). A complex deconvolution is required to account for the energy lost by the ion beam impinging on the sample and the energy lost by charged particles escaping from the specimen. On the other hand, NDP analysis avoids this problem by using an incident beam of cold neutrons which lose negligible amounts of energy as they penetrate into the sample bulk and possibly react with a helium atom through the the ^{3}He(n,p)T nuclear reaction. Using known stopping powers and energy loss, the depth of the reaction can be determined. The resultant proton is counted by a solid state detector at some fraction of the initial energy (572 keV) depending on the depth at which the reaction occurred. Depth profiles are then compiled from the data. A general schematic for operation and the NDP chamber at NIST are shown in Figure 3.11.

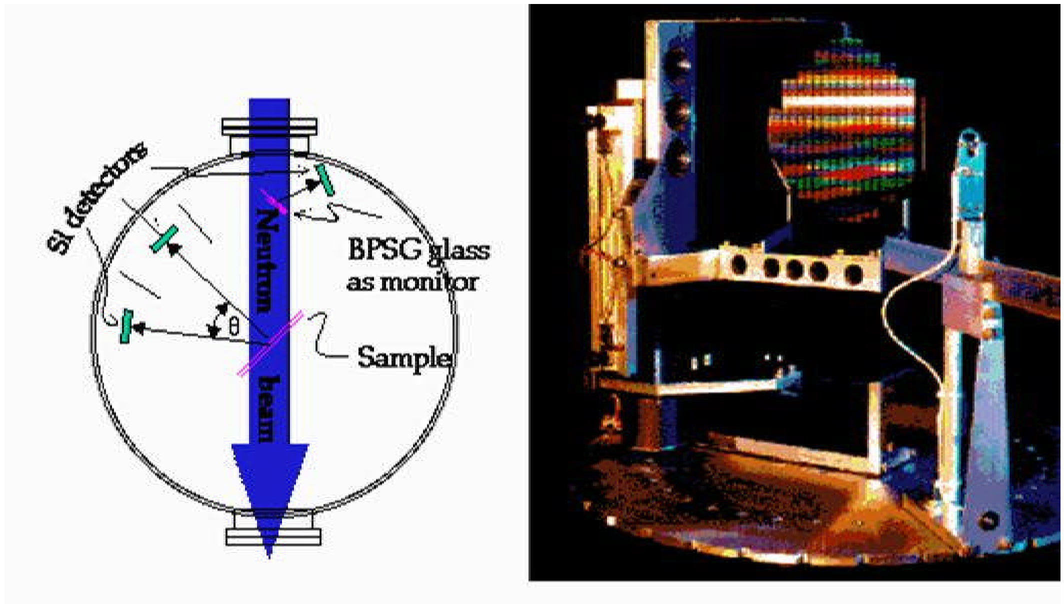

Figure 4-21: Neutron depth profiling (NDP) schematic and test chamber located at the NIST Center for Neutron Research. [14]

4.6. References for Chapter 4

1. Cipiti, B.B. (2004). The fusion of advanced fuels to produce medical isotopes using inertial electrostatic confinement. (Doctoral dissertation, University of Wisconsin - Madison).

2. Radel, R. F. (2007). Detection of highly enriched uranium and tungsten surface damage studies using a pulsed inertial electrostatic confinement fusion device (Doctoral dissertation, University of Wisconsin – Madison).

3. Santarius, J. F. et al., (2005) Overview of university of wisconsin inertial-electrostatic confinement fusion research. *Fusion Science and Technology*, 47 (4), 1238-1244.

4. Ashley, R.P. et al., (2003) Recent Progress in Steady State Fusion Using D-3He. *Fusion Science and Technology*, 44, 564.

5. Egle, B. J. (2010). Nuclear fusion of advanced fuels using converging focused ion beams (Doctoral dissertation, University of Wisconsin – Madison)

6. Peifer, G.R., et al. (2005) Design of an Ion Source for ^{3}He Fusion in a Low Pressure IEC Device. *Fusion Science and Technology*, **47**, 1255-1259.

7. Kaminsky, M., (1965) *Atomic and Ionic Impact Phenomena on Metal Surfaces*. Springer Verlag: Berlin, Germany.

8. Baroody, E. M., (1950) A theory of secondary electron emission from metals. *Physical Review*, 78 (6).

9. Large, L.N. (1963) Secondary electron emission from a clean tungsten surface bombarded by various positive ions. *Proc. Phys. Soc.*, **81**, 1101-1103.

10. University of Wisconsin – Experimental IEC Logbook (HELIOS, Run 327).

11. Private e-mail communication (2010) Marie Williams.

12 Touloukian, Y.S., (1970) *Thermo-physical Properties of Matter, Vol. 7: Thermal Radiative Properties*. IFI/Plenum, New York.

13. Wright, G.M. et al, (2005) An experiment in the dynamics of plasma surface interactions. Presented in Boston, MA at the US-Japan Workshop on Plasma Surface Interactions.

14. Downing, R.G. et al. (1993) Neutron depth profiling: overview and description of NIST facilities, *NIST Journal of Research*, 98, 109.

15. Radel, R.F. and Kulcinski, G.L., (2006) Effects of high temperature pulsed helium implantation on tungsten surface morphology. *Fusion Science and Technology*, 52 (3), p. 544-548.

CHAPTER 5. EXPERIMENTAL RESULTS

5.1. Experimental Results from the IEC devices HOMER and HELIOS

5.1.1. Introduction

The effects of helium implantation were examined for a wide range of materials. These materials include: silicon carbide (SiC), carbon-velvet (CCV), W-coated CCV, single-crystalline W (SCW), polycrystalline W (PCW), fine-grain W (FGW), nano-grain W (NGW), and W needles. Three different implantation facilities were used to perform these experiments, in chronological order of use: HOMER, HELIOS, and the MITE-E. For experimental results acquired from the HOMER and HELIOS devices, a discussion of the results will be given in this chapter. A summary of observations on materials implanted using the HOMER and HELIOS apparatus are given in Chapter 6 of this thesis. However, only the results acquired using the MITE-E will be presented in this chapter, while the discussion of these results will be deferred to Chapter 6 of this dissertation. Table 5-1 below shows the different materials that were implanted in each of the devices. Chapter 4 discusses the progression from one device to the next and the reasons that the various transitions were made. Construction and operation of these three devices are also presented in the preceding chapters of this thesis.

HOMER	HELIOS	MITE-E
SiC	CCV	W needles *(prototype ion gun facility)*
CCV	W-coated CCV	PCW
W-coated CCV	SCW	
	PCW	
	FGW	
	NGW	

Table 5-1 : Summary of each of the materials which were implanted with 30 keV He^+ by the author for this thesis. Materials are listed under the device in which they were implanted. W-coated CCV and PCW were studied in two different devices and are listed doubly.

Unless otherwise specified, all the examined materials were implanted with helium ions at an energy of 30 keV, with the exception of W needles which were implanted with 100 keV He^+ in the MITE-E's prototype ion gun. Fluences are presented in units of helium ions per centimeter squared (He^+/cm^2) and temperatures are listed in degrees Celsius (°C). This report is mainly concerned with the large scale surface morphology changes occurring on the implanted specimens. Because of this, the primary pre-irradiation analysis of these materials was conducted with a scanning electron microscope (SEM). Except for CCW and W-coated CCV, all specimens were analyzed after implantation using SEM and focused ion beam (FIB) analysis. Although additional post-implantation analysis techniques were used (the employed techniques varied with the investigated material) these analyses are introduced and discussed as needed on a material-by-material basis.

In order to provide a clear comparison between experiments performed within the UW IEC laboratory and the conditions of a large-scale fusion reactor, the implant fluences are cast in terms of equivalent IFE and MFE reactor operation times. The fluences implanted using the UW IEC apparatus are given in the left-hand column of Table 5-2. The central column of Table 5-2 scales the implanted fluence in the UW IEC laboratory to full power days (FPD) of operation for a standard, dry wall, direct-drive laser IFE system. For the ITER divertor system, implanted helium fluences are stated in units of seconds of full power operation time (right-hand column of Table 5-2). It is important to note that these are estimates for the reader's reference and that these extrapolated operation times fall drastically, short of the times needed to make fusion energy commercially viable. All of the calculations presented in Table 5-2 assume that the total helium flux to the first wall armor and divertor plates of these systems is at 30 keV.

Implanted fluence, He^+/cm^2	**HAPL** *Total He^+ spectrum*	**ITER** *Total He ash flux*
10^{17}	0.02 FPD	0.04 FPD
10^{18}	0.2 FPD	0.4 FPD
10^{19}	2.0 FPD	4.3 FPD

Table 5-2: In the left-hand column the implanted fluences on PCW in the UW IEC apparatus are given. The central column gives a correlation between UW IEC implant fluences and full power days (FPD) of operation in reference HAPL chamber (chamber radius = 10.5 m, duty cycle 5 Hz). [1,2] The right-hand column gives a correlation between the implanted fluence in the UW IEC laboratory and the alpha flux to the ITER divertor plate for all incident ash particles for P_α – 240 MW, A_{div} – 400 m^2, and t_{pulse} - 400 s.

5.1.2. Helium implantation results from the UW IEC device HOMER

5.1.2.1. Silicon Carbide – HOMER

Despite their brittleness and large scale fabrication difficulties, SiC and graphite are desirable materials for high temperature nuclear reactors. This is due to their low induced radioactivity, low cost, availability, and high temperature strength. [3]

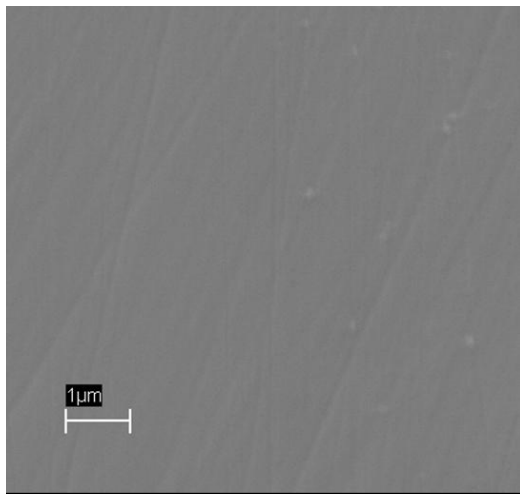

Figure 5-1 Micrograph of unirradiated CVD SiC

Six SiC samples acquired form Dr. Lance Snead at Oak Ridge National Laboratory (ORNL) were irradiated in the UW IEC device HOMER to fluences of 10^{18} and 10^{19} He^+/cm^2 at three different temperatures (750, 850, and 950 ºC) to determine He^+ implantation effects as a function of fluence and temperature. For comparison, a pristine SiC sample is shown in Figure 5-1 prior to irradiation with helium ions. The ion implantation energy ranged from 20 – 50 keV and the background neutral pressure was held constant at ~500 µTorr. The average implantation currents ranged from 2 – 8 mA depending on the chosen implantation temperature. Samples irradiated at 750 °C exhibited substantial surface erosion and morphology changes. The sample irradiated to 10^{18} He^+/cm^2 at 750 °C (Figure 5-2(a)) sustained substantial flaking but no noticeable pores, while the sample implanted to 10^{19} He^+/cm^2 at 750 °C (Figure 5-3(a)) exhibited larger "craters." These craters were presumably caused by flaking even though no flakes were observed during post-irradiation analysis on the higher fluence sample. An increased cratering and flaking effect was observed, as well as pore formation, at both implantation fluences at 850 °C. This extensive flaking can be observed at 10^{18} He^+/cm^2 (Figure 5-2(b)) and 10^{19} He^+/cm^2 (Figure 5-3(b)). A summary of the irradiation experiments on SiC is shown below in Table 5-3.

Sample	**Fluence, He^+/cm^2**	**Temperature, °C**
S2	10^{19}	~950
S3a	10^{18}	~950
S3b	10^{19}	~950
S4a	$1.1x10^{18}$	~750
S4b	10^{18}	~850
S5mask	$1.6x10^{19}$	~950
S6a	10^{19}	~750
S6b	10^{19}	~850

Table 5-3: Summary of steady state helium implantation experiments on SiC carried out in the HOMER device.

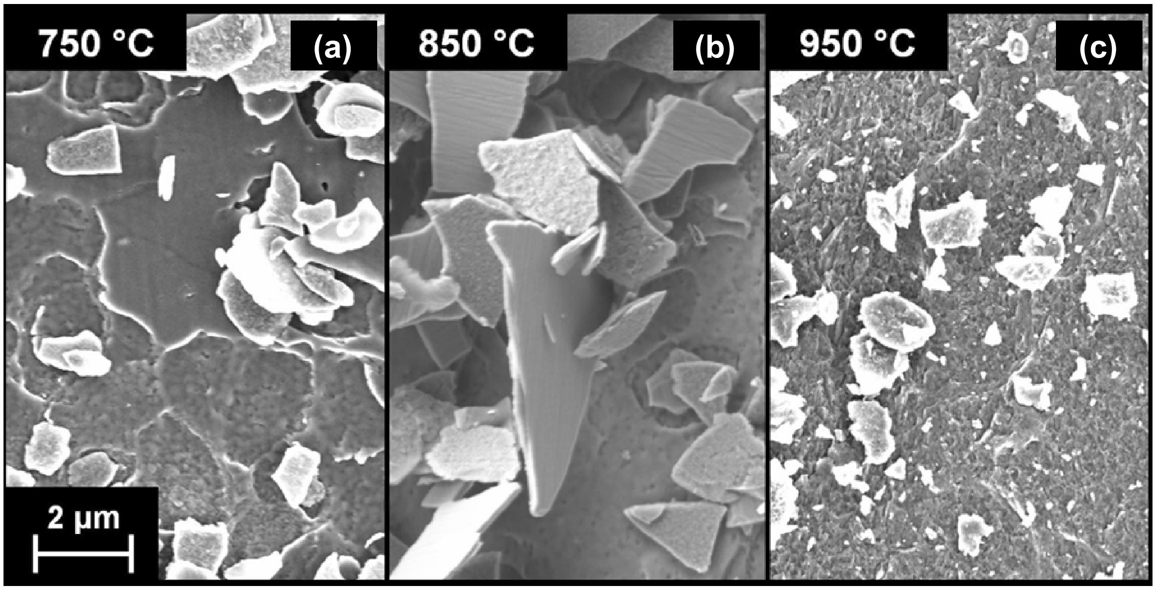

Figure 5-2: CVD SiC irradiated to 10^{18} He^{+}/cm^{2} at (a) 750, (b) 850, and (c) 950 °C in HOMER.

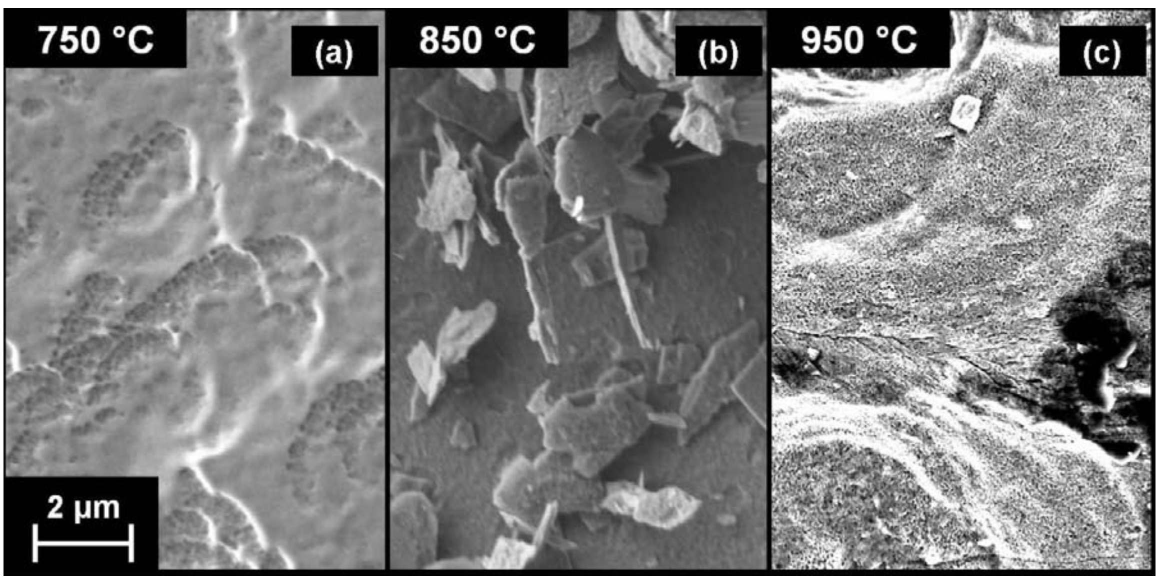

Figure 5-3: CVD SiC irradiated to 10^{19} He^{+}/cm^{2} at (a) 750, (b) 850, and (c) 950 °C in HOMER.

Another important observation is the thickness of the flakes on the samples irradiated at 850 °C. Their average thickness is several tenths of a micron, very close to the range of helium in SiC as calculated by SRIM (Figure 5-4). It is also clear from Figure 5-2(b) that individual flakes have a smooth side (originally polished surface) and a roughened or porous side (presumably caused by helium bubbles and erosion). One explanation for this repeated flaking may be the formation of a helium bubbles below the surface of the SiC at the depth which the helium is implanted. At some point, the built up helium gas pressure is great enough to cause flaking of the SiC. Flaking of SiC blisters and their redeposition from He^+ bombardment has also been observed by Yamauchi et al. [4]

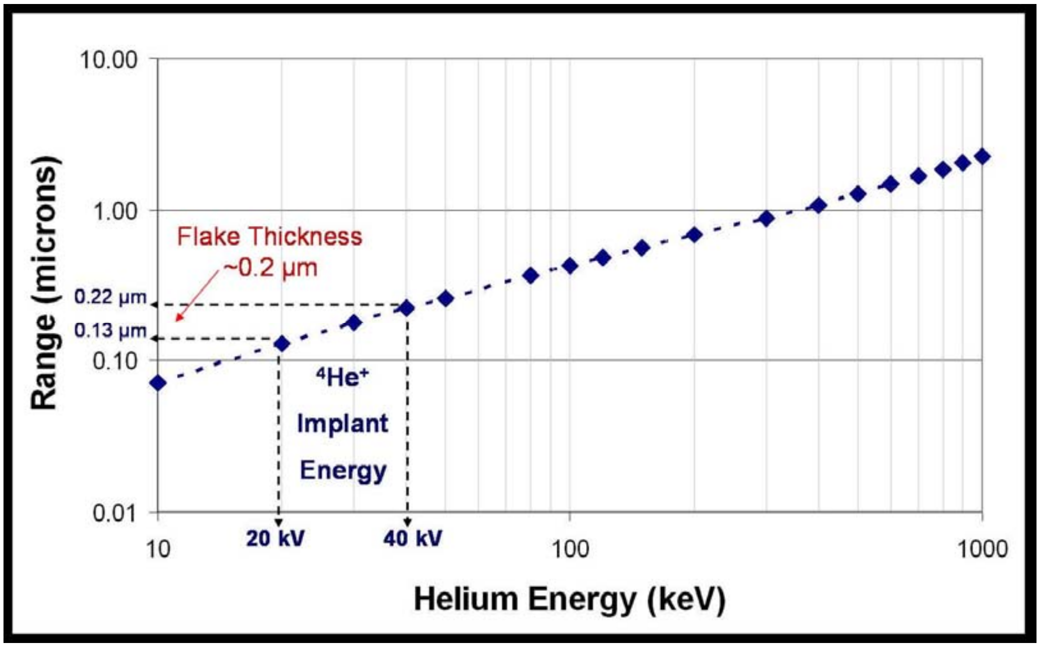

Figure 5-4: Predicted range of He^+ in amorphous SiC presented as a function of energy using the TRIM program. The ranges corresponding to the various IEC implantation energies are called out along with the approximate flake thicknesses.

Increasing the irradiation temperature to 950 ºC resulted in pore formation as well as flaking. In fact, at 10^{19} He^+/cm^2 pore formation seems to dominate the damage, and the surface exhibits a "pumice-like" appearance. The large, layered depressions are regions that have undergone repeated flaking during implantation. SEM observation showed that crater size and depth increases with temperature. At 950 °C, the craters then became large depressions in the surface ~10 µm. SiC samples also exhibited inhomogeneous surface damage. Large flake redeposition regions dubbed "lakes" were observed near the center of one SiC specimen irradiated to 10^{18} He^+/cm^2 at 850 °C (Figure 5-5).

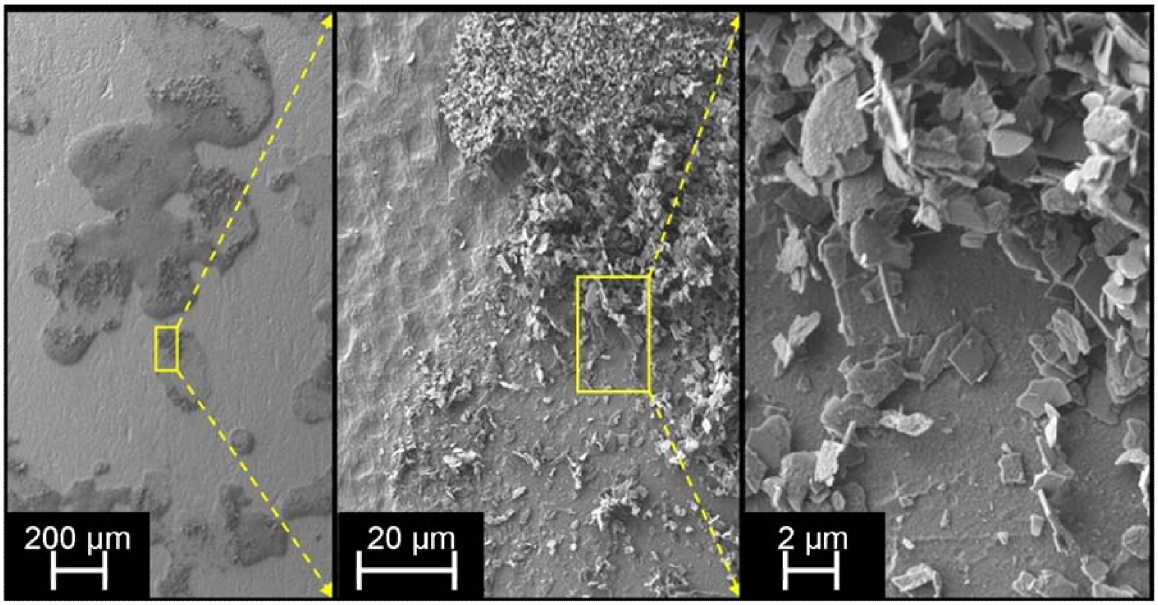

Figure 5-5: SiC specimen implanted to 10^{18} He^{+}/cm^{2} at 850 °C with 30 keV helium ions in HOMER. The series of pictures shows the surface morphology change at progressively higher magnifications at the same geographic point on the specimen, which reveals the darkened regions on the surface to be areas of redeposited SiC flakes.

The nature of the surface morphology changes incurred during initial SiC irradiation experiments required the verification that ion fluence, not high temperature, was causing the effects. An experiment was devised which involved masking half of a SiC sample with a tantalum foil. The sample was irradiated to a fluence of ~1.6×10^{19} He^{+}/cm^{2} at 950 ºC. The results of the experiment are presented in Figure 5-6. After comparing the portions of the sample which are shielded and unshielded, it is clear that the ion fluence is the source of the damage seen on the surface of the SiC samples, not the temperature. Because the tantalum mask was not completely flush against the SiC, the contaminants seen in the unirradiated zone are most likely a result of SiC flakes falling between the tantalum mask and the sample surface. An approximate depth of the surface craters induced by the He^{+} was obtained by tilting the masked sample in the SEM stage at 35° and performing SEM analysis. Results show one of the depressed regions exceeded several microns (~3 µm), where it is assumed that repeated flaking occurred. A more detailed presentation of SiC response to He^+ implantation can be found in [5,6], along with the implications of this response to the HAPL chamber.

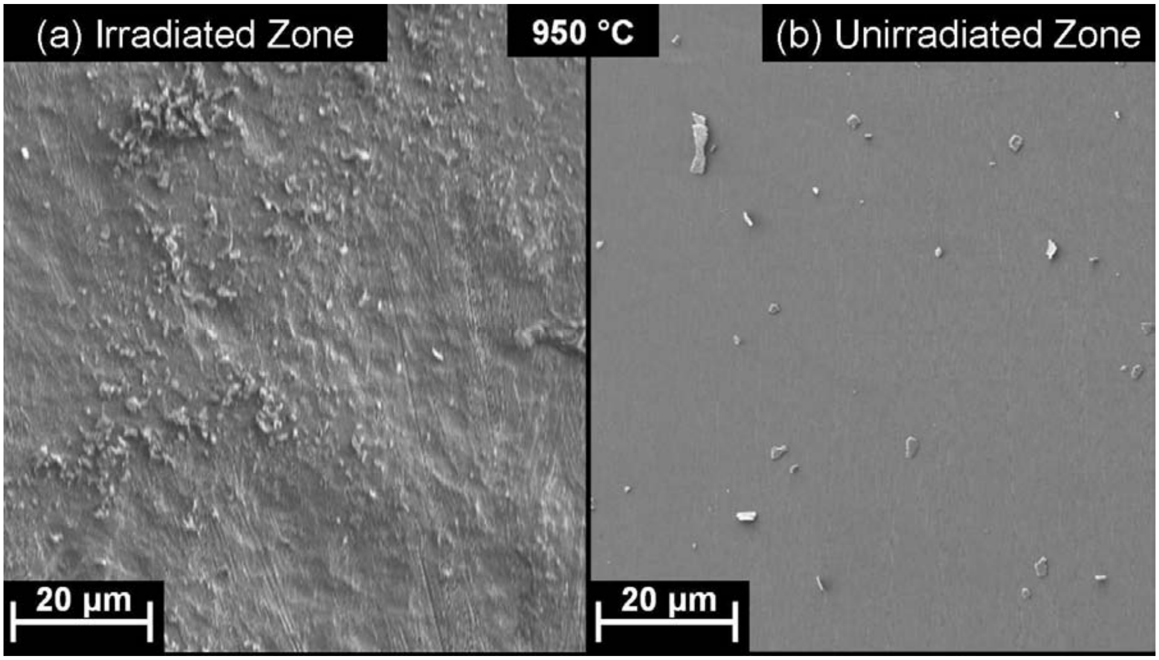

Figure 5-6: (a) Irradiated region of masked SiC specimen showing flaking and craterinig after implantation with 30 keV He^+ to a fluence of $1.6x10^{19}$ cm^{-2} at 950 °C, and (b) the unirradiated region of the SiC exposed to the 950 °C temperature, but masked from the bombarding helium by a Ta foil. Performed in HOMER.

5.1.2.2. Carbon-carbon velvet – HOMER and HELIOS

After the investigation of SiC materials irradiations, experiments shifted to two materials recently developed by Energy Science Laboratories, Inc. (ESLI) [7] as candidate first wall armor for the HAPL chamber – carbon-carbon velvet (CCV) and W-coated carbon-carbon velvet (W/CCV). The carbon and W-coated carbon fibers which generate this “velvet” structure are adhered to a graphite disk substrate ~1 cm in diameter and 3 mm in thickness. Specimens investigated in this work have a highly unique geometry, therefore the composition of these fibers are described here and illustrated in Figure 5-7. Fibers are ~1000 μm long and ~10 μm in diameter. The core material of the fibers is pitch graphitic carbon approximately 9 μm in diameter. These fibers are then coated (through chemical vapor deposition) by an amorphous carbon layer (~0.5 μm). The final step in fabrication of the W-coated CCV samples is applying an additional sputter coating of tungsten (~1 μm thickness). Dr. Timothy Knowles at ESLI provided each of the specimens irradiated at the UW IEC laboratory.

Implantation experiments on CCV and W-coated CCV included both He^+ and D^+ implantation. A complete set of experiments, along with their conditions, is listed in Table 5-4; however, the results of the D^+ implantations are not treated in this document. In general, helium implanted specimens sustain much more extensive damage than that seen in deuterium implanted specimens. More detailed information on the setup, irradiation, and implications of these CCV and W-coated CCV specimens can be found in references [6] and [8], as well as a detailed discussion of D^+ implantation results.

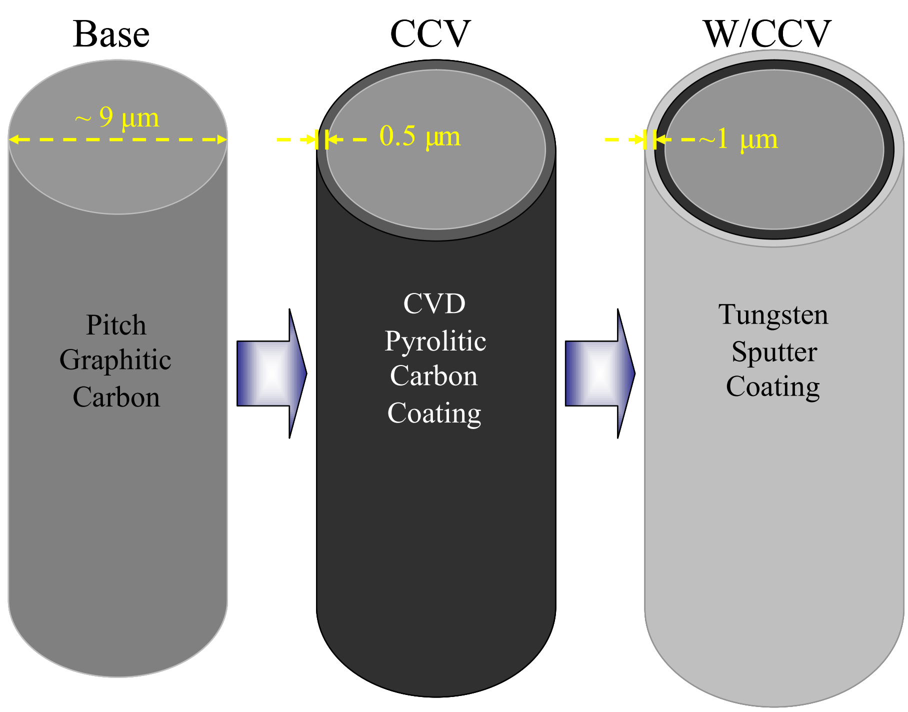

Figure 5-7: Schematic of fabrication process for CCV and W-coated CCV fibers

Sample	Ion	Fluence, He^+/cm^2	Temperature, °C
CCV2	He	10^{19}	~1150
CCV3	D	10^{18}	~1150
CCV5	He	$5x10^{18}$	~1150
W/CCV1	He	10^{19}	~1150
W/CCV3	D	10^{19}	~1150
W/CCV4	D	$5x10^{19}$	~1150
W/CCV5	He	$5x10^{19}$	~1150

Table 5-4: Summary of velvet specimen irradiation experiments in HOMER.

Steady state helium ion implantation of CCV samples was performed at 1150 ºC to a fluences of $5x10^{18}$ and 10^{19} He^+/cm^2 using 30 keV ions. After implantation to $5x10^{18}$ He^+/cm^2 the outer pyrolitic coating of carbon fiber is almost completely eroded away, leaving the inner pitch graphite substrate exposed (Figure 5-8(b)). Helium ions have a range of ~0.2 µm in amorphous carbon which is appreciably shorter than the ~0.5 µm coating on the fiber shafts. Most likely, this effect occurs due to a gradual erosion of the amorphous layer during the He^+ implantation process, eventually exposing the core of the fiber shaft. Once vulnerable, the helium ions attack the graphene planes causing their separation and expansion. The results of exposing this pitch graphite can be seen at 10^{19} He^+/cm^2 (Figure 5-8(c)). A final result is the severe exfoliation of the fiber tips and fiber shaft corrugation. Graphitization of the carbon fibers comprising these velvet specimens is not believed to occur during irradiation at 1150 °C, since these carbon fibers have been annealed to 3000 ºC by the vendor. [9] In each of the irradiations performed on the CCV specimens, significant morphology change is evident.

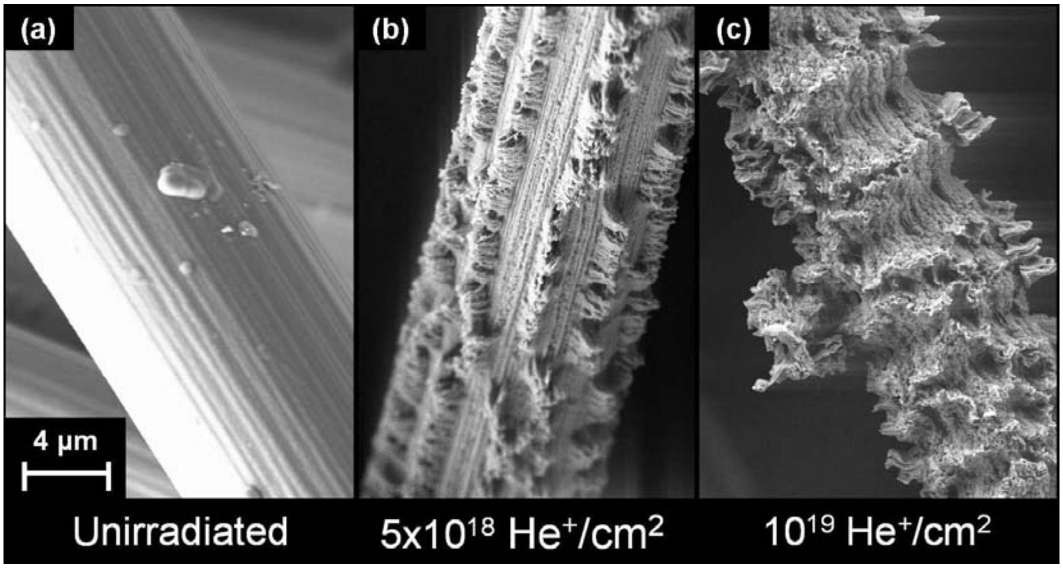

Figure 5-8: (a) Unirradiated CCV, (b) CCV implanted to $5x10^{18}$ at 1150 °C, and (c) CCV implanted to 10^{19} He^{+}/cm^{2} at 1150 °C in HOMER and HELIOS.

It is inferred that the threshold fluence of these specimen is much lower than the minimum tested fluence of $5x10^{18}$ He^{+}/cm^{2}. Similar experiments were performed by Ekern et al. [10] on graphite cloth and showed flaking of the graphite surface after He^{+} implantation. It should be noted that the experiments by Ekern et al. were carried at temperatures between 25°C and 800 °C and showed a decrease in damage with increasing temperature. Moreover, the type of graphite composing the velvet fibers might play a large role in either reducing or enhancing radiation damage. Thomas [11] observed cracking perpendicular to the sample surface in edge-orientated graphite as opposed to flaking in basal orientate graphite after bombardment with 300 keV He^{+}. It is quite possible that a pan (stacked graphene planes) fiber might respond more favorably to ion implantation.

5.1.2.3. W-coated carbon-carbon velvet – HOMER and HELIOS

The second type of velvet material investigated in the HOMER and HELIOS devices was W-coated CCV. The composition and fabrication process of this material is treated in the preceding section. W-coated CCV specimens were implanted at ~1150 °C to a fluence of 5×10^{18} and 10^{19} He^+/cm^2. SEM micrographs in Figure 5-9 illustrate the unirradiated W-coated CCV. Helium implantation caused surface roughening and pore formation over the entire tip and shafts of the fibers at both fluences. Unlike CCV samples, tip erosion is not observed, but the tungsten sputter coating has ruptured along shafts and on the tips of various fibers (Figure 5-9(c)). Once ruptured, fiber shafts and tips undergo the same tip exfoliation and fiber shaft corrugation seen in the He^+ implanted CCV specimen (Figure 5-8(b)-(c)). It appears that the rupturing of the tungsten coatings is caused by the different thermal expansion coefficients between tungsten (4.9×10^{-6} m/m-K) and the graphitic carbon (8×10^{-6} m/m-K). [12] The coefficients listed above are average values, but under heat pitch carbon will shrink vertically and expand radially. The expansion coefficient for radial expansion of pitch graphite is 27×10^{-6} m/m-K, and the vertical expansion coefficient is -1.5×10^{-6} m/m-K. Using the values of the average expansion coefficients, for a 10 μm diameter fiber at ~1150 ºC the tungsten coating will expand ~55 nm radially, while the carbon will expand ~90 nm radially. This difference results in high stresses on the W coating and is possibly the cause of the observed rupturing.

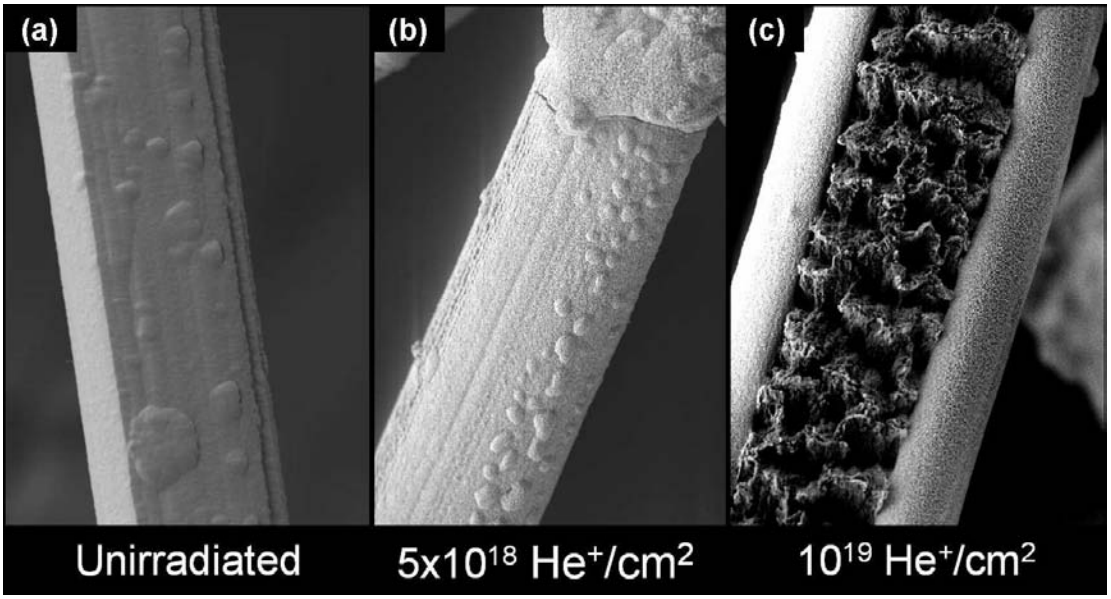

Figure 5-9: (a) Unirradiated W-coated CCV, (b) W-coated CCV implanted to $5x10^{18}$ at 1150 °C, and (c) implanted at 10^{19} He^+/cm^2 at 1150 °C in HOMER and HELIOS.

A final observation of the W-coated fiber tips implanted to $5x10^{18}$ He^+/cm^2 at 1150°C reveals pore formation and a coral structure very similar to that of a flat, pure W specimen irradiated to 10^{19} and 10^{20} He^+/cm at 1100 °C (Figure 5-10). It appears that the W-coated CCV responds to He^+ implantation in the same way as pure W responds; that is, until fiber shafts undergo rupturing. After rupturing and exposure of the graphite, fibers sustain the same extensive damage as the uncoated CCV.

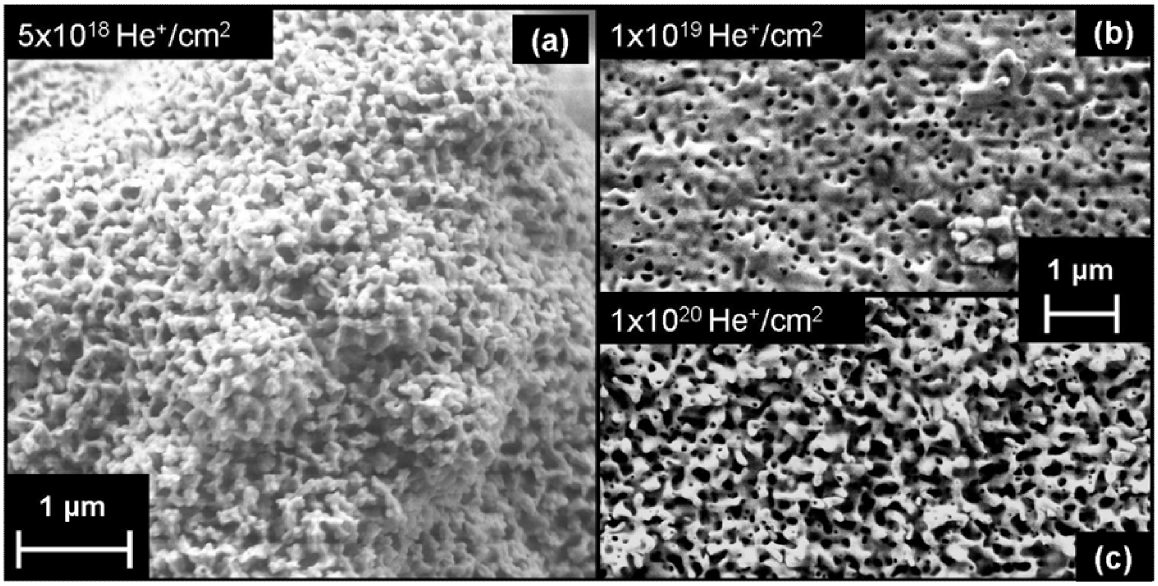

Figure 5-10: Comparison of W-coated CCV and flat, pure W after exposure to helium ions at high temperature in the HOMER device. In (a) W-coated CCV is irradiated to 5x10^{18} He^{+}/cm^{2} at 1150 °C, (b) pure W implanted at ~1150 °C to a fluences of 10^{19} He^{+}/cm^{2}, and (c) pure W implanted to 10^{20} He^{+}/cm^{2} at 1150 °C. [13]

5.1.3. Helium implantation results on pure W from the UW IEC device HELIOS

5.1.3.1. Single- and polycrystalline tungsten – HELIOS

Experiments have shown that the high energy (>1 MeV) helium ions results in the blistering of polycrystalline tungsten [14] and helium ion bombardment results in a W-nanostructure or "tungsten fuzz" at low implantation energies (<1 keV). [15] Other research has observed substantial melting and cracking on the surface of pure PCW after pulsed implantation of ~700 keV ions. [16] A detailed discussion of previous work on helium implantation into pure W is given in Chapter 2 of this dissertation. The research presented in this portion of this report focuses on the effects of helium implantation on single- (SCW) and polycrystalline tungsten (PCW) for intermediate ion energies (30 keV). The resilience of SCW and PCW to implantation with 30 keV ^{3}He ions were assessed for implant fluences of 5x10^{16} – 5x10^{18} He^{+}/cm^{2} at temperatures ranging from

850 – 1000 °C. All the W specimens discussed in this section were provided by Dr. Lance Snead at ORNL. The implant fluences were chosen as upper and lower bounds to the damage threshold (~10^{17} He^+/cm^2) observed in previous work at the UW IEC laboratory. [17,18] The isotope ^3He was used instead of ^4He so that the helium retention depth profiles could be determined using nuclear reaction analysis (NRA) and neutron depth profiling (NDP). This section summarizes the surface morphology change as well as the helium retention characteristics of SCW and PCW after helium ion implantation. A summary of experiments is shown in Table 5-5.

Sample	**Fluence, He^+/cm^2**	**Temperature, °C**
SW7	$5x10^{16}$	~850
SW8	$4x10^{17}$	~1000
SW9	$5x10^{18}$	~1000
P17	$5x10^{16}$	~850
P18	$4x10^{17}$	~1000
P19	$5x10^{18}$	~1000

Table 5-5: Summary of helium implantation experiments on single-crystalline W (SW-) and polycrystalline W (P-) carried out in the HELIOS device. The implantation energy was 30 keV for all specimens. The neutral background pressure during implantation was ~100 µTorr of helium.

A large part of the recent experimentation on SCW and PCW included the development of new analysis techniques. Tungsten was useful in this regard for the following reasons: 1) the previous work on W by Cipiti [19] and Radel [20,21,22] at the UW IEC facility provided a large inventory of data, 2) tungsten is the primary choice for first wall armor and divertor plates, and 3) the simulation codes [23] use tungsten to describe the onset and evolution of ion damage caused by helium ions.

5.1.3.2. Surface morphology changes on SCW and PCW – HELIOS

Figure 5-11 illustrates an unirradiated W specimen for comparison to the specimens implanted with helium. Figure 5-12 below shows the evolution of surface morphology with increasing fluence for both SCW and PCW. At an implantation temperature of 850 ºC and fluence of $5x10^{16}$ He^{+}/cm^{2} no discernable difference is visible between the irradiated and unirradiated specimens, therefore these images are not included in this report.

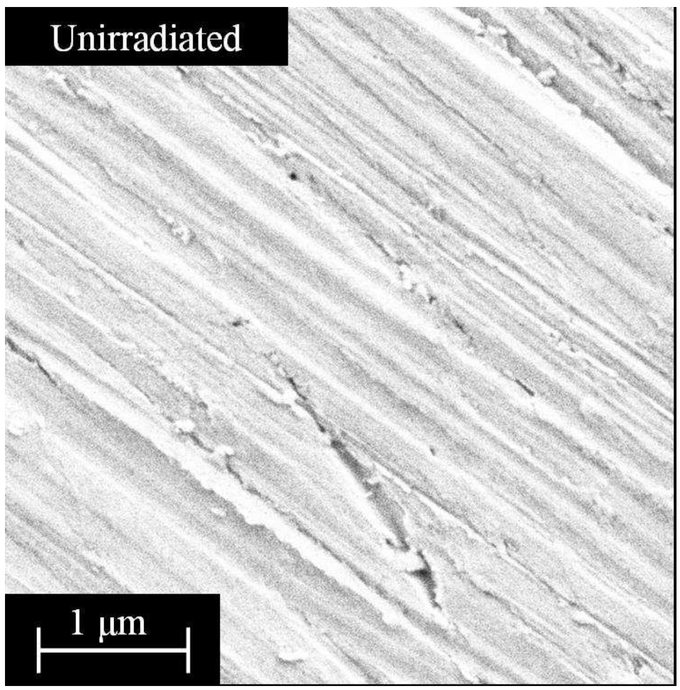

Figure 5-11: Unirradiated polycrystalline tungsten polished to a mirror finish.

After SCW was implanted to $4x10^{17}$ He^{+}/cm^{2} (Figure 5-12(a)), surface roughening is evident as well as sparse pore formation on SCW. Surface pore density was measured to be $1.5x10^{8}$ pores/cm^{2}. Observation indicates that this SCW specimen is just above the threshold fluence for surface pore formation, visible with an SEM; which in turn, aligns well with the previous work done by Cipiti [19] and Radel [20,21]. It is important to note that the onset of surface pore formation is preceded by extensive evolution of He vacancies and clusters which coalesce into these macro-bubbles (pores) and migrate to the surface [23]. At the maximum implant fluence of $5x10^{18}$ He^{+}/cm^{2} (Figure 5-12(b)), dramatic changes in surface morphology are observed for SCW. Pore formation is extensive with a surface pore density of $1.1x10^{10}$ pores/cm,^{2} and surface pore density appears to be saturated.

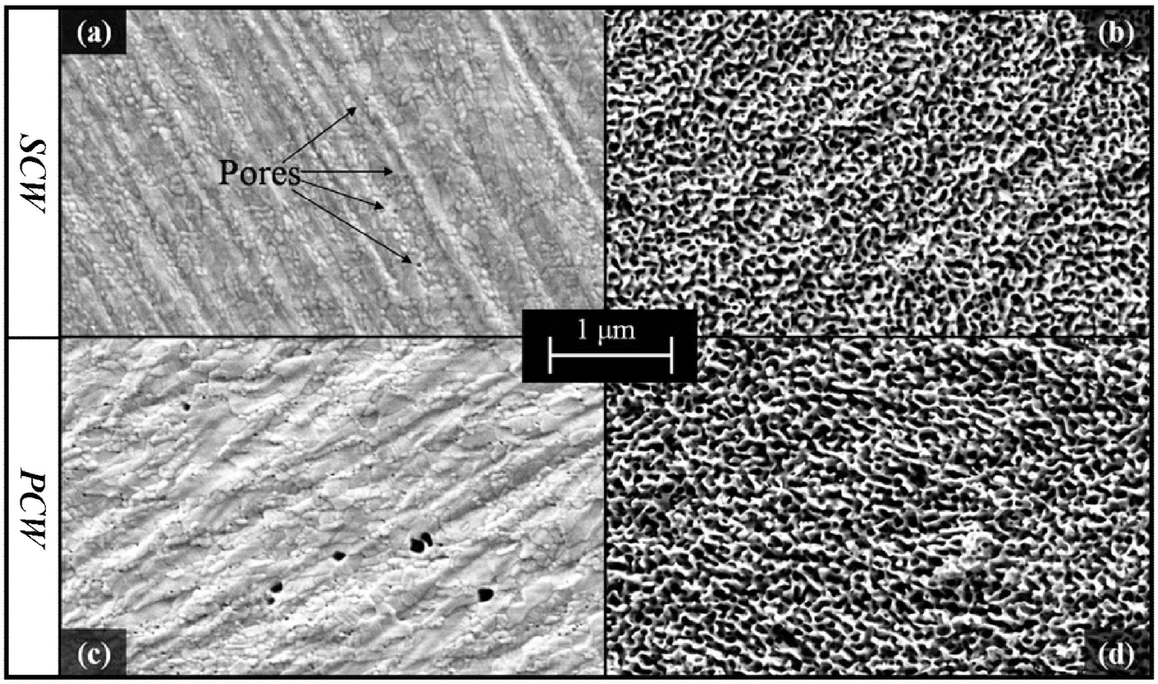

Figure 5-12: SEM micrographs of pure W irradiated with 30 keV $^{3}He^{+}$. SCW irradiated in HELIOS to (a) $4x10^{17}$ He^{+}/cm^{2} and (b) $5x10^{18}$ He^{+}/cm^{2} cm^{-2} at 1000 °C. PCW irradiated to (c) $4x10^{17}$ He^{+}/cm^{2} and (d) $5x10^{18}$ He^{+}/cm^{2} at 1000 °C

The same SEM analysis was performed on PCW after helium ion implantation and showed very similar qualitative results. No surface damage was visible after implantation at 850 °C to the lowest fluence, $5x10^{16}$ He^{+}/cm^{2}. After irradiation at 1000 °C to $4x10^{17}$ He^{+}/cm^{2} (Figure 5-12(c)), surface roughening and pore formation is observed with a pore density of $1.1x10^{9}$ pores/cm^{2}. Increasing the fluence on the PCW specimen to $5x10^{18}$ He^{+}/cm^{2} (Figure 5-12(d)) resulted in extensive damage and pore formation. Surface pore density in the PCW specimen also appears saturated at $1.3x10^{10}$

pores/cm.^{2} Comparison of the two materials indicates that the threshold for pore formation in SCW might be slightly above that of PCW. In both materials the threshold is observed to be ~10^{17} He^+/cm^2, agreeing with references [19,20,21]. For PCW implanted to $4x10^{17}$ He^+/cm^2 with $^3He^+$ at 1000 ºC, surface pore density is comparable to that reported by Cipiti [19] ~$1x10^9$ pores/cm^2. Cipiti implanted to $3x10^{17}$ He^+/cm^2 using 30 keV $^4He^+$ at 920 °C. Conversely, the pore densities reported by Radel [20,21] for PCW implantation with $^4He^+$ to $6x10^{18}$ He^+/cm^2 at 1120 ºC are ~3x lower than those observed in this work on PCW implanted to $5x10^{18}$ He^+/cm^2 at 1000 °C; furthermore, the Radel samples have a slightly larger surface pore diameter.

5.1.3.3. Surface morphology changes on SCW and PCW – HELIOS

SCW and PCW specimens irradiated to the lowest fluence were not extensively examined in this analysis, due to the lack of visible pore formation. The results from the remaining specimens are shown in Figure 5-13. Sub-surface penetration depth of the visible porous or roughened layer was 130 and 210 nm in SCW irradiated at 1000 °C, while corresponding to helium fluences of $4x10^{17}$ cm^{-2} and $5x10^{18}$ cm^{-2}, respectively (Figure 5-13(a)-(b)). For implantations on PCW at 1000 °C, the sub-surface porous layers extended to depths of 140 and 290 nm, while corresponding to helium fluences of $4x10^{17}$ cm^{-2} and $5x10^{18}$ cm^{-2}, respectively (Figure 5-13(c)-(d)). An increase in bubble depth is observed with increasing implant fluence, while bubble distribution is observed to be uniform and ends quite abruptly. Calculated diffusion lengths from Brownian motion are ~5 nm for both tungsten species, indicating the extended porous layers does not result from random thermal diffusion. Moreover, assuming that small helium bubbles initially were formed near the peak concentration of implanted 30 keV $^3He^+$ (~73 nm), one expects to see the characteristic Gaussian distribution of bubbles associated with Brownian motion. This is not consistent with the analyzed FIB data. In the results presented by Radel [21,22], increased helium bubble depth was also observed with increasing fluence, confirming the present thesis' results. One reason for this might be that higher implant fluences, which require longer experimental durations, allow more time for atomistic diffusion of the helium, and result in increased bubble depth. At a implantation temperature of 1150 °C, the semi-porous layer depths in PCW as reported by Radel are ~90 nm and ~290 nm for fluences of 10^{18} and 10^{19} He^{+}/cm^{2}, respectively. At normalized fluences, these penetration depths measured in [21] are decreased from this paper's results at 1000 °C, supporting the argument that Brownian diffusion is not the mechanism behind the observed phenomenon. Furthermore, pore depth in PCW is greater than in SCW. The average migration distance of bubbles from grain boundary diffusion in PCW was calculated to be ≤5 nm – not nearly enough to account for the measured difference of ~100 nm.

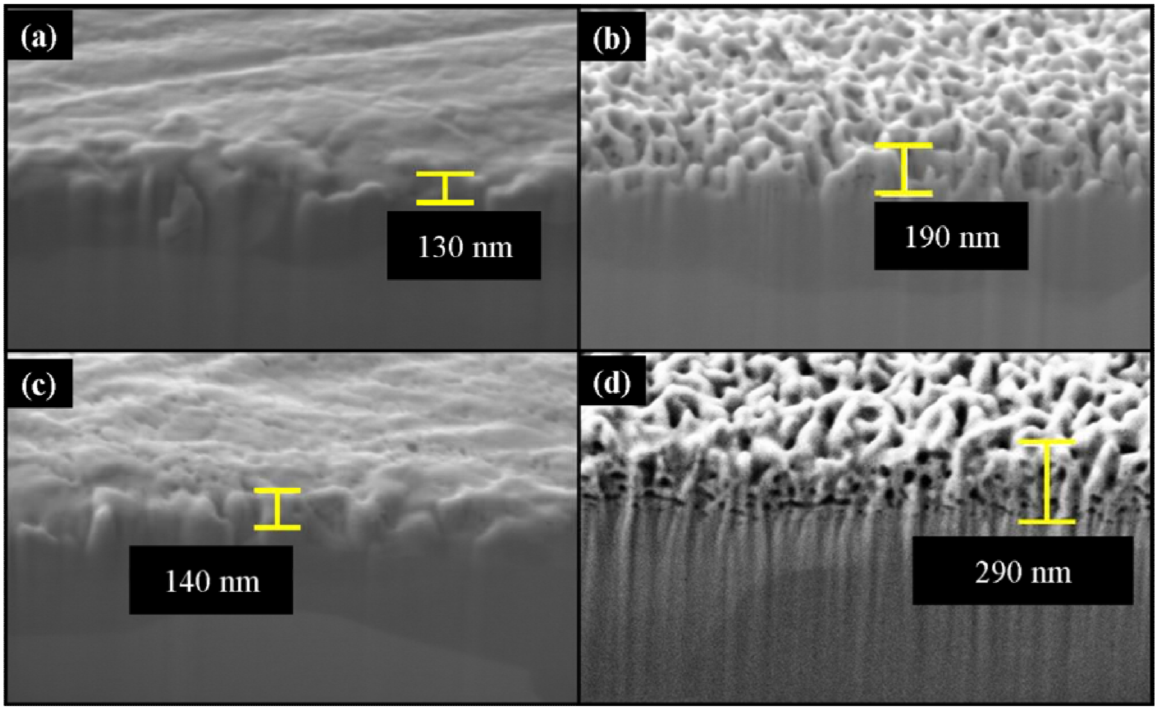

Figure 5-13: FIB analysis of tungsten irradiated in HEIOS with 30 keV $^3He^+$. SCW irradiated to (a) 4x10^{17} He^+/cm^2 and (b) 5x10^{18} He^+/cm^2 at 1000 °C. PCW irradiated to (c) 4x10^{17} He^+/cm^2 and (d) 5x10^{18} He^+/cm^2 at 1000 °C

By analyzing SEM and FIB data with the Matlab software, bubble concentrations in the surface layer were found to be 3x10^{16} (SCW) and 5x10^{16} bubbles/cm^3 (PCW) at the maximum implant fluence of 5x10^{18} He^+/cm^2. Using the same analysis, the average bubble radii was determined in order to estimate the bubble pressure and number of helium atoms present in the bubbles, *m'*. This can be done using the following equations:

$$Pressure = P = \frac{2\gamma}{r_B}, \qquad \text{Equation 5-1}$$

where P is the bubble pressure, γ is the surface tension of tungsten, and r_B is the bubble radius, and

$$m' = \frac{8\pi\gamma r_B^3}{3(kTr_B + 2\gamma b)}, \qquad \text{Equation 5-2}$$

where b is the Van der Waal's gas constant, k is the Boltzmann constant, and T is the temperature. Applying this analysis to the sub-surface porous layer of the SCW and PCW specimens implanted at 5×10^{18} He^{+}/cm^2, an "effective density" of the subsurface porous layer can be calculated. This analysis yielded an estimated atomic density in the examined surface layer of ~6×10^{21} atoms/cm^3 for SCW and ~10^{22} atoms/cm^3 in PCW. The atomic density of solid tungsten is taken as 6.3×10^{22} W atoms/cm^3. Assuming a homogeneous distribution of He in the semi-porous region, the effective density in the semi-porous layer decreased from 19.35 g/cm^3 (solid W) to 12.2 g/cm^3 in the SCW and 8.0 g/cm^3 in the PCW. From these values, SRIM determined the corresponding ranges of the peak He concentration at 114 and 176 nm. A more thorough report on this work, its implications and conclusions are given in [24]. It was concluded that there is a complex relationship between bubble diffusion, atomistic diffusion, and a decrease in the effective density of the implanted layer which governs the depth of this sub-surface porous layer.

5.1.3.4. Helium retention in SCW and PCW – HELIOS

Using the $^{3}He(d,p)^{4}He$ Nuclear Reaction Analysis (NRA) technique, the total retained helium fluence was determined for the six implanted W specimens. The $^{3}He(n,p)T$ nuclear reaction was used for the Neutron Depth Profiling (NDP) technique to determine the retained helium along with the depth profile of the retained helium. Helium retention results for both techniques are plotted in Figure 5-14 and expressed numerically as a retained helium percentage in Table 5-6. Both SCW and PCW exhibit increased retention ratios at lower implant doses, but the PCW shows ~2-4x higher helium trapping efficiencies than SCW. This behavior is most likely a result of the presence of grain boundaries in the PCW resulting from the powder metallurgy fabrication process.

The maximum retained helium fluence in PCW is ~$3x10^{17}$ He atoms/cm^2. This result agrees with earlier helium retention studies on pure W at the UW-IEC laboratory. In these earlier experiments, which used the elastic recoil detection technique to measure retained fluence, a maximum retained helium fluence of $4x10^{17}$ He atoms/cm^2 for PCW after helium implantation to 10^{19} He^+/cm^2 at 1150 ºC. [18] Hino et al. [25] and Fu et al. [26] both reported that the retained helium fluence in PCW saturated at ~10^{17} He/cm^2 after implantation with 1 to 8 keV helium ions at room temperature. These data indicate that the implanted helium is released from the surface of the tungsten after saturation is achieved. Surprisingly, surface morphology continues to evolve and worsen as the retention fluence saturates (Figure 5-12). For steady-state implantation, surface damage increases and worsens with total dose despite the gradual release of the implanted helium from the tungsten surface and a decreasing helium retention ratio.

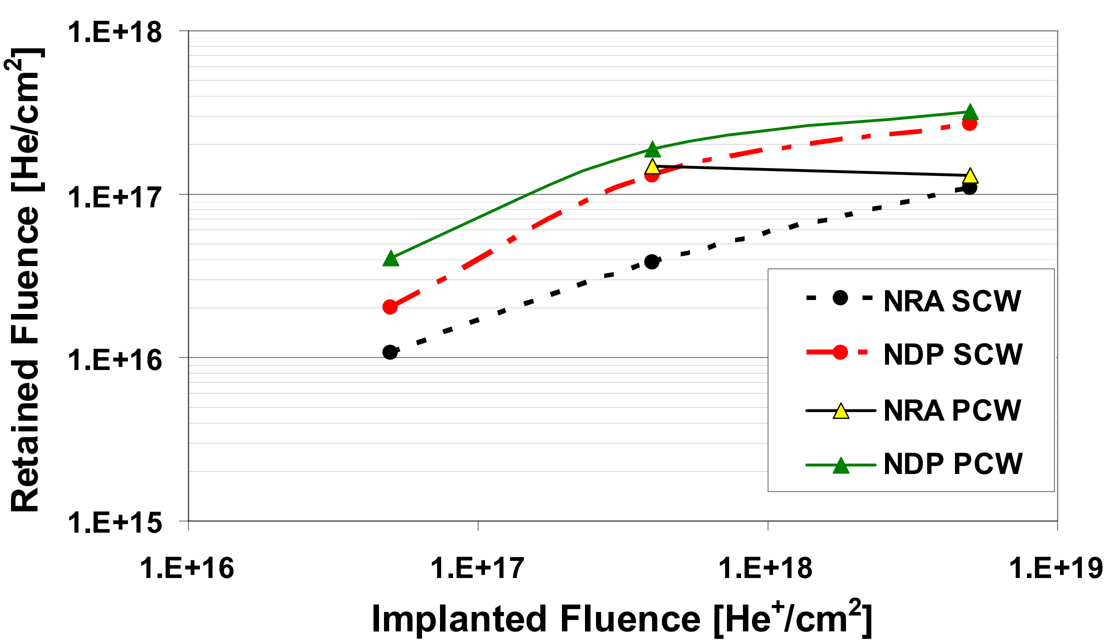

Figure 5-14: Measured retained He fluence in tungsten samples after He^+ implantation in HELIOS at 850 – 1000 °C using NRA and NDP analyses.

Implanted Fluence, He^+/cm^2		$5x10^{16}$	$4x10^{17}$	$5x10^{18}$
SCW	NRA	22%	10%	2%
	NDP	40%	33%	5%
PCW	NRA	--	37%	3%
	NDP	82%	48%	6%

Table 5-6: Ratio of the implanted helium fluence to the retained helium fluence (given in percent) for SCW and PCW specimens as measured by NRA and NDP analyses. Implanted helium fluences are listed in the top row. The blue numbers report retention measurements using NRA and the red numbers report retention measurements using NDP.

5.1.3.5. Neutron depth profiling of SCW and PCW – HELIOS

NDP was also used to determine the depth profile of the implanted helium in all six tungsten specimens. For comparison, the SRIM program was used to simulate 30 keV $^3He^+$ implanted into 100% dense W. The predicted peak concentration was ~9600 [(atoms/cm^3)/(atoms/cm^2)] at a depth of ~75 nm. When multiplied by the implant fluence, the peak atomic concentration in the tungsten specimen is found. Taking the threshold of pore formation to be $1x10^{17}$ He^+/cm^2 and using $6.3x10^{22}$ atoms/cm^3 for the atomic density of solid W, SRIM predicts that the peak helium concentration required to cause surface modification is 1.5 at% He. Average helium concentrations (in at%) for W specimens at the intermediate and low doses are summarized in (Table 5-7). The SCW and PCW specimens implanted to fluences $\leq 4x10^{17}$ He^+/cm^2 were assumed to be 100% dense tungsten, despite the minor pore formation on the surface. It is not anticipated that the minor surface pore formation on W specimens implanted to $4x10^{17}$ He^+/cm^2 will significantly modify the surface density of the W from that of the bulk.

Sample	Implanted Fluence, $^3He^+/cm^2$	Total at% of He in W *in irradiated zone*
SW7	$5x10^{16}$	0.7
P17	$5x10^{16}$	1.3
SRIM predicted threshold	10^{17}	1.5
SW8	$4x10^{17}$	4.2
P18	$4x10^{17}$	6.1

Table 5-7: Average He concentrations (at%) in W are given for SCW and PCW specimens implanted at fluences $\leq 4x10^{17}$ $^3He^+/cm^2$. The red data reported is the helium concentration predicted by the SRIM program if it is assumed the threshold helium fluence for visible pore formation is 10^{17} He^+/cm^2. Calculations assume 100% dense tungsten.

SEM analysis showed no visible surface morphology change at an implantation fluence of $5x10^{16}$ He^+/cm^2 on SCW or PCW. Furthermore, NDP analysis showed that the retained atomic helium concentration in these specimens is below the 1.5 at% predicted by the SRIM program for W implanted to 10^{17} He^+/cm^2 (where one first expects to see morphology changes). The results in Table 5-7 appear to agree with the predictions from the SRIM program.

Depth profiles for all six specimens (Figure 5-15) confirm that PCW is slightly more efficient at trapping implanted helium atoms than SCW. SCW and PCW implanted to a dose of $5x10^{16}$ He^+/cm^2 showed no observable surface morphology change and had peak He concentrations of ~2 and 4 at%. Whereas, peak He concentrations for specimens implanted to $4x10^{17}$ He^+/cm^2 are 14 and 18 at% for SCW and PCW, respectively. Recalling Figure 5-12, one can observe minor pore formation and surface roughening, which appears to be very near the threshold for surface damage. From this observation, we conclude that the peak helium concentration necessary to cause surface pore formation is between 14 and 18 at%. These values are much greater than the ~2 at% peak helium concentration predicted by SRIM. Assuming 100% density of the tungsten specimens, He concentration was measured to be 8.6 and 10.2 at% for SCW and PCW implanted to 5×10^{18} He^+/cm^2, respectively, with peak He concentrations of ~25 at% in both tungsten species. At 5×10^{18} He^+/cm^2, the helium concentration in the SCW appears slightly depleted in the semi-porous layer in comparison to the other SCW specimens shown in Figure 5-15. One possible explanation for this depletion would be the vertical coalescence of smaller bubbles, which form "chimney" sites for the He gas to escape from the porous layer. Re-examination of FIB analysis presented in Figure 5-13(b) reveals many "open" pores that do, in fact, penetrate the total depth of the semi-porous layer.

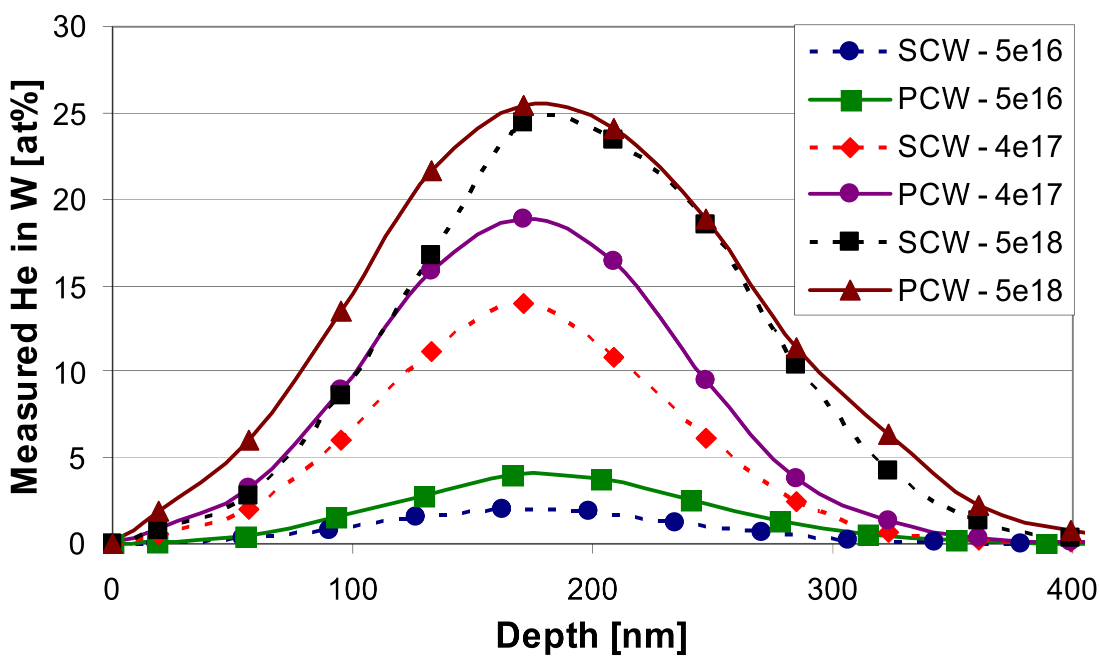

Figure 5-15: Depth profiles of retained He in W (at%) as measured by NDP. The total density of W (19.35 g/cm^3) was used to calculate the depth scale.

Due to these sub-surface pores, one cannot assume perfect density throughout the tungsten specimens. For this reason, the FIB analysis done in the previous section was used to augment the NDP data. SCW and PCW specimens implanted to 5x10^{18} He^{+}/cm^{2} were split into two layers: 1) the porous layer and 2) the specimen "bulk" layer. Layer depth was determined by FIB analysis, and the new NDP proton stopping powers for the new layer densities (SCW – 12.2 g/cm^{3}, PCW – 8.0 g/cm^{3}) were adjusted using SRIM. As an estimate, stopping powers were adjusted assuming linear scaling. After adjustment, the average He concentration was found to be 7.6 and 11.4 at% for SCW and PCW implanted to 5x10^{18} He^{+}/cm^{2}, respectively (Table 5-8:).

Sample	**Average He [at%]**	**Adjusted He Average [at%]**
SW9	8.6 (19.3 g/cm^{3})	7.6 (12.2 g/cm^{3})
P19	10.2 (19.3 g/cm^{3})	11.4 (8.0 g/cm^{3})

Table 5-8: The average helium concentration in SCW and PCW after implantation to 5x10^{18} He^{+}/cm^{2}. The central column assumes that the W is 100% dense and the right-hand column shows the adjusted values for helium concentration in SCW and PCW assuming the density of the W is decreased by the presence of helium bubbles in the semi-porous sub-surface region.

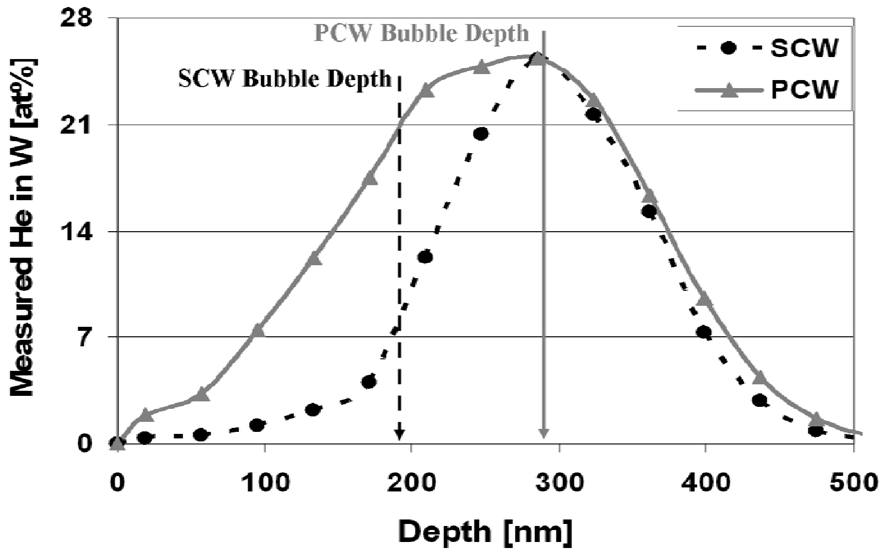

Figure 5-16: Depth profile of He concentrations in SCW and PCW implanted in HELIOS at 1000 °C to $5x10^{18}$ He^{+}/cm^{2} as measured by NDP and adjusted for density change. The arrows represent the observed bubble penetration depths for SCW (190 nm, dashed) and PCW (290 nm, solid).

Comparing Figure 5-15 and Figure 5-16 reveals this adjustment shifts the peak concentration of the retained He deeper into the material by ~100 nm. The peak He concentration in the PCW specimen was found to be 25 at%. Using the elastic recoil detection technique, Radel [18] reported peak He concentrations in PCW of ~40 at% after implantation with 30 keV $^{4}He^{+}$ to 10^{19} He^{+}/cm^{2} at 1150 ºC. Analyzing the results for these adjustments indicates depletion of the helium in the semi-porous region in the SCW. Interestingly, the PCW sample exhibits the exact opposite behavior – enhanced retention of helium in the semi-porous layer. In recalling the FIB analysis in Figure 5-13(b), one could now point out that most of the pores are “closed,” and effectively trap the pressurized helium in the bubble region. For these two specimens the difference in total retained He fluence was $5x10^{16}$ He atoms/cm^{2}, with the PCW retaining the greater amount. Approximately $^{2}/_{3}$’s of this difference ($3.3x10^{16}$ He atoms/cm^{2}) is accounted for in the first ~300 nm of the sample’s surfaces. The similar shape between the two curves, in Figure 5-16 after ~300 nm, suggests that the morphology of the porous region plays a large role in the retention characteristics of the tungsten species. Looking at the ratio of the measured He concentration between the two tungsten species, at equal implant fluences, one finds that SCW retains 60% less (on the average) helium than PCW, when atomic concentrations are adjusted for the decrease in effective density of the porous layer.

5.1.4. Helium implantation results on engineered W materials – HELIOS

One of the most important results from the implantations on SCW and PCW in HELIOS was their agreement with previous work done on pure W in HOMER. SEM and FIB analysis showed consistency between the two devices. Unfortunately, this agreement also meant that pure W still responded very poorly to helium implantation at high temperatures. Yet, the new understanding of how helium is retained in the W surface motivated the investigation of engineered W materials: fine-grain W (FGW), nano-grain W (NGW) and W needles. [27] The first two materials are discussed in the following section.

5.1.4.1. Fine-grain and nano-grain tungsten – HELIOS

Both fine-grain W (FGW) and nano-grain W (NGW) materials were engineered using plasma spray technology as opposed to the PCW discussed in the previous section, which is fabricated through the powder metallurgy process. On average, powder metallurgy specimens had an average grain size of ~5 μm; whereas, the FGW had an average grain size <5 μm, and the NGW had an average grain size of approximately 0.24 μm. The FGW specimen dimensions were 25 x 25 x 5.1 mm^3 and it was cut into four equal area specimens using electrical discharge machining (EDM). The plasma sprayed tungsten of the FGW samples was approximately 100 μm thick and rested on 5 mm thick ferritic steel substrate. EDM was also used to section the NGW specimen (10 x 40 x 1 mm^3) into four specimens of equal area. The NGW plasma sprayed layer was ~70 μm thick and was placed on a pure W substrate 1 mm thick. Each of the FGW and NGW samples implanted at the UW IEC laboratory were provided by Scott O'Dell from Plasma Processes Inc. (PPI).

5.1.4.1.1. Surface morphology change and FIB analysis of FGW – HELIOS

Three FGW specimens were implanted with 30 keV ^{3}He ions in the IEC device in HELIOS. The isotope ^{3}He was implanted so that NRA could be performed using the ^{3}He(d,p)^{4}He reaction. A summary of the implantation parameters is given in Table 5-9. From inspection of Figure 5-17, one can see that at an implantation temperature of 850 °C the threshold for visible pore formation on the surface of FGW is just below 9×10^{17} He^+/cm^2. Furthermore, Figure 5-17(c) does not appear to show any preferential collection of helium induced pores at the grain boundaries. The intention of engineering small grain sized materials, such as FGW and NGW, was to make it easier for the implanted helium to diffuse to grain boundaries; and in turn, make it easier for them to release from the surface. Clearly, the FGW specimens do not exhibit this behavior. As the implanted helium fluence was increased to 10^{19} He^+/cm^2 the pore formation became extensive and resulted in the familiar W coral structure.

Sample	Fluence, He^+/cm^2	Temperature, °C
FGW1	10^{19}	~1050
FGW2	$9x10^{17}$	~850
FGW3	$3x10^{17}$	~700
NGW1	10^{19}	~1000
NGW2	10^{18}	~1050
NGW3	10^{17}	~1150
NGW4*	10^{20}	~1000

Table 5-9: Experimental summary of implantations performed on NGW and FGW using 30 keV $^3He^+$ in the IEC device HELIOS. *Implanted with $^4He^+$.

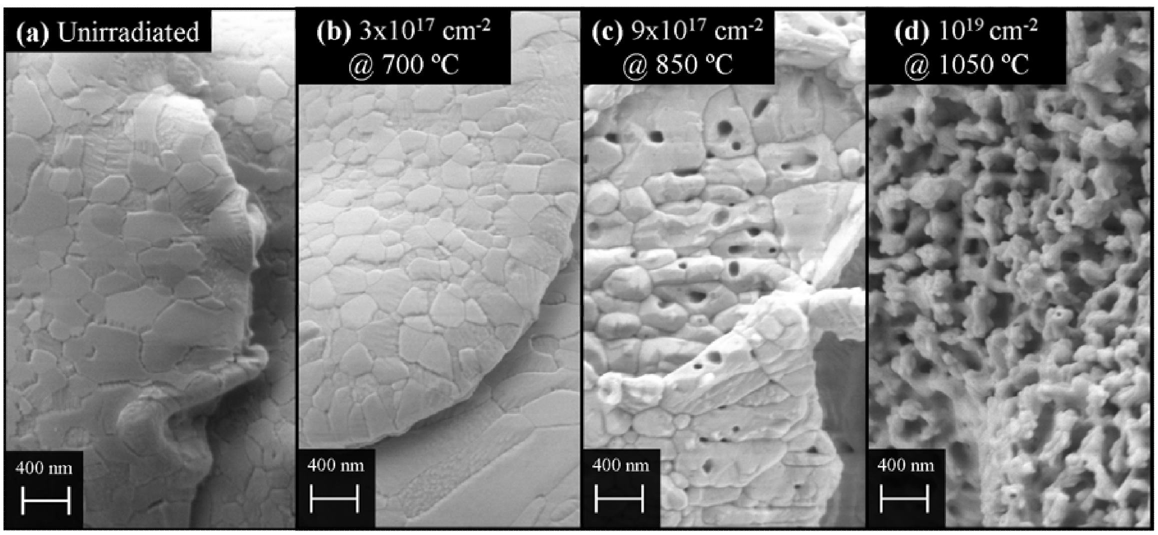

Figure 5-17: SEM comparison showing FGW (a) unirradiated, (b) implanted to $3x10^{17}$ He^+/cm^2 at 700 °C, (c) implanted to $9x10^{17}$ He^+/cm^2 at 850 °C, and (d) implanted to 10^{19} He^+/cm^2 at 1050 °C in HELIOS.

FIB analysis was also performed on the FGW specimens (Figure 5-18). Results showed that the depth of the sub-surface porous layer increased with increasing fluence by about a factor of 5 between the specimen implanted at $9x10^{17}$ He^+/cm^2 (170 nm) and the specimen implanted to 10^{19} He^+/cm^2 (920 nm). Comparing the depth of the sub-surface semi-porous layer observed on PCW at $5x10^{18}$ He^+/cm^2 (Figure 5-13(d)), one notices that the depth of this layer in FGW is ~3x greater for only a doubling of implant fluence at approximately the same temperature (Figure 5-18(b)). One can also compare this with Radel's results in HOMER [13], which reported a sub-surface porous layer depth of 300 nm after helium implantation in PCW to 10^{19} He^+/cm^2 at 1000 °C. Although this material exhibits a slightly higher fluence threshold for pore formation than PCW, the formation of sub-surface pores and the development of a coral-like surface morphology appear accelerate between 10^{18} – 10^{19} He^+/cm^2. The end result is that the material responds <u>less</u> favorably to helium ion implantation than PCW at fluences $>10^{18}$ He^+/cm^2 and high temperatures.

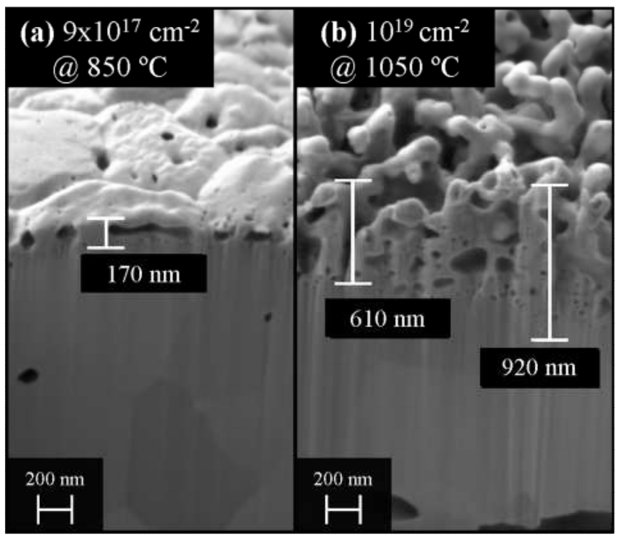

Figure 5-18: FIB micrographs showing the subsurface pore depth in FGW (a) 170 nm for $9x10^{17}$ He^+/cm^2 at 850 °C, and (b) 600-920 nm for 10^{19} He^+/cm^2 at 1000°C. The specimen implanted to $3x10^{17}$ He^+/cm^2 is omitted due to the absence of visible sub-surface pores. Specimens implanted in the HELIOS device.

5.1.4.1.2. Surface morphology change and FIB analysis of NGW – HELIOS

Table 5-9 shows the experimental parameters for each of the irradiated specimens. Note that the highest fluence (10^{20} He^+/cm^2) specimen was implanted with $^4He^+$, and not $^3He^+$. Results from the SEM analysis are shown in Figure 5-19. Visible pore formation is not observed in the specimen implanted to 10^{17} He^+/cm^2 at 1150°C, indicating a "threshold" for visible pore formation between 10^{17} and 10^{18} He^+/cm^2 at temperatures over 1000 °C.

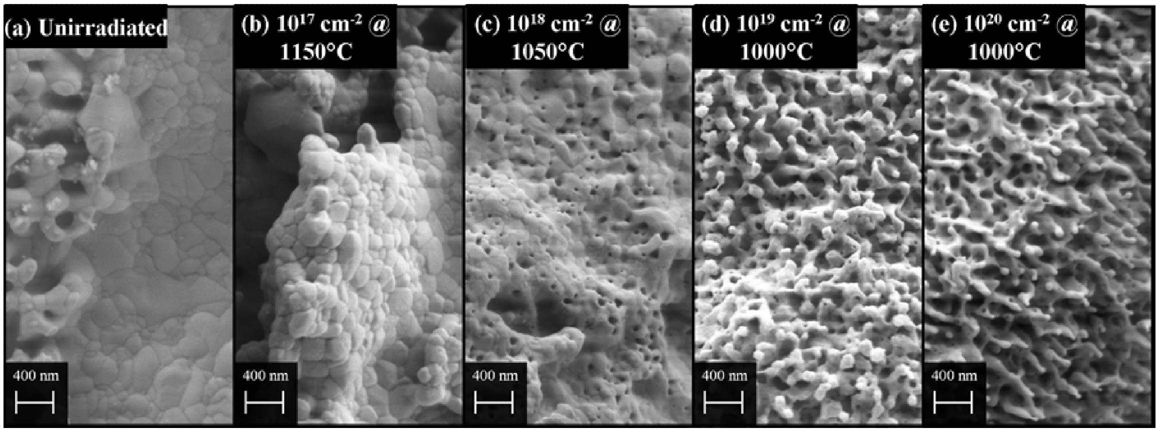

Figure 5-19: SEM micrographs of (a) unirradiated NGW, implanted in HELIOS with He^+ to (b) 10^{17} cm^{-2} at 1150 °C, (c) 10^{18} cm^{-2} at 1050 °C, (d) 10^{19} cm^{-2} at 1000 °C, and (e) 10^{20} cm^{-2} at 1000 °C.

Implantations of NGW were performed at the same energy, temperatures, and doses as previous implantations on polycrystalline W (PCW), and show consistent formation of pores at or slightly below 10^{17} He^+/cm^2 [13,19]. This indicates that NGW requires slightly higher doses to experience visible surface pore formation. In addition, past experiments on tungsten have not shown significant differences in threshold fluence for temperatures varying from approximately 800 – 1200 °C. Therefore, one does not expect a large effect on the morphology change or diffusion of helium with regard to NGW at these temperatures. The micrographs of Figure 5-19 reveal that surface modifications continue to worsen with increasing fluence. Figure 5-19(c) shows a uniform pore distribution on the surface of the NGW, but as implant dose is increased, a coral-like structure forms (Figure 5-19(d)-(e)). Analysis of these figures yielded a saturated pore density of ~$3x10^9$ pores/cm^2 at doses $\geq 10^{19}$ He^+/cm^2, which was similar to prior data on single- and polycrystalline W [24]. Pore density remained approximately constant from 10^{18} to 10^{20} He^+/cm^2, but average surface pore diameter increased from 30 to 65 nm. Close inspection of Figure 5-19(e) reveals the enhanced coral structure over that of Figure 5-19(d). It appears that after surface pore density is saturated, existing pores combine to form a dendritic surface structure, resulting in a larger average pore size.

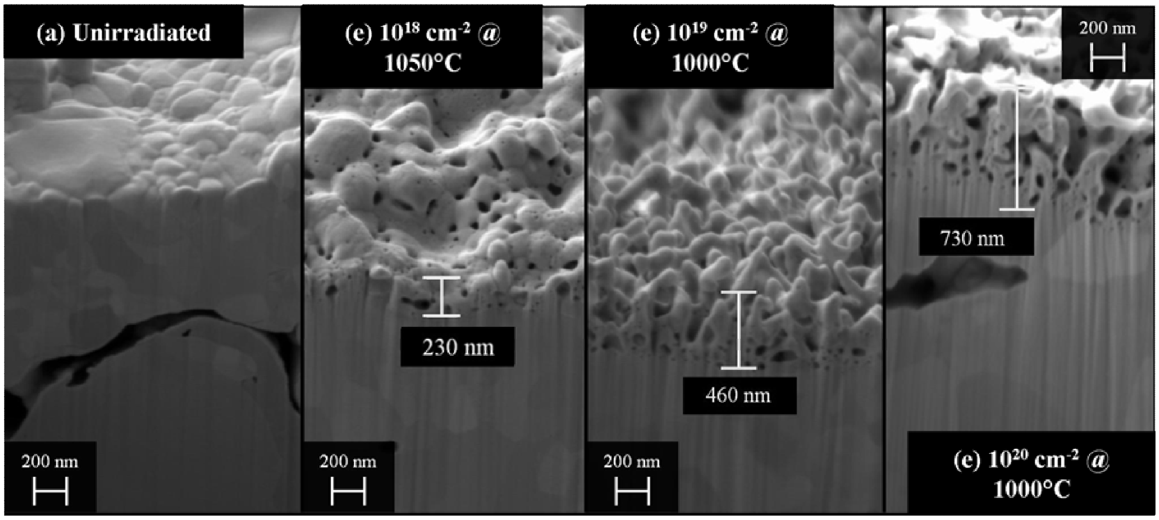

Figure 5-20: FIB micrographs of (a) unirradiated NGW and implanted NGW showing the visible subsurface pore depths of (b) 230 nm for 10^{18} cm^{-2} at 1050 °C., (c) 460 nm for 10^{19} cm^{-2} at 1000 °C, and (d) 730 nm for 10^{20} cm^{-2} at 1000 °C. Specimens were implanted in the HELIOS device.

Increased fluence results in greater penetration depths of visible pores beneath the NGW surface (the specimen implanted to 10^{17} He^+/cm^2 is omitted due to the absence of visible pore formation, Figure 5-19). SRIM® calculations predict the range of $^3He^+$ and $^4He^+$ in W to be 73 and 84 nm, respectively, much lower than the observed W porous layer thicknesses. At high temperatures, one might expect either atomistic or bubble diffusion of the implanted helium is responsible for the increasing depths of these porous layers. Baldwin and Doerner [15] also observed the growth of a "tungsten fuzz" layer at temperatures between 850 and 1050 °C, which increased with increasing He^+ fluence, albeit at implantation energies of 60 eV and much higher ion fluences. Using W surface diffusion parameters presented by Sharafat et al. [28] and following the analysis given by

Barnes and Nelson [29] suggests maximum bubble diffusion lengths in NGW of <10 nm. These length scales cannot account for the observed penetration depths, leaving atomistic diffusion to explain this subsurface morphology change. It is hypothesized that a complex combination of atomistic diffusion and dynamic density changes affecting ion range during implantation work in tandem to produce the observed behavior of these layers.

5.1.4.1.3. Helium retention in FGW and NGW – HELIOS

As mentioned above, the helium retention of FGW and NGW were measured using NRA and are compared to measurements on PCW. Depth profiling was not able to be performed on FGW and NGW using NRA. The retained helium fluence for FGW was between 1.2×10^{17} and 4.5×10^{17} He atoms/cm^2. In NGW, the retained helium fluence ranged from 4.0×10^{16} to 4.5×10^{17} He atoms/cm^2. Figure 5-21 shows that above fluences of $\sim 3 \times 10^{17}$ He^+/cm^2 there is little difference in the retention characteristics of these materials. Only at the lowest implanted fluence does the NGW retain less helium than the PCW. The formation of helium clusters, voids, and eventually macroscopic bubbles and pores is believed to be responsible for the high He retention values in fusion materials. [30] This suggests the evolution of microscopic bubbles in the NGW may take longer to progress than in PCW, which is evidenced by the slightly higher threshold fluence for visible surface pore formation in NGW over that of the PCW. This also might be due to the much smaller grain size (~0.24 μm) of the NGW, which initially allows more helium to escape, or because of additional trappings sites at grain boundaries. However, implantation temperatures (~1000 °C) are not sufficient to anneal out the implanted helium, and due to the abundance of nucleation sites (grain boundaries) in NGW, these bubbles could become even more problematic. Data shows that FGW, NGW, and PCW share similar helium retention profiles when implanted steady-state with 30 keV He^+ for temperatures between 700 – 1150 °C. These observations suggest that incremental doses and subsequent anneals might release the implanted He in a fine- or nano-grain material before the He bubbles grow and become immobile, resulting in increased He retention. Gilliam et al. have examined this process on single- and polycrystalline W species with some success [14]. Further discussion of NGW can be found in [31].

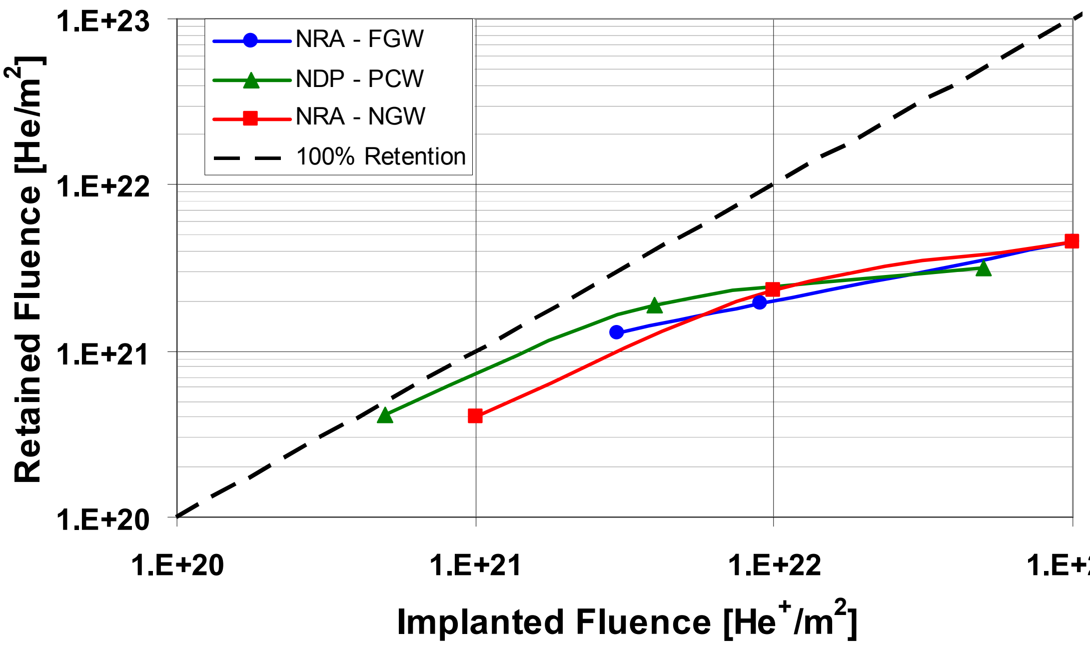

Figure 5-21: Retention data determined for FGW and NGW using NRA, standard PCW using the NDP technique, and a 100% retention line for reference. All specimens were implanted in HELIOS with 30 keV He^+. Implantation temperature ranges for the FGW, PCW, and NGW were 700 – 1050 °C, 900 – 1000 °C, and 1000 – 1150 °C, respectively.

5.1.4.2. W needles – ion gun prototype facility (SIGFE)

The final engineered material discussed in this thesis is W needles. This material was also developed by Energy Science Laboratories, Inc. (ESLI), again in response to the poor performance of flat, pure W under energetic helium bombardment. W needles were approximately 25 mm long and 0.25 mm in diameter. The final 3.5 mm of the W needles were very gradually "tapered" (slope of ~4°) to a submicron tip. All the implanted W needles were either etched at the UW IEC laboratory in a slightly basic solution (Micro-90® and distilled water) or electropolished at ESLI. Investigation of these needles was carried out concurrently with experiments on FGW and NGW. All specimens were provided by Dr. Timothy Knowles at ESLI.

Sample	Fluence, He^+/cm^2	Temperature, °C
UW Etched W Needle	$3x10^{18}$	~700
ESLI Electro-polished W needle	$1.3x10^{19}$	~1000

Table 5-10: Experiment summary for helium implanted W needles. He^+ implantation energies were 100 keV. One W needle was etched using Micro-90® and distilled water and is designated as "UW Etched" and the other needle was electropolished at ESLI and is designated "ESLI Electro-polished" – the formula used for the electropolish is not available. Implanted in the SIGFE prototype ion gun facility.

Table 5-10 gives the implantation conditions for the two W needles. Original attempts to implant these W needles were performed in the IEC device HELIOS, but due to the high cathode (sample) potentials and the "needle" shape of these specimens, they became efficient field emitters. The high field emission currents (~10 mA) made it impossible to accurately monitor the implanted helium current in the device HELIOS. To eliminate field emission and implant these W needles, experiments were moved to the prototype ion gun facility for the Materials Irradiation Experiment (MITE-E). At the time of these experiments, the ion gun existed within another UW IEC device – the Six Ion Gun Fusion Experiment, (SIGFE). Cathode potentials during these experiments were -100 kV. Two W needles were implanted using the following procedure: 1) exposure to -100 kV cathode potential without the presence of helium plasma, 2) implantation of 100 keV He^+ to fluences of $3x10^{18}$ and $1.3x10^{19}$ cm^{-2} (Table 5-10), and 3) exposure to -100 kV cathode potential after the helium plasma source was turned off. Field emission was not observed at any point during the -100 kV exposures of these needles. In the HELIOS, device W needles were placed at a potential of -30 kV and acted as the device's cathode, with the closest ground point at the chamber wall ~30 cm away. This results in an electric field gradient of ~1 kV/cm. On sharp points of conductors, such as the W needle tip, field enhancement can occur causing a further increase in existing electric field gradients [32]. When these electric field gradients become large enough, W will emit electrons from its surface via field emission [33]. Therefore, the absence of any measurable current at exposure to -100 kV in the prototype ion gun facility suggests that either field gradients do exist within the cathode, or that they are inadequate to produce field emission. Further detail on the experimental setup used to implant these W needles is found in Chapter 4 and a more thorough discussion of the implications of field emission on these W needles, and other W materials implanted in UW IEC devices, is given in Chapter 6 of this dissertation.

It is important to note that these W needles were implanted with 100 keV He^+, not the nominal 30 keV He^+ used in most of the previous W implantation experiments. Figure 5-22 shows the SEM and FIB analysis of the UW etched W needle implanted to a fluence of $3x10^{18}$ He^+/cm^2 at 700 °C. Prior to irradiation, the specimen has no visible pore formation and the grains are clearly evident on the W needle (Figure 5-22(a)). After implantation SEM analysis reveals extensive and uniform formation of visible pores on the surface of the W needle and what appears to be the ejection of a grain near the needle tip (Figure 5-22(b)). FIB analysis of the W needle reveals a uniform sub-surface, semi-porous layer distributed circumferentially up to depths of 330 nm. This is much greater than the SRIM predicted range of ~90 nm when 100 keV He^+ is incident on W at 85° (a glancing angle to the surface). The depth of this layer is close to that observed on flat PCW for an implanted helium fluence of $5x10^{18}$ He^+/cm^2, even though the flat tungsten was implanted at the higher temperature of 1000 °C (Figure 5-13(d)). W needles implanted look very similar to W-coated CCV specimens after helium irradiation at high temperatures (Figure 5-10).

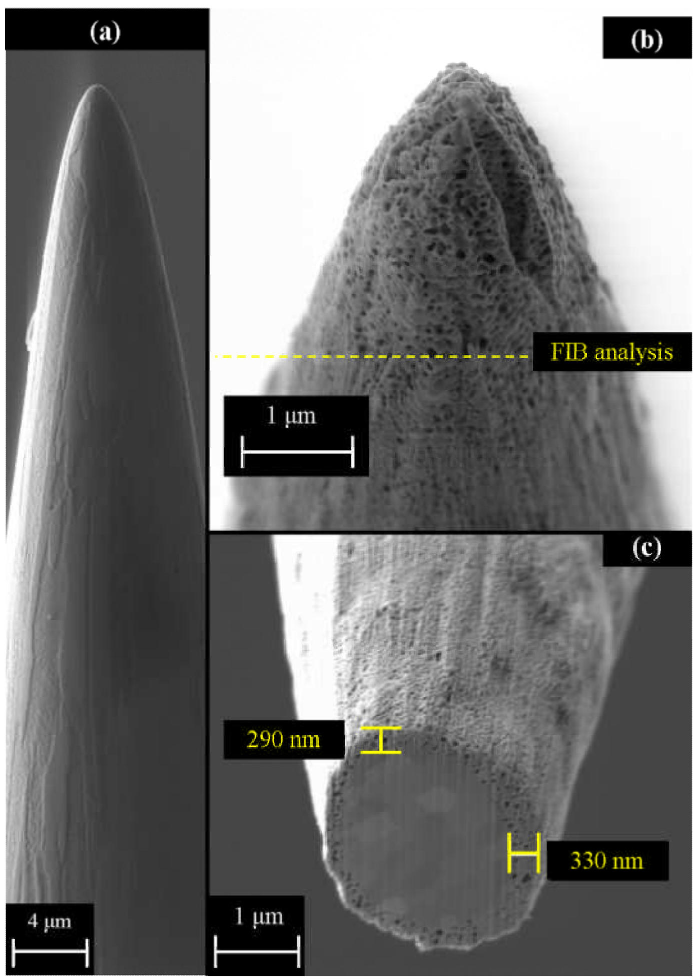

Figure 5-22: Micrographs showing a W needle tip after (a) etching but before implantation, (b) SEM and (c) FIB analysis for implantation to $3x10^{18}$ He^+/cm^2 at 700 °C. Specimen implanted in the SIGFE prototype ion gun facility.

After implantation of the electropolished W needle to a fluence of $1.3x10^{19}$ He^{+}/cm^{2} at a temperature of 1000 °C, drastic surface morphology changes were observed. SEM analysis presented in Figure 5-23(a) shows a growth in the scale of the surface morphology. Protrusions at the tip of the needle are on the order of microns and appear to have resulted in an “unraveling” of the extruded W grains which come together at the tip of these W needles. Within the UW IEC group, this micrograph has been dubbed the “Chihuly Needle” because of its resemblance to the Dale Chihuly glass art® illustrated in Figure 5-23(b). [34]

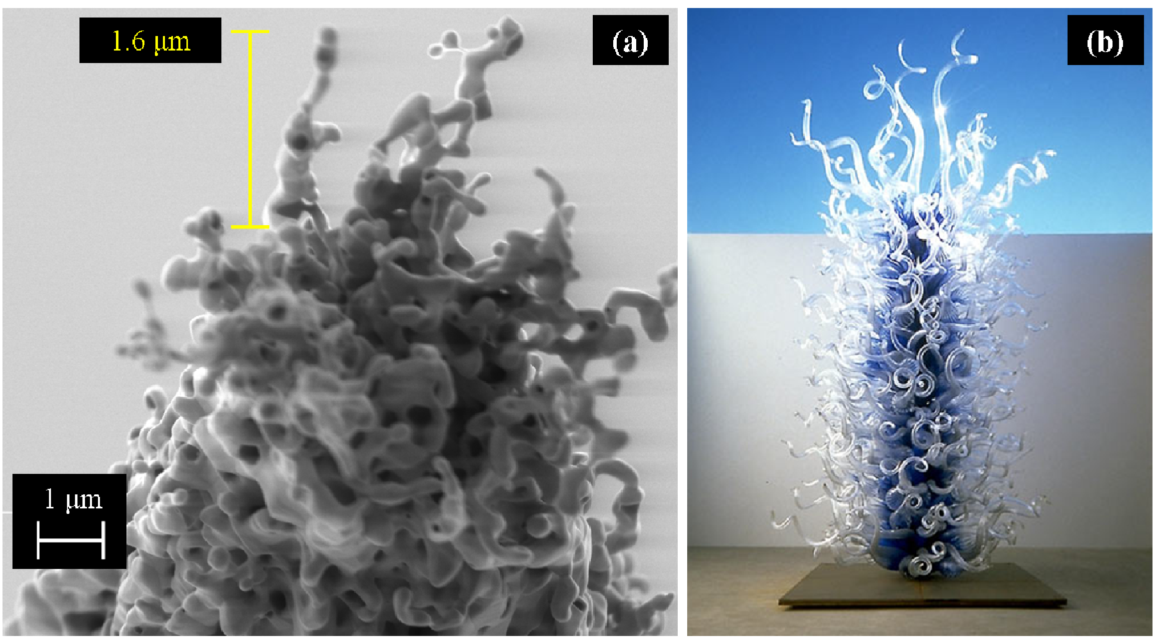

Figure 5-23: (a) Shows the “Chihuly” morphology on the tip of a W needle implanted to $1.3x10^{19}$ He^{+}/cm^{2} at a temperature of 1000 °C, and (b) a photograph of Dale Chihuly’s glass art from which the W needle morphology takes its name. [34] Ion energy was 100 keV. Implanted in the SIGFE prototype ion gun facility.

FIB analysis was performed on the W needle illustrated in Figure 5-24 and shows a drastic increase in the penetration depth of the sub-surface semi-porous layer from a maximum of 330 nm after implantation to $3x10^{18}$ He^{+}/cm^{2} and 700 °C and to 1,600 nm after implantation to $1.3x10^{19}$ He^{+}/cm^{2} and 1000 °C. From comparison of micrographs for flat PCW (Figure 5-13), W-coated CCV (Figure 5-10) and W needles (Figure 5-22), it does not appear that the geometry of the surface has the ability to abate the surface morphology changes induced by helium bombardment.

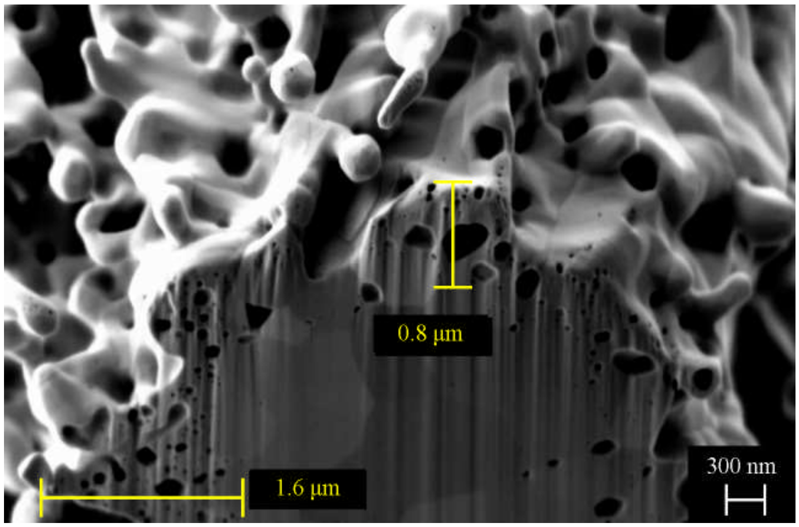

Figure 5-24: FIB analysis of the "Chihuly Needle" after implantation in the SIGFE prototype ion gun facility to a fluence of 1.3×10^{19} He^+/cm^2 at 1000 °C. Helium ion energy was 100 keV.

5.2. Implantation results from the Materials Irradiation Experiment (MITE-E)

The Materials Irradiation Experiment (MITE-E) was used to irradiate thirteen PCW specimens at a range of fluences and temperatures. All experiments on PCW carried out in the MITE-E were performed with $^4He^+$ at 30 keV. Table 5-11 lists the implant temperatures and average helium fluences to which each of the specimens were exposed. In addition to Table 5-11, Figure 5-25 gives a graphical representation of the parameter space (in helium fluence and temperature) which was explored for PCW using the MITE-E (filled red circles). Also included in Figure 5-25 are all of the previous implantations performed on PCW within the UW IEC laboratory using the devices HOMER and HELIOS in steady-state operation. These results can be found in the following open literature sources [17,18]. The examined range of the average fluence scan spanned from $6x10^{16}$ He^+/cm^2 to $6x10^{18}$ He^+/cm^2 at an implantation temperature of 900 °C. The specimens implanted as part of the temperature scan were irradiated at a fixed average fluence over the specimen of $5x10^{18}$ He^+/cm^2 and temperatures ranging from 500 – 900 °C.

	Sample	Fluence, He^+/cm^2	Temperature, °C
Fluence Scan	P33	$6x10^{16}$	900
	P28	10^{17}	900
	P32	$3x10^{17}$	900
	P31	$6x10^{17}$	900
	P29	10^{18}	900
	P30	$3x10^{18}$	900
	P27	$6x10^{18}$	900
Temperature Scan	P24	$5x10^{18}$	500
	P23	$5x10^{18}$	600
	P25	$5x10^{18}$	700
	P26	$5x10^{18}$	800
	P22	$5x10^{18}$	900
	P2 (Radel)*	$5x10^{18}$	900

Table 5-11: Summary of implantations performed in the MITE-E using 30 keV He^+. *Specimen P2, originally implanted using HOMER [21] was electropolished to remove existing surface damage and helium and re-implanted with helium using the MITE-E to for comparison between the two apparatus.

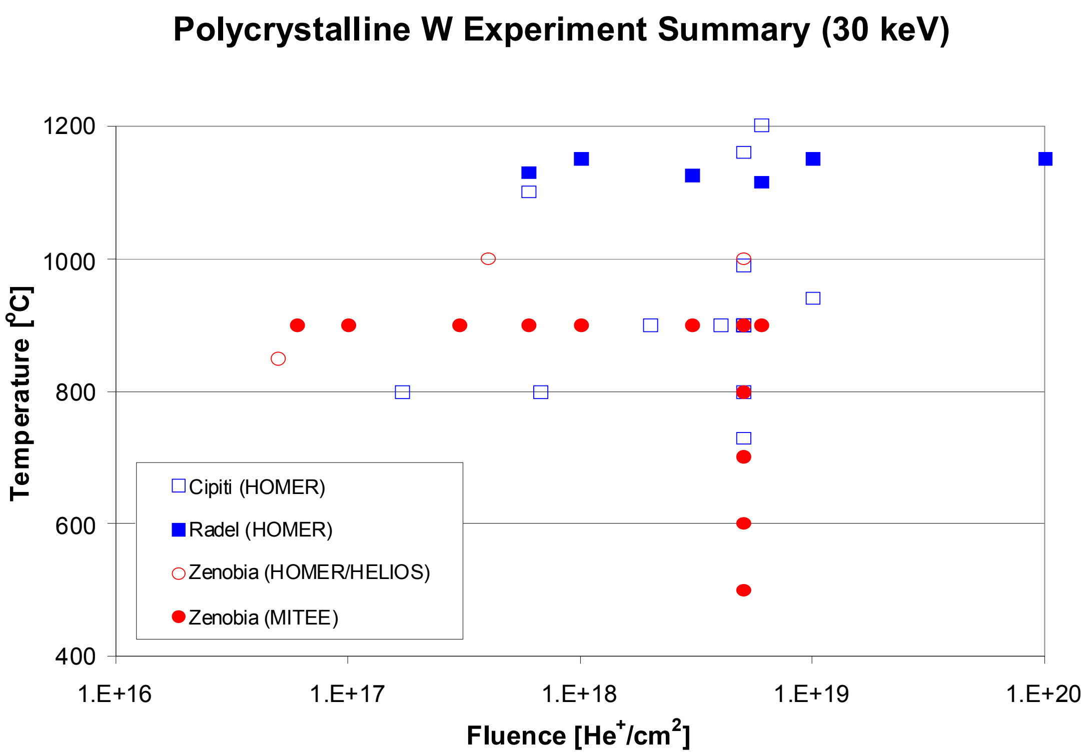

Figure 5-25: Experimental summary of PCW implanted with He^+ at 30 keV. Each of the three UW IEC devices is represented. The filled red circles represent the primary experiments in MITE-E to date

Specimens were manufactured by Alfa Aesar®, but acquired from Dr. Lance Snead after they were cut and mechanically polished at ORNL. Approximate specimen dimensions were 10x10x1 mm^3. The final sample preparation before implantation was an electropolish using a 1% KOH aqueous solution in distilled water. During implantation the background helium neutral pressure was ~200 μTorr. Prior to irradiation with helium ions, the specimens were annealed for 15 minutes using the infrared heating laser (described in Chapter 4 of this thesis) to outgas any residual hydrogen adsorbed by the specimen from the electropolishing procedure. The annealing temperature was set at the designated implantation temperature (e.g. a sample that was implanted to an average fluence of 5×10^{18} He^+/cm^2 at 700 °C was held at 700 °C for 15 minutes before ions were implanted). For all implanted specimens, the average total current during implantation was 200±10 μA. To calculate the ion current, one must adjust for the secondary emission coefficient of 30 keV He^+ on flat polished W (1.8, [35]). This yields an average ion current of 75±3 μA and an average ion flux to the PCW specimen of 9.1x10^{14} He^+/cm^2-s (for an implanted sample area of 0.5 cm^2).

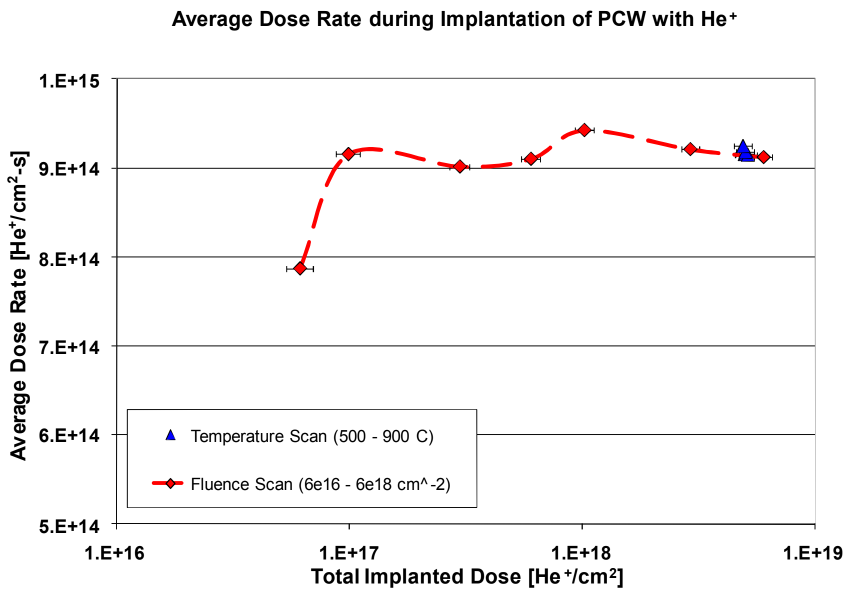

Figure 5-26: Dose rate for PCW implanted in the MITE-E. It is assumed that the ion beam is uniformly distributed over 0.5 cm^2 on the specimen surface. All implanted specimens are included with the exception of specimen P2(Radel).

5.2.1. Determination of local implant fluence on PCW – MITE-E

Each specimen was photographed after implantation for visual inspection. These photographs are summarized in Figure 5-27. After specimens were implanted in the MITE-E, it was observed that the current density of the ion beam was not completely uniform over the ~8 mm beam size. This final beam size is set by a final beam collimation aperture called the diaphragm which sits about 3 cm in front of the specimen surface. The details of this collimation system are discussed in Chapter 4.

Inspection of the specimens implanted at 800 °C and 900 °C in Figure 5-27(b) show that the beam is effectively collimated by this diaphragm to a diameter of ~8mm.

This is evidenced by the perfectly circular ring that appears slightly darkened from the outer corners of the PCW specimens. An ovular shaped region approximately 6 mm in diameter, which is much darker than the outer implanted ring, is also observed in Figure 5-27(a) for all specimens implanted to average fluences ≥3x10^{17} He^{+}/cm^{2} as well as for all specimens that were part of the temperature scan and implanted to an average fluence of 5x10^{18} He^{+}/cm^{2} (Figure 5-27(b)). Typically, rough surfaces will reflect light more poorly and appear darker. In this case, it is assumed that darker regions indicated regions that have been implanted to higher local helium fluence than lighter regions. This increased roughening of the surface can result in a decrease in the reflective properties of the W specimens [36]. Tungsten reflectivity measurements were not performed.

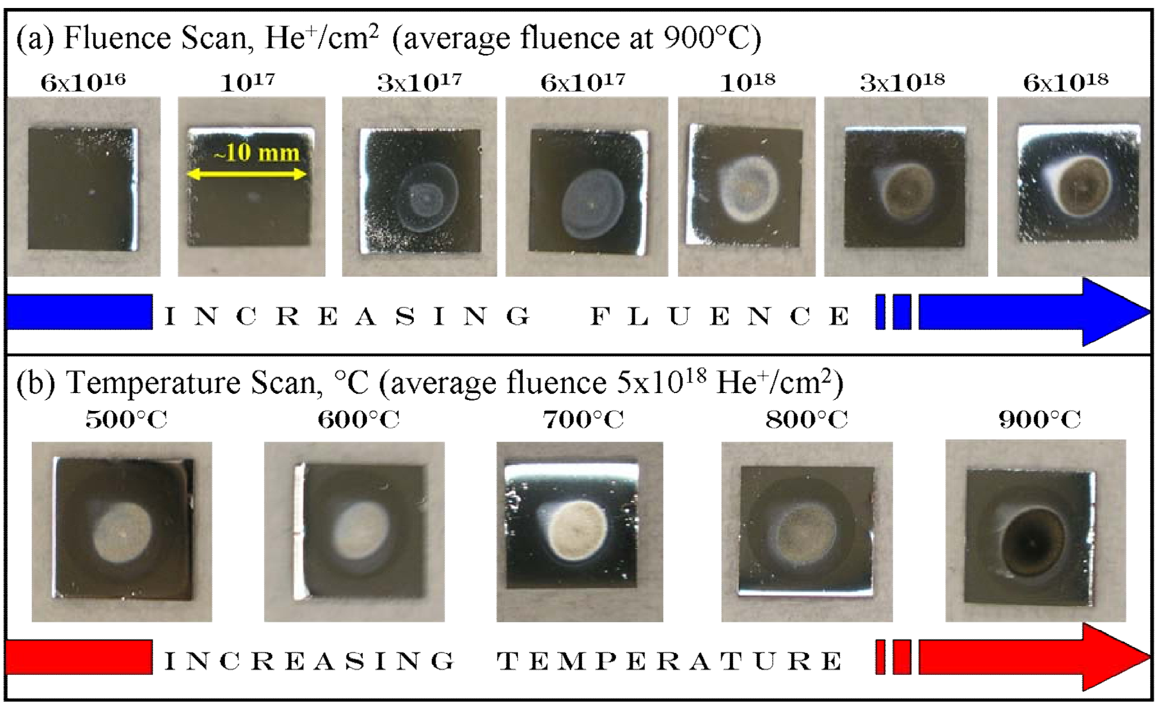

Figure 5-27: Summary of photographs taken on PCW after helium implantation in the MITE-E. In (a) the fluences listed are averaged over the total 0.5 cm^{2} flux area for an implantation temperature of 900 °C and in (b) the average fluence over the total 0.5 cm^{2} flux area was held constant at 5x10^{18} He^{+}/cm^{2} for temperatures between 500 – 900 °C.

From Figure 5-27(a) it can be seen that as the average implanted helium fluence increases, the 5-6 mm wide central irradiated region becomes more uniform and defined. At the lowest average fluences of $6\text{x}10^{16}$ He^{+}/cm^{2} and 10^{17} He^{+}/cm^{2} it is possible to see the onset of visual surface modification from the ion beam, but the total extent of the central irradiated region has not yet been marked on the specimen surface (Figure 5-27(b)). For the temperature scan shown in Figure 5-27(b), the total average fluence implanted was held constant at $5\text{x}10^{18}$ He^{+}/cm^{2}, and implantation temperature was varied. If one compares the specimens implanted at 500 °C and 900° C, a clear darkening of the central irradiated region is evident. This contrast in reflective properties of the W surface is thought to be caused by a difference in the characteristic surface morphology change of the W under He^{+} implantation at these two temperatures. Analysis of the surface morphology change on the W specimens is presented later in this section.

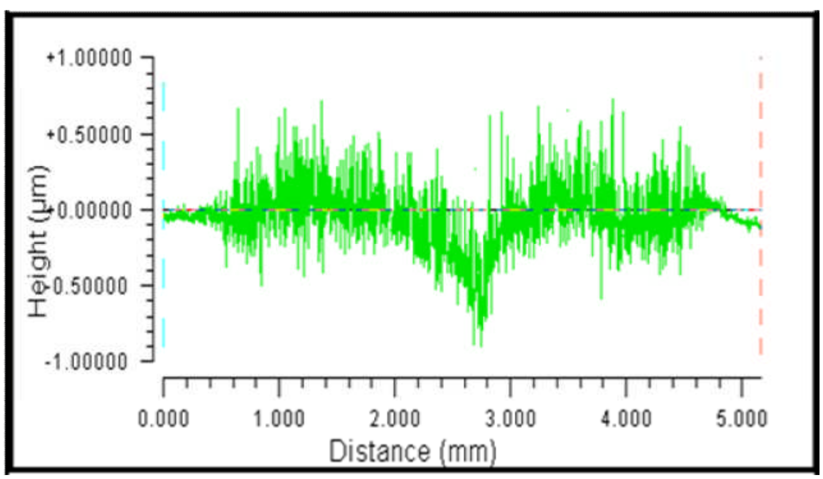

Figure 5-28: Surface roughness profile of a PCW specimen implanted in the MITE-E to an average fluence of $3\text{x}10^{18}$ He^{+}/cm^{2} at 900°C (Figure 5-27(a)), confirming an increased current density at the center point of the MITE-E ion beam. The center of the irradiated region for this specimen is shown at a position of 2.8 mm in the plot.

Samples shown in Figure 5-27, which were implanted to high average fluences, also reveal a small point at the center of the primary irradiated region. Examination of these points on each of the specimens, using an optical profilometer, reveals that this center point is a region of increased current density within the ion beam, even from that of the central irradiated region. Taking the average of the profilometer measurements on the PCW specimens, this spot was observed to have an average size of ~0.7 mm (Figure 5-28). It is believed that the increased current density of the beam at this point results in increased sputtering and erosion on the W surface from the incident He^+, and that this is responsible for the vertical dip at the center of the primary irradiated region. The data shown in Figure 5-28 also confirms that the profile of the beam's current density is not flat; rather, it is peaked in the central 5-6 mm of the beam and falls off greatly between 6 and 8 mm.

Due to the discovery that the current density profile of the ion beam is not flat, it is necessary to redefine the helium fluence measurements reported for the PCW specimens. The fluence parameters listed in Table 5-11 and Figure 5-25 were derived by summing up the total charge collected by the sample, while under bombardment with He^+, and dividing it by the total flux area of the PCW specimens (8 mm diameter, or 0.5 cm^2). For the remainder of this report the fluence values listed in Table 5-11 and Figure 5-25 will be referred to as the "average" implanted helium fluence.

In reality, the implanted fluence within the central irradiated region is higher than the average fluence, while the implanted local fluence outside of the central irradiated region is lower than average fluence. Using measurements from the profilometer and visual inspection of the specimens, the samples were broken up into five different local regions based on the radial distance from the center of the irradiated region. It is important to note that the geographic center of the specimen does not necessarily coincide with the center of the irradiated region. This is due to variations in process by which specimens were mounted for implantation in the MITE-E. Therefore, the "center" is assumed to be the radiation center throughout the remainder of this thesis.

As previously mentioned, the irradiated area of the specimen (0.5 cm^2) was broken into five different regions which are referred to as "position 0", "position 1", etcetera up to "position 4" (position 0 is at the radiation center of the specimen). From the designated boundaries of these local positions, the flux area (in cm^2) was calculated for five annular regions. For example, "position 1" would be classified as an annulus swept out by the two radial points (0.35 mm – 1.5 mm), as this ~1 mm line segment is rotated around the center of the irradiated region. The visualization of this sectioning is presented in Figure 5-29. For each of these local positions, the average helium fluence for these specimens (Table 5-11) was multiplied by a fluence factor which corresponded to one of the five local positions. The fluence factors were adjusted until the sum, over all five local positions, of the product of the "local" helium fluence (φ_L, in units of He^+/cm^2) and the local annular flux area (in units of cm^2) equaled the total charge implanted. The local fluences which resulted from this calculation are illustrated in Figure 5-29 for a PCW specimen implanted with He^+ to an average fluence of 5×10^{18} He^+/cm^2 at 900 °C.

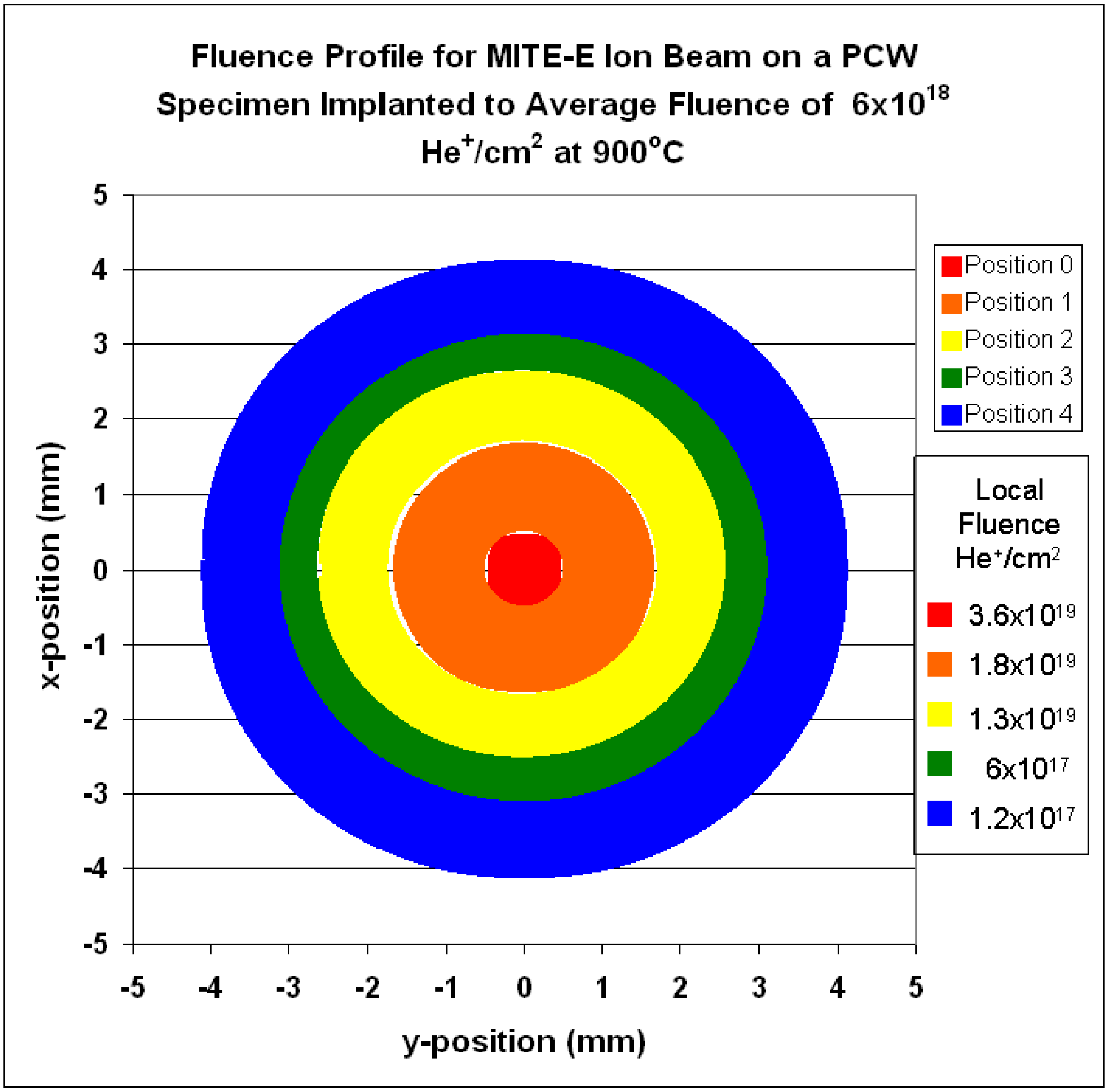

Figure 5-29: Illustration of the position dependent fluence profile for the ion beam used in the MITE-E. Local fluences are calculated for a PCW specimen implanted with He^{+} to an average fluence of $5x10^{18}$ He^{+}/cm^{2} at 900 °C. Position 0 is taken as the radiation center and local fluences are derived assuming a perfectly shaped annulus. The plot is sized for a 10x10 mm^{2} PCW specimen with a total flux diameter and area of 8 mm and 0.5 cm^{2}, respectively.

Although the variations in the MITE-E's ion beam density profile add uncertainty to the average fluences measured, the total implanted He^{+} for these specimens is well known. Because each specimen was divided into five different positions, each with its own local fluence, SEM and FIB micrographs were taken at a point within each of these five local positions for each specimen implanted. In a few cases, additional positions were analyzed. The advantage of having distinct helium fluences at these different local positions is that a much larger fluence parameter space can be examined, beyond what was initially shown in Table 5-11.

5.2.2. Surface morphology changes on PCW – MITE-E

Prior to helium implantation, SEM analysis was performed on PCW to examine the surface and verify the success of the electropolishing technique in revealing the grains. As stated earlier, SEM and FIB analysis was performed on each implanted PCW specimen. For comparison with the results of helium implantation, Figure 5-30 shows an unirradiated PCW sample.

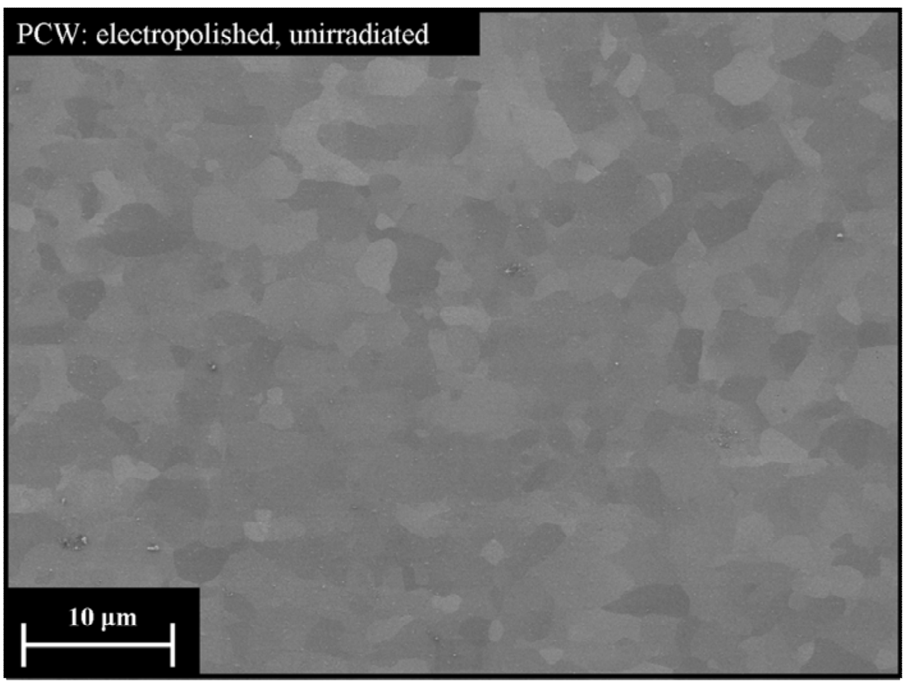

Figure 5-30: SEM micrograph of PCW after mechanical polishing and electropolishing, but prior to implantation with helium ions. Note that individual grains are clearly visible with an average size of ~5 µm.

Figure 5-31 shows the results of helium implantation on PCW for specimens implanted to local fluences of 6.3×10^{17} He^+/cm^2 – 1.8×10^{19} He^+/cm^2 at a constant implantation temperature of 900 °C. PCW implanted to 6.3×10^{17} He^+/cm^2 (Figure 5-31(a)) shows very minor pore formation on the surface, and what appears to be an enhanced height variation between grains, possibly due to grain growth at these high temperatures. As the local helium fluence is increased to 1.8 x10^{18} He^+/cm^2 (Figure 5-31(b)), blisters are observed on the surface with approximately half of the blister caps missing. Pores appear uniformly distributed on the surface at a moderate density, but where individual blister caps have been removed, extensive pore formation is also apparent beneath the surface.

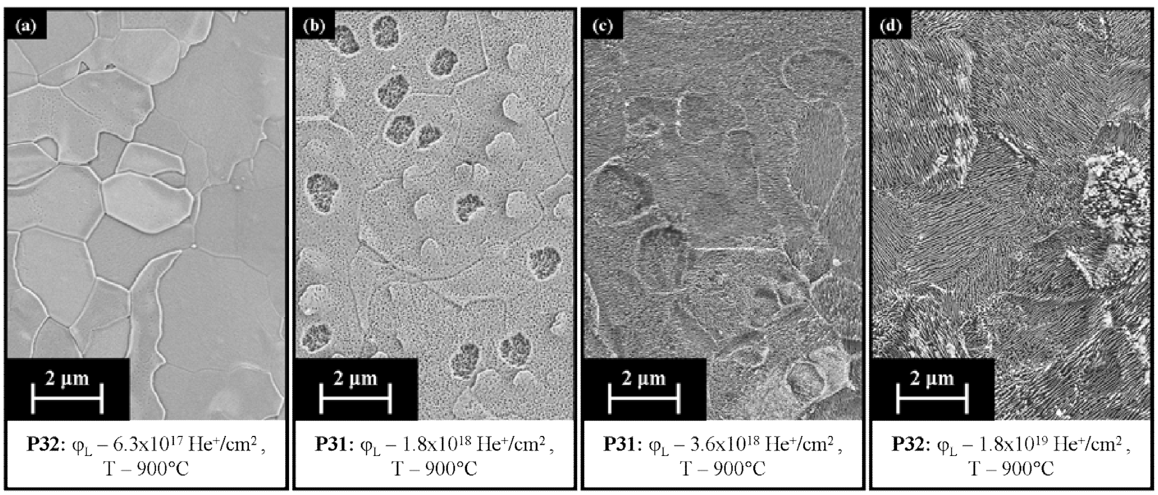

Figure 5-31: SEM micrographs of PCW implanted in the MITE-E at 900 °C to local He^+ fluences (φ_L) of (a) 6.3x10^{17} cm^{-2}, (b) 1.8x10^{18} cm^{-2}, (c) 3.6x10^{18} cm^{-2}, and (d) 1.8x10^{19} cm^{-2}.

Doubling the implant fluence to 3.6 x10^{18} He^+/cm^2 (Figure 5-31(b)) reveals the evolution of a “grass-like” surface morphology with micron-sized depressions appearing sporadically on the surface. Presumably, these depressions are craters left over from blisters that were formed at lower fluences but have lost their blister caps, and have sustained further morphology change from He^+ bombardment. At the highest local helium fluence 1.8 x10^{19} He^+/cm^2 (Figure 5-31(d)), extensive surface damage and the W “grass” appears to be the dominant morphology. Few, if any, blister remnants remain. The orientation of the W grass surface structure varies with individual grains. The possible mechanisms responsible for W grass are treated in Chapter 6 of this thesis.

Blister formation appeared somewhat independent of the implantation temperature (Figure 5-32). It was observed that blister densities increased with increasing local implant fluence. For the specimens on which blisters where observed, the average blister density was 0.153 blisters/μm^2, and the maximum blister density measured was 0.285 blisters/μm^2 and occurred at a local implant fluence of ~10^{19} He^+/cm^2 at 800 °C (Figure 5-32(a)). The minimum blister density (0.05 blisters/ μm^2) was observed at a local implant fluence of 5x10^{17} He^+/cm^2 at 800°C (not shown). The average thickness of blister caps was ~160 nm, which is approximately twice as large as the range of 30 keV He^+ in W (~80 nm). At all temperatures (500 – 900 °C), blisters were not observed for local fluences (φ_L) >10^{19} He^+/cm^2. The threshold local helium fluence necessary for blister formation was observed to be ~5x10^{17} He^+/cm^2.

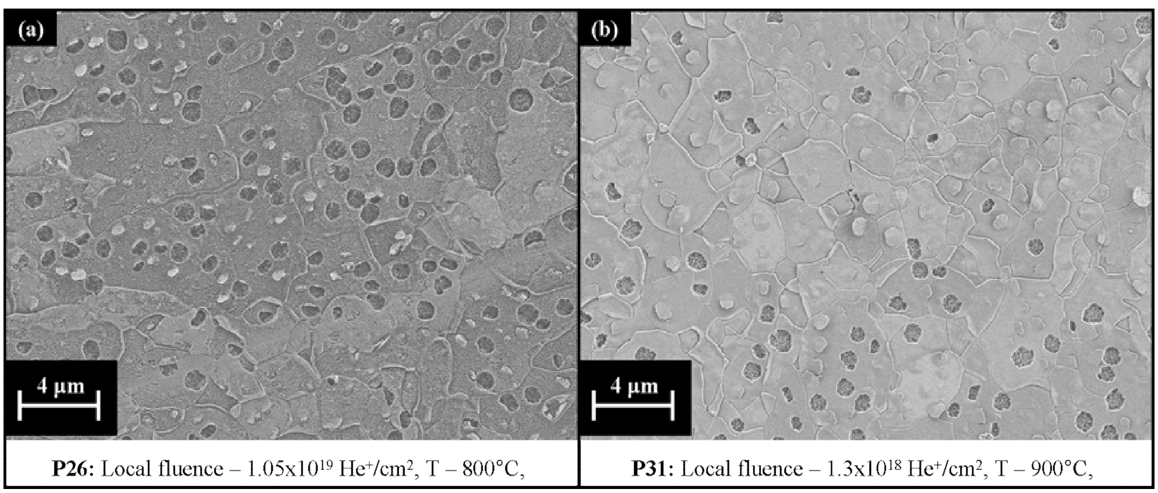

Figure 5-32: SEM micrographs illustrating blister formation on the surface of PCW implanted in the MITE-E with 30 keV He^+ to local fluences of (a) ~10^{19} He^+/cm^2 at 800 °C (blister density – 0.285 μm^{-2}), and (b) 1.3x10^{18} He^+/cm^2 at 900 °C (blister density – 0.224 μm^{-2}).

FIB analysis revealed the presence of a sub-surface semi-porous layer in PCW specimens implanted to local fluences above 9x10^{17} He^+/cm^2 at implant temperatures of 800 and 900 °C. Pores were not observed in a sub-surface layer below 800 °C, but very minor visible pore formation was observed on the surface of PCW even at the lowest implantation temperature of 500 °C. Figure 5-33 shows the FIB analysis for a local fluence scan ranging from 1.8×10^{18} He^{+}/cm^{2} to 3.6×10^{19} He^{+}/cm^{2} at an implantation temperature of 900 °C.

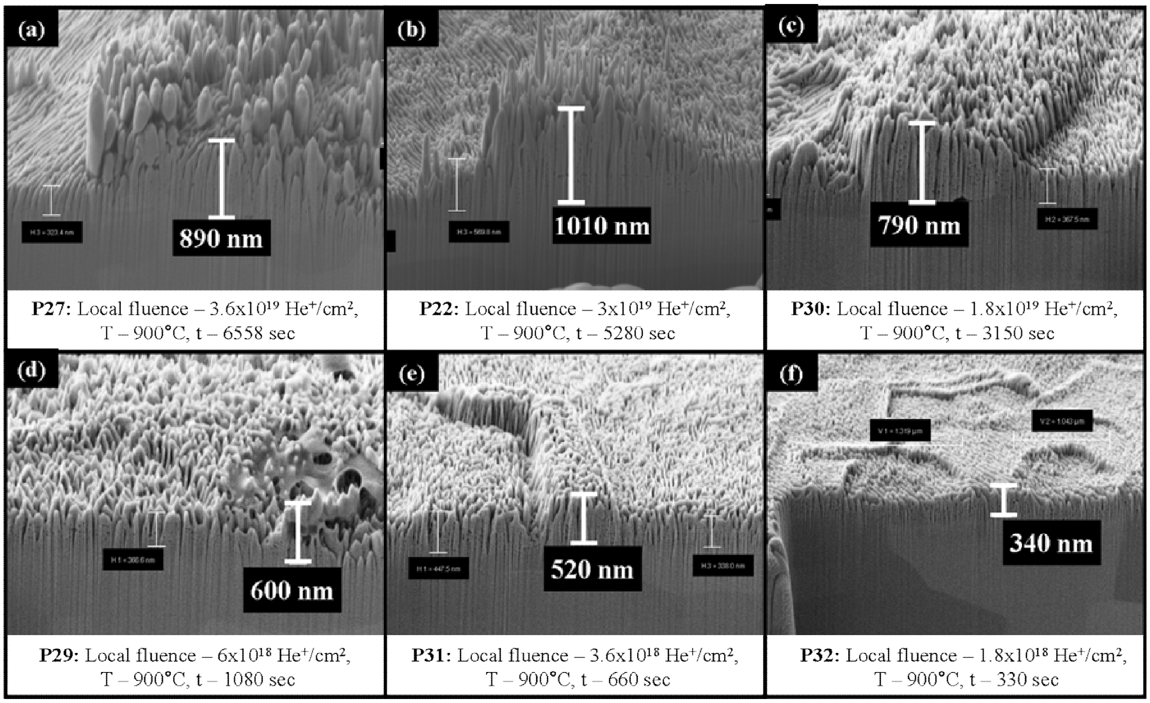

Figure 5-33: FIB micrographs showing the visible sub-surface semi-porous layer depths at 900 °C for PCW at (a) 1.8×10^{18} He^{+}/cm^{2} [340 nm] (b) 3.6×10^{18} He^{+}/cm^{2} [510 nm], (c) 6×10^{18} He^{+}/cm^{2} [600 nm], (d) 1.8×10^{19} He^{+}/cm^{2} [790 nm], (e) 3×10^{19} He^{+}/cm^{2} [1010 nm], and (f) 3.6×10^{19} He^{+}/cm^{2} [890 nm]. The time under helium implantation is also shown for each specimen. Specimens were implanted in the MITE-E.

As inspection of Figure 5-33 reveals, the height of the surface feature under examination and depth of the semi-porous layer can vary on a grain-by-grain basis. For this reason, the maximum measured semi-porous layer depth was chosen to be consistent between different samples. The depth of this semi-porous layer increased with increased local He fluence and ranged from 340 nm – 1010 nm for implant fluences of 1.8×10^{18} He^{+}/cm^{2} (Figure 5-33(f)) and 3×10^{19} He^{+}/cm^{2} (Figure 5-33(b)), respectively. At the highest implant fluence shown (Figure 5-33(a)), the depth of penetration of these pores into the sub-surface of the PCW is more than 10x greater than the predicted range of 30 keV He^+ in W at room temperature. At the examined implantation temperatures, helium bubbles are expected to diffuse <10 nm once they have coalesced in the W sub-surface. For specimens implanted at temperatures ≥800 °C, Figure 5-34 plots the depth of the sub-surface, semi-porous layer against the local implant fluence for every specimen where these layers were observed. Figure 5-34 shows that at both 800 and 900 °C, the growth of this layer is strongly linked to the local implanted fluence. The growth rate of this layer also decreases as implantation temperature is decreased. These data suggest that the depth of these sub-surface, semi-porous layers is tied to the diffusion of helium at the implantation temperature.

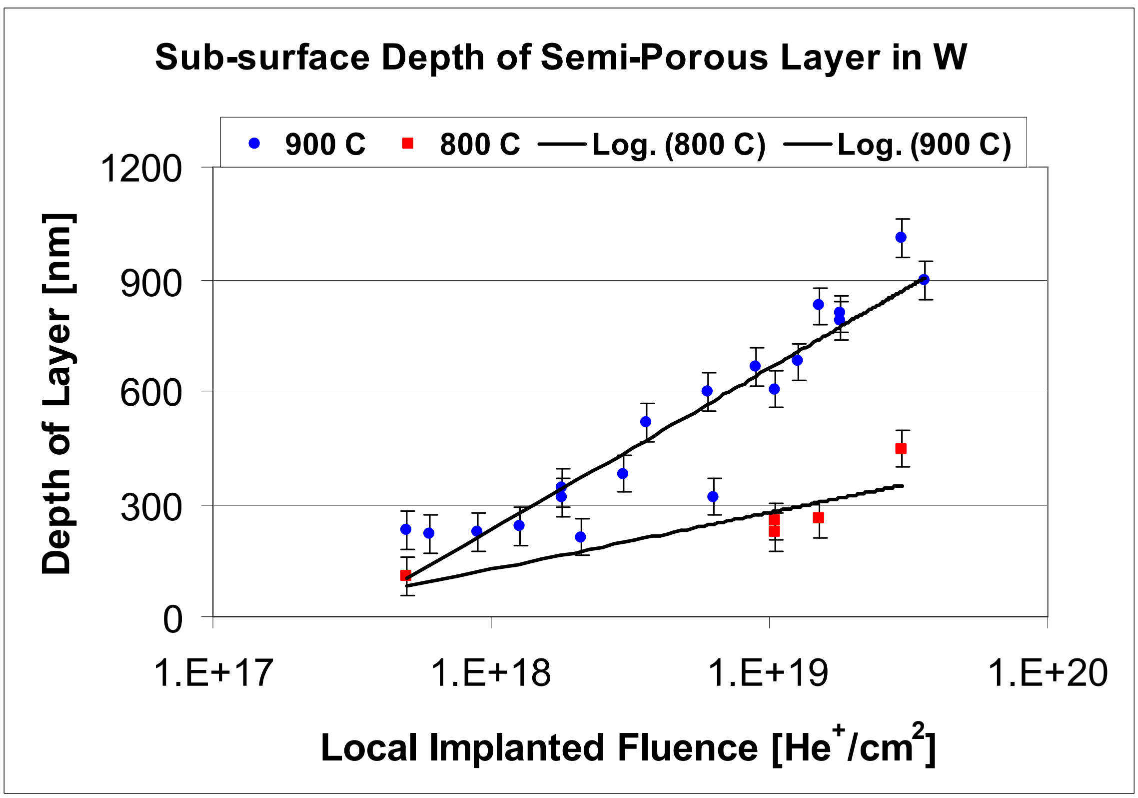

Figure 5-34: The depth of the sub-surface, semi-porous layer in PCW resulting from He^+ implantation in the MITE-E is plotted against the local implant fluence for each specimen and local position where the layer was observed via FIB analysis. Only specimens implanted at temperatures ≥800 °C are examined.

Each of the micrographs in Figure 5-33 represents the depth of this semi-porous layer at the very center of the irradiated region (local "position 0") for PCW specimens which were implanted to six different average helium fluences at 900 °C. Because the helium ion current on each of these specimens was held constant at ~200 μA, the implantation times decreased as the average He fluence was lowered. If one plots the square root of the total irradiation time ($t^{1/2}$) for each of these specimens versus the maximum porous layer depth at center of the implanted region, the growth of this layer can be approximated by a one-dimensional form of Fick's law (Figure 5-35). This growth is described by the following relationship:

$$d = (2Dt)^{\frac{1}{2}}, \qquad \text{Equation 5-3}$$

where d is the depth of the semi-porous region, D is the effective diffusion coefficient of the He in W, and t is the implantation time for each of the six W specimens. The fitted line shown in Figure 5-35 corresponds to a diffusional growth of this semi-porous layer which is characterized by an effective diffusion coefficient of He in W of $D_{900°C} = 1.3 \pm 0.2 \times 10^{-12}$ cm^2/s. Inputting this coefficient into the standard diffusion formula results in a thermal activation energy of 2.1 eV for He diffusion in W. While it cannot be conclusively stated that this layer growth is completely characterized by this one-dimensional diffusion process, it does lend one possible explanation for the decreased semi-porous layer depths in W at 800 °C from layer depths observed at 900 °C in W (Figure 5-34).

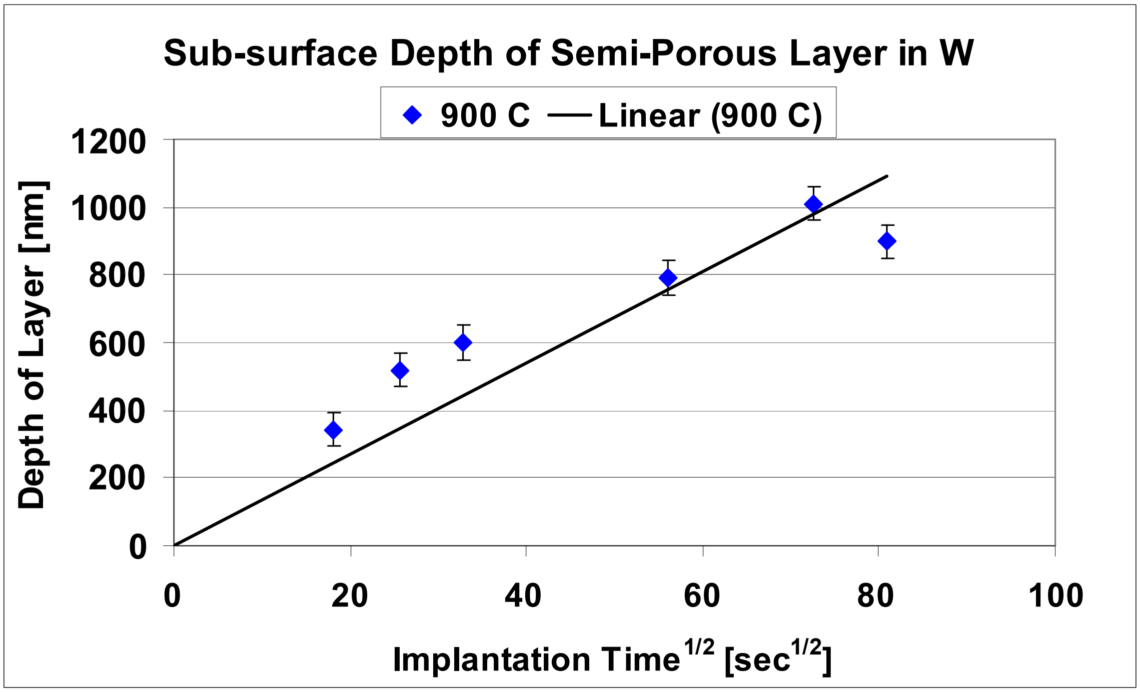

Figure 5-35: Semi-porous depths measured by FIB analysis of the specimens shown in Figure 5-33, plotted against the square root of the irradiation time in the MITE-E. Data are shown for temperature a temperature of 900 °C. The straight line corresponds to an effective diffusion coefficient of (1.3±0.2)x10^{-12} cm^2/s (refer to text).

The surface morphology response occurring on helium implanted PCW at 900 °C is broken up into seven different features and summarized in Figure 5-36. The plot assumes the same positional variation in the ion beam current density profile as enumerated in Figure 5-29, and the local fluences are derived from the aforementioned fluence factors. The radial positions refer to each of the five local positions where the fluence was calculated and corresponding SEM and FIB micrographs were taken to diagnose the surface morphology change.

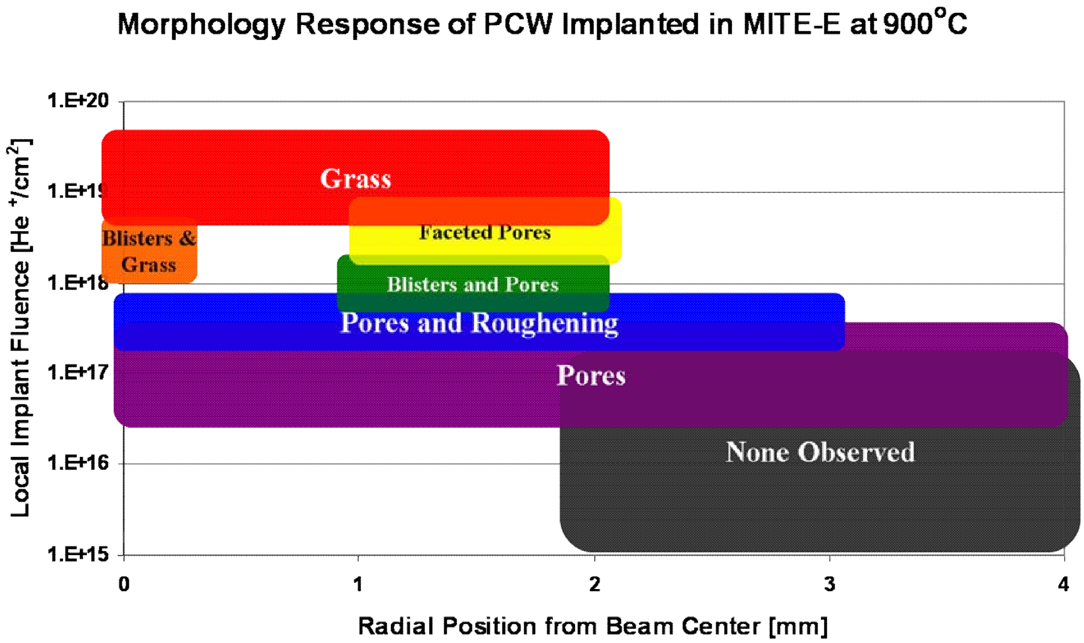

Figure 5-36: Morphology summary of implantation experiments in the MITE-E from local fluence and temperature scan data. The above named morphologies are briefly defined: (1)"grass" – a "combed" surface structure, whose orientation appears dependent on the crystallographic orientation of individual grains; (2) "blisters and grass" – the same structure as (1), but with the addition of circular depressions which appear to be the remnants of blisters; (3) "faceted pores" – the W surface has sustained pore formation in which the size and shape of the pores varies with individual grains, and is dependent on crystallographic orientation, (4) "blisters and pores" – classic blisters caps are raised from the surface or completely exfoliated, and the surface, sub-surface, and blister caps are all reveal visible pores; (5) "pores and roughening" – visible pore formation is observed in conjunction with texturing of grains, again dependent on crystallographic orientation; (6) "pores" –visible pores are formed; and (7) "none observed" – no surface morphology change is evident between pre- and post-implanted specimens.

For specimens implanted to an average fluence of $5x10^{18}$ He^+/cm^2, a temperature scan was performed between 500 and 900 °C. The SEM images in Figure 5-37 show the results of this temperature scan up to 800 °C. At an implantation temperature of 500 °C the surface has sustained extensive "pitting" (Figure 5-37(a)). This pitting on the surface of the PCW appears to be random. No trends in the size or shape of the surface structures on pitted samples were observed, but samples revealed that certain grains have sustained less erosion than others. For the specimen implanted to $3x10^{19}$ He^+/cm^2 at 600 °C, a similar "pitting" effect is observed as well as what might be the remnants of blisters that have had their caps removed after substantial He^+ irradiation (Figure 5-37(b)). As the temperature is increased to 700 °C, SEM analysis reveals that a combination of both the "pitted" and "grass" morphologies exist on the surface of the PCW (Figure 5-37(c)). Furthermore, several regions, which look like small mountain ranges, were observed on the surface and are made up of flakes of eroded W. The implantation temperature of 700 °C seems to be a transition temperature between the "pitting" morphology at lower temperatures and the "grass" morphology discussed earlier at 900 °C. At implantation temperatures of 800 °C, the highly orientated "grass" morphology reappears.

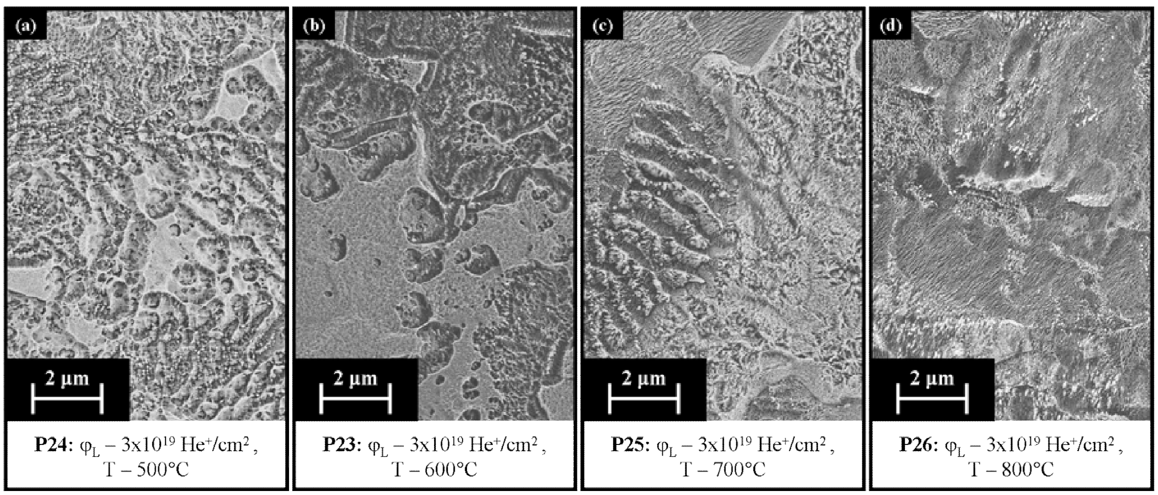

Figure 5-37 SEM micrographs of PCW implanted in the MITE-E to local He^+ fluence $3x10^{19}$ cm^{-2} at (a) 500 °C, (b) 600 °C, (c) 700 °C, and (d) 800 °C.

One difficulty in examining these specimens was the random nature of the morphology change. FIB analysis did not reveal any discernable trends as the local implant fluence increases, but in every specimen examined, the height variation on the W surface was substantially greater than the range of 30 keV He^+. For specimens implanted at a local fluence of $3x10^{19}$ He^+/cm^2 at temperatures of 700 °C or lower, FIB analysis shows maximum height variations of ~0.5 µm. A more detailed discussion of the "pitting" morphology and the mechanisms by which it is formed is given in Chapter 6 of this thesis.

5.2.3. Erosion of PCW from He$^+$ bombardment – MITE-E

PCW specimens implanted in the MITE-E were weighed on a micro-balance before and after implantation with helium ions. At 900 °C, specimens with an average fluence $\geq 10^{18}$ He$^+$/cm^2 exhibited statistically significant mass loss (Figure 5-38). The maximum mass loss for the PCW tungsten specimens in the fluence scan at 900 °C was 275±51 μg at an average fluence of 6x10^{18} He$^+$/cm^2. Above an average implanted fluence of 10^{18} He$^+$/cm^2, the mass loss rate was observed to increase rapidly with increased fluence. The mass losses predicted, if purely physical sputtering is assumed, are much less than the actual mass lost on the PCW specimens as indicated by the red curve in Figure 5-38. The sputtering yield was taken from [37] and assumes that ions are normally incident on the surface of an amorphous W target.

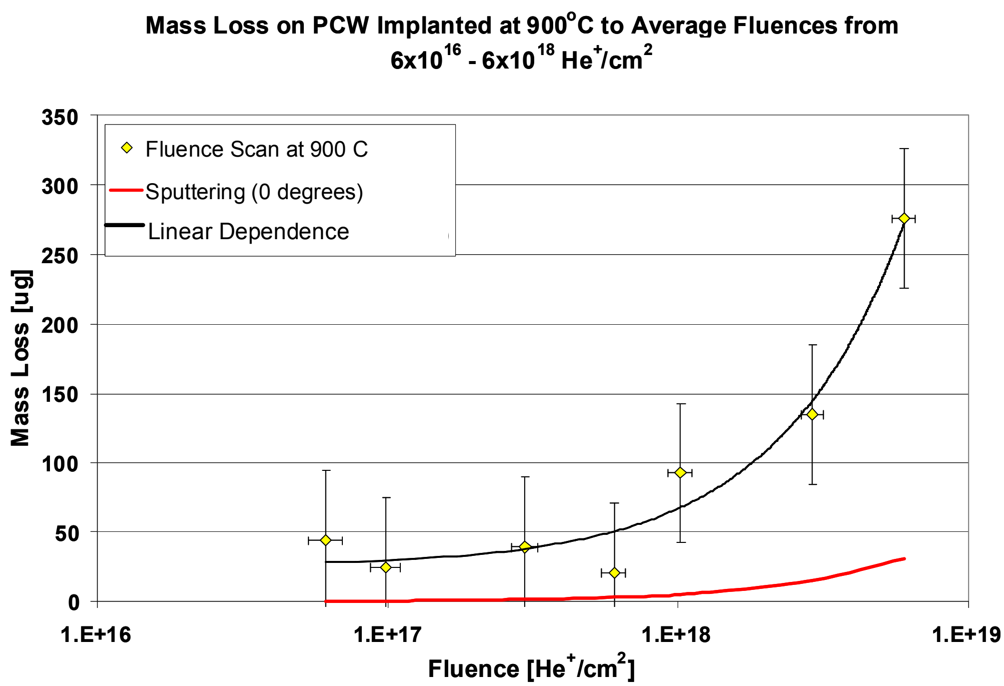

Figure 5-38: Measured mass loss on PCW after irradiation in the MITE-E with He$^+$ to total average fluences between 6x10^{16} He$^+$/cm^2 and 6x10^{18} He$^+$/cm^2 at 900 °C. The red solid line is the predicted sputtering yield for an equivalent average implanted fluence. [37] The black solid curve would represent a linear dependence on fluence

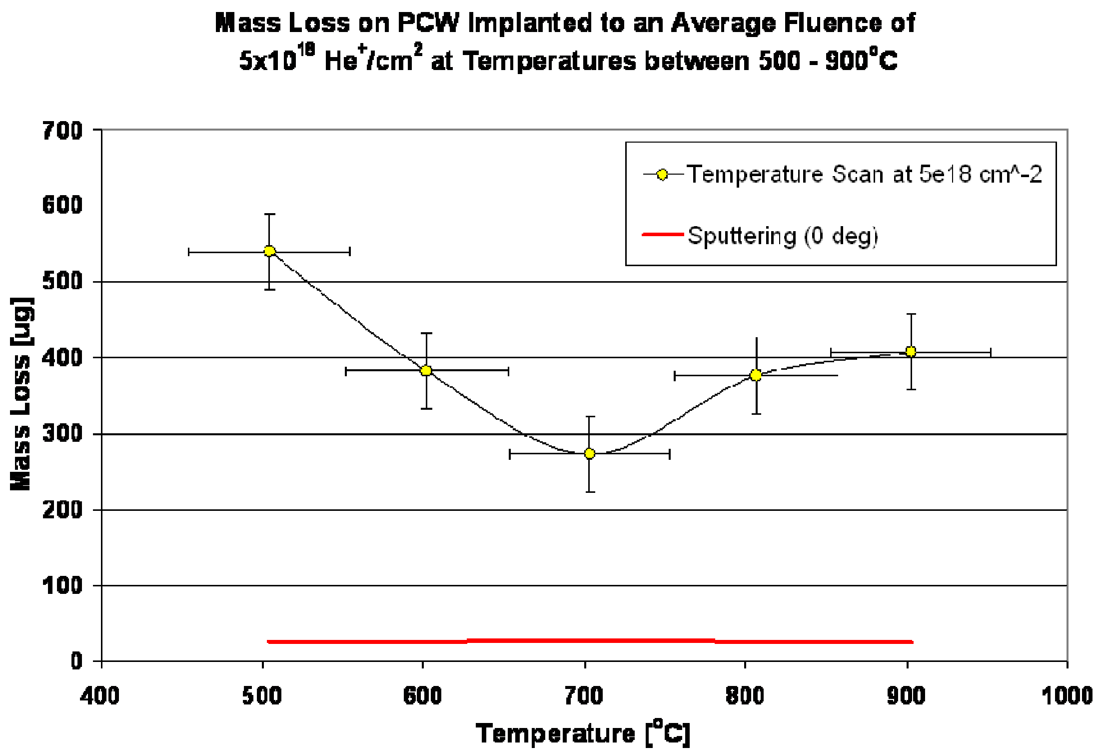

Figure 5-39: Measured mass loss on PCW after irradiation in the MITE-E with He^+ to total average fluence of $5x10^{18}$ He^+/cm^2 for temperatures between 500°C and 900°C. The red solid line is the predicted sputtering yield for an equivalent average implanted fluence [37]

Mass loss measurements were also performed on PCW specimens that were part of the temperature scan at a constant average fluence of $5x10^{18}$ He^+/cm^2 (Figure 5-39). Each specimen sustained statistically significant mass loss, which were much greater than that predicted by pure physical sputtering processes for ions incident normal to the specimen surface. The minimum observed mass loss was 273±50 μg (700 °C) and the maximum was 540±50 μg (500 °C). One hypothesis for the "dip" in the mass loss at an implantation temperature of 700 °C is as follows: at low temperatures, the W is more brittle and the observed "pitting" morphology may be due to large chunks of W being exfoliated from the surface. These W chunks might erode less often than the nano-scale protrusions seen at high temperatures, but are much larger in volume, and therefore, result in more mass loss to the specimen. Conversely, at high temperatures the surface structure is comprised of the "grass" morphology with many nano-scale protrusions from the surface. It is possible these protrusions are frequently exfoliated, but their small volume requires that many more of them must be removed before substantial mass loss occurs. At the intermediate temperature, a balance between these two extremes may exist, resulting in the least mass loss to the PCW specimen.

In [37], the sputtering yields were calculated for an amorphous W target with ions impinging normal to the specimen surface. Since W specimens implanted in the MITE-E were polycrystalline, it may be possible that there is enhanced sputtering of certain crystallographic orientations of individual grains (see Figure 5-31 and Figure 5-37). Moreover, it is possible that this could account for the large difference between the measured mass loss and that predicted by purely physical sputtering for ions bombarding amorphous W at normal incidence. This hypothesis is discussed in Chapter 6 of this report.

As a final point of comparison, one can use Table 5-2 to convert the implanted helium fluence in the MITE-E to reactor operation times in an IFE or MFE system. Incorporating the mass loss data reported in Figure 5-39, for the temperature scan on PCW at an average fluence of $5x10^{18}$ He^{+}/cm^{2}, one can estimate the mass loss to the IFE and MFE using a W first wall armor or W divertor plate. The resulting estimates of mass loss to a fusion reactor system are presented in Table 5-12. It is important to note that the calculation of these numbers require extrapolations to much longer time periods than were simulated in the MITE-E. The ion fluxes used in MITE-E are also not equivalent in quantity or in the method by which ions are implanted in the discussed IFE or MFE systems. These results are intended to give general estimates. The middle column of

Table 5-12 shows that a dry wall, laser driven IFE system, such as the HAPL chamber [1], could lose ~15 kg of W from the first wall armor over a one full power day of continuous operation. The right-hand column of Table 5-12 shows that the divertor plate slated for use in ITER could lose up to 2 kg of W in a full power day of continuous operation (a 400 s pulse length and 1600 s cycle time is assumed). Both of these are unacceptable erosion rates even if the estimates were decreased by a factor of 10. This poses a serious materials challenge for any fusion reactor with W-based plasma facing components.

PCW Specimen, $5x10^{18}$ He^+/cm^2	HAPL (kg/FPD)	ITER (kg/FPD) *[400 s pulse]*
500°C	15±2	2.0±0.3
700°C	7±1	1.0±0.2
900°C	11±2	1.6±0.2

Table 5-12: W mass lost in the reference HAPL chamber in a full power day (FPD) of continuous operation assuming that the erosion rates observed on the PCW implanted in MITE-E can be extrapolated out to a year. The same analysis is performed for the ITER divertor plate for one 400 second pulse length and 1600 s cycle length. Table 5-2 is used for the correlation factor.

5.3. References for Chapter 5

1. Sethian, J.D., et al., (2003) Fusion energy with lasers, direct-drive targets, and dry wall chambers. *Nuclear Fusion*, 42, 1963.

2. J. Perkins, personal communication.

3. Matheny, R.A. et al., (1979) Radiation-damage in silicon carbide and graphite for fusion-reactor 1st wall applications. *Journal of Nuclear Materials*, 83 (2) 313-321.

4. Yamauchi, Y. et al., (2003) Blister formation and erosion due to blister fracture of SiC or Si. *Journal of Nuclear Materials*, 313 and 316, 408-412.

5. Zenobia, S.J. and Kulcinski, G.L., (2006) Effects of He^+ implantation on the surface morphology of SiC," prepared for 17th ANS Topical on Fusion Energy (TOFE). UWFDM 1339.

6. Zenobia, S.J. et al., (2009) High temperature surface effects of He^+ implantation in ICF fusion first wall materials. *Journal of Nuclear Materials*, 389, 213-220.

7. Knowles, T.R., (2006) Tungsten velvet armor for HAPL fusion energy systems. Presented at the 15th High Average Power Laser Program Workshop, August 8, 2006, San Diego, CA.

8. Zenobia, S.J. (2007) Simulation of inert gas effects to fast reactor SCWR fuel cladding and ion implantation of first wall armor materials for fusion reactors. Master's Thesis, University of Wisconsin-Madison.

9. Private communication (2008) Dr. T. Knowles, ESLI Laboratories, Inc.

10. Ekern, R. et al., (1975) Irradiation of graphite cloth at various temperatures with deuterons and helium ions, IEEE 6. Symposium on Engineering Problems of Fusion Research, San Diego, CA November 17, 1975.

11. Thomas, G.J., (1976) Blister He and H implantation of vitreous silica and graphite. *Proceedings of The American Chemical Society Meeting,* Chicago, Illinois, 8/25-26/75.

12. Marques, F.C. et al., (2003) Thermal expansion coefficient of hydrogenated amorphous carbon. *Applied Physics Letters*, 83 (15).

13. Radel, R. F. and Kulcinski, G. L., (2007) Implantation He^+ in candidate fusion first wall materials. *Journal of Nuclear Materials*, 367, 434-439.

14. Gilliam, S.B. et al., (2005) Retention and surface blistering of helium irradiated tungsten as a first wall material, *Journal of Nuclear Materials*,, 347 (3), 289-297.

15. Baldwin, M.J. and Doerner, R.P. (2008) Helium induced nanoscopic morphology on tungsten under fusion relevant plasma conditions, *Nuclear Fusion*, 48, 035001 (5pp).

16. Renk, T.J. (2005) Chamber wall materials response to pulsed ions at power-plant level fluences. *Journal of Nuclear Materials*, 347 (3), 266-288.

17. Cipiti, B.B. (2004). The fusion of advanced fuels to produce medical isotopes using inertial electrostatic confinement. (Doctoral dissertation, University of Wisconsin - Madison).

18. Radel, R. F. (2007). Detection of highly enriched uranium and tungsten surface damage studies using a pulsed inertial electrostatic confinement fusion device (Doctoral dissertation, University of Wisconsin – Madison).

19. Cipiti, B.B. and Kulcinski, G.L. (2005) Helium and deuterium implantation in tungsten at elevated temperatures. *Journal of Nuclear Materials*, 347, 298-306.

20. Radel, R. F. and Kulcinski, G.L., (2005) Implantation of D and He in W-coated refractory carbides. *Fusion Science and Technology*, 47 (4), 1250.

21. Radel, R. F. and Kulcinski, G. L., (2007) Implantation He^+ in candidate fusion first wall materials. *Journal of Nuclear Materials*, 367, 434-439.

22. Radel, R. and Kulcinski, G., (2007) Effects of high temperature pulsed helium implantation on tungsten surface morphology. *Fusion Science and Technology*, 47 (3), 544-548.

23. Hu, Q. et al., (2007) Modeling space-time dependent helium bubble evolution in tungsten armor under IFE conditions. *Fusion Science and Technology*, 52 (3), 544-548.

24. Zenobia, S. J. and Kulcinski, G. L., (2009) Retention and surface pore formation in helium implanted tungsten as a fusion first wall material. *Fus. Sci. and Technology*, 52, 544.

25. Hino, T. et al., (1999) Helium retention in plasma facing materials. *Journal of Nuclear Materials*, 266-269, 538-541.

26. Fu, Z. et al., (2004) Thermal desorption and surface modification of He^+ implanted into tungsten. *Journal of Nuclear Materials,* 329-333, 692-696.

27. Sharafat, S. et al., (2005) Micro-engineered first wall tungsten armor for high average power laser fusion energy systems. *Journal of Nuclear Materials*, 347 (3), 217.

28. Sharafat, S. et al., (2009) A description of stress driven bubble growth of helium implanted tungsten. *Journal of Nuclear Materials*, 389, 203.

29. Barnes, R. and Nelson, R., (1967) Theories of swelling and gas retention in reactor materials in *Radiation Effects* (New York: Gordon and Breach Science Publishers).

30. Bloom, E. et al., (2004) Materials to deliver the promise of fusion power – progress and challenges. *Journal of Nuclear Materials*, 329-333 (3), 12.

31. Zenobia, S. and Kulcinski, G., (2009) Formation and retention of surface pores in helium-implanted nano-grain tungsten for fusion reactor first-wall materials and divertor plates. *Physica Scripta*, T138, 014049.

32. Geshev, P. et al., (2004) Calculation of the electric-field enhancement at nanoparticles of arbitrary shape in close proximity to a metallic surface. *Physical Review B*, 70, 075402.

33. R. Gomer, *Field Emission and Field Ionization*, American Vacuum Society Classics, American Institute of Physics, NY 1993.

34. Image available at www.chihuly.com

35. Large, L.N. (1963) Secondary electron emission from a clean tungsten surface bombarded by various positive ions. *Proc. Phys. Soc.*, **81**, 1101-1103.

36. Tokunaga, K. et al., (2004) Synergistic effects of high heat loading and helium irradiation of tungsten. *Journal of Nuclear Materials*, 329-333, 757-760.

37. ALLADIN Database, International Atomic Energy Agency: Nuclear Data section/Atomic and Molecular Data unit.

CHAPTER 6. DISCUSSION OF RESULTS

6.1. Helium ion damage on fusion materials – early work

Early materials work done in the University of Wisconsin–Madison Inertial Electrostatic Confinement (UW IEC) group grew out of the necessity to increase the lifetime of cathode grids used to study advanced fuel cycles, such as D-D and D-^{3}He in nominal IEC operation modes. [1] The extreme surface modification of these cathode materials, like W and W-Re alloys, under ^{3}He and ^{4}He bombardment was somewhat unexpected; yet, it found a quick application in the High Average Power Laser Program (HAPL) fusion reactor study. [2] All of the preliminary studies reported that W, W alloys, and several engineered W materials would degrade and fail very quickly in any inertial- or magnetic fusion reactor. [3,4,5,6] These results are discussed in Section 2 of this report. Because of the poor response of tungsten at high temperatures to He^+ in 30 keV range (~1000 °C), the UW IEC materials program mounted a campaign to find a suitable material for plasma facing components in fusion reactors. A two-pronged approach was adopted in order to focus in the following areas: 1) implant other materials besides W metallics, such as SiC, carbon, and engineered materials, and 2) expand the parameters of He^+ implantation in W, specifically dose, dose rate, and temperature.

6.1.1. Discussion of results by Zenobia in HOMER and HELIOS

For the materials examined by this author in the devices HOMER and HELIOS, the discussion has been integrated with the results in Chapter 5. These results will be summarized in this chapter. See open literature references providing more thorough discussion of the materials investigated by this author [7,8,9,10]. Also, a more thorough report on the implantation results from the Materials Irradiation Experiment (MITE-E) and their comparison with results in HOMER and HELIOS follows this discussion (Section 6.2). These observations are based on recent experiments, but they also take into account the previous work done on a materials comparison basis. For a discussion and listing of conclusions from the materials implantation experiments performed in the IEC device HOMER by authors Cipiti and Radel refer to Chapter 2 of this thesis.

Below is a summary of the observations of the various materials studied by this author after irradiation with helium ions in the UW IEC devices HOMER and HELIOS.

- A partially masked CVD SiC sample verified that ion flux, not high temperature exposure, causes the observed surface modification of SiC. It was found that SiC responds very poorly to He^+ irradiation in the parameter space studied in this work. Light ions easily penetrate the material, flaking and exfoliating the SiC surface thus resulting in severe damage to specimens. [7,8]
- Carbon-carbon velvet specimens experience severe erosion of the fiber tips and shafts. The pyrolytic carbon coating has been partially or completely eroded away in each of the performed irradiations. [8]
- Tungsten-coated carbon-carbon velvet sustained extensive pore formation over the tungsten coating surface and appears to respond very similarly to PCW. Irradiation temperatures of 1150 °C cause rupturing of the tungsten coating and exposure of the graphite on the carbon fibers. [8]
- Both SCW and PCW exhibited a threshold for pore formation at $\sim 10^{17}$ He^+/cm^2, confirming previous results in HOMER. The SCW showed a slightly higher threshold for pore formation than did PCW. [9]

- The maximum retained helium in both SCW and PCW did not exceed ~$4x10^{17}$ He atoms/cm^2. The saturation of the retained fluence did not hinder the evolution of surface morphology on either tungsten material, as pore formation became extensive above 10^{18} He^+/cm^2. [9]
- For nano-grain W (NGW) and fine-grain W (FGW) engineered materials, the threshold for visible surface pore formation lies between 10^{17} and 10^{18} He^+/cm^2, becoming extensive at 10^{19} cm^{-2}. This is somewhat higher than the same threshold on PCW. In addition, retention characteristics of both NGW and FGW resemble that of PCW above ~10^{17} He^+/cm^2. [10]
- W-Needles did not show increased robustness to He^+ implantation over that of flat PCW, nor do they show any noticeable increase in the threshold fluence necessary for pore formation.

From the results presented in Chapters 2 and 5 of this thesis, it is clear that none of the examined materials weathered the high temperature of the helium implantation to a significantly better degree than any other material. In fact, for the materials examined, pure W still appears to be one of the most robust. For this reason, the primary experimental suite in the MITE-E chose PCW as the implanted material to be studied. This serves as a benchmark against a wealth of previous data in the UW IEC group and elsewhere. Moreover, among the examined materials, W continues to exhibit the most favorable response to light ion (D, He) bombardment. Because of the inability for HOMER and HELIOS to implant to high fluence at very low temperatures, the minimum irradiation temperature was set at 500 °C and incrementally increased to a maximum of 900 °C in steps of 100 °C. Also, due to the inherently high dose in these devices, a fluence scan at high temperature (900 °C) was chosen to expand the knowledge of the threshold fluence for visible pore formation. A graphical summary of the implantation experiments in HOMER, HELIOS and the expanded parameters for the MITE-E are shown in Figure 6-1 which is a repeat of Figure 5–25.

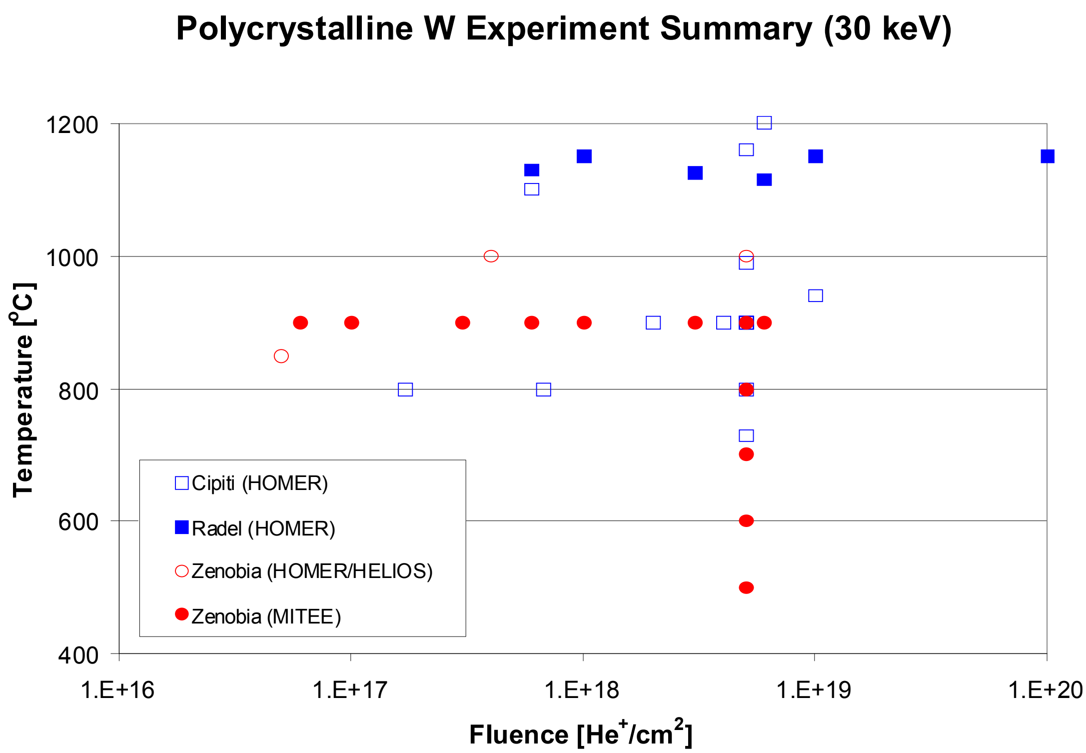

Figure 6-1: Experimental summary of PCW implanted with He^+ at 30 keV. Each of the three UW IEC devices is represented. The filled red circles represent the primary experiments in the MITE-E to date.

6.2. Results of helium implantations in the MITE-E and comparison with previous results in HOMER and HELIOS

6.2.1. PCW implanted with He^+ in the MITE-E

The bulk of this discussion will focus on the morphological analysis of the He^+ implanted PCW in the MITE-E. This analysis is primarily accomplished through scanning electron microscopy (SEM) and focused ion beam (FIB) analysis techniques. As shown in Figure 6-1 the primary experimental suite consisted of a fluence scan at 900 °C and temperature scan at $5x10^{18}$ He^+/cm^2. The results presented in Chapter 5 of this report showed that the number of data points in the fluence parameter space is actually increased beyond the seven points originally intended for both the temperature and fluence scans. This is due to the "local fluence" effect from the ion guns beam density profile, which is discussed in Chapter 4 of this thesis. Although, this was not an intended effect, it has provided a wealth of additional data by which one can characterize the behavior of PCW under energetic helium bombardment. One caveat of the local fluence measurements is that they also have local dose rate variations, since the total local fluences were accumulated over the same time period. HOMER results reported by Radel [5] on pulsed implantation of PCW do not show significant changes in the qualitative characteristics of the surface structure from results on steady-state implantations. This is despite a pulsed implantation dose rate ~100 times greater than the steady-state implantation dose rate. Therefore, one does not expect those factors of 2 or 3 variation in dose rate across a given sample during the MITE-E implantations to cause significant changes in the surface morphology of PCW. The morphology of PCW specimens implanted in the MITE-E can be broken up into three main effects: 1) a "grass-like" surface structure, 2) "pitting", and 3) blisters. All three of these morphologies changes are somewhat different than the "coral" structure developed in HOMER and HELIOS.

Before each of these three effects is discussed it should be noted that the grass structure and blisters were accompanied by an extensive network of helium bubbles visible to SEM and FIB analysis. Minor visible pore formation was also seen on specimens that sustained pitting, but they did not appear to penetrate past the surface of the W. Undoubtedly, all the implanted PCW specimens (including those which sustained pitting) have some population of helium bubbles beneath the surface which are not visible without the aid of a transmission electron microscope. A TEM analysis was not able to be performed in the course of this thesis. Moreover, it is recognized by the author that helium retention and helium bubbles play an integral role in the viability of W as a plasma facing material, especially due to the effects implanted helium can have on the retention of hydrogenic species. [11,12,13] Theories regarding the nucleation, growth, and importance of these bubbles are discussed in Chapter 3 of this thesis; however, the phenomena are not classified as a primary surface structure, but an intrinsic feature of helium implanted W which contributes to the grassy, blistered, or pitted morphology.

Figure 6-2 is a compilation of selected SEM images from the PCW temperature scan, which further classifies the three main surface structures listed above. Because of the local fluence at different geographic locations on the specimens, an effective fluence scan was performed at each of the temperatures examined. From these data one can "bound" the regions where certain morphological effects dominate within the fluence-temperature parameter space. In Chapter 5 of this report, a chart describing morphology response was generated for the PCW fluence scan versus radial position on specimens implanted at 900 °C (Figure 5-35). Figure 6-3 generates a similar response chart for the PCW temperature scan.

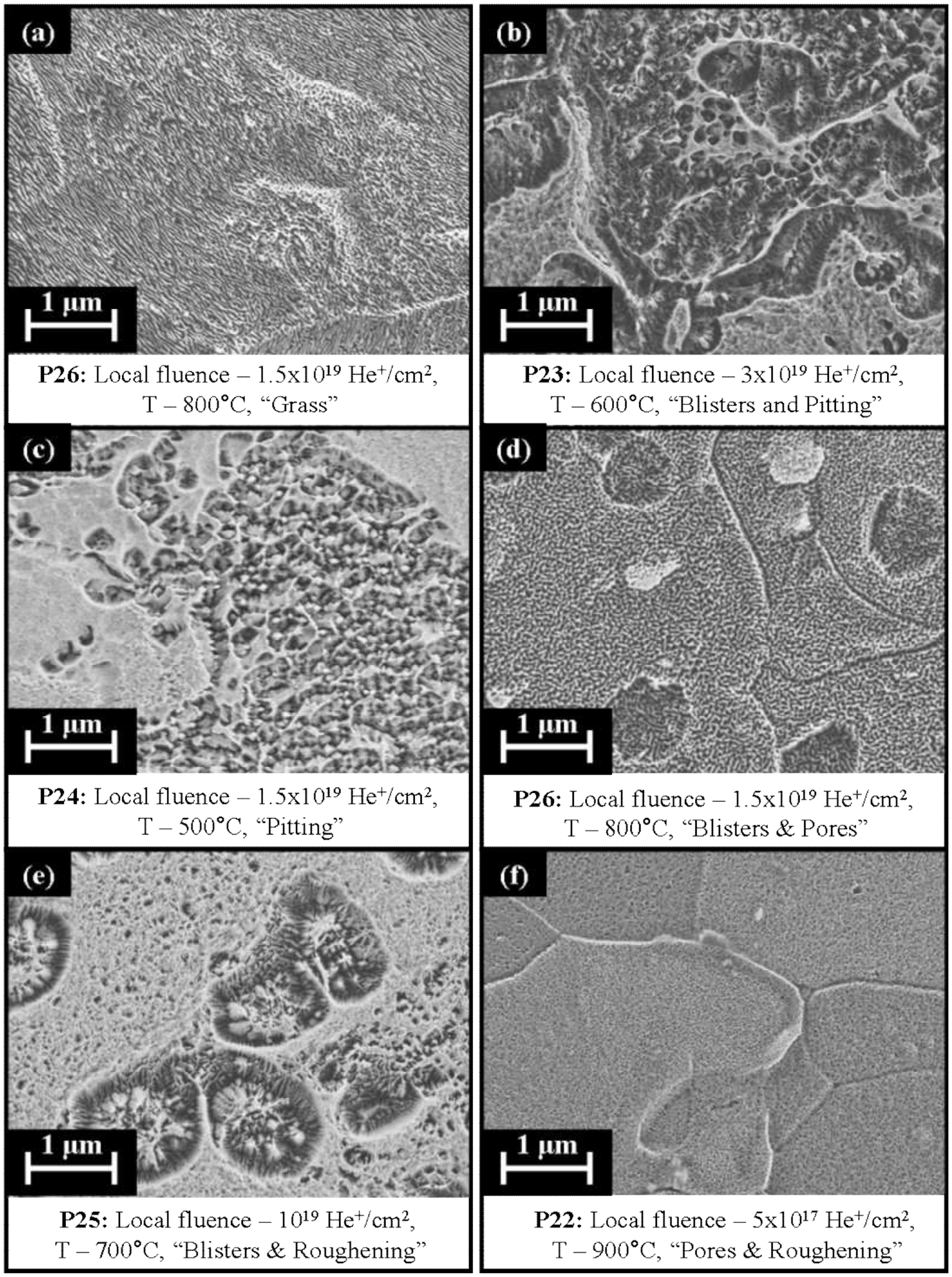

Figure 6-2: A detailed breakdown of six different morphology responses of PCW implanted with 30 keV He^+. Specimens are part of the temperature scan on PCW in the MITE-E implanted at $5x10^{18}$ He^+/cm^2. The captions under each image give (1) the internal sample designation, (2) the local fluence at the radial position (in mm) where the SEM photograph was taken, (3) the implantation temperature, and (4) the morphology response of the material surface.

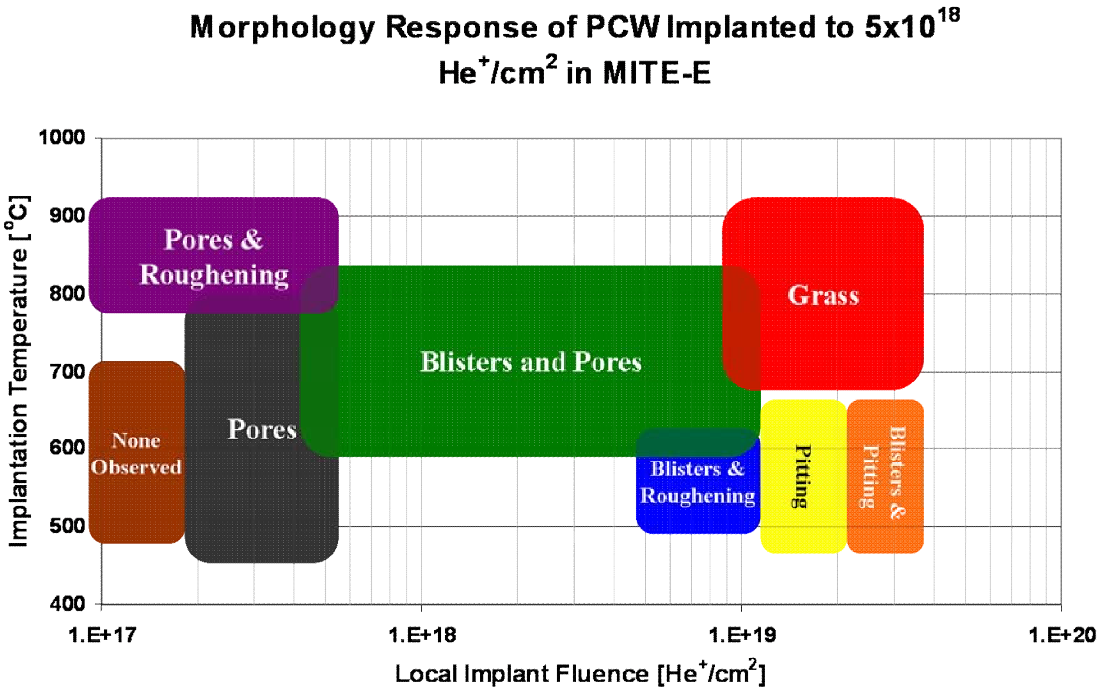

Figure 6-3: Morphology summary from local fluence and temperature scan data. The above named morphologies are briefly defined: (1)"grass" – a "combed" surface structure, whose orientation appears dependent on the crystallographic orientation of individual grains; (2) "blisters and pitting" – the W has sustained significant erosion, often from circular regions which are possibly the remnants of blisters; (3) "pitting" – also has sustained significant erosion, but blister remnants are not clearly observed; (4) "blisters and pores" – classic blisters caps are raised from the surface or completely exfoliated, and the surface, sub-surface, and blister caps all reveal visible pores; (5) "pores and roughening" – visible pore formation is observed in conjunction with texturing of grains, again dependent on crystallographic orientation; (6) "pores" –visible pores are formed; and (7) "none observed" – no surface morphology change is evident between pre- and post-implanted specimens. All specimens analyzed were implanted in the MITE-E.

Although Figure 6-3 maps the observed surface structures into seven different regions, the eighth region in Figure 6-3 being no observable damage or "none observed", the distinctions made in Figure 6-2 can be further generalized into the three aforementioned effects. In this discussion, Figure 6-2(a) is designated as "grass," Figure 6-2(b)-(c) are designated as "pitting," and Figure 6-2(b),(d)-(e) are designated as "blisters." For reasons already discussed, Figure 6-2(f) is not given its own designation due to the presence of pores in almost all of the specimens. At this point, it is clear that the drawn boxes are approximate bounds which exhibit overlapping and a combination of two or even three morphology effects.

6.2.1.1. "Grass" morphology

At 900 °C, the grass morphology appeared at fluences as low as $3x10^{17}$ He^+/cm^2 (corresponding to a local fluence [φ_L] of ~$2x10^{18}$ He^+/cm^2). This grass also appeared at 700 and 800 °C on specimens implanted to $5x10^{18}$ He^+/cm^2 and for $\varphi_L > \sim 10^{19}$ He^+/cm^2. The direction or "combing" of the grass morphology appears to be strongly dependent on the orientation of individual grains (Figure 6-4). Examination of Figure 6-4(b) also reveals a superposition of this effect at grain boundaries, which results in a "stitched" pattern formed by overlapping vertical and horizontal morphological lines. A final observation on Figure 6-4(a) is the presence of circular depressions which appear to be the remnants of blisters whose blister caps have been eroded away. Examination of specimens implanted to high fluences do not show any blister remnants indicating that as the total dose increases, the grass morphology overwhelms any indication of blisters. Blister formation will be discussed later in this chapter.

In every instance that the grass morphology was observed by SEM analysis, the FIB analysis would always reveal the presence of a sub-surface layer of visible pores (Figure 6-5). One can suggest three competing processes that might drive this grass surface morphology: (1) the coalescence and swelling of helium bubbles near the W surface, (2) the preferential sputtering and erosion dependent on crystallographic orientation, and (3) "masking" of tungsten tips covered by a thin layer of WC or WN.

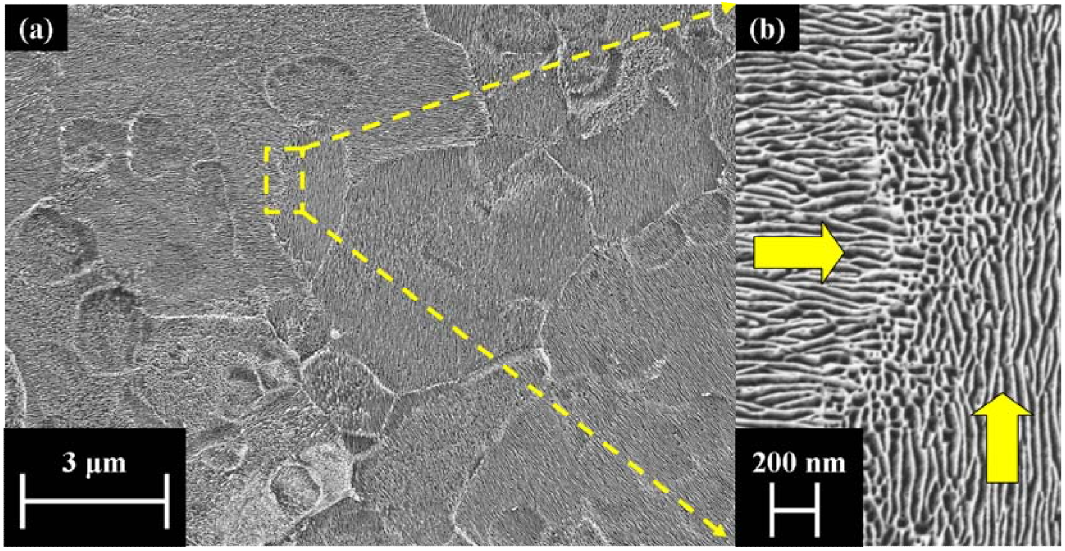

Figure 6-4: PCW implanted in the MITE-E to $6x10^{17}$ He^{+}/cm^{2} at 900 °C (a) showing the grass-like surface morphology, and (b) a blowup of the micrograph on the left, showing the strong directionality of morphology with individual grains. At the center a micrograph (a) a "stitched" morphology is observed from the superposition of the horizontal and vertical morphologies of adjacent grains.

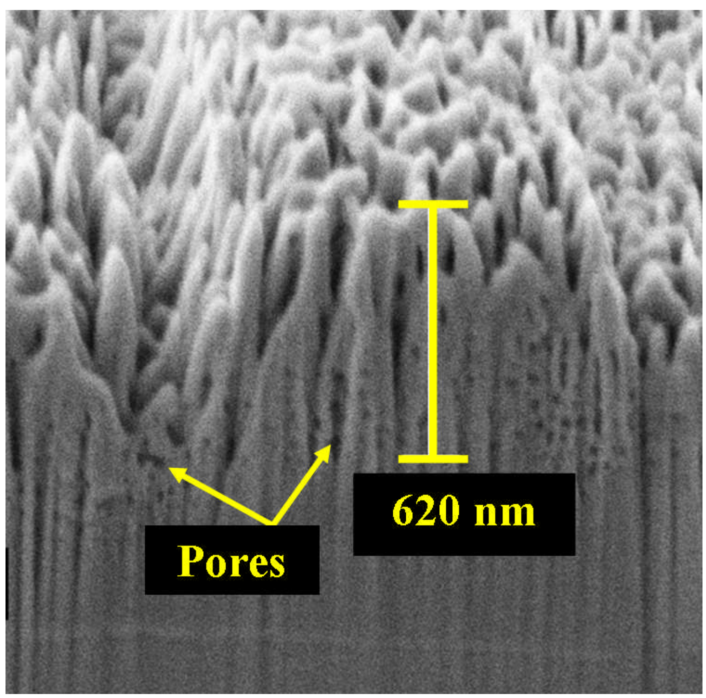

Figure 6-5: PCW implanted in the MITE-E to a fluence of $6x10^{17}$ He^{+}/cm^{2} (local fluence ~ $3.6x10^{18}$ He^{+}/cm^{2}) at 900 °C showing the highly oriented surface structure and a layer of visible pores extending ~400 – 500 nm below the surface. This is a cross-section of the same specimen shown in Figure 6-4.

Let us examine the first process, which was postulated by Kajita et al. to explain the vertical growth of nano-structured W. [14] It is important to note that the work by Kajita et al. was carried with bombarding ions of energy < 100 eV, which is much lower than implantation experiments in the MITE-E (30,000 eV). It has been observed in the MITE-E that, as implanted fluence increases for temperatures ≥700°C, the first visible morphology change on the surface is the appearance of pores. Figure 6-2(f), which is implanted to a low local fluence, illustrates this point. This is also consistent with prior work which reported the threshold fluence for visible pore formation in PCW of $\sim 10^{17}$ [8,9]. As initial pores are formed and helium continues to be implanted, coalescence of other bubbles near the bottom of surface pores will cause the existing hole to develop in the depth direction. Another aspect of this process is that the swelling of helium bubbles present within the nano-structure would further extrude the protrusion. Kajita et al. also reported that simulations predict surface pores will be unable to form under approximately 730 °C. This is very close to the temperature threshold for the sub-surface porous layer observed on specimens implanted in the MITE-E. Currently, data does not exist to determine whether this process significantly contributes to the grass morphology observed in the MITE-E. However, this process may contribute to the vertical enhancement of features generated by preferential sputtering.

For the second process, one must consider the angular dependence of W sputtering yield from He^+ bombardment (Figure 6-6), as well as, the possibility of W self-sputtering [15]; however, W self-sputtering is not thought to be important in the MITE-E. On a flat specimen, different grains have different crystalline planes exposed to the surface, and consequently, will have different crystalline planes exposed to the ion beam.

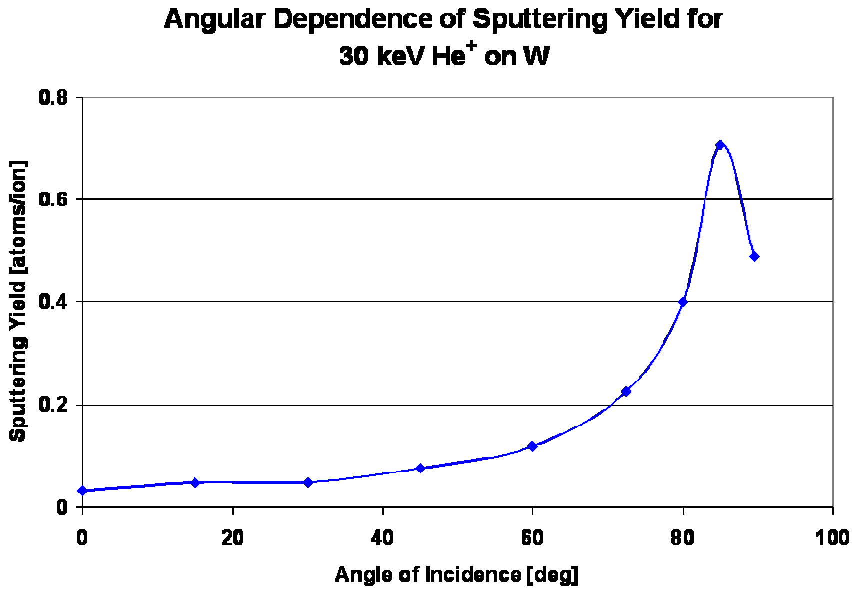

Figure 6-6: SRIM calculation of sputtering yield for 30 keV He^+ on W (amorphous target). [16]

In the case of the MITE-E, the ion beam is completely perpendicular to the surface of the implanted specimen. Several studies have shown that preferential sputtering and erosion occurs on metals as ions are implanted at various incidence angles. [17,18] Moreover, the induced surface morphology from these sputtering effects is dependent upon implantation temperature as well as crystallographic orientation and incidence angle of bombarding species. [19] For a beam of ions impinging perpendicular to the surface of a polycrystalline specimen, one can imagine that there are effectively many ion incidence angles depending on the crystalline plane exposed to the beam for that particular grain. On a polycrystalline specimen, one might expect a different surface morphology to develop for every crystalline plane exposed to the beam. If the crystalline orientation exposed to the beam was known, then it would also be possible to predict the surface morphology induced by the ion sputtering (given that the sputtering induced morphology for the crystalline planes are also characterized). As shown in Figure 6-4, PCW specimens implanted in the MITE-E exhibited this highly orientated surface morphology which varied from grain to grain.

Vasiliu [19] noticed a similar surface structure to that of Figure 6-4(b), though larger in scale on Fe implanted with 20 keV Ar^+ at 900 °C (Figure 6-7). The report makes no mention of argon bubbles or pores below the surface or breaking the surface. It is possible these were not visible at the available magnifications or that samples were not cross-sectioned to reveal any sub-surface morphology. Additionally, at a 30° incidence angle the range of 20 keV argon is ~10 nm. This low range in combination with a high melt-fraction implantation temperature for Fe (900 °C → T/T_m ~0.6) makes it unlikely that significant amounts of argon remain in material to cluster and form bubbles before diffusing out of the surface. This high homologous temperature of the irradiations is one difference between the work of Vasiliu, et al. [19] and that performed in the MITE-E, since the highest implantation temperature on the W amounts to a homologous temperature of $T/T_m \sim 0.26$.

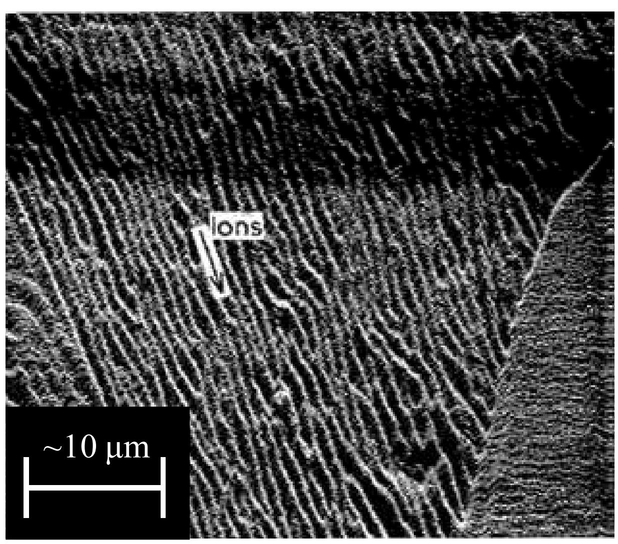

Figure 6-7: Polycrystalline Fe implanted with 20 keV Ar^+ to 3.4×10^{18} cm^{-2} at 900 °C. Ions were incident at 30° to the specimen normal. Magnification is at 6 kX. [19]

What is most interesting about Figure 6-7 is that ions incident on the grain in the center of the micrograph have induced a "combed" appearance, yet the grain in the lower right of the image has sustained only minor roughening. This leads one to believe that the oriented grass surface structure observed in the MITE-E is, in fact, driven by preferential sputtering of He^+ as it bombards grains of different crystallographic orientation. Work published by Southern et al. [20] showed that sputtering yields on single-crystalline Cu bombarded with 5 keV Ar^+ at room temperature varied strongly with the orientation of the monocrystals (Figure 6-8, also repeated in Figure 3–3). Sputtering yields for these various crystals varied by factors greater than two. If similar behavior holds for various crystalline planes in W, then this process could account for the large variation in surface structure observed between different grains (Figure 6-9).

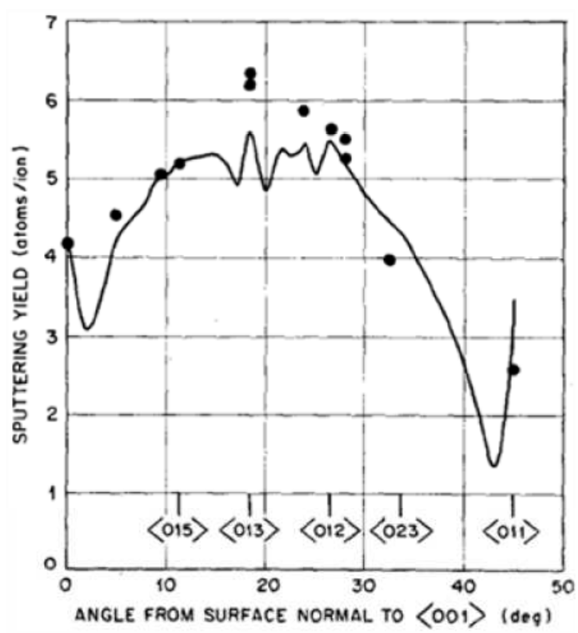

Figure 6-8: Sputtering yields of <0*kl*> Cu monocrystals under normally incident 5 keV Ar^+, plotted against the angle between the surface normal and <001>. The line represents the theoretical yield, the points, and the experimental data. [20]

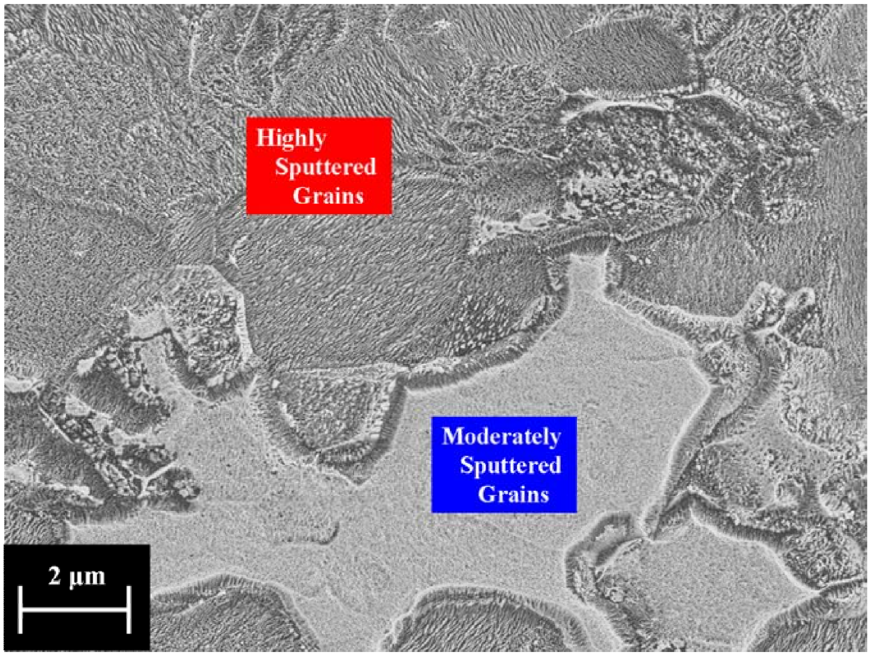

Figure 6-9: W specimen implanted in the MITE-E at 700 °C to $5x10^{18}$ He^{+}/cm^{2} ($\varphi_L \sim 1.5x10^{19}$ He^{+}/cm^{2}) illustrating grains where grass-like surface morphology has developed next to grains which have sustained far less erosion and sputtering.

Figure 6-10 presents a bar graph which has been compiled from the data reported by Southern et al. [20] and Carlston et al. [21]. Sputtering yields from Cu monocrystals show significant differences (approximately a factor of 4) for different crystallographic orientations; and for Mo monocrystals, sputtering yields vary by almost a factor of 2. Despite the use of lower energy argon ions, one expects the qualitative trends to hold for W, since many of its properties closely resemble those of Mo. It appears very plausible that differences in sputtering yields corresponding to differences in crystallographic orientation of individual grains is responsible for the unique and diverse surface structure of W specimens implanted in the MITE-E, including the grass like morphology.

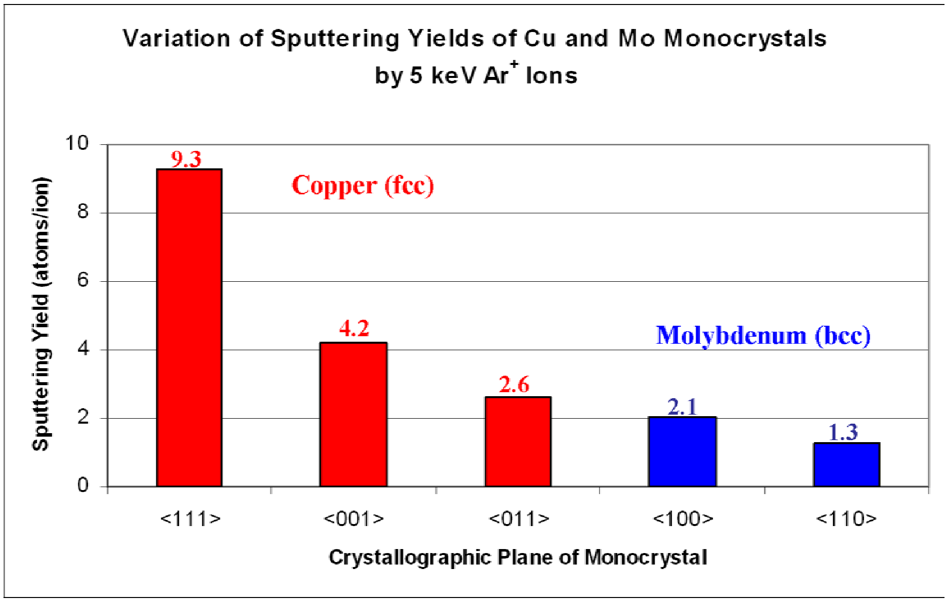

Figure 6-10: Sputtering yields of Cu monocrystals at room temperature [20], and Mo monocrystals at 527 °C. [21] Both the Cu and Mo were bombarded with 5 keV Ar^+. The data illustrates a substantial dependence of sputtering yield on crystallographic orientation in both FCC and BCC metals.

A final process by which this grass morphology and "lamellar" type structure may develop is from the "masking" of the tungsten tips by thin layers of WC or WN. [22]. It is possible that carbon or nitrogen impurities already present, adsorbed, or even implanted in the specimen surface, can form thin layers of WC or WN sporadically across the surface. These two elements were chosen based on their prevalence in vacuum systems and ease of compound formation with pure W and high binding energy of the WC or WN molecule. As ions bombard the specimen, it is possible that this thin layer (having a lower sputtering yield than pure W) would allow the "unmasked" regions of pure W to be preferentially eroded away. There is no conclusive data to support or dispel this process, but it may warrant future investigation.

6.2.1.2. "Pitting" morphology

The second morphology effect observed on specimens implanted in the MITE-E is "pitting." In the MITE-E, ion bombardment induces pitting at temperatures ranging from 500 – 700 °C. Generation of this surface structure may be possible at lower temperature, but this report does not treat temperature effects below 500 °C. Pitting was also fluence dependent while not occurring at local fluences less than ~10^{19} He^+/cm^2 (see Figure 6-2(b)-(c)). The pitting effect appears to be induced by these mechanisms: 1) blistering of W at lower temperatures, and 2) preferential sputtering of specific crystallographic orientations.

Just as the grass morphology observed at higher temperatures, the pitted surface structure on tungsten is strongly dependent on the grain's orientation to the incoming ion beam. The pitting morphology is distinguished from blisters because the size, shape and depth of the "pits" formed on the W surface appear random. This is in contrast to blisters which are round or ovular, with diameters of ~1 – 2 μm, and blister cap thicknesses near 0.1 μm. Inspection of the FIB image in Figure 6-11(a) shows a PCW specimen implanted with He^+ at 500 °C, and indicates that blisters may have formed on the specimen surface; these were then eroded, leaving a ~1μm wide and several hundred nanometer deep depression. Further pitting, though smaller in scale, has developed on the specimen surface, especially in areas which appear to have been vacated by blisters. The specimen implanted at 600 °C shows numerous conical protrusions formed on the surface. These pores are several hundred nanometers in height and appear to be induced by preferential sputtering. Similar conical structures were also observed at 700 °C and had average heights approximately 100 nm greater than those shown in Figure 6-11(b).

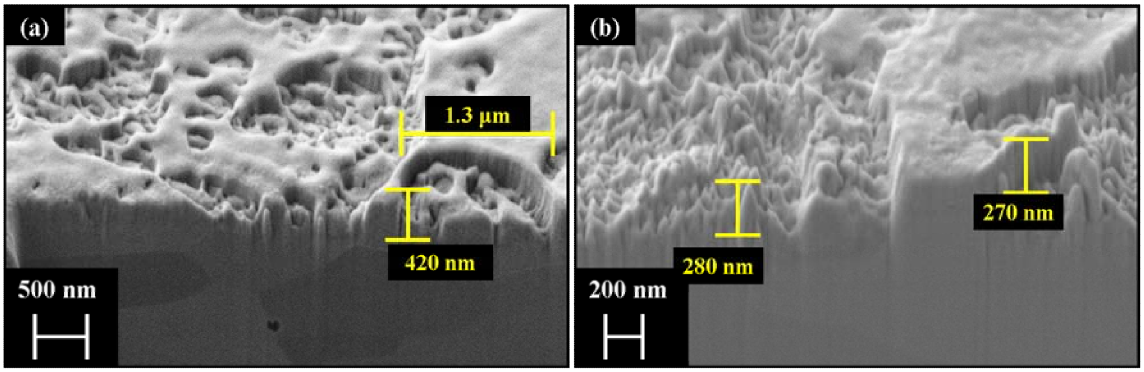

Figure 6-11: FIB micrographs illustrating the different types of pitting induced by helium bombardment of W in the MITE-E. (a) PCW implanted at 500 °C to 5x10^{18} He^{+}/cm^{2} (φ_L ~ 1.5x10^{19} He^{+}/cm^{2}) showing remnants of blisters and smaller scale pitting dispersed on specific grains, and in (b) a PCW specimen implanted at 600 °C to 5x10^{18} He^{+}/cm^{2} (φ_L ~ 3x10^{19} He^{+}/cm^{2}) small conical features have developed on certain grains, while adjacent grains are relatively unaffected.

This preferential sputtering does not appear to be unique to tungsten. Both Fe [19] and Cu [23,24,25] are shown to exhibit this behavior. It is reasonable to assume that such sputtering effects will be observed on any polycrystalline material. Figure 6-12 shows the data reported by Williams [23] but conducted by Whitton [24,25] after Cu is bombarded with 40 keV Ar^{+} to a fluence of ~10^{19} Ar^{+}/cm^{2} at temperatures below 350 °C. It was determined that these surface topography changes on copper were a result of different crystalline planes perpendicular to the argon ion beam. Unfortunately, the temperature of this specimen is not reported, but this structure is very similar to that observed on PCW implanted in the MITE-E. This suggests that the pitted morphology is caused by preferential sputtering dependent upon which crystalline plane is exposed to the MITE-E's helium ion beam.

Figure 6-12: Polycrystalline Cu bombarded with 40 keV Ar^+ to a fluence of ~10^{19} cm^{-2} (T < 350 °C) which resulted in conical surface structures and showing large variation in sputtering coefficients between grains. The scale marker is equivalent to 1 μm. [23,25]

6.2.1.3. "Blister" morphology

The final morphology change of interest is the formation of blisters on the PCW surface. Blisters are not an uncommon occurrence on metals implanted with ions, specifically helium ions, and has been observed for a long time in various metals. [26] Yet, within the experience of the UW IEC materials program, blisters are a nascent morphological feature. At 900 °C the blisters were observed at local implant fluences as low as $6x10^{17}$ He^+/cm^2. As local fluence is increased passed ~$1.5x10^{19}$ He^+/cm^2, there is a transition from blisters who have their caps still intact to depressed regions dominated by the grass morphology where it is clear blisters once existed (see Figure 6-4(a)). Blisters are also observed at all temperatures examined at local fluences of $5x10^{17}$ He^+/cm^2. This is very near the range they were observed in fluence scan at 900 °C. This suggests that for the temperatures examined (500 – 900 °C), the onset blister formation is fluence dependent and beginning in the mid-10^{17} He^+/cm^2 range. Results reported by Fu et al. [27] and Tokunaga et al. [28] agree well with this number. As reported in Chapter 5 of this report, the average blisters diameters were ~1 – 2 μm for the W specimens implanted in the MITE-E. One study by Das and Kaminsky [29], which compiled data from various experiments on He^+ implantation in Nb and Mo, correlated the He^+ implantation energy to the average blister diameter. They reported average blister diameters of ~0.5 – 2 μm for He projectiles with energies ranging from 10 – 100 keV, which also agrees well with observations on W implanted with He^+ in the MITE-E.

The blister formation in the MITE-E implantations appears to follow a four stage evolution (Figure 6-13). Formation of blisters begins with the implantation of helium which coalesces into bubbles approximately 100 nm below the surface of the W. At these temperatures (<900 °C), the implanted helium gas is trapped as shown in Figure 6-13(a). It is important to note that the competing effect of crystallographic sputtering, which will eventually result in either the grass or pitted morphology, is also developing. The initial effects of the crystallographic sputtering can also be seen in the upper half of Figure 6-13(a). From these observations, one expects blisters not only to form at the lower fluences, but all temperatures, which agrees with the assessment given in Figure 6-3. Continuing to the second phase of blister formation, as fluence passes ~10^{18} He^+/cm^2, the pressure of the trapped helium is great enough to cause separation between the surface of the W and the implanted layer, or "blister gap," which results in the classic blister (Figure 6-13(b)). Increasing the fluence even further induces rupturing and exfoliation of the blister caps and exposes a region of very high pore density. This third stage in the evolution of blisters is shown in Figure 6-13(c), which also reveals that the blister caps, sub-surface region, and beam-exposed surface are sustaining extensive pore formation. The fourth stage of blister evolution is dominated by crystallographic sputtering effects which take over at high fluences and result in either a grass morphology (at temperatures ≥ 700 °C) (Figure 6-13(d)) or a pitted morphology (at temperatures ≤700 °C).

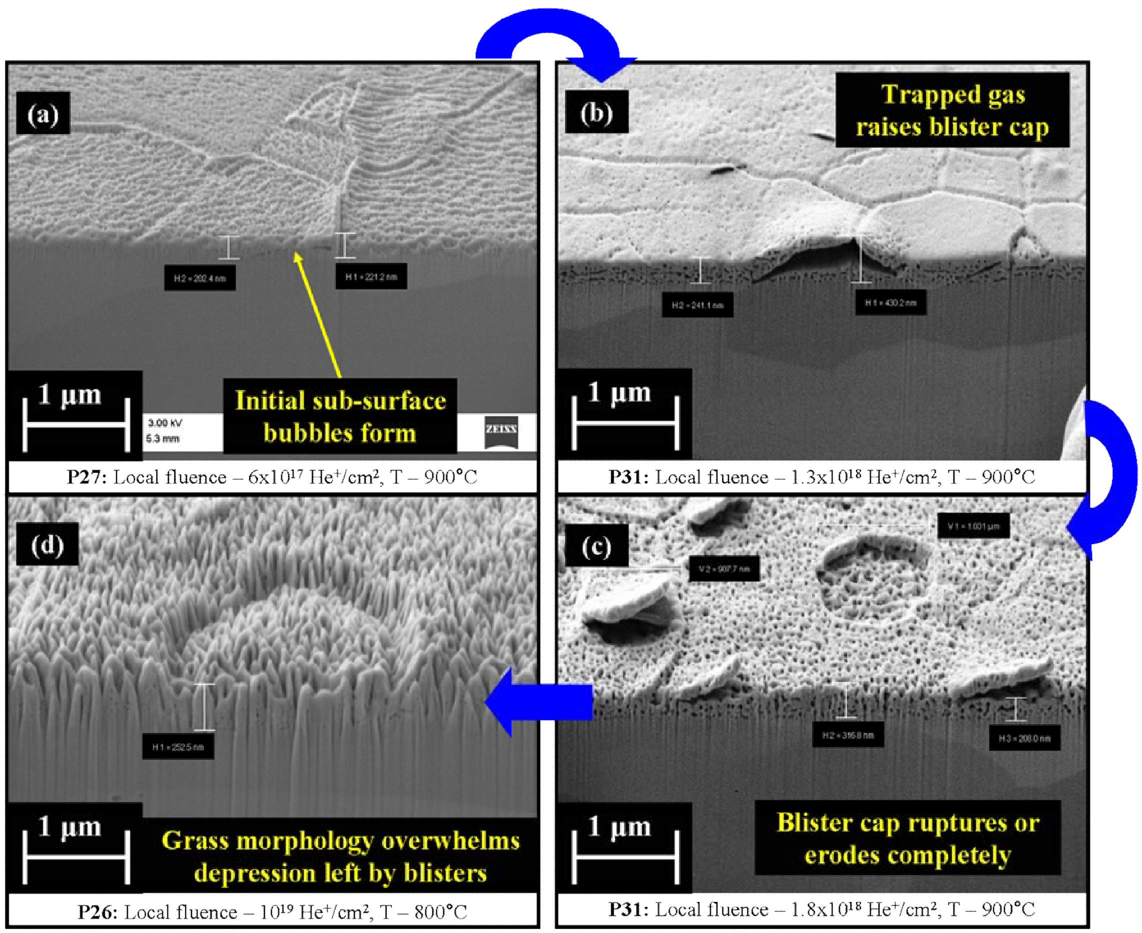

Figure 6-13: Blister formation on PCW implanted with He^+ in the MITE-E showing the four stages of blister evolution: (1) initial formation of sub-surface pores in the He^+ implanted region, (2) the raising of the blister cap and formation of a blister gap, (3) rupturing and erosion of blister caps, and (4) the left over depression from exfoliated blister caps overwhelmed by crystallographic sputtering effects. The captions indicate the internal sample designation, local implanted helium fluence, and implantation temperature.

To summarize, there are three predominant surface morphologies observed on PCW implanted with 30 keV He^+, they include: a grass-like surface, a pitted surface, or a blistered surface. Both the grass and pitting morphologies require high fluences for development, but are sensitive to implantation temperature, with the grass generated at high temperatures (≥ 700 °C) and the pitting at lower temperatures (≤ 700 °C). Conversely, blisters, or blister remnants, appear at all temperatures, but are not developed until implant fluences reach ~$5x10^{17}$ He^+/cm^2. At high fluences, blisters are eroded by preferential sputtering mechanisms and remain only as depressions filled with small lamellar structures or small pits characteristic of the grass and pitting structures, respectively. If one applies the morphological data to what may be considered an acceptable surface structure on first walls of IFE reactors or divertors of MFE reactors, a materials viability assessment curve can be produced. Figure 6-14 shows the materials viability assessment for PCW implanted with 30 keV He^+ in the MITE-E. It is also important to clarify that this assessment applies to helium ions only. Undoubtedly, plasma facing components in fusion reactors will experience a wide range of particle fluxes from multiple ion species. Therefore, this curve represents the author's best estimate of temperature and fluence constraints which might be acceptable on a tungsten first wall or divertor plate in a fusion reactor under helium bombardment. The assessment for PCW presented in Figure 6-14 will be compared to other materials examined in the UW IEC group's materials studies at the end of this chapter.

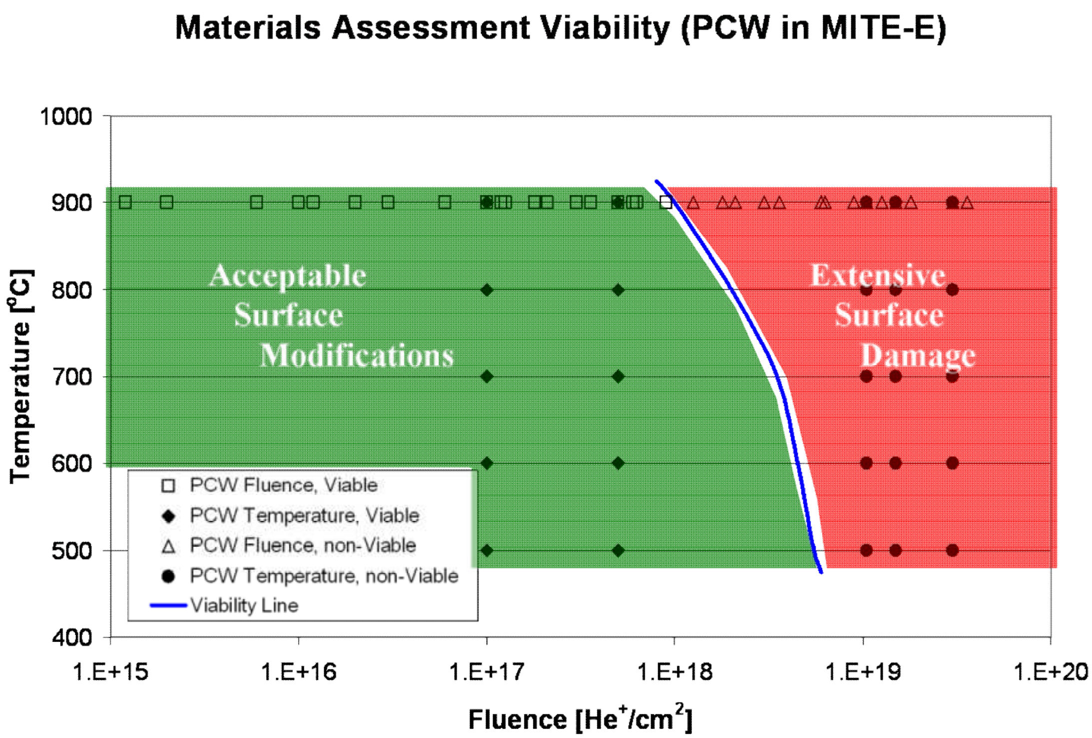

Figure 6-14: Viability assessment of PCW as a function of temperature and fluence under helium bombardment at 30 keV. The data points which generated the viability curve were taken from the fluence and temperature scans of PCW in the MITE-E.

6.2.2. Understanding the difference in surface morphology change between the HOMER and HELIOS devices, and the MITE-E

As mentioned before, the previous work done by Cipiti [1] and Radel [30] on He^+ implantation in polycrystalline W (PCW) was carried out, exclusively, in the IEC device HOMER. As shown in Chapter 2 of this thesis, the inherent result of these implantations was a porous or "coral-like" surface morphology, distributed uniformly across the surface of the specimen. Additionally, the initial work by this author was also carried out in the HOMER device as well as the IEC device HELIOS - these results are discussed in Chapter 5 of this report. Up until the construction of the MITE-E device, it was assumed that the porous and coral-like morphology was the characteristic morphology for tungsten implanted at the chosen parameters: ion energy – 30 keV, temperature ~1000 °C, and fluences above 10^{17} He^+/cm^2. From a comparison of the results in Chapters 2, 3, and 5, it is clear that there is a significant visual change in the surface morphologies of W specimens implanted in the MITE-E (highly dependent on grain orientation) versus that of the HOMER and HELIOS devices which predominantly result in random pore formation and coral structure. Figure 6-15 illustrates this difference. In HOMER, we see the classic pores and coral morphology, which appears to be uniform and random; but in the MITE-E we have a fine "combed" or "grass" structure, which appears to vary with crystallographic orientation of each grain. This leads us to the following question:

- What is the fundamental difference between the way the HOMER and MITE-E devices implant ions which gives different morphologies on the tungsten surface?

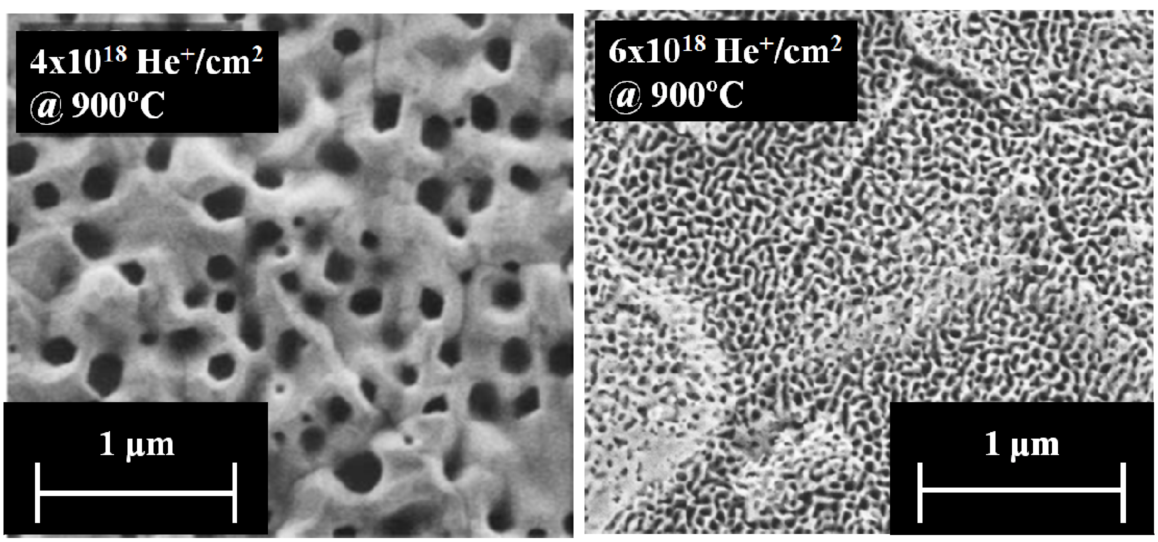

Figure 6-15: Comparison of PCW implanted to (a) $4x10^{18}$ He^+/cm^2 at 900 °C in HOMER [3] and (b) implanted to $6x10^{17}$ He^+/cm^2 (local fluence ~ $6x10^{18}$ cm^{-2}) at 900 °C in the MITE-E.

Clearly there are a wide range of differences in the construction, geometry, ion sources, etc. of each irradiation chamber. Yet, what is it about these differences in construction and operation that make the material behave one way in HOMER and differently in the MITE-E? One variable which must be eliminated is variation in the manufacturing of the implanted tungsten specimens themselves. All specimens classified in this report as polycrystalline W and implanted by this author or Radel, were acquired from Oak Ridge National Laboratory (ORNL), where the specimens were cut, ground, polished, and then shipped. The material vendor to ORNL was Alfa Aesar® who manufactured these specimens through a powder metallurgical process. Lot numbers were provided for each of the multiple sample shipments sent to the UW IEC group. The specimens implanted in Figure 6-15(a-b) do not share the same lot number. Therefore, the possibility of different morphological response base on specimen manufacturing must be eliminated before fair comparison is made between the results of these two devices.

For this purpose, an experiment was devised in which a sample previously implanted in the HOMER device by Radel was electropolished to remove the helium implanted layer and then re-implanted with He^+ in the MITE-E. The initial implantation results of this specimen are reported by Radel in 2007 [5]. Secondary implantation was carried out in the MITE-E. A Comparison of the results is illustrated in Figure 6-16:

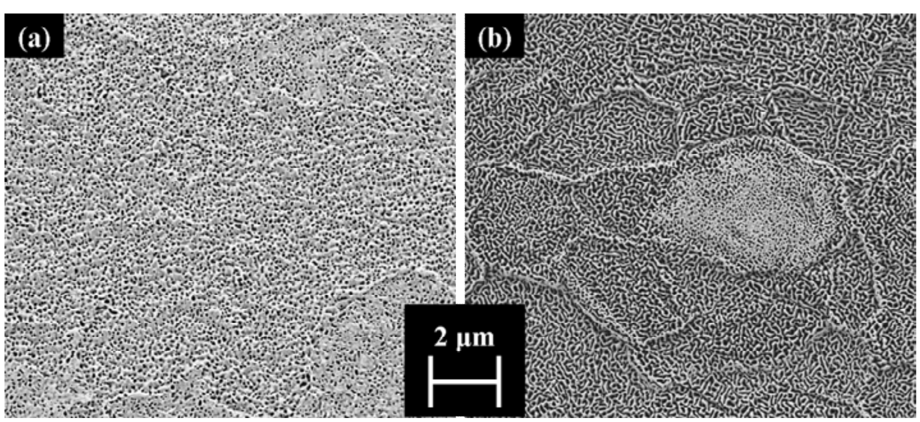

Figure 6-16: (a) PCW implanted in the HOMER device to $6x10^{18}$ He^+/cm^2 at 1130 °C by Radel and (b) the same specimen, electropolished and re-implanted to $5x10^{18}$ He^+/cm^2 (local fluence 10^{19} cm^{-2}) at 900 °C in the MITE-E.

In comparing Figure 6-15(a) and Figure 6-16(a), where both specimens were implanted in HOMER, it is evident that the porous surface morphology between these two samples is consistent. However, once this specimen was electropolished and re-implanted with helium in the MITE-E, the resultant morphology (Figure 6-16(b]) was consistent with that of the W specimen show in Figure 6-15(b), which was also implanted in the MITE-E. From this analysis, one can safely conclude that major differences in the nature of the W surface morphology of Figure 6-15 are a result of the different implantation devices, not the variations inherent in the powder metallurgy manufacturing process. With this knowledge in hand, one can suggest four different hypotheses which may answer the previously posed question:

1. In the HOMER and HELIOS there is a spread in the energy of the ions bombarding the specimen due to either higher neutral background pressures, ion source geometry, or operation modes. This results in a population of ions and fast neutrals at lower energies, for the same cathode voltage or injection energy, thus implanting helium at a continuum of depths rather than a single depth.
2. W specimens implanted in the MITE-E were mechanically polished and electropolished to reveal the grain structure. Whereas, W specimens implanted in HOMER and HELIOS were mechanically polished, leaving a "damage layer" of several microns, which may convolute any crystallographic morphology dependence.
3. Due to source geometry in HOMER and HELIOS, the He ions strike the surface at varying incident angles, causing implantation at varying depths and,

more importantly, inhibiting ion channeling and preferential sputtering in grains of certain crystal orientation.

4. In HOMER and HELIOS the specimen acts as the device cathode, so the vacuum field lines terminate on the PCW polished surface and the surface sees a vacuum field gradient. Conversely, specimens in the MITE-E are completely within the metallic cathode where the vacuum field gradient is essentially zero. At adequate cathode potentials in HOMER and HELIOS, small features may be "enhanced" through field emission due to high local electric field gradients.

It is possible that each of these four mechanisms contributes, in part, to this difference; but that one, or some combination of these mechanisms, dominate morphology change. It is also possible that some, or all of them, do not play any part in the observed difference in surface morphology.

<u>Hypothesis 1</u>: the MITE-E's ion gun, which accelerates the ions into the specimen, is fairly compact (~18 cm from the plasma extraction aperture to the specimen surface) and operates at low neutral background pressures (200 μtorr). At these neutral pressures, helium has a relatively low charge exchange cross section and long mean free path (compared to H or D) [31,32]; so, one anticipates that the ions are very nearly at the full cathode potential of -30 kV. This gives a nearly mono-energetic beam, essentially perpendicular to the W surface.

While the same cross sections and mean free paths are very similar over the operating pressure regime of HOMER and HELIOS (100 – 500 μtorr), they are both "larger" devices. The separation between the anode and cathode in HOMER and

HELIOS are 45 and 30 cm, respectively. As a result, an ion traveling from the source region to the cathode (W specimen) “sees” many more background neutrals to interact with, giving the ion a larger probability of charge exchanging. This gives a population of fast neutrals in these devices which are not at the full potential of the cathode. A larger distance to the specimen also increases the probability of collisions which slow the ions down before reaching the cathode, but it does not neutralize them.

A spread in energy of the bombarding ions means there will be a continuum of depths at which these ions implant. This hypothesis suggests that pores are formed at a continuum of depths simultaneously, and coalesce to form “chimney” sites which allow release of the implanted helium. Whereas, for a 30 keV mono-energetic beam, one expects the implanted helium to build up pressure under the surface until blistering occurs. Blistering on W has not been observed in HOMER or HELIOS at temperatures above ~800 °C.

To determine if there is a large population of particles at lower energies which bombard the specimen, an integral equation code was used to calculate the energy distribution of the ions and fast neutrals in HOMER and HELIOS. [33,34] The code calculated the energy spectrum of helium ions and neutrals in these two devices given their geometry and operating parameters during implantation experiments.

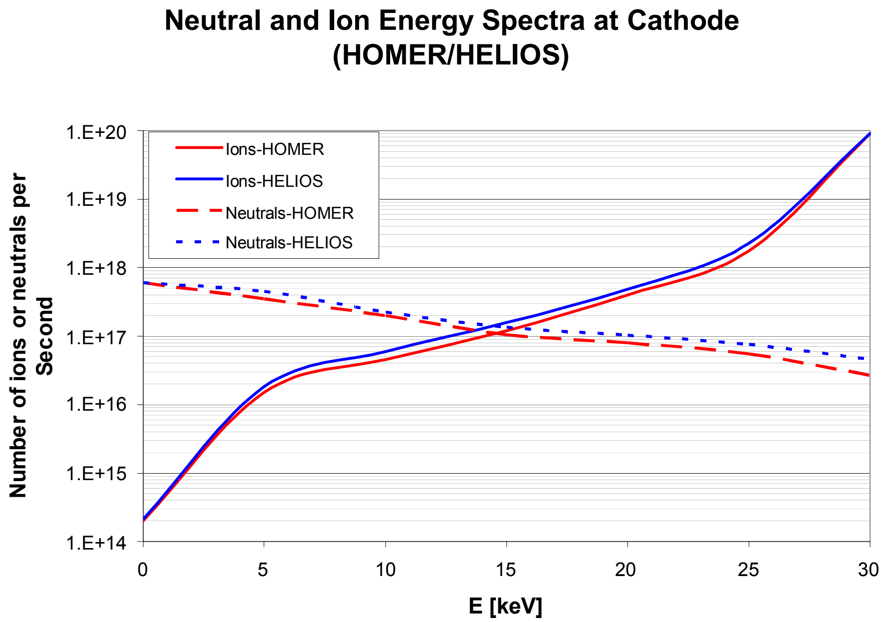

Figure 6-17: Number of ions or neutrals per second in (a) HOMER: V_o=30 kV, I=5 mA, P=0.5 mTorr, r_c= 0.01 m, r_a=0.5 m, and (b) HELIOS: V_o=30 kV, I=5 mA, P=0.2 mTorr, r_c= 0.01 m, r_a=0.3 m. Units in the plot above are converted from #/sec/keV to #/sec by multiplying by the particle energy.

Figure 6-17 shows that the vast majority of ions are born with energies of 25 – 30 keV. From these analyses, there does not appear to be a sufficient number of ions present at low energy to form the network of pores at each of these implantation depths. Inspection of the chart shows the number of particles per second produced in the HOMER and HELIOS devices, at the full available 30 keV cathode energy, are several orders of magnitude higher than any particles lower in energy than 25 keV. Additionally, the ions at full cathode energy outnumber the neutral particles in the chamber by ~100. Separating these results into 5 keV bins (using the 5 keV interval as the midpoint [i.e. Bin 1: 0 – 2.5 keV, Bin 2: 2.5 – 7.5 keV, etc.]) for a rough integration of the total number of particles, shows the particles between 27.5 and 30 keV make up just over 90% of the total particles (ions and neutrals) bombarding the specimen. This holds true in both devices. For illustration, if one were to implant to 10^{18} He^{+}/cm^{2}, there would be roughly

10^{17} He/cm^2 at energies below our cathode potential. This is approximately the threshold for any observable pore formation, so we do not expect large effects from low energy ions to be a large contributor to the resulting surface morphology.

Another aspect of these results is the fast neutral flux. Since these are “single pass” particles, they will either bombard the specimen after charge exchange, or be eliminated via some loss mechanism, such as impacting the chamber wall. Because these particles are neutralized by picking up an electron, there are no nuclei colliding and very little momentum is transferred to the neutralized atom. This results in a ballistic trajectory following the last trajectory of the accelerated ion before charge exchange. With that said, one must assume most of these neutrals are heading toward the cathode (specimen), and a majority of them may bombard the specimen. This gives us a low energy particle flux as well as an angular distribution of particles bombarding the specimen, since particles are not turned in any way by the electric field between the anode and cathode. Because of these arguments, it is assumed that the majority of these neutrals end up bombarding the cathode (sample). But since the magnitude of their flux is small compared to the ion population, one does not expect that these low energy particles have a significant impact on the resulting surface morphology. The comparison of the spectra from the integral equation code for both HOMER and HELIOS suggest a similar energy distribution of ions in both devices.

<u>Hypothesis 2</u>: W specimens implanted in HOMER and HELIOS were mechanically polished to a mirror finish at ORNL with final polishing using 3 μm diamond paste. Specimens implanted in the MITE-E were mechanically polished and also

electropolished. Mechanical polishing leaves a "damage layer" whose depth is approximately equal to the size of the final polishing grit (i.e. several microns). [35]

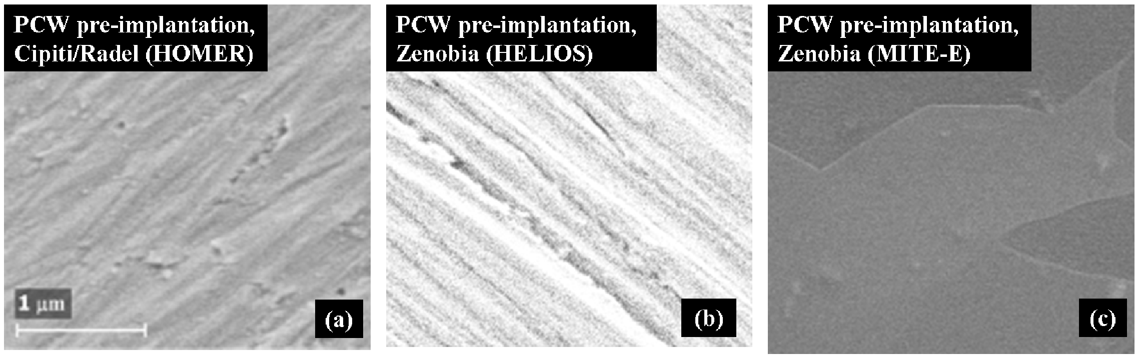

Figure 6-18: Comparison of surface of pre-implanted PCW in the HOMER and HELIOS devices, and the MITE-E. The surface in (c) has been treated with an electropolish (1% KOH in distilled water)

A mechanically polished W surface is illustrated in Figure 6-18(a-b); comparatively, Figure 6-18(c) shows a W specimen which has also been electropolished. This damage layer (an artifact of mechanical polishing) may "wash out" or convolute morphological effects which are dependent on the crystallographic orientation of individual grains. For discussion of this hypothesis, it is assumed the ions are normally incident and mono-energetic (30 keV).

For a mono-energetic beam, one would expect this damage layer to sustain blistering just as readily as W specimens with the grains clearly exposed. Yet, blisters have not been observed in either the HOMER or HELIOS devices, but blisters are seen at a wide range of implantation parameters in the MITE-E. The absence of blistering indicates the helium can be released or diffuse out from the surface before substantial pressures in the gas-filled cavities cause blisters. Certainly, the observed "chimney" sites allow easy release of the helium, but it is not immediately clear why this damage layer would promote pore formation and inhibit blisters. This suggests the damage layer left from mechanical polishing is not the root of the observed morphological differences.

As a final point in this hypothesis, if the damage layer is responsible for the difference in surface morphology change observed between W specimens implanted in the “classic” IEC configuration and those implanted in the MITE-E, this effect should be temporary. This means that, at some point, the implanted helium dose is great enough that this “damage” layer has been sufficiently eroded, and that the morphology is driven by the grain structure and orientation in the “bulk” or near-surface region. Yet, ions must “erode” this layer before any preferential, crystallographic morphology change becomes apparent. When the implant dose is high enough, we can assume that the characteristic morphology is no longer “evolving” (i.e. any increase in dose worsens the existing morphology). Saturation of pore density and the coral morphology has been observed by Radel [5], and Zenobia [10] to occur in the mid-10^{18} $He^{+}cm^{2}$ range on W specimens.

One might argue, that by the time the fluence that would erode this layer has been achieved, (mid 10^{18} – 10^{19} He^{+}/cm^{2}) the subsurface porous structure is so developed that any effects of preferential damage brought on by varying grain orientation are not discernable. This does not appear to be supported by Figure 6-19. From the surface micrograph in Figure 6-19(a) no preferential morphology change due to crystallographic orientation is apparent. The coral structure is uniform, but it does show some height variation at grain boundaries, possibly caused by thermal expansion of grains at high temperature. In comparison to Figure 6-19(b), different grains show different orientations of this “grass” morphology. Moreover, the average pore diameter of the specimen implanted in HOMER is much larger than the specimen implanted in the MITE-E, which is probably because of the temperature difference. Both of the FIB sections in Figure 6-19 reveal surface morphology changes on the order of the thickness of the polishing damage layer (~1 μm). The specimen implanted using the MITE-E shows surface variations larger than 1 μm. Such height variations were found to be common on samples implanted to high fluence in the MITE-E. If a grain-orientated surface structure is initially convoluted by the artifact of the mechanical polishing process, one expects the drastic height variations on the implanted surface would eventually become visible. Meaning, if the surface structure formed in the FIB micrograph of Figure 6-19(b) was capable of forming in the HOMER device, this artificial damage layer would not be sufficiently thick to convolute the large height variations due to preferential erosion of different crystallographic planes on the individual grains. From these data, it appears that the artificial damage layer on polished W specimens is not responsible for the morphology difference observed between the HOMER device and the MITE-E.

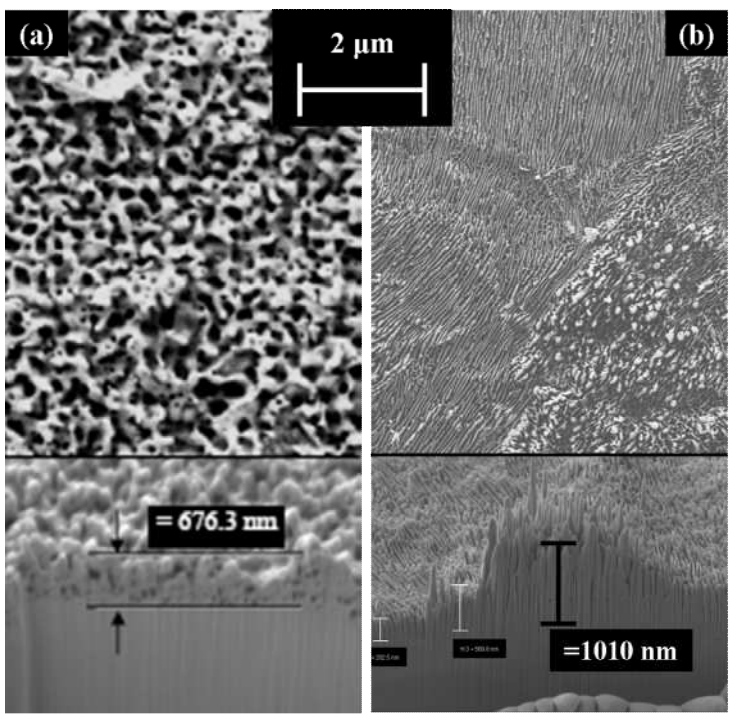

Figure 6-19: Comparison of (a) PCW implanted to 10^{20} He^{+}/cm^{2} at 1150°C in HOMER, and (b) PCW implanted to $5x10^{18}$ He^{+}/cm^{2} at 900 °C in the MITE-E. Both (a) and (b) show surface micrographs and FIB cross sections.

A final indication that this damage layer is not solely responsible for the difference in surface morphology change between the IEC devices and the MITE-E is found in several implantation experiments performed on W-needles. These were preliminary experiments testing the suitability of the ion gun technology developed for the SIGFE [36] as an ion implantation system. The results are given below and show that the needle in Figure 6-20(a) has a clear distinction between grains near the surface, showing the etching procedure successfully removed the damage layer present from the manufacturing of the needles. Figure 6-20(b) – (c) show the needle after implantation, and reveal the development of the porous surface morphology inherent to flat PCW implanted using HOMER and HELIOS (Figure 6-15(a), Figure 6-16(a), and Figure 6-19(a)). This indicates that the porous and coral surface structure is not a direct result of the damage layer left over from mechanical polishing. Figure 6-20 is also repeated in Figure 5–22.

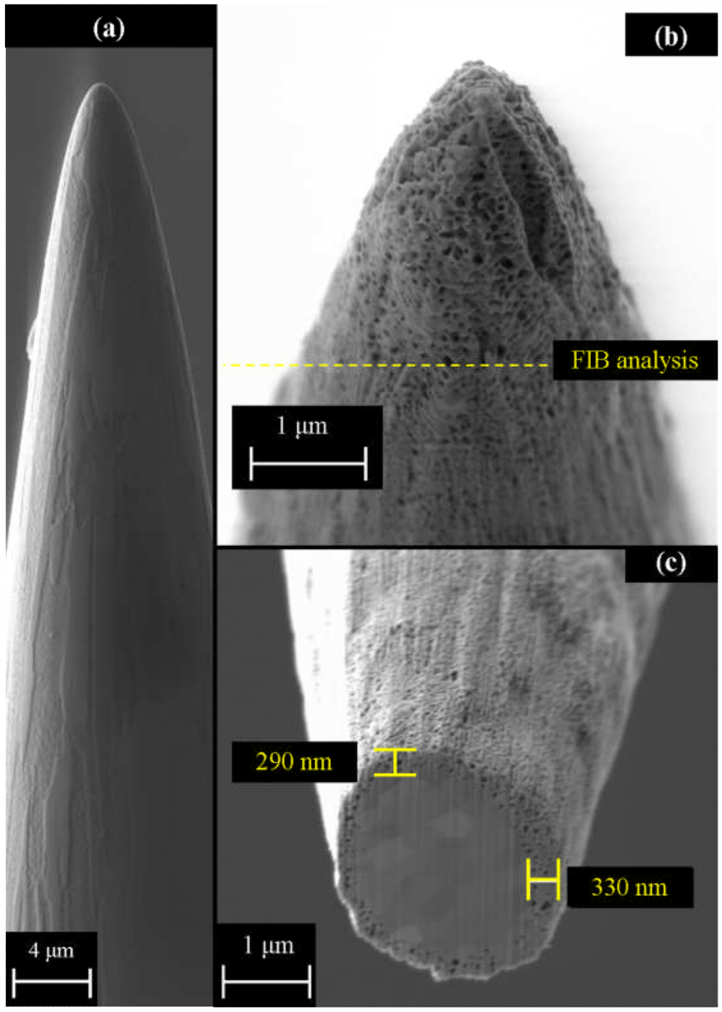

Figure 6-20: W-needle (a) pre-implantation after etching to reveal grain the grain structure of the needle, (b) an SEM micrograph after implantation in the proto-type ion gun facility to $3x10^{18}$ cm^{-2} at 700 °C with 100 keV He^{+}, and (c) a cross-sectional FIB cut showing the existence of visible sub-surface pores. Specimen was implanted in the SIGFE prototype ion gun facility.

Because these implantations were carried out in the early stages of the ion gun design, the current and temperature measurement have substantial margins of error and the scarcity of data on these needles, prevents one from drawing strong conclusions. Yet, one must consider the striking resemblance between the morphology on these needles and that of flat PCW implanted in HOMER. The ion beam is highly collimated and impinges on the needle at a constant angle. This angle is approximately 85° from the normal (i.e. nearly glancing) for the W-needles, which is very near the peak sputtering yield angle for W (Figure 6-6). It is possible that the porous or coral morphology is the preferred morphology on W for He^+ implantation at angles near the peak sputtering yield. This leads us to our next hypothesis, in which the dependence of incidence angle on sputtering and surface morphology is treated in detail.

Hypothesis 3**:** In the MITE-E, the beam direction is normal to the sample surface, essentially giving a uniform implantation angle of ions at 0°. While in HOMER, ions will be impinging on the sample surface at a continuum of angles. This is due to the source geometry and device geometry. In HOMER, the cathode during materials implantations has a zero transparency; therefore, it is assumed that few ions make multiple passes before bombarding the specimen. Most ions either bombard the specimen upon their initial acceleration to the cathode or charge exchange, in which case, they may bombard or miss the cathode on their ballistic trajectory. The source region in HOMER is roughly spherical and should draw ions from a spherical shell whose radius is equivalent to the anode radius (~50 cm). Three sets of electron source filaments are spaced around the chamber every 120°. There are two filaments to each of these sets vertically separated by roughly 30 cm.

Combining the data from W-needles implanted with the ion gun, the strong angular dependence of sputtering yield, and the filament placement in HOMER, one can see a common thread – geometry of the specimen to the bombarding ions, specifically the surface normal orientation to ion flux. In HOMER, implanted specimens were visually aligned to a window port on the vacuum vessel, with the line of sight through that window normal to the polished face of the specimen (within ~10°). This put the three sets of filaments at ~30, 90, and 210° with respect to the normal of the polished face of the

PCW sample. Because of the intensity of emitted electrons from the ion source filaments falls off as ~$1/r^2$, where r is the distance from the filament, it is likely that the ionization fraction of the source region is somewhat higher near the filaments. [37] It is then reasonable to assume that a larger fraction of the total ion current to the sample is drawn out of regions near the filaments; therefore, a larger fraction of the ions bombard the polished side of the specimen surface at angles of ~30 and 90°.

Radel [6] reported that a PCW specimen lost a mass of ~10.2$\pm$0.1 mg after implantation to 10^{20} He^+/cm^2, and for completely normal incidence (0°), the loss from sputtering is predicted be ~2.1 mg. In a different report, Radel points out that non-perpendicular incidence will not increase the sputtering yield enough to account for the observed mass loss. [30] This is correct if one assumes the ion incidence angle is not weighted toward the high scattering angles. However, assuming the sputtering yield is an average of the yields at 30 and 90° filament spacings, the total mass loss increases by a factor of ~8.5, giving a predicted mass loss of 17.7 mg. This is almost twice the measured amount. To balance this argument, one must concede the sputtering process in the HOMER and HELIOS environments are extremely complex. Most certainly, <u>not all</u> of the ions impinge at these two angles. Additionally, the specimen is held at high negative potential, so sputtered tungsten atoms could be ionized and redeposited causing self-sputtering. Further complication is added by the changing surface morphology during implantation which certainly obfuscates the well characterized sputtering behavior of flat specimen. Implications for the specimens implanted in the MITE-E are discussed later in this section. Further investigations and suggestions of this topic are treated in Chapter 8 of this thesis.

In HELIOS, the source is quite different. Ions are extracted from a helicon ion source through a ~1 cm diameter aperture via plasma pressure and coulomb attraction from a -30 kV cathode potential. Specimen surfaces were orientated perpendicular to the ion beam from the helicon source, and it was initially assumed that the angle of incidence of particles bombarding specimens in HELIOS was at a normal or perpendicular angle. Piefer [31] showed that the beam coming from the helicon source did not have good collimation but was ~ 10 cm in diameter. The experiment verifying this is illustrated in Figure 6-21.

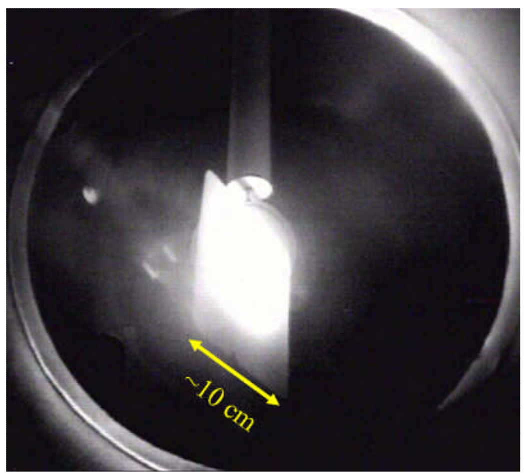

Figure 6-21: Polished tungsten sheet bombarded by a 90 kV, 20 mA beam in HELIOS. The bright spot indicates the beam size and is caused by the helium ion energy deposition.

Specimens implanted in HELIOS were approximately 1 cm in diameter, meaning a large fraction of the incoming beam missed the specimen on the initial pass. These ions either bombarded the back of the specimen, or after multiple passes, impacted the front of the specimen. Despite a "linear" geometry between the helicon extraction aperture and the specimen surface, the source behavior also gives the possibility for ions to bombard the specimen at varying angles of incidence.

A single- (SCW) and a polycrystalline tungsten specimen were mounted in HELIOS for implantation. The samples were placed “back-to-back” with the polished surface of the PCW specimen facing toward the ion source and perpendicular to the beam direction. The polished surface of the SCW specimen faced away from the source but was still perpendicular to the beam direction. Both specimens had the same surface morphology after implantation to $5x10^{18}$ He^{+}/cm^{2} at 1000 °C (Figure 6-22). The morphology of these W specimens is consistent with those shown in Figure 6-15(a) and Figure 6-16(a), both specimens which were implanted in HOMER. The same porous, coral morphology suggests there is a common factor in the operation of these devices generating this unique surface structure. In close examination of the specimens implanted in HELIOS (Figure 6-22), one sees a closer resemblance to the “grass” surface structure observed in the MITE-E than in results on W from the HOMER device. Although accomplished through different processes, it appears that the multi-angular ion impact is present in both the HOMER and HELIOS devices, but to a lesser degree in HELIOS.

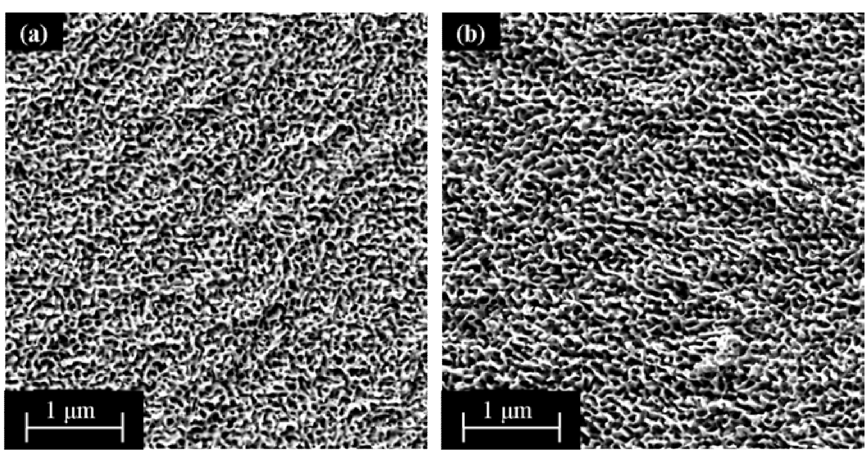

Figure 6-22: (a) SCW implanted in HELIOS facing away from helicon ion source aperture, and (b) PCW implanted in HELIOS facing toward the source aperture. Specimens were implanted simultaneously to a fluence of $5x10^{18}$ He^{+}/cm^{2} at 1000 °C.

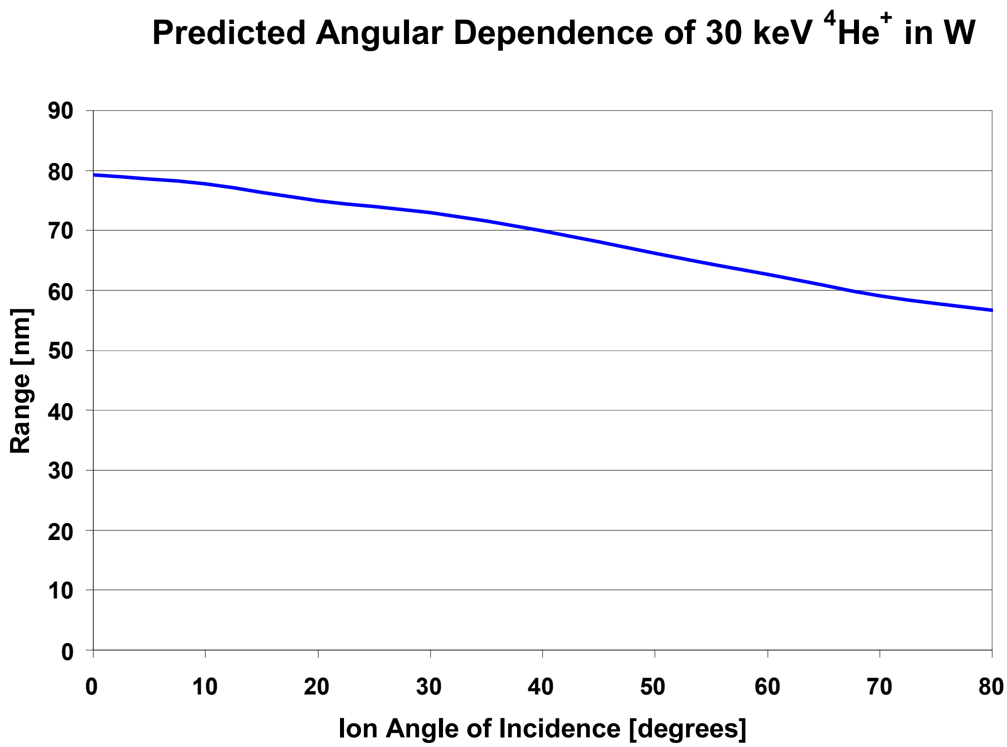

Figure 6-23: TRIM Calculation of the Angular Dependence of Ion Range for 30 keV $^{4}He^{+}$ implanted into W, where 0° is perpendicular to the sample surface.

Ions implanted at high angles (low angle to the surface) will not penetrate as deep into the W surface as ions implanted at a normal incidence. Therefore, the ions would deposit themselves at varying depths within the material. This would accomplish the same effect discussed in Hypothesis 1, but rather through varied implantation angle and no variation in the ion energy. Figure 6-23 shows the range of 30 keV He^{+} in W over a 0° to 80° incidence angle. These data show the total projected range decreases by ~25 nm over the examined incidence angles. Lowering the implantation energy to ~20 keV would give an equivalent decrease in range. Ions implanted at grazing incidences do not appear to produce the continuous concentration of helium with depth, which would produce a continuum of pores over the entire implantation range (0 – 80 nm) and allow release of the helium without blistering. Moreover, the absence of blisters on W specimens implanted in HOMER and HELIOS is not explained by a mere reduction in implantation depths due to angular incidence. Essentially, these reductions in range are equivalent to modest reductions in ion energy. Both Fu et al. [27] and Tokunaga et al. [28] observed blistering on W after implanting with He^+ at energies as low as 8 keV and temperatures between 600 – 800 °C.

Hypothesis 4: As previously mentioned, during implantation experiments in HOMER and HELIOS, specimens act as the cathode and are placed at a large negative potential (-30 kV). Positive ions are introduced, accelerated by this potential, and eventually bombard the specimen. Because of this configuration, two important questions arose: 1) are "arc spots" forming on the sample, complicating mass erosion measurements, and 2) does the high field environment produce, enhance, or give no contribution to the observed surface morphology in HOMER and HELIOS. Question one was originally posed by Dr. Bertie Robson [38] and was based on his previous experience with the phenomenon of arc spots. [39,40] This question deals with the mass loss measurements reported on PCW and NGW after implantation with He^+ in the devices HOMER and HELIOS. Because this discussion is concerned with the difference in surface morphology between specimens implanted in HOMER versus those implanted in the MITE-E, question one will not be emphasized. A detailed report was written regarding the two questions posed above and concluded that it was likely the mass loss measured on PCW and NGW in HOMER and HELIOS were a result of the implantation of He^+ and not solely due to arc spots.[41]

The second question asked if the surface morphology inherent to the HOMER and HELIOS systems is a product solely of helium implantation, arc spots and electric-field gradients, or a combination of effects. To begin this discussion, it should be pointed out that arcing alone cannot account for the observed surface morphology change in HOMER and HELIOS. This is shown by comparison of implantations with D^+ rather than with He^+. D^+ implantation has not been observed to cause the surface modification observed after implantation with helium ion species. Deuterium implanted PCW HAPL test specimens show grain growth, but no observable pore formation or coral-like structures (Figure 6-24). [1,3] Normal operating conditions of the IEC device include cathode potentials in excess of -100 kV and cathode currents between 15 and 60 mA. Spherical cathode grids during nominal IEC operation do not show surface damage characteristic of ^3He & ^4He ions, despite their subjection to much higher currents (~30 mA) and voltages (-130 kV and above).

In Figure 6-25, a cathode used in nominal operation of the IEC device is shown. These grids are constructed using W-Re(25%) wire. Based on the studies on W-Re by Radel [4], one expects these grids to experience qualitatively similar morphology change when exposed to ion bombardment at high temperature.

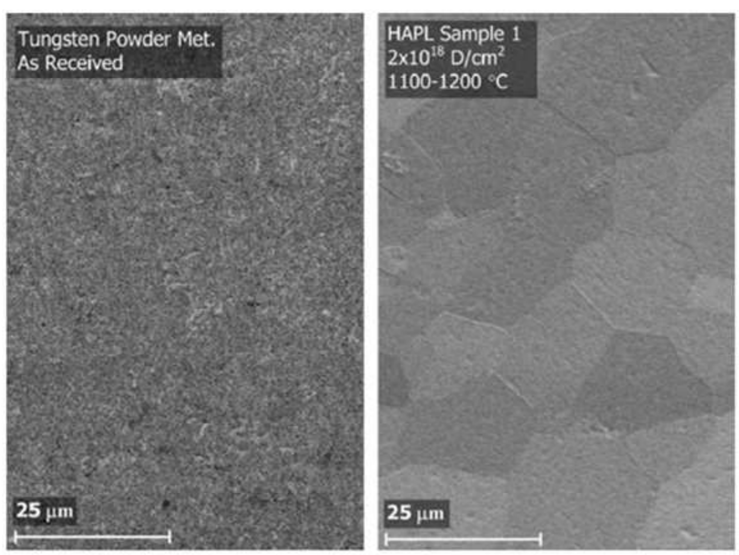

Figure 6-24: PCW as received (right-hand picture) and after deuterium implantation in the HOMER device to $2x10^{18}$ D^+/cm^2 on PCW (right-hand picture). [3]

In normal IEC operation, cathode potentials routinely reach -120 kV and currents from 30 to 60 mA. Average grid temperatures are estimated at ~500 ºC or greater. Conversely, implantation conditions for implanted materials are a -30 kV potential, currents of ~5 mA, and temperatures near 1000 ºC. An SEM image of one of HOMER's W-Re cathodes is shown in Figure 6-25. Based on logbook data, these wires were at an average potential of 78 kV and experienced a maximum potential of 130 kV. [42] The average cathode currents to the entire grid were 41 mA, with a maximum of 60 mA. The estimate (a lower bound) of the fluence to this grid is approximately 10^{19} D^+/cm^2 at an average temperature of 500 ºC. This grid was only exposed to deuterium plasma, and there is no evidence that these grid wires have sustained surface damage which resembles that observed on PCW and W alloys implanted with helium ions (Figure 6-26). It is worth mentioning that no blisters are observed on the grid wires, which is likely due to cathode grid operation temperatures at or above the desorption peaks of D in W. [43]

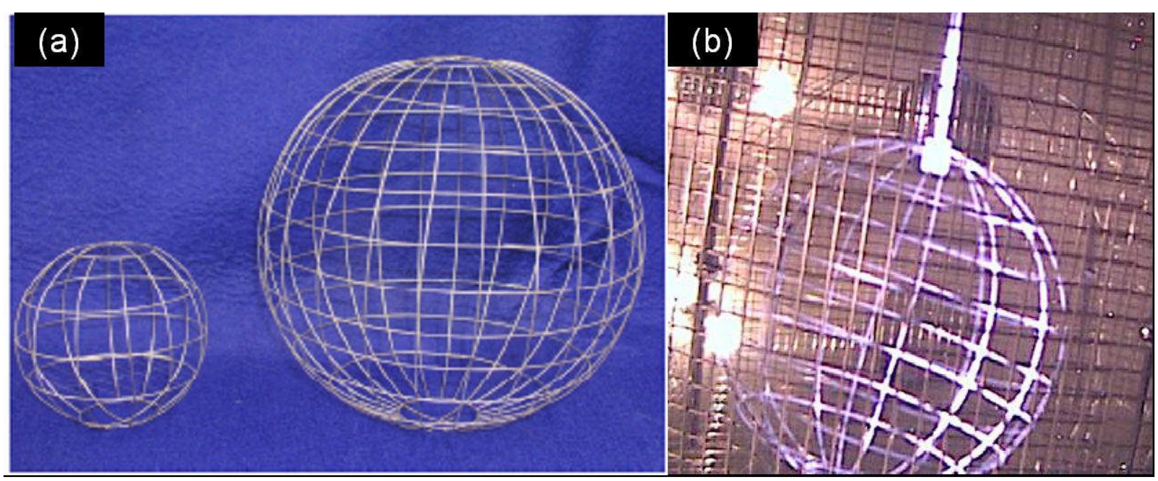

Figure 6-25: (a) Two W-Re spherical IEC cathodes of two different diameters - 10 cm (left) and 20 cm (right) after assembly, and (b) a 20 cm grid during nominal IEC run conditions. Used in the HOMER device.

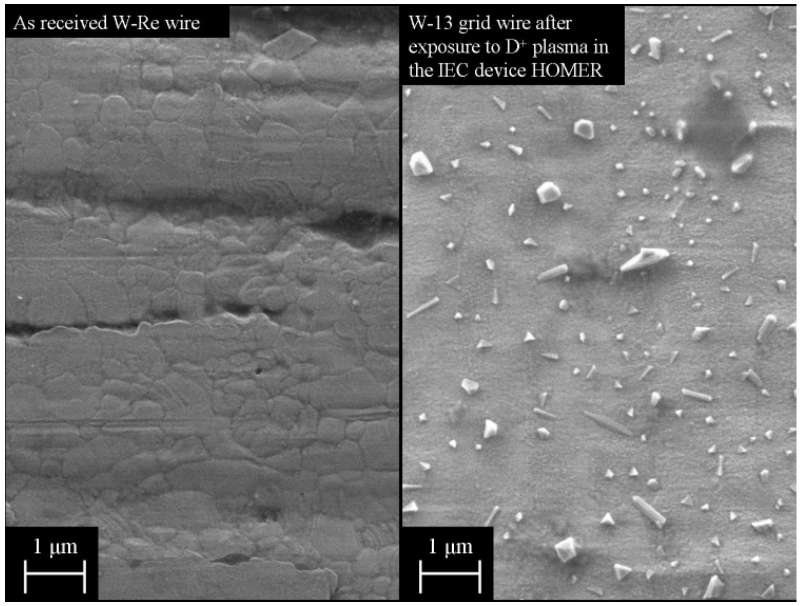

Figure 6-26: SEM photo of W-Re wire as received (left) from the vendor and after exposure to D^+ plasma in the IEC (right), estimates of fluence exposure are 10^{19} D^+/cm^2

A further confirmation of this assertion can be made by the results of Piefer [31], who observed surface modification on cathodes limited the ability to achieve consistently high cathode potentials (Figure 6-27), after continued exposure to He^+. Piefer hypothesized local enhancement of electric fields at the tips of these dendrites caused more frequent arcing and IEC shutdowns. Exposure of IEC cathode grids to deuterium plasma alone does not induce the surface morphology change. Rather, dendritic structures form on grid wires only after exposure to the following plasmas: ^4He, ^3He, or a D – ^3He combination.

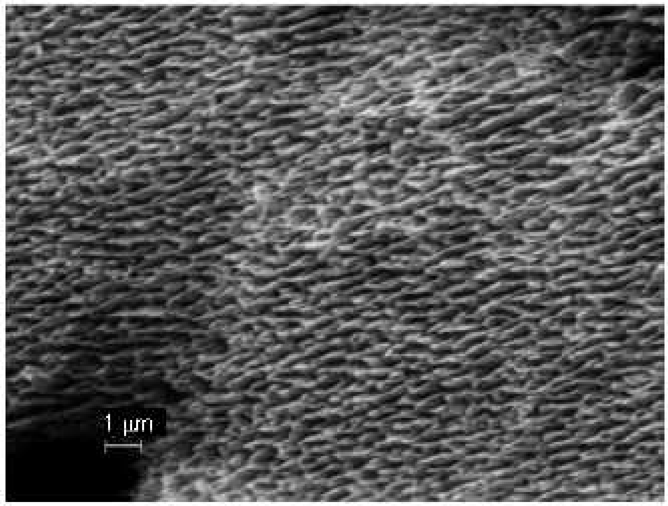

Figure 6-27: W-Re wire from an IEC cathode exposed to $>10^{19}$ He atoms/cm^2 in HELIOS. [31]

Furthermore, in standard operation of the IEC device, high voltage conditioning is initially performed with deuterium plasma. Dendrites, such as those shown in Figure 6-27, result in decreased stability of IEC operations at high voltage. Observations indicate that high voltage performance of grids exposed to He^+ species can be improved by "re-conditioning" them in a solely deuterium plasma. While grids never achieve pre-helium exposure conditioning levels, grids can partially recover their performance. This indicates deuterium plasma exposure may be smoothing the dendritic (or coral) structure induced by helium implantation. The mechanism by which this is accomplished is unclear, but it could be related to surface smoothing due to D^+ sputtering.

It is possible that the morphology observed on IEC grids and materials test specimens implanted in HOMER and HELIOS are initially formed by He^+ implantation, but aggravated by arc spots at or near dendrites and protrusions on the surface. If this is so, one might expect the onset of coral formation to be a "point of no return" for cathode grids. It is not immediately obvious how conditioning could improve if damage was aggravated by arc spots, but it might merit future experimental investigation.

A final possibility exists which could affect the observed surface morphology and erosion measurements on W specimens. That is, electric field enhancement at the tips of the dendrites formed after He^+ implantation. The process occurs if a feature (dendrite or coral protrusion) becomes “pointed” enough to enhance the local electric-field near the tip of the feature. Should the field enhancement exceed the threshold electric-field required for field emission of the given material (in this case W), ohmic heating by the emitted electrons on the “tip” or “point” could cause melting of the feature if sufficient electron current is emitted. The melted material may also undergo extrusion from the surface by electromechanical stresses, or even vaporization, given sufficient electron emission. Mesyats [44] reported that jets, called “ectons,” were ejected from the cathode surface for a wide range of different materials, including metals. The report gives many mechanisms for the production of ectons, one of which is joule heating and melting of surface protrusions initiated by field emission. An independent experiment at the UW IEC laboratory exposed a W-needle to high voltage in HELIOS. Observations supported Mesyats conclusions; and so, these observations are discussed according to their relevance to surface morphology change on flat PCW specimens

The experiment consisted of placing the W-needle in the HELIOS device and exposing it to a series of high voltages between -5 and -30 kV. Figure 6-29 summarizes the experimental setup. It appears that melting occurred on the needle tip due to substantial arcing and field emission. Emission currents of up to ~10 mA were measured. It is worth mentioning that a striking similarity between the morphology induced by the arc spots on the W-needle and the arcs spots on the cathodes reported by Robson and Hancox (Figure 6-29). [40]

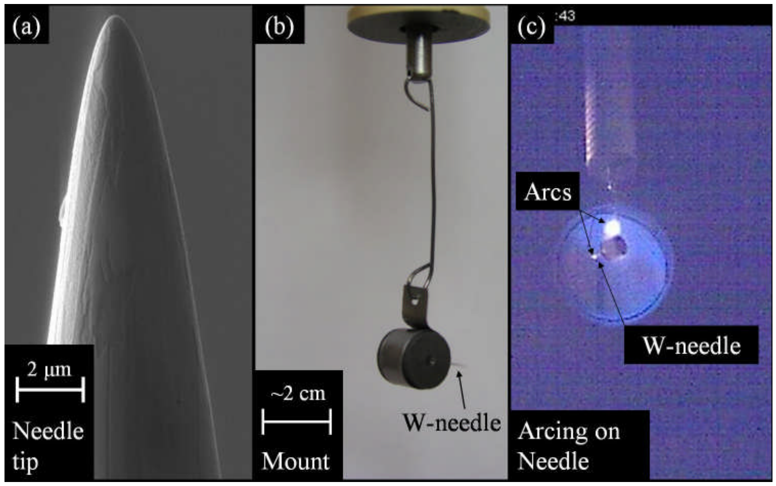

Figure 6-28: (a) SEM micrograph of etched W-needle tip, (b) mounting system for preliminary W-needle "high-pots" and irradiations, and (c) in-situ photograph of arcing occurring on W-needle tip and mount under high voltage. Experiments were performed in the HELIOS device.

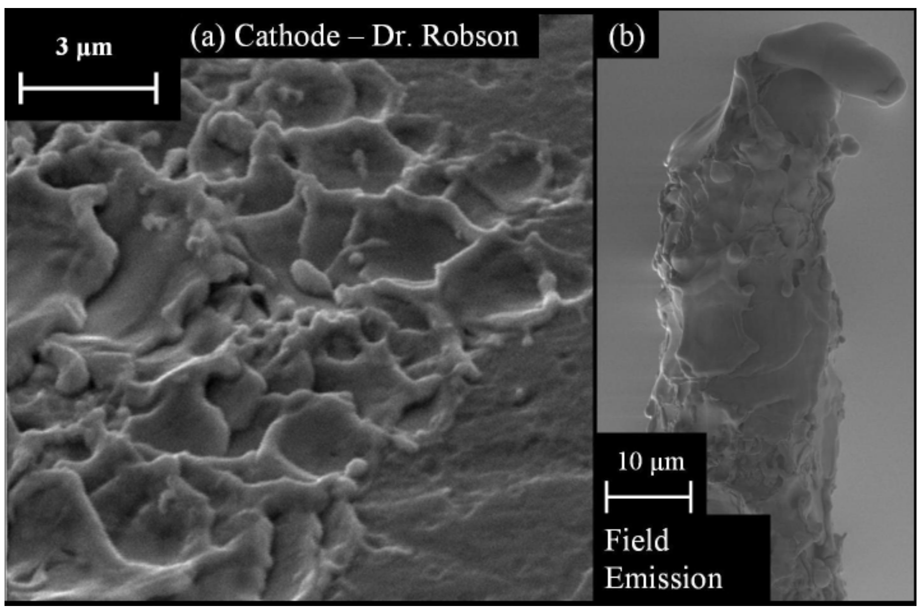

Figure 6-29: SEM photograph comparison of cathode damage observed by Robson and Hancox [40], and (b) a W-needle after field emission under a -30 kV potential in HELIOS without He^+ implantation. Note the change in scale between (a) and (b).

While this report is not specifically concerned with performance of W-needles, the results of these experiments provide useful data that may in fact be applicable to the behavior of flat PCW specimens in the HOMER and HELIOS environments. Given the morphology of the W-needle in Figure 6-29(b), it is necessary to confirm whether field omission could occur on a W-needle under a -30 kV potential. Moreover, if field emission is possible, would ohmic heating from ~10 mA of electron emission be sufficient to melt the W. The ensuing calculation and assumptions were originally performed by Dr. Knowles [45] and confirmed by the author of this report.

On a metal cathode, such as tungsten, field emission will occur if the field strength is approximately 10^7 V/cm or greater [46]. The HELIOS vacuum chamber (radius, 30 cm) acts as the anode and the W-needle acts as the cathode. Under a -30 kV potential, the field strength will be roughly 10^3 V/cm. In the field emission experiment, approximately 1 cm of the needle extended past the carbon mounting holster (Figure 6-28(b)). Since the needles are tapered to a tip diameter of approximately 1 μm, there is an effective field enhancement of approximately10^4. This factor is derived by taking the ratio of the exposed needle to the radius of curvature of the needle tip. The result is increased field strength at the needle tip from 10^3 V/cm to 10^7 V/cm, which is sufficient to initiate field emission on tungsten. It is assumed that the tapered W-needle can be approximated as a thin cylindrical W wire undergoing ohmic heating and purely radiative cooling. The temperature of the wire will be calculated based on the emission current. Emission current is given by i and the resistance of the wire by R. At the melting point of W, electrical resistivity, ρ, is assumed to be ten times greater than the room temperature value. The length of the wire is L, the cross-section area, A_{cs}, and the needle diameter is D. The power dissipated through the tapered needle, $\dot{Q}_D$, is given by the following:

$$\dot{Q}_D = i^2 R = \frac{i^2 L\rho}{A_{cs}} = \frac{i^2 L\rho}{\frac{\pi D^2}{4}} \qquad \text{Equation 6-1}$$

Power dissipated must equal the power radiated, $\dot{Q}_R$, (based on a radiative cooling assumption, because the background gas pressure (~10^{-6} Torr) is too low for convection. Additionally, conduction is not considered because the surface area at the point of contact between the W-Re wire of the sample mount and the molybdenum conductor is very small, see Figure 6-28) and is given in the following equation:

$$\dot{Q}_R = A_{sur}\varepsilon\sigma_{SB}T^4 = \pi DL\varepsilon\sigma_{SB}T^4 \qquad \text{Equation 6-2}$$

Where A_{sur} is the surface area of the needle, ε is the W emissivity (taken as 0.3), σ_{SB} is the Stephan-Boltzmann constant and T is the temperature. Setting Equation 6–1 and Equation 6–2 equal to each other and solving for T yields the temperature of the W-needle tip based on field emission current and the needle's physical dimensions.

Equation 6-3

$$T = \left(\frac{4\rho}{\pi^2\varepsilon\sigma_{SB}}\frac{i^2}{D^3}\right)^{1/4} = \left(\frac{4\left(5x10^{-7}\Omega - m\right)}{\pi^2(0.3)\left(5.67x10^{-8}\dfrac{W}{K^4 - m^2}\right)}\frac{\left(10^{-2}A\right)^2}{\left(2x10^{-6}m\right)}\right)^{1/4} = 3493K$$

The melting point of W is approximately 3300 °C, which indicates that a needle tip of radius ≤2 μm could melt. These two calculations validate the results of the W-needle experiments and might be an indication of what is happening at a much smaller scale on flat W specimens.

The intent of discussing the W-needle studies is to bring application to the implantation experiment on PCW in HOMER and HELIOS, and to answer the following question: does field emission and melting occur on individual dendrites of flat PCW? As previously mentioned, field strengths of 1 kV/cm are not enough to result in field emission; therefore, some mechanism for field enhancement must occur to begin the emission process from the surface. A consultation with Professor Max Lagally of the UW Materials Science and Engineering program, an expert in nano-scale structures and electronic properties, has suggested that field emission from the resultant coral structure at a -30 kV potential is occurring [47]. The extent and effects of this emission are yet to be determined. Gomer [46], one of the pioneers in field emission, describes the effect that ions can have on inducing field emission. If one has an initially clean surface and inadequate field strengths to induce emission, then no field emission will occur. In actuality, small imperfections on the surface allow for points of field concentration or field enhancement. If gas is present, this gas can be ionized and energetically bombard the surface. Gomer states, this will cause pitting, which results in further depression and elevations. In the case of the IEC, He^+ implantation will cause pores to form on the surface of the W. One can imagine a “bridge” or “filament” of W between two pores with some very small radius of curvature (approximately 1000 Å). This acts as a “tip” at which the electric field lines can concentrate and enhance the local electric field. The field strength is governed by:

$$F = {}^{V}\!/_{kr_{impf}} \qquad \text{Equation 6-4}$$

where F is the field strength, k is a constant with a value of approximately 5, and r_{impf} is the radius of curvature of the given imperfection. For the NGW specimen shown in Figure 5–19(e), an average tip radius was calculated for the dendritic protrusions.

Substituting the values of the cathode potential and feature dimensions observed on W materials after implantation experiments, an effective electric field strength of $6x10^8$ kV/cm is derived. This field strength could easily induce field emission from dendrites or at high points between pores.

The preceding analysis demonstrates that is it possible for He^+ to produce the porous "seed" morphology on the W surface, which is intensified by field enhancement. To experimentally verify this possibility, two NGW specimens that were previously implanted to 10^{19} He^+/cm^2 at 1000 ºC (NGW1) and 10^{20} He^+/cm^2 at 1000 ºC (NGW4), in HELIOS, were re-inserted into the device and exposed to high voltage. These specimens were chosen because the coral surface morphology had been well developed (micrographs are presented in Chapter 5). The experimental setup was very similar to that described in Chapter 2 for implantation experiments in HELIOS. Each specimen was placed under cathode potentials ranging from -40 to -75 kV in high vacuum (7 μTorr). Total exposure times at these potentials were approximately 30 minutes for both specimens. Sample mass was measured pre- and post-exposure to determine if additional material had been eroded.

Results showed that no significant mass loss occurred after high voltage exposure (Figure 6-30), despite numerous arcs observed on the current measurement software and video recording data. It should be reiterated that this specimen had pre-existing dendrites which have been postulated to serve as sites for cathode arc spots and further aggravate the morphology induced by implanted He^+. The nature of the experimental setup in HELIOS requires extensive handling of specimens. It is possible that the minor mass loss measured on these NGW specimens after exposure to a high voltage vacuum field (20 –

40 μg) is just as likely to be a result of repeated handling as it is a result of arcing. For comparison, Figure 6-30 plots the mass loss for these two specimens before and after He^+ implantation (red and blue data points). Even if the mass loss after high voltage exposure is due to sputtering caused by field emission or arcing, it is miniscule compared to erosion measurements after implantation. A steady-state current of 0.2 to 0.3 mA was observed during each of the NGW high voltage exposures transients showing higher current values.

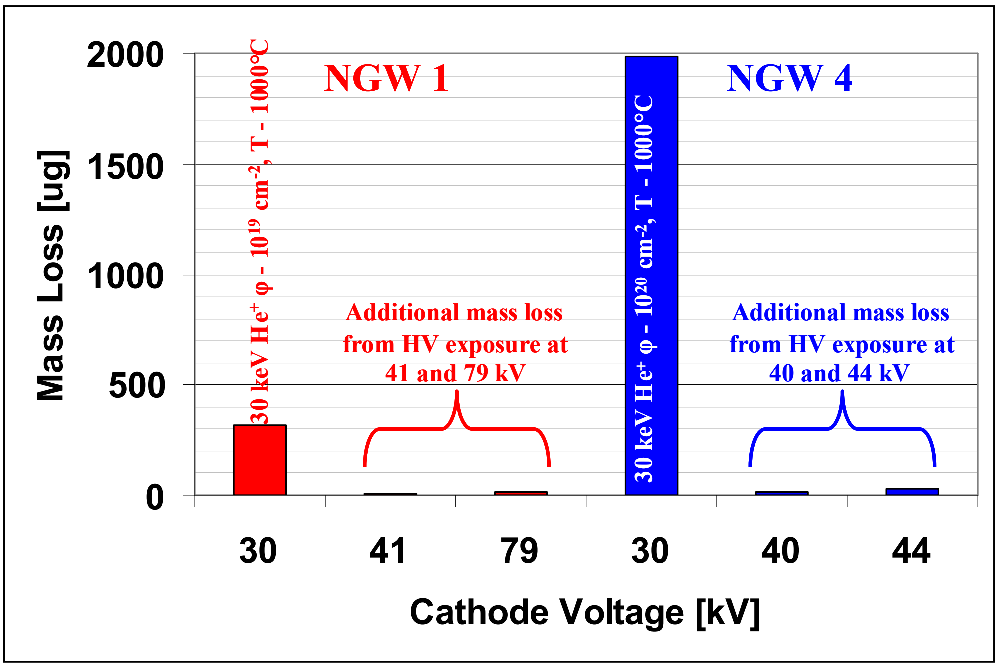

Figure 6-30: Mass loss results on nano-grain W (NGW). The red bars indicate mass loss on sample NGW1 and the blue bars mass loss on sample NGW4. The two tallest bars captioned with fluence and temperature data indicate mass loss resulting from the He^+ implantation at a 30 kV cathode potential. The four lesser red and blue bars called out with brackets indicate additional mass loss on these two NGW specimens resulting from high voltage exposure (without the presence of ions) on the previously implanted specimens, and range from 20 – 40 μg. Experiments performed in HELIOS.

This supports previous sources [44,46,47] indicating that field emission is occurring in the classical IEC implantation setup and verifies the preceding calculations. Yet, it does not appear to have a large effect on erosion. If a "background" field emission current of this magnitude exists on all implantation experiments, it would affect fluence measurements by 10 to 20%, which is at most a 10% increase from assumed fluence errors in prior experiments. The measurements from the experiments performed on NGW imply that field emission does occur, as evidenced by a small steady-state current, and likely plays a role in the evolution of the surface morphology on He^{+} implanted W specimens, but it does not substantially contribute to erosion measurements.

A zeroth order computational benchmark of these experiments was performed using the ANSYS® program. The goal was to more accurately model the electrostatic field strengths near the surface of W specimens. Initial simulations modeled a single "bump" on a flat surface with heights of 1 and 2 μm with various tip radii from 7.5 to 60 nm. The results are presented in Figure 6-31.

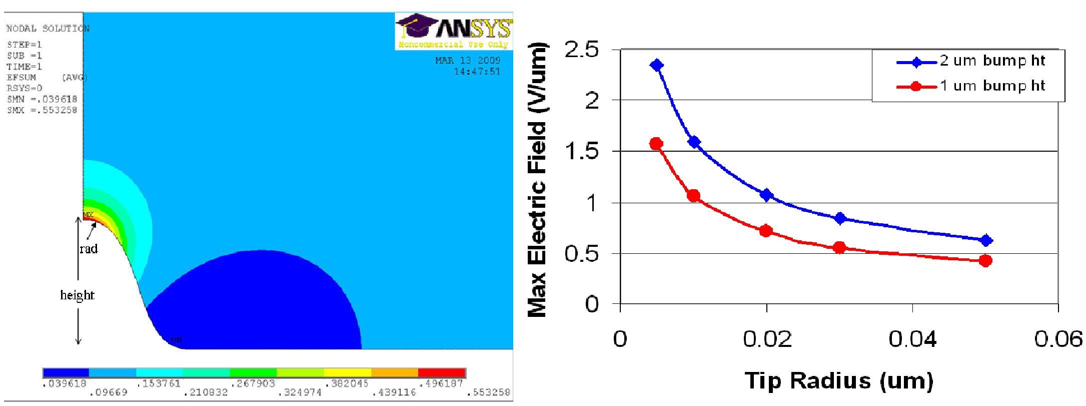

Figure 6-31: The left-hand picture shows the geometry of a micron-sized bump input into the ANSYS program. The graph on the right shows the maximum simulated electric field strength at the surface of the bump feature for bump heights of 1 and 2 μm and tip radii ranging from 7.5 to 60 nm.

Results show that the surface electric-field strength is very near those calculated previously in this discussion and within an order of magnitude for all tip radii. More accurate modeling of coral W surfaces would be achieved by placing many of these bumps on a surface in some periodic fashion. In addition, the length to radius ratio of the bump illustrated in Figure 6-31 is modest in comparison to some of the protrusions observed on surfaces of W specimens implanted with He^+.

6.2.3. Summary of observations on hypotheses

To reiterate, it does not appear the minor softening of spectra in HOMER & HELIOS from the intended 30 keV He^+ is responsible for the morphology difference between those devices and MITE-E. In addition, the damage layer remaining from mechanical polishing on PCW does not appear to be the culprit of the unique porous, coral structure generated in the classic IEC implantation regimes. Finally, the effective decrease in implantation range of the ions due to multi-angular bombardment of HOMER and HELIOS, in itself, does not explain the absence of blisters or the very near surface bubble formation. From the discussion presented in this chapter, one expects the differences responsible for the characteristic morphology generated by these three devices could be coming from one or two processes: 1) variation in sputtering mechanisms between the MITE-E and the classic IEC devices and 2) field emission effects resulting from exposure to enhanced vacuum fields in HOMER and HELIOS. It is likely that both of these processes are having an effect. In the MITE-E, morphology changes are dictated by sputtering effects dependent upon the exposed crystalline plane in concert with the formation of pores and blisters resulting from coalesced helium bubbles. In the device HOMER, multi-angular impact and sputtering produces a uniformly porous layer whose morphology is further agitated by field emission from nano-scale surface features in the presence of enhanced electric field gradients.

6.2.4. Final comparison of surface morphology change and tungsten's viability as a fusion material

Figure 6-32 summarizes the results of all of the materials irradiation experiments performed on tungsten metallics in the University of Wisconsin IEC apparatus and presented in Chapters 2 and 5 of this report. CCV, W-coated CCV, and CVD SiC are omitted due to the lack of statistically significant data at fluence and temperature parameters where the materials need to acceptably weather ion bombardment. The plotted lines of Figure 6-32 each represent the author's best estimate of a material's response to He^+ implantation, and of course, are limited to the available data points for the given material. Regions to the right of the curves indicate at what temperatures and fluences the materials would not be viable for application in an IFE design with a dry first wall, or in an MFE device with high alpha flux to the divertor plate. In each case, these curves are far past the "threshold curve" for what is considered to be unacceptable damage in each of the investigated materials. Recent experiments in the MITE-E have allowed the extension of the materials viability assessment curve down to 500 °C, whereas previous data on polycrystalline W implanted in the devices HOMER and HELIOS only extended to ~800 °C. At high temperatures (>800 °C), the lifetime of W metallics is near 10^{18} He^+/cm^2, while at lower temperatures (<800 °C) the lifetime of these materials increases slightly to the mid-10^{18} He^+/cm^2. Lower implantation temperatures on W specimens does not inhibit extensive surface morphology change, although the effects of the helium implantation is postponed to slightly higher fluences than those specimens implanted at temperatures >800 °C.

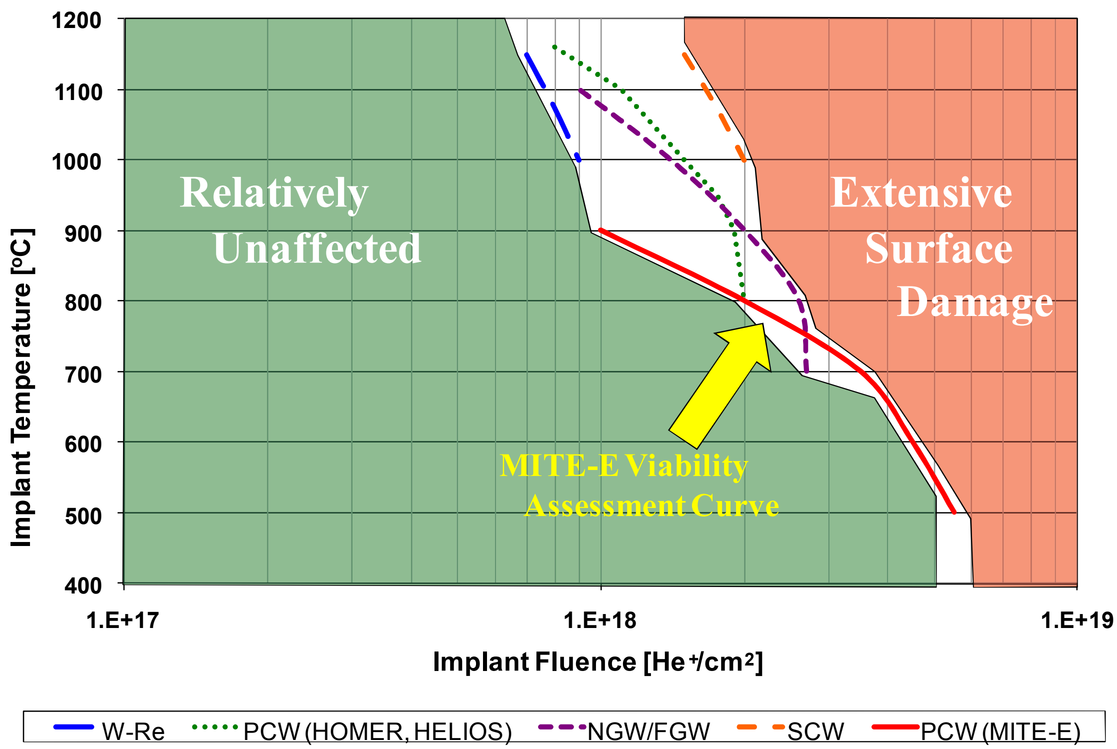

Figure 6-32: Materials viability assessment curve for W metallics implanted in HOMER, HELIOS, and the MITE-E. Samples which have acceptable surface morphology changes predominantly lie in the "Relatively Unaffected" region and specimens with unacceptable surface damage predominantly lie in the "Extensive Surface Damage" region. The assessment curve generated by the MITE-E (black curve) is pointed out.

6.3. References for Chapter 6

1. Cipiti, B.B. (2004). The fusion of advanced fuels to produce medical isotopes using inertial electrostatic confinement. (Doctoral dissertation, University of Wisconsin - Madison).

2. Sethian, J.D., et al., (2003) Fusion energy with lasers, direct-drive targets, and dry wall chambers. *Nuclear Fusion*, 42, 1963.

3. Cipiti, B.B. and Kulcinski, G.L., (2005) Helium and deuterium implantation in tungsten at elevated temperatures. *Journal of Nuclear Materials*, 247, 298-306.

4. Radel, R. F. and Kulcinski, G.L., (2005) Implantation of D and He in W-coated refractory carbides. *Fusion Science and Technology*, 47 (4), 1250.

5. Radel, R. and Kulcinski, G., (2007) Effects of high temperature pulsed helium implantation on tungsten surface morphology. *Fusion Science and Technology*, 47 (3), 544-548.

6. Radel, R. F. and Kulcinski, G. L., (2007) Implantation He^+ in candidate fusion first wall materials. *Journal of Nuclear Materials*, 367, 434-439.

7. Zenobia, S. J. and Kulcinski, G. L., (2006) Effects of He+ implantation on the surface morphology of SiC. Prepared for 17th ANS Topical on Fusion Energy (TOFE), UWFDM 1339.

8. Zenobia, S. J. et al., (2009) High temperature surface effects of He^+ implantation in ICF fusion first wall materials. *Journal of Nuclear Materials*, 389, 213-220.

9. Zenobia, S. J. and Kulcinski, G. L., (2009) Retention and surface pore formation in helium implanted tungsten as a fusion first wall material. *Fus. Sci. and Technology*, 52, 544.

10. Zenobia, S. J. and Kulcinski, G., (2009) Formation and retention of surface pores in helium-implanted nano-grain tungsten for fusion reactor first-wall materials and divertor plates. *Physica Scripta*, T138, 014049.

11. Iwakiri, H. et al., (2002) Effects of helium bombardment on the deuterium behavior in tungsten. *Journal of Nuclear Materials*, 307-311, 135-138.

12. Nishijima, D. et al., (2005) Characteristic changes of deuterium retention on tungsten surfaces due to low-energy helium pre-exposure. *Journal of Nuclear Materials*, 337-339, 927-931.

13. Alimov, V. Kh. et al., (2010) Surface morphology and deuterium retention in tungsten exposed to low-energy, high flux pure and helium-seeded deuterium plasmas. *Physica Scripta*, T138, 014048.

14. Kajita, S. et al. (2009) Formation process of tungsten nanostructure by the exposure to helium plasma under fusion relevant plasma conditions. *Nuclear Fusion*, 49, 095005.

15. Eckstein, W. and Laszlo, J. (1991) Sputtering of tungsten and molybdenum. *Journal of Nuclear Materials*, 183, 19-24.

16. Ziegler, J. F., (2010) *SRIM version 2003*. www.srim.org.

17. Rusponi, S. et al., (1999) Patterning a surface on the nanometric scale by ion sputtering. *Applied Physics Letters*, 75 (21), 3318-3320.

18. Valbusa, U. et al., (2002) Nanostructuring surfaces by ion sputtering. *Journal of Physics, Condensed Matter*, 14, 8153-8175.

19. Vasiliu, F. et al., (1975) SEM investigation of iron surface ion erosion as a function of specimen temperature and incidence angle. *Journal of Materials Science*, 10, 399-405.

20. Southern, A. L. et al., (1963) Sputtering experiments with 1- to 5-keV Ar^+ ions. *Journal of Applied Physics*, 34 (1), 153-163.

21. Carlston, C. E., et al, (1965) Effect of elevated temperatures on sputtering yields. *Phys. Rev.*, 138 (3A), 759-763.

22. Private communication, (May, 2010) Dr. Max Lagally.

23. Williams, J. S., (1986) Materials modifications with beams. *Rep. Prog. Phys.*, 49, 491-587.

24. Whitton, J. L. et al., (1976) Title. *Symposium on Physics of Ionized Gases*, 76 ed (Lublyana: Yugoslavian Inst. Phys.), p. 247.

25. Whitton J. L. et al., (1980) Influence of surface morphology on the angular distribution and total yield of copper sputtered by energetic argon ions. *Applied Physics Letters*, 36 (7), 531-533

26. Behrisch, R and Scherzer, B. M. U., (1982) Surface topography due to light ion implantation. *Sputtering by Particle Bombardment*, 2, 198.

27. Fu, Z. et al., (2004) Thermal desorption and surface modification of He+ implanted into tungsten. *Journal of Nuclear Materials*, 329-333, 692-696.

28. Tokunaga, K. et al., (2004) Synergistic effects of high heat loading and helium irradiation on tungsten. *Journal of Nuclear Materials*, 329-333, 757-760.

29. Das, S.K. and Kaminsky, M., (1975) Radiation blistering in metals and alloys. *Proceedings of the 'Symposium on Radiation Effects on Solid Surfaces'*, Advances in Chemistry Series.

30. Radel, R. F. (2007). Detection of highly enriched uranium and tungsten surface damage studies using a pulsed inertial electrostatic confinement fusion device (Doctoral dissertation, University of Wisconsin – Madison).

31. Piefer, G. R. (2006). Performance of a low-pressure, helicon driven IEC ^{3}He fusion device (Doctoral dissertation, University of Wisconsin – Madison).

32. Janev, R. K., ALADDIN Database, IAEA-AMDIS (2010).

33. Emmert, G. and Santarius, J., (2010) Atomic and molecular effects on spherically convergent ion flow. I. Single atomic species. *Physics of Plasmas*, 17, 013502.

34. Emmert, G. and Santarius, J., (2010) Atomic and molecular effects on spherically convergent ion flow. II. Multiple molecular species. *Physics of Plasmas*, 17, 013503.

35. Mills, K. et al., (1985) Metals handbook ninth edition: volume 9 metallography and microstructures. Metals Park, Ohio: American Society for Metals.

36. Egle, B. J. (2010). Nuclear fusion of advanced fuels using converging focused ion beams (Doctoral dissertation, University of Wisconsin – Madison)

37. Private communication, (2010) Dr. John Santarius.

38. Private e-mail communication, (December, 2008) Dr. Bertie Robson.

39. Craston, J.L., et al., (1958) The role of materials in controlled thermonuclear research.in peaceful uses of atomic energy. (United Nations, Geneva, 1958), Vol. 32, p. 414.

40. Robson; A. E. and Hancox, R., (1959) Choice of materials and problems of design of heavy current toroidal discharge tubes. *Proc. IEE,* 106A (2), 47.

41. Dr. Bertie Robson and Dr. John Sethian, private communication 2009.

42. University of Wisconsin IEC Experimental Logbook. Run Numbers 2016 – 2044.

43. Yoshida, N., (1999) Review of recent works in development and evaluation of high-Z plasma facing materials. *Journal of NuclearMaterials*, 266-269, 197-206.

44. G.A. Mesyats, "Ectons and their role in plasma processes," *Plasma Physics and Controlled Fusion*, 47, A109-A151, 2005.

45. Dr. Knowles, ESLI private communication, June 2008.

46. R. Gomer, *Field Emission and Field Ionization*, American Vacuum Society Classics, American Institute of Physics, NY 1993.

47. Professor Lagally, private communication, February 9th 2009.

CHAPTER 7. CONCLUSIONS

Overall, the Materials Irradiation Experiment proved to be a successful project. The primary goal of the MITE-E – to decouple implantation temperature from input ion power, which in HOMER and HELIOS was set by the cathode voltage and current, in order to increase the parameter space in which materials are implanted – was met. The MITE-E expanded the total range of implantation temperatures and ion energies, and it increased dynamic range of the implanted dose rate from those of HOMER and HELIOS.

- In initial testing, the MITE-E produced and implanted ions ranging in energy from 20 keV to 130 keV, and achieved implantation temperatures ranging from 400 °C to 1100 °C.
- A custom high voltage feedthru and stalk design successfully operated cathode voltages of -130 kV while current sense circuitry measured ion currents ranging from 20 to 180 μA with an error ±2 μA at an ion current of 75 μA.

Helium ion implantation of polycrystalline W in the MITE-E resulted in three distinct surface morphology changes as described by the terms: "grass", "pitting," and "blisters."

- "W grass" occurs at implantation temperatures ≥ 700 °C, and at fluences greater than ~10^{19} He^+/cm^2 and exhibits strong directionality based dependent on crystallographic orientation.
- "Pitting" of polycrystalline W is widespread for temperatures ≤ 700 °C and fluences above ~10^{19} He^+/cm^2 and appears to be driven by sputtering. Both "W grass" and "pitting" morphologies are temperature dependent and require fluences ≥10^{19} He^+/cm^2 to develop.

- Implantation produces "blisters" at all examined implantation temperatures as implant fluences exceed ~5x10^{17} He^+/cm^2, but are overwhelmed by the "grass" and "pitting" morphologies at higher doses.
- Visible formation of pores occurs on W surfaces after implant fluences reach ~10^{17} He^+/cm^2 at all implantation temperatures, but sub-surface layers of visible pores are not observed below 700 °C.

There is a fundamental difference in the way polycrystalline W surfaces respond under bombardment by 30 keV helium ions when irradiated in the HOMER/HELIOS devices and the MITE-E. Coral surface morphologies inherent to polycrystalline W implanted in HOMER and HELIOS were shown to develop from interplay between sputtering at multi-angular ion incidences, ion energy spectra, and field emission from nano-scale surface features. In the MITE-E, highly orientated "grass" and "pitting" morphologies observed on helium implanted polycrystalline W are induced by preferential sputtering of crystallographic planes exposed to the ion beam that is normally incident to the surface.

As a materials implantation apparatus, both HOMER and HELIOS are better suited to simulate magnetic fusion reactor environments where particles impact the first wall and divertor over a wide range of angles and energies with respect to the surface normal. On the other hand, the MITE-E lends itself to simulation of inertial fusion reactor environments in which the particle trajectories intersect the first wall armor perpendicularly to the first wall's surface.

Among the three UW IEC implantation facilities, a wide range of materials were tested for resilience to helium ion bombardment at fusion reactor relevant conditions.

These include: silicon carbide, carbon velvet, W-coated carbon velvet, fine-grain W, nano-grain W, W needles, and single- and polycrystalline W. None of these materials appear to be resistant to the bombardment of helium atoms while they are at temperatures > 800 °C. However, unalloyed W appears to have the superior resistance of all the materials tested in this harsh environment.

CHAPTER 8. RECOMMENDATIONS FOR FUTURE WORK

Although there has been a significant improvement in the understanding of surface morphology changes brought on by high temperature He^+ bombardment of W using the Materials Irradiation Experiment (MITE-E), there exists a wide array of parameters and experimental variations as of yet, unexamined. Nearly all of the results discussed by the author of this thesis were acquired after implantation using 30 keV He^+. MITE-E allows the energy of the implanted ions to be extended up to 150 keV to better simulate the IFE energy spectrum and down to 10 keV to simulate divertor conditions in MFE devices. Modifications to the high voltage feedthru can also make operation using 200 keV ions possible. Moreover, excluding high voltage breakdown, the current power supply at UW-Madison is capable of supplying -300 kV (300 keV ions). Higher energy ions allow simulation of a larger portion of the threat spectrum of helium ions in inertial fusion reactor studies, and will determine to what degree the current results and trends can be extended to higher energies. Beam-target fusion studies using D-D or D-^{3}He advanced fuels would also benefit from increasing the beam energy; although, this should be a secondary study to primary investigations of the surface morphology effects from helium implantation on candidate materials for plasma facing components in fusion reactors.

The flexibility in implantation temperature provided by the MITE-E allows detailed fluence scans to be performed at a wide range of temperatures. Up to this point, fluence scans have not been applied to W at temperatures other than 900 °C. Such scans, between 400 – 1000 °C, will supply important data regarding the threshold for surface damage for a large range of reactor relevant temperatures and should be the starting point of future investigations with the MITE-E. One experimental improvement necessary to achieving this task is to eliminate the spatial variation in the ion beam's density profile over the specimen's surface. Section 5.2.1 showed a central irradiated region, ~5-6 mm in diameter, on implanted specimens which received the majority of the total implanted charge from the beam. This effect introduced some uncertainty into the fluence measurements, which is common to the implantation devices HOMER and HELIOS, but that the MITE-E was designed to eliminate. Through optimization of the extraction aperture size, focus lens and extraction lens spacing, this improvement may be accomplished. The SIMION® program, coupled with experimental verification in the MITE-E, should be used to guide this modification of the ion gun module.

The results of this thesis revealed that the surface morphology change on a polycrystalline W is highly sensitive to the angle of incidence of the incoming ion and the crystallographic plane exposed to the beam. This phenomenon indicates that specific grains are more resilient to helium implantation than others (Section 6.2.1) and merits further investigation. On polycrystalline specimens, the electron backscatter diffraction (EBSD) analysis technique could be used to map the orientation of individual grains on the specimen surface prior to and following implantation. Such information will help determine which of the crystallographic planes (grains) are more, or less, resilient to helium implantation. The next set of experiments in the MITE-E should include such analysis. Further expansion of these experiments might employ single-crystalline W specimens to be implanted which have the same crystallographic orientation as grains that have shown superior robustness against helium sputtering and bubble formation.

One investigation which would further address the formation of the coral morphology on W, after helium ion implantation at 30 keV, would be to measure the angular distribution of implanted ions in the HOMER device in both pulsed- and steady-state implantation modes. Any such investigations would serve as a complement to the studies presented in this thesis, but they are not essential to continued research using the MITE-E.

For the porous and lamellar structure exhibited by the helium implanted W in Section 6.2.1 (Figure 6-5), it was hypothesized that a “mask” of WC or WN (or some other self-forming impurity) may be formed sporadically on the surface of the specimens. When implanted, the “unmasked” regions are preferentially eroded away by sputtering, leaving the lamellar structure. Several local analysis techniques should be utilized to diagnose the chemical composition on or near the tips of these lamellar structures and determine if a more sputter resistant layer is present. One possible method is energy dispersive spectrometry (EDS).

It has been observed that the surface of W specimens is darkened after implantation with He^+. The reflectivity or emissivity of the W surface should be measured before and after implantation to determine the magnitude of any changes in the reflectance or emittance of the W specimen surface. In addition, a campaign should be initiated which attempts to model the different morphologies on the W surface after He^+ implantation. It is also recommended that the surface morphology change on W resulting from helium implantation at different dose rates be investigated.

At lower implanted fluences ($<10^{17}$ He^+/cm^2), transmission electron microscope (TEM) analysis should be performed to study the evolution of helium clusters and bubbles as they form in the W matrix. This analysis might prove especially useful after data is gathered regarding the resilience of different grains (based on crystallographic orientation to the ion beam) to helium sputtering and bubble formation. Helium retention measurements on W specimens implanted in the MITE-E will be highly valuable when used in tandem with the aforementioned studies.

The campaign to assess a wide range of materials (such as WC, WN, W-1%LaO_2, and W-1.1%TiC) should also continue. This should include engineered tungsten materials and alloys, as well as other refractory metals and nonmetals.

Finally, the species of ions implanted could also be varied. Hydrogenic species retention (especially that of tritium) is an integral part of any fusion reactor system; and so, surface morphology changes and retention characteristics resulting from implanted hydrogen, deuterium, or tritium warrants investigation.